UNIVERSITÁ DEGLI STUDI DI MILANO

DEPARTMENT OF PHYSICS

PHD SCHOOL IN PHYSICS, ASTROPHYSICS AND APPLIED PHYSICS

CYCLE XXXV

Studies of coherent Free-Electron Lasers driven by compact Linacs or by plasma wakefield accelerators

---

Disciplinary Scientific Sector FIS/07

PhD Thesis of:
Michele Opromolla

Director of the School: Prof. Matteo PARIS
Supervisor: Prof. Vittoria Petrillo
Co-Supervisor: Prof. Giorgio Rossi

A. Y. 2022-2023

Abstract

Free-Electron Lasers (FELs) constitute the last generation of synchrotron light sources: they are conventionally driven by a radio-frequency linear electron accelerator (LINAC), where the electron beam is accelerated to relativistic energies, followed by a chain of undulator magnets, which force the electron beam to oscillate and emit radiation. High brightness, tunable and transversely coherent radiation pulses with unique properties are finally delivered to the downstream experimental stations for a wide range of applications in the fields of physics, biology, medicine and chemistry. External seeding techniques aimed at improving the intrinsically poor temporal coherence and shot-to-shot stability of a FEL starting from shot noise have been proposed and experimentally demonstrated. State-of-the-art fully coherent FELs make use of an external coherent signal, which is basically a high-power laser system seeding and imprinting its coherence properties on the electrons at the undulator entrance, and exploit seeded schemes based on frequency up-conversion to increase the low frequency of the seed laser and generate fully coherent radiation at shorter wavelengths. Independently of the specific seeded scheme, the output FEL radiation properties, such as wavelength and repetition rate, strongly depend on those of the seed laser. In particular, the repetition rate capability of conventional high-power lasers is limited to few kHz at maximum, which is incompatible with the MHz-class ones of a superconducting LINAC, while their wavelength limits the minimum output wavelength that can be achieved with reasonable harmonic up-conversions: the study of alternative seeding sources and FEL configurations overcoming this limitation, thus exploiting the potentials of superconducting LINACs, is the new frontier of FEL science. Such research line has synergies with another ambitious and innovative frontier of accelerator science, the study and development of plasma-based accelerators as well as advancements towards their application in light sources, whose ultimate goal is to make advanced radiation sources available to a wide range of users with the realisation of compact user facilities that could be built in small-scale laboratories.

This thesis deals with theoretical and numerical studies of novel schemes for a fully coherent FEL driven by a compact LINAC at high repetition rate or by a plasma-wakefield accelerator. Coherent and high repetition rate FEL pulses would enable high resolution experiments and more data collection in shorter experimental times respectively, greatly improving the ongoing science at FELs by supporting new experiments. In this scenario and in the framework of the

MariX and BriXSinO projects in Milan, Italy, I investigated the FEL oscillator (FELO) configuration in different spectral regions from the THz down to the X-rays by means of a simulation code, written in Fortran, which iterates the required simulation steps for its study.
Based on the acquired knowledge of the FELO scheme, producing high-power coherent pulses suitable for FEL seeding, this thesis proposes two novel FEL oscillator-amplifier setups capable of generating high repetition rate and coherent radiation at short wavelengths in the tender X-ray range ($0.3 - 0.5$ nm). In these two schemes, the seed pulses are provided by an Extreme-Ultra-Violet (EUV) FELO equipped with Molibdenum/Silicium multilayer mirrors and frequency up-conversion based on the electron beam phase space manipulation is performed. The first proposed scheme, seeded by the EUV FELO, similarly to a fresh bunch High-Gain Harmonic Generation (HGHG) FEL scheme, is a three-stage harmonic FEL cascade made of different undulator sections, where the seed modulates the electron bunches inducing non-linear phase space motions and the emission of higher harmonics in the following undulators. FEL emission in the final radiator up to the 35th harmonics of the FELO wavelength has been predicted by simulations, with the generaton of $10^9 - 10^{10}$ coherent photons per shot in the tender X-ray range at 0.5 MHz. The same EUV FELO has been considered for seeding an Echo-Enhanced Harmonic Generation (EEHG) FEL cascade: the generation of intense ($10^8 - 10^{10}$ photons per shot), ultra-short (down to 1 fs) and coherent FEL pulses up to the 50th harmonics of the seed has been simulated, demonstrating a higher versatility, tunability and efficiency.

The second topic of this thesis is the ongoing collaboration with the SPARC_LAB laboratory of INFN in Frascati in the framework of the EuPRAXIA project: objects of this collaboration are the demonstration of FEL lasing with a compact beam-driven plasma-wakefield accelerator at SPARC, whose plasma module is made of a cm-scale, 3D-printed capillary, and the design study of the EuPRAXIA FEL beamlines.
I contributed to the analysis of the experimental data obtained in two experiments at SPARC and the connected simulation of the FEL process. Single-spike FEL amplification at about 827 nm from shot noise with up to tens-nJ energy, characterized by high shot-to-shot energy fluctuations, has been measured and observed from both the experiment and simulations. A second experiment with the same FEL, driven by the plasma-accelerated electron beam and seeded by a portion of the same laser used for the electron photo-emission, has shown increased energy levels and stability conditions. This cumulative thesis finally presents the still ongoing design study of the second beamline of the EuPRAXIA@SPARC_LAB project, a compact and seeded low-energy beamline in the standard HGHG configuration, which can be driven by either the plasma accelerator or the EuPRAXIA X-band LINAC. Simulations of its performances in the whole spectral range of operation and in the two electron

beam modes are compared, showing the production of fully coherent single-spike pulses in the Vacuum-UV range from 50 to 180 nm starting from a long wavelength state-of-the-art laser pulse.

Acknowledgements

My PhD has occurred in a very particular and difficult period for everyone, in which the COVID pandemic and the related economic crisis, as well as the Russian crazy war to Ukraine with its huge effects on the world relations and energetics, have dominated for three long years. My original PhD plan included a period at Stanford Linear Acceleration Center: due to this situation, it had to be modified. During the last year of PhD, the theft of my laptop, including most of the PhD materials and documents, has nicely closed these long hard times.
I need to thank all the people that helped me overcoming all the negative sides of this period.

I would like to express my thanks to: my supervisor Vittoria Petrillo, for her precious human and scientific help since the Master thesis and throughout all the PhD studies. Her presence has been always important. A special thanks goes to Massimo Ferrario, who suggested me Vittoria Petrillo as thesis supervisor.
I want to thank my parents Paolo and Diana for their support, as well as my brothers Andrea and Davide.

I need to thank all my friends which have been always present for a good time on videocall, or better together when possible, and helped me in living this period in a more positive way.
I want to thank Marcel Ruijter, Sanae Samsam & Marcello Rossetti Conti for their comradery.

I want to thank the research group with which I collaborated during the last 5 years of academics: Luca Serafini, Marcel Ruijter, Marcello Rossetti Conti, Andrea Rossi, Alberto Bacci, Illya Drebot, Sanae Samsam and Cesare Maroli, for their collegiality and friendly discussions.

Contents

List of Figures

List of Tables

Chapter 1

Introduction: the Free-Electron Laser

Free-Electron Lasers (FELs) constitute the last generation of synchrotron light sources (a brief overview of light sources is given in Appendix A): they are linear machines, where the radiation is longitudinally emitted by a high-brightness relativistic electron beam propagating in the periodic field of an undulator magnet, through which the electron beam kinetic energy is transformed into electromagnetic radiation with laser-like properties.

In analogy to conventional lasers, in 1971 John Madey described its emission mechanism by means of a quantum mechanical description, based on stimulated emission between quantum states of the electron beam [1]. The name of this device, Free-Electron Laser, comes from the fact that the electrons are not bound to any optical medium; moreover, the lasing medium is the electron bunch itself, whose power corresponds to the pump power, offering continuously tunable resonant wavelength by changing either the energy of the driving electron beam or the strength of the undulator field [2, 3]. Thanks to their high tunability, these machines can be used as sources of coherent light down to spectral regions such as the X-ray range, where conventional lasers are not available.
The FEL process takes place in vacuum, so that another important advantage with respect to solid-state sources of coherent radiation is that the amplification is not constrained by dispersion or absorption processes. Appendix B deals with the FEL theory.

Since the first studies in the late 1960s [4, 5] and their implementation [6, 7], it has been clear that FELs are capable of bridging the gap between conventional electron-based sources, such as synchrotrons, and lasers, allowing experiments intrinsically impossible at storage ring-based facilities and to explore nature at ultra-small spatial and ultra-short temporal scales. Appendix A also contains a small digression on the science enabled by X-ray FEL facilities compared to Synchrotrons.

1.1 FEL physics and configurations

As shown in Appendix B, the resonant interaction between the transverse motion of the wiggling electrons, the undulator magnetic field and the emitted transverse electromagnetic field leads to an instability that converts the electron kinetic energy into the electromagnetic radiation.

Accelerator technology is the basis for both synchrotron radiation sources and FELs: however, while synchrotron radiation is emitted incoherently by independent radiating electrons, the FEL radiation process benefits from multi-particle coherence, resulting in coherent photon beams (10 to 100 times better than in synchrotron beam lines) combining the intensity and coherence of a laser with the broad spectral coverage of a synchrotron. In addition, depending on the repetition rate of the FEL, the average flux and brilliance can exceed the ones achieved by storage rings.

Thanks to their high peak brilliance, implying a significant number of photons impinging on the sample in a very short time, FELs allow multi-photon processes and time-resolved experiments; on the other hand, the high average brilliance enables more sophisticated and selective experiments in a shorter experimental time [8].

FELs are highly flexible and tunable radiation sources: the wavelength emission range as well as the pulses' bandwidth, peak power and temporal structure can be tailored for any kind of experiment, making different design strategies possible, including multi-frequency operation, polarization control and pump-probe configurations with naturally synchronized beams.

On the contrary, other laser light sources are limited in tunability: for instance, Optical Parametric chirped pulse Amplifiers offer large wavelength tune-ability in the UV regime and laser diodes radiate down to about 346 nm, but the soft and hard X-ray regime are out of reach. The FEL therefore offers to the users the unique possibility of tailoring the radiation characteristics for specific applications.

Scaling laws

Some important scaling laws governing the FEL emission are here reported, while more details on FEL theory and their derivation are given in Appendix B.

FEL sources are driven by a high-brightness relativistic electron beam previously accelerated in a linear accelerator (LINAC) up to an energy $E = \gamma mc^2$ (γ being the electron Lorentz factor) and sent through an undulator, whose main parameters are its period length λ_u and its normalized magnetic field

strength $a_u = eB_0/(\sqrt{2}mck_u)$, usually referred to as undulator parameter[1], where e represents the electron charge, m its mass, c the speed of light, B_0 the undulator peak on-axis magnetic field and $k_u = 2\pi/\lambda_u$ the undulator wave number.

The undulator transverse periodic magnetic field induces transverse sinusoidal oscillations of the electron beam, resulting in the longitudinal emission of synchrotron radiation at each bend of their trajectory, and allowing an energy exchange with the co-propagating electric field. Appendix B also deals with basic concepts of undulator physics.

The radiation field naturally moves faster than the electron bunch: by reducing the mean longitudinal velocity v_z of the bunch, the transverse oscillations can enhance the rate at which the emitted radiation slips ahead the electrons in the bunch. Depending on the electron-radiation relative phase, the electrons can indeed gain or lose energy: the electrons oscillate in phase with the radiation field, losing energy for the benefit of the radiation field, when the radiation slips one optical wavelength per undulator period, meaning that the optical wavelength λ is such that $\lambda = \lambda_u(1 - v_z/c)$.

The field power grows with the rate of the electron energy loss, and the energy modulation induced by the radiation field within the undulator is then converted into a spatial modulation of the electrons, the so-called *electron bunching*, with the periodicity of the radiation wavelength. As a result of the density modulation, the electrons get concentrated in regions where the energy transfer from particle to field is maximized, and the radiation becomes coherently amplified.

For an electron beam with a given energy travelling in a planar undulator, the resonance condition for the wavelength of the emitted radiation is

$$\lambda = \frac{\lambda_u}{2\gamma^2}(1 + a_u^2) \ . \tag{1.1}$$

The efficiency of energy transfer and the gain of the process are summarized by the Pierce parameter

$$\rho = \frac{1}{4\pi\gamma}\sqrt[3]{2\pi\frac{J_e}{I_A}\left(JJ\lambda_u a_u\right)^2} \tag{1.2}$$

where $JJ(\chi) = J_0(\chi) - J_1(\chi)$ is the planar undulator Bessel correction factor of argument $\chi = \frac{a_u^2}{4+2a_u^2}$ and $I_A \sim 17$ kA the Alfvén current. The current density

[1] Another notation is ofter used in literature, which expresses the undulator parameter as $K_u = a_u/\sqrt{2}$

J_e is given by

$$J_e\left[\frac{A}{m^2}\right] = \frac{I_{peak}[A]}{2\pi\sigma_x[m]\sigma_y[m]}$$

where $\sigma_{x,y} = \sqrt{\beta_{x,y}\epsilon_{n_{x,y}}/\gamma}$ are the rms (root mean squared) transverse dimensions of the electron beam[2] ($\Sigma_e \sim 2\pi\sigma_x\sigma_y$ is the beam cross section), and the peak current I_{peak} can, for a Gaussian beam, be expressed as

$$I_{peak}[A] = \frac{Q[C]}{\sqrt{2\pi}\sigma_\tau[s]}$$

in terms of the bunch rms time duration σ_τ and of the bunch charge Q.

The gain length, determining the FEL growth rate and expressing the distance over which the power grows by a factor e, can be expressed in terms of ρ as follows:

$$L_g = \frac{\lambda_u}{4\pi\sqrt{3}\rho} \ . \tag{1.3}$$

The solution of the third order equation describing the FEL process in the 1D theory (in Appendix B) leads to the field

$$E = \frac{E_0}{3}\left[\exp\left(\frac{i+\sqrt{3}}{2}\Gamma z\right) + \exp\left(\frac{i-\sqrt{3}}{2}\Gamma z\right) + \exp\left(-i\Gamma z\right)\right] \tag{1.4}$$

with $\Gamma = \frac{4\pi}{\lambda_u}\rho$ and z the longitudinal undulator coordinate. The last two terms describe an exponentially decaying and an oscillating mode respectively, whereas the exponentially growing mode of the first term is the dominant one while z increases. The oscillatory term is important in the so-called FEL lethargy regime, where the field amplitude remains constant for the first two gain lengths in the undulator. Following the model described in Appendix B, the power growth is fitted by the logistic function, which can be written in the simplified form:

$$P(z) = \frac{P_0}{9}\frac{\exp(z/L_g)}{1+\frac{P_0}{9P_{sat}}\exp(z/L_g)} \ , \tag{1.5}$$

where P_0 is the input seed power and $P_{sat} \cong \sqrt{2}\rho P_{beam}$ the power at saturation, with the power carried by the electron beam $P_{beam} = mc^2\gamma I_{peak}$.

Saturation is reached after about 20 gain lengths; the resonance condition is no longer satisfied in this regime, often called non linear FEL regime, where the energy is transferred back and forth between the electron beam and the radiation. The saturation length, which is namely the required length to reach

[2] The basic concepts of electron beam physics are outlined in Appendix B. $\beta_{x,y}$ are the transverse Twiss beta functions of the beam, while $\epsilon_{n_{x,y}}$ refers to its normalized transverse emittance in x,y respectively.

the power P_{sat}, is

$$L_{sat} = 1.066 L_g ln\left(\frac{9P_{sat}}{P_0}\right) . \tag{1.6}$$

The Pierce parameter ρ gives an estimate of both the FEL power at saturation P_{sat} and natural bandwidth:

$$\frac{\Delta\omega}{\omega} \cong \rho \tag{1.7}$$

as well as of the energy conversion and FEL process efficiency (Eq. (B.68) in Appendix B).

The gain deterioration due to non ideal electron beam qualities (non negligible energy spread and emittance), can be embedded in the previous formulas [9] as discussed in Appendix B.2.2.

The number of emitted photons per pulse can be estimated as

$$N_{ph}/\text{pulse} = \frac{P_{sat}}{\hbar\omega}\sigma_{ph} \tag{1.8}$$

where $E_{ph} = \hbar\omega$ represents the photon energy and σ_{ph} is the photon pulse time duration. The number of emitted photons per second is easily obtained by multiplyng this last expression by the FEL repetition rate, that is the number of emitted pulses per second.

The output FEL phase correlation is given by its degree of temporal coherence (see Appendix A), which can be evaluated by considering the normalized correlation function [10, 11, 12]

$$\Gamma_{nm}(\tau) = \left| \frac{\int dt E_n(t) E_m(t-\tau)}{\sqrt{\int dt \left|E_n\right|^2}\sqrt{\int dt \left|E_m\right|^2}} \right| , \tag{1.9}$$

between two different pulses ($n \neq m$, representing the shot-to-shot stability) or for one single pulse ($n = m$) respectively. The cooperation (or coherence) length

$$L_c = \frac{\lambda}{2\pi\rho} \tag{1.10}$$

represents the longitudinal length over which the electrons emit coherently.

The longitudinal density modulation of a pre-bunched beam is quantified with the so-called bunching factor $b_n =< e^{-in\psi} >$, where n is the harmonic number and ψ the electron beam ponderomotive phase [13, 14]. The coherent emissiuon from pre-bunched beams evolves as

$$P(z) = \frac{1}{3}\rho|b|^2 P_{beam}\left(\frac{z}{L_g}\right)^2 . \tag{1.11}$$

This quadratic growth is valid up to a threshold $P_{th} = \rho|b|^2 P_{beam}$, after which the power grows exponentially. The saturation level is always the same, while higher bunching values allow a faster transition.

A similar FEL process is also valid for the harmonics of the fundamental wavelength:

$$\lambda_n = \frac{\lambda_u}{2\gamma^2 n}(1 + a_u^2) \tag{1.12}$$

where n is an odd integer for a planar undulator. Planar undulators indeed allow for a resonant on-axis FEL interaction with odd harmonics of the fundamental resonant field, while even harmonics are emitted off-axis and therefore weakly amplified. The radiated spectrum is composed by a series of square sinc functions, centered on odd harmonics.

Referring to the case of a single electron, the relative linewidth of the harmonics is given by $\Delta\lambda/\lambda_n = 1/(nN_u)$, where N_u represents the number of undulator magnetic periods. The emission is narrow in the frequency domain, even if undulator line broadening may result from the electron beam energy spread, size and divergence [15].

The Pierce parameter of the harmonics is

$$\rho_n = \rho \left[\frac{JJ_n}{JJ_1}\right]^{\frac{2}{3}} \rightarrow L_{g,n} = \frac{\lambda_u}{4\pi\sqrt{3}\rho_n}$$

with $JJ_n = J_{\frac{n-1}{2}}(n\chi) - J_{\frac{n+1}{2}}(n\chi)$. The harmonics' power at saturation is

$$P_{sat,n} = \frac{1}{\sqrt{n}} \left(\frac{JJ_n}{nJJ_1}\right)^2 P_{sat} \ .$$

The number of photons per pulse emitted at the n^{th} harmonics is given by

$$N_{ph,n} = \frac{P_{sat,n}}{n\hbar\omega}\sigma_{ph} = \chi_n N_{ph} \ , \tag{1.13}$$

where the parameter $\chi_n = \frac{1}{n\sqrt{n}} \left(\frac{JJ_n}{nJJ_1}\right)^2 \frac{\sigma_{ph,n}}{\sigma_{ph}}$ represents the harmonic conversion efficiency (which for the third harmonics is around 0.1%).

Main FEL configurations

A sketch of the basic layout of a FEL machine, featuring the electron injection, acceleration and radiation amplification, is shown in Fig. 1.1.
The first building blocks of any FEL machine are the electron beam injection and acceleration stages. Linear accelerators for FELs tipically use photo-injectors, where the electrons are extracted via photo-electric effect from a drive

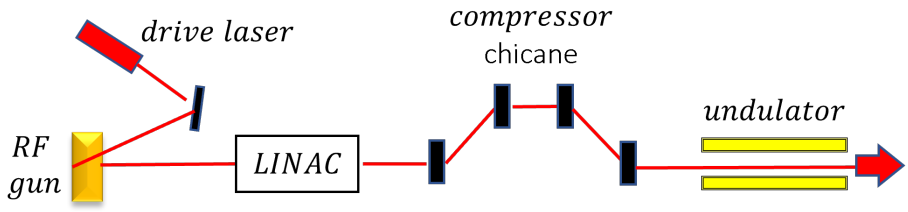

FIGURE 1.1: Sketch of the basic FEL scheme. The typical injection scheme consists of a drive laser beam impinging on a cathode and emitting the electrons via photo-emission in the radio-frequency (RF) gun. Electron acceleration occurw in the linear accelerator (LINAC) and the electron longitudinal phase space is manipulated with a bunch compressor, followed by the undulators for FEL amplification.

laser beam incident on a photo-cathode, allowing to control the electron beam distribution by laser pulse shaping. The LINAC itself, constituted by radio-frequency (RF) cavities, either normal-conducting (NC) or super-conducting (SC), and generating high gradient electric fields for particle acceleration, follows.

A magnetic bunch compressor is tipically placed at an intermediate stage of acceleration and before the light amplification stage, constituted by a chain of undulator magnets.

The electron beam properties at injection, such as charge and current, are influenced by the cathode and LINAC type. The warm cathodes of a NC system work at low repetition rates in the 1-100 Hz range, allowing the extraction of long (ps-scale) and high charge (nC range) electron bunches with low emittances, as needed for successful FEL operation. On the other hand, the cathode of a SC accelerator requires a cooling system and works at high, MHz-class, repetition rates. This operating mode comes with a few drawbacks: the maximum electron average current (of the order of tens-mA) is the main constraint, limiting the extracted bunch charge per shot to about hundreds-pC, while the moderate beam peak current (below the kA-range at high repetition rate) can be increased by compressing the electron bunches.
SC RF cavities are the most efficient accelerating devices to convert the RF power into charged particles' energy: despite requiring a cryogenic system, they are usually preferred thanks to the very small energy dissipation in the cavity and the fact of being well suited for continuous-wave (CW) operation at high repetition rate.

The beam repetition rate from the injector affects the temporal pulse structure. Accelerators can operate in two main modes: pulsed operation allows the acceleration of only few electron bunches per second, while SC LINAC-based

facilities can also operate in CW mode, characterized by the production of millions of bunches per second with a μs-scale equidistant temporal separation, which is recorded as a continuum by any detector.
A typical example of pulsed operation mode is Eu-XFEL [16], featuring an hybrid structure made of several micropulses with hundreds-ns separation and grouped in macropulses with a spacing of hundreds-ms. Examples of CW LINACs are LCLS-II [17] and SHINE [18].

Depending on the required number of passes of the electron beam in the undulator before FEL saturation, FELs are grouped in two main configurations:

- Single-pass FEL
- Multi-pass FEL

The choice of FEL configuration and radiation scheme is based on user-defined requirements of the output FEL pulse properties, as radiation wavelength, peak power, polarization and average repetition rate. The time structure of the pulse needs as well to be matched to the characteristic time-scales of the physical processes under study. High intensity applications, such as X-ray imaging, require photons to be delivered in ultra-short, high-intensity pulses. On the other hand, spectroscopic studies require limited peak intensity so as to avoid non-linear processes, but also high repetition rates in order to collect sufficient data in acceptable experimental periods [8].

1.1.1 Multi-pass FEL

Historically, the first operating FELs were multi-pass FELs, also called FEL oscillators.

Similar to a conventional laser oscillator, this FEL scheme features an undulator embedded in an high-Q optical cavity, allowing the radiation power to build up during successive passes of several electron bunches in the undulator until an equilibrium state is reached at saturation.

It is a low-gain device with reasonable accelerator requirements: the use of the optical cavity makes oscillator FELs less demanding in terms of electron beam quality and allows working with lower values for peak current. Conventionally, the FEL process is started by the electron beam spontaneous emission (the shot noise), and the interaction between trapped light and electron bunches lead to micro-bunching and fully coherent emission.

The optical cavity itself poses the most stringent requirements and strongly influences the FEL characteristics, such as its repetition rate, the transverse size of the radiation field and its synchronization with the electron beam. Its operation and design is strictly linked to the wavelength operation range and the mirror availability in that range. Besides, to ensure a good synchronization of the radiation field and the successive electron bunches at the beginning of

each passage in the undulator, the cavity length needs to be consistent with the electron beam repetition rate and may need to be adjusted during operation.

During the first two decades of the operation of FELs, the technological lack of reasonably reflective mirrors below 100 nm has restricted the use of these devices to a wavelength range from THz to Ultra-Violet (UV) [19, 20, 21]. Most oscillator FELs operate in the infrared (IR) and optical regime [22, 23, 24, 25, 26, 27, 28, 29]. However, multi-layer mirrors have been proved successful for wavelengths in the deep-UV and beyond, where no broad-band high reflectivity mirrors for normal incidence are available [30, 31, 32].

In the last few years, thanks to technological advancements in the field of mirror fabrication aimed at extending their operation at short wavelengths, there have been a growing number of studies also on high-gain FEL oscillators, referred to as regenerative amplifier FELs (RAFELs)[33, 34], or oscillators relying on Bragg reflectors and mirrors [35, 36, 37, 38, 39].

A RAFEL combines a high-current electron beam and a low-Q resonator, with relaxed requirements on reflectivity: in this case the radiation intensity grows exponentially in each pass and requires only a few passes to reach saturation.

The underlying physics, design strategies and operation of FEL oscillators are discussed in more details in Chapter 3.

1.1.2 Single-pass FEL

Single-pass FELs were developed on the basis of theoretical works in the 1980s [7, 40, 41] and have been used since the 1990s for wavelength regimes from UV down to X-rays, where mirrors were not available.

In this FEL configuration, saturation needs to occur within one single pass of the electron bunches through the undulator. Therefore, in this case the accelerator performances should fulfill the best qualities in terms of high brightness electron beams, with low emittance and energy spread: such stringent requirements can be satisfied by using the new generation of injectors based on photo-electron guns. In order to preserve the beam transport from the electron source to the undulator and operate these FELs with a small energy spread, a laser heater is usually employed before entering the undulator line.

The FEL emission in a single-pass FEL can be initiated either by the electron shot noise in the so-called Self Amplified Spontaneous Emission (SASE) FEL, or by an external signal in a seeded FEL configuration.

1.2 SASE FEL

Self-Amplified Spontaneous Emission is a straightforward approach to single-pass amplification, where the FEL process is initiated by the electrons' incoherent spontaneous emission at the beginning of the undulator.

It presents an ample and solid experimental validation in all the wavelength domains from optical to X-rays [42, 43, 44, 45, 46, 47, 48, 49], and best explains the basic working principle of a FEL (see Appendix B).

The electron bunch driving a SASE FEL consists of stochastically distributed electrons and the emitted radiation from the different trains of bunches is not correlated. Depending on the electron beam quality and the undulator length, such FEL operation results in highly brilliant, high peak power (∼GW) radiation pulses with quite high transverse coherence, but the random phase and amplitude of the initial shot noise limit its longitudinal coherence and result in strong pulse-to-pulse fluctuations in both spectral and temporal domains.
In the first part of the amplification, many transverse modes are excited (low transverse coherence). As the electrons travel within the undulator, diffraction effects get counteracted by the gain guiding mechanism, in which the selective amplification of the central part of the co-propagating field overlapping with the area of high electron bunch density takes place. In combination with the natural diffraction of the co-propagating field, this effect leads to mode selection: by the end of the exponential growth, only the highest growth rate mode dominates. Therefore, this process results in a radiation pulse characterized by a quite high transverse coherence level, which can exceed 90% before high-order mode amplification occurs in deep saturation. The bandwidth of the spontaneous emission spectrum is larger than the FEL amplification bandwidth, so that the SASE FEL is always tuned at the resonant frequency with the largest growth rate.

Due to the poor temporal coherence of the SASE process, the output radiation exhibits a sequence of M uncorrelated temporal spikes, whose duration as well as spectral width are about $2\pi L_c$, where L_c is the cooperation length (Eq. 1.10). Tipically, the electron bunch length is several cooperation lengths long, and the output FEL longitudinal structure is made of several spikes, separated by $2\pi L_c$. The approximate number of uncorrelated radiation spikes, or longitudinal modes in frequency domain, is therefore

$$M = \frac{L_{beam}}{2\pi L_c}. \tag{1.14}$$

The frequency spectrum of the emitted radiation corresponds to the white noise associated to the initial electron random distribution, filtered by the FEL gain bandwidth, and the spectral spikes correspond to the excited longitudinal

modes. SASE FEL pulses' duration is approximately a replica of the electron bunch duration and, due to the amplification of many longitudinal modes, they suffer from very low longitudinal coherence.

The radiation beam quality can be improved and its frequency coverage increased by means of various techniques.

The longitudinal coherence of a SASE FEL can be partially improved by driving the FEL emission with electron bunches shorter than the cooperation length ($L_{beam} < 2\pi L_c$), so as to confine all electron that contribute to lasing within one coherence length. This single-spike SASE regime [50, 51, 52] leads to one single longitudinal mode in the temporal distribution of the FEL radiation, as well as to a single-spiked spectral distribution. However, despite permitting operation at low charge, with good control of emittance and energy spread, this single-spike operation results in the amplification of pulses characterized by 100% shot-to-shot fluctuations of the photon pulse energy due to the stochastic behaviour of the SASE radiation; saturation may help in reducing such fluctuations.
Therefore, a substantial coherence in each single radiation shot is achieved (first-order coherence), but with very low shot-to-shot stability. In this regime, the FEL pulse length is of the order of the cooperation length L_c, which is limited by the maximum current.

The spectral range of operation can be extended by operating the FEL in other modes. Two basic mechanisms able to create coherent micro-bunching at harmonic frequencies in FELs are non-linear harmonic generation and harmonic lasing. The former method [53, 54, 55] is driven by the fundamental FEL interaction close to saturation, when the electron density modulation becomes non-linear; the relative spectral bandwidth of the harmonic radiation is similar to that of the fundamental, but the harmonics' intensity is weaker (tipically at a level of a percent or less) and is more strongly subjected to shot-to-shot fluctuations. As already anticipated, this harmonic microbunching regards the odd harmonics generated in the forward direction for a planar undulator. Harmonic microbunching of the electron beam can also be exploited by tuning the last part of the undulator on some harmonics.

Harmonic lasing, first proposed and experimentally demonstrated for FEL oscillators [56, 57, 58], is an FEL instability in which the SASE amplifier is interrupted when the bunching is maximum before saturation (at roughly 80%), and the bunched beam current containing large Fourier components at the harmonics of the SASE fundamental frequency is injected into a radiator (called afterburner undulator) tuned at one of the harmonics. The advantages over non-linear harmonic generation can include much higher power, better stability, smaller bandwidth and no need for filters, if lasing at the fundamental frequency is suppressed [59, 60].

The performances of a SASE FEL are strictly dependendent on the electron beam qualities at the undulator entrance. For instance, an enhancement of the electron peak current entering the SASE FEL can lead to a considerable reduction of the FEL gain length. This has been demonstrated with the so-called Enhanced Self Amplified Spontaneous Emission (ESASE) configuration [61, 62], in which the electron peak current is increased by using a conventional short optical laser with high peak power, overlapping with a short longitudinal section of the electron beam in a first undulator segment. The electrons interact with the laser field in the undulator and acquire an energy modulation exceeding their uncorrelated energy spread. A second acceleration stage follows, not affecting the introduced energy modulation and allowing to reach the final energy needed for FEL emission. The electron beam then passes through a dispersive magnetic chicane, which produces microbunching of the electrons and periodic enhancement of the electron peak current, and are finally driven in the long undulator of the standard SASE FEL.

A similar technique, called High-Brightness SASE (HB-SASE) and aimed at improving the SASE radiation production, has been also proposed [63]: many small delay chicanes in-between the different undulator sections are employed to enhance the slippage effect, delocalising the collective FEL interaction and breaking the dependence of the radiation coherence length on the FEL cooperation length.
The SASE performance with energy-chirped beams, as well as the effect of undulator tapering, has been also investigated [64, 65].

Due to its different velocities, the radiation field moves faster and slips over the electron beam along the undulator: the so-called slippage length $L_{slip} \sim N_u\lambda$ (N_u indicates the number of undulator periods) is the difference between the distance covered by light and electrons in the undulator. When slippage of the radiation with respect to the electrons can be neglected, in the so-called steady-state regime, the emitted radiation intensity scales as N, where N is the number of electrons in a cooperation length.

In case of unbunched electrons, the intensity of the emitted radiation is initially proportional to N (spontaneous radiation); when interacting with the spontaneous and undulator radiation, the electrons begin to bunch and to emit radiation with an intensity proportional to N^2. In this second situation, the FEL operates in the superradiant regime [66]: this can occur when operating both with short electron pulses (shorter than the slippage length) or in the tails of the electron pulse with long-pulse high-gain FELs, if slippage is not negligible. In the former case, where N is the total number of electrons, the regime is usually called *weak superradiance* and leads to lower peak intensities than the one predicted in the steady-state theory; in the latter, emission arising from the trailing region of a long electron pulse evolving as a short electron

pulse and exhibiting a spiking behavior with intensities much greater than the steady-state saturation value (N is the number of electrons in a slippage length) is referred to as *strong superradiance*.
The substantial difference between the steady-state and superradiant regimes is given by the slippage effect. Radiation intensities scaling as the squared number of electrons may also arise from coherent synchrotron radiation emitted by pre-bunched electrons[3].

As discussed in the next section, the stability and longitudinal coherence of SASE FEL pulses can be improved by means of FEL seeding.

1.3 FEL seeding

The poor quality and coherence degree of single-pass SASE FEL pulses have led to the development and application of seeding techniques, whose basic principle is based on the injection of a coherent signal superimposed to the electron beam at the undulator entrance [67, 68, 15].

FEL seeding aims at improving the longitudinal coherence and shot-to-shot stability of a SASE FEL configuration, simultaneously increasing its brilliance, and at synchronizing the FEL signal with an external seed signal for pump-probe experiments.
Nearly fully coherent radiation beams, whose temporal coherence can be of the order of tens of femtoseconds, are produced in the seeded operation. Longitudinal coherence of the pulses is achieved by phasing the emitting electrons and is one of the biggest advantages of FELs compared to Synchrotron-based light sources.

Nevertheless, as pointed out in the next chapters, the produced pulses come with some limitation posed by the seed laser itself. The next sections will also address different seeding techniques for an high-gain FEL.

Seed requirements

In a seeded configuration, the FEL amplifies an initial external seed, tipically a laser pulse superimposed to the electron beam, which imprints its coherence properties on the electron modulation and provides electron bunching, thus allowing to improve the phase stability, longitudinal coherence as well as shot-to-shot stability of the amplified FEL pulses.

The emitted peak power is simultaneously increased to approximately the SASE power level at saturation within a shorter distance. At the beginning of the undulator, power is emitted incoherently from the electron beam and grows linearly, till the FEL amplification process starts after a few gain lengths; as the

[3] Pre-bunching of the electrons is tipically achieved by means of a strong external laser field.

electrons emit coherently, the radiated power grows quadratically. The effect of the seed is a shorter FEL lethargy regime.

The FEL pulse spectral and temporal distributions get cleaned from the SASE multiple spikes but may be then altered by the FEL saturation process, due to slippage and the earlier saturation of the radiation field with respect to the electron beam. Depending on the seed pulse duration L_{seed} with respect to the slippage length L_{slip}, different regimes can occur [15]: when $L_{slip} \ll L_{seed}$, the local heating of the electrons at saturation leads to a pulse splitting regime[69], characterized by an intensity drop at the peak of the pulse and deeply used for pump-probe two-color experiments; when $L_{slip} \sim L_{seed}$, the FEL dynamics enters a strongly non-linear superradiant regime [70], with pulse duration narrowing and simultaneous emission of harmonics (up to the 11th order).

Depending on the laser seed intensity, the result is a coherent emission at the undulator resonance and its higher order harmonics in the following sections of undulator. Furthermore, the amplified FEL pulses are naturally synchronized with the seed pulse for pump-probe experiments. Wavelength tuning of a seeded FEL can be achieved by simultaneously changing the seed wavelength and the undulator gap or by applying a chirp on the modulated electron bunch.

The seed choice plays a major role for seeded FELs. It influences the output FEL properties and performances, its length, wavelength and repetition rate affecting the amplified FEL pulses.

In order to be effective, any seeding source needs to fulfill few important conditions: the main constraint is linked to the required seed intensity, which should overcome the electron beam shot-noise power level without exceeding the FEL saturation power [15, 67]. The shot-noise intensity is estimated as $I_{sn} \sim \omega\rho^2\gamma mc^2$, being proportional to the square of the Pierce parameter ρ and growing linearly with the resonant frequency ω and the electron beam energy $mc^2\gamma$. For typical high-gain FEL parameters, it can bary around hundreds of watts to tens of kilowatts. SASE performances are achieved when seeding with a power below the spontaneous radiation level, and a contrast ratio of at least $10 - 10^2$ between the seed and the background noise is needed.

Ultra-Violet (UV) lasers are the most suitable candidates for external seeding setups: due to the heat load of laser systems, which is proportional to the pulse energy and repetition rate, the high peak power requirements often limit the repetition rate of these lasers to few tens of Hz up to the kHz regime. Furthermore, shorter-wavelength seeding sources are poor and tipically have lower efficiency in terms of output power, while the shot-noise power increases with frequency, making laser seeding at short wavelengths another non-trivial problem.

Moreover, only a fraction of the input seed power is matched to the FEL growing

mode: based on the one-dimensional theory, approximately 1/9th of the power contributes to the exponential growth and requires about two gain lengths (see Eq. 1.3) to overcome the lethargy regime of seeded FELs and be able to measure proper amplification by the seed pulse; such fraction is also affected by transverse coupling [67, 68]. The seed duration determines the minimum FEL pulse duration, which affects its maximum bandwidth. Even the bandwidths have to be matched: in particular, the SASE FEL peak brightness is improved if the seed has a smaller bandwidth (length greater than the FEL coherence length).

Seeded FELs, such as FERMI [71], tipically work with long electron bunches, with a low peak current, to which the seed is easily superimposed; the seed pulse moves longitudinally on the electron beam current distribution and the output pulse properties are determined by laser pulse shaping techniques. Other FELs, such as DALIAN in China [72], use a different approach that relies on a long seed pulse and short electron bunches.

Therefore, FEL seeding requires a tunable seeding source with approximately hundreds nJ-tens μJ pulse energy, excellent stability, less than 1% rms energy fluctuations and wavelength stability below 1% rms with respect to the spectral bandwidth.

1.3.1 Conventional seeding schemes

Starting from direct laser seeding, where the wavelength of the seed signal equals the FEL resonance wavelength (see Eq. 1.1), various techniques have been studied and experimentally applied.

Their layouts, relative advantages and main motivations behind their proposal are here discussed.

Direct seeding and harmonic generation

Direct seeding is the basic seeding scheme, where the seed signal gets amplified along the undulator. The shortest wavelength achievable through direct seeding is limited by the seed laser wavelength. Despite the huge efforts and developments of laser technology, commercial seed laser systems for FEL seeding with high-power levels suitable for FEL seeding cannot go beyond the Vacuum-UV spectral range.
However, high intensity seed pulses can induce non-linear electron beam phase space motions and the amplification of high-order harmonics of the seed fundamental wavelength, if the undulator is properly tuned at that harmonic. Such operation is exploited in cascaded high-gain FEL schemes.

In order to reach shorter wavelengths, the FEL can be seeded by laser harmonics: in this direction, High Harmonic Generation (HHG) [73] is a promising

technique to produce high harmonics from the interaction of an intense laser pulse with a noble gas. Some other seeding techniques, combining laser seeding with electron beam phase space manipulation, have been proposed and are also used nowadays to extend FEL seeding to short wavelengths.

Three common and successfully demonstrated approaches are High-Gain Harmonic Generation (HGHG) [74, 15, 68], Echo-Enabled Harmonic Generation (EEHG) [75, 76] and Self-seeding [77, 78, 79]; the first two are harmonic up-shift cascaded schemes that take advantage of a pre-bunched electron beam to transfer the coherence properties of a relatively long-wavelength laser seed to a much shorter-wavelength FEL output pulse.

High Gain Harmonic Generation (HGHG)

Due to the difficulty in reaching a large ratio (order 10^3) between the seed and the shot-noise intensities at short wavelengths, a successful strategy is that of seeding the FEL in a more accessible spectral range and then exploit the higher harmonic bunching generation process to extend this modulation to shorter wavelengths.

The scheme of a typical HGHG FEL cascade is shown in Fig. 1.2.

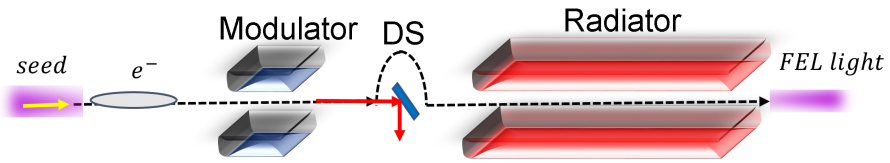

FIGURE 1.2: Schematic layout of an FEL in the high-gain harmonic generation configuration. The scheme consists in a modulator, where the seed (indicated by the yellow arrow) modulates the electron beam (in gray) in energy, followed by a dispersive section (DS) generating electron bunching at the desired harmonics and the final radiator.

The electron bunches initially overlap with the external seed (usually a UV laser beam) and get energy-modulated in a short undulator segment, the modulator, which is about two gain lengths long and resonant with the seed laser wavelength. The undulator encodes the phase and amplitude information of the seed onto the electron beam longitudinal phase space: as a result, the electron bunches are sinusoidally modulated in energy with a periodicity equal to the seed laser wavelength. The interaction with the seed of intensity I_L induces the initial energy modulation $\Delta\gamma$: it depends on the laser power and transverse size, as well as on the undulator length and strength [68], and for a diffraction

dominated setup[4] it can be expressed as:

$$\frac{\Delta\gamma}{\gamma} = \frac{1}{\sqrt{2}N_{mod}}\sqrt{\frac{I_L}{I_{s,mod}}}\ , \tag{1.15}$$

where $I_{s,mod} \propto \frac{1}{2N_{mod}}\frac{P_{beam}}{\sigma_{beam}}$ is the saturation intensity in the modulator (characterized by N_{mod} periods). Such energy modulation can be also expressed as an induced energy spread $\Delta\gamma = \sqrt{2}\sqrt{\sigma_\gamma'^2 - \sigma_\gamma^2}$, where σ_γ' is the total energy spread after the modulator and σ_γ the uncorrelated electron beam energy spread at its entrance. It is typical referring to the normalized energy modulation $A = \frac{\Delta\gamma}{\sigma_\gamma}$. The electron beam then traverses a chromatic dispersive chicane, characterized by a certain dispersion strength R_{56}, where the energy modulation is converted into spatial density modulation having significant harmonic content at harmonics of the seed fundamental wavelength: the final position of each particle changes according to

$$\Delta\zeta = R_{56}(\Delta\gamma/\gamma)\ . \tag{1.16}$$

The effect of the chicane can be expressed as a normalized dispersion $B = \frac{R_{56}k_{seed}\sigma_\gamma}{\gamma}$, where γ is the reference electron energy and k_{seed} the seed laser wavenumber. By tuning the seed intensity and the dispersion R_{56}, the electron beam gets bunched, corresponding to the formation of current peaks equally spaced at some harmonics of the seed wavelength, and coherently emits it in the following longer radiator, properly tuned at this harmonic frequency. The emission at higher harmonics of the seed wavelength during the FEL interaction in the radiator is therefore a direct consequence of the periodic modulation of the electron beam at the emission wavelength [68].

The harmonic current generated from the HGHG process can be characterized by calculating the bunching factor at a certain harmonic n of the seeding laser. The bunching factor at the n^{th} harmonic, resulting from the energy modulation $\Delta\gamma$ and the dispersion R_{56}, can be expressed as [68]:

$$b_n = |J_n(nAB)|\exp(-\frac{1}{2}n^2B^2) = J_n\left(\frac{2\pi n}{\lambda_L}\frac{\Delta\gamma}{\gamma}R_{56}\right)\exp\left[-\frac{1}{2}\left(\frac{2\pi n}{\lambda_L}\right)^2\left(\frac{\sigma_\gamma}{\gamma}\right)^2 R_{56}^2\right]\ , \tag{1.17}$$

where λ_L and $\lambda_0 = \lambda_L/n$ are the seed laser wavelength and the resonance in the amplifier, respectively. This expression assumes a Gaussian energy spread distribution $\propto \exp(-\gamma^2/2\sigma_\gamma^2)$ with standard deviation σ_γ, an infinitely long laser and electron beam, thus in the limit $L_{beam} \gg \lambda_L$.
The pre-existing beam energy spread becomes more critical at high harmonic orders and results in the decaying exponential function in Eq. (1.17), while

[4] This condition is verified for most external seeding experiments.

the Bessel function of the first kind is maximized when the energy modulation is larger than the uncorrelated energy spread and its argument equals $X(n) = \frac{2\pi n}{\lambda_L}\frac{\Delta\gamma}{\gamma}R_{56}$.

The bunching coefficient depends on both the harmonic number n and the ratio between the induced modulation and the intrinsic energy spread, and draws a hyperbole in the space $(\Delta\gamma, R_{56})$ at a given n: thus, for a given seed wavelength and harmonic conversion factor, the lower is the energy modulation $\Delta\gamma$ the larger has to be the dispersion R_{56}. On one hand, the presence of R_{56} in the decaying exponential (Eq. 1.17) imposes a low value of the dispersion when the initial energy spread is large: for sufficient bunching, the contribution of the exponential term in Eq. 1.17 should be minimized by setting $B \approx n$ while the Bessel function should be maximized, corresponding to $A \approx n$ for the normalized energy modulation.
On the other hand, an increase of the energy spread, required to induce the density modulation (higher harmonics require larger energy modulations), will affect the exponential growth in the final amplifier, according to the gain/saturation power scaling relations, and the relative uncorrelated electron beam energy spread must satisfy the condition $\sigma'_\gamma/\gamma \ll \rho$.

Efficient energy extraction occurs when saturation is reached at the end of the amplifier, when the induced energy spread is the minimum required to generate "sufficient" induced bunching, significantly above the shot-noise level [67]. This is more likely to happen when the laser induced energy modulation $\Delta\gamma$ is about as large as the energy spread of the electron bunch σ_γ multiplied by the harmonic number n, i.e. $\Delta\gamma \simeq n\sigma_\gamma$. By combining the induced bunching in Eq. (1.17) with the scaling relations of the exponential growth, and inverting the resulting equation, the bunching factor required to reach the power ΓP_{sat} (the condition with $\Gamma = 1$ is reached only asymptotically at $z \to \infty$) can be derived [68]

$$|b_n|^2 \sim B(L_u, L_{g,3d}) = \frac{\Gamma}{0.8}\left[\frac{\frac{1}{3}(L_u/L_{g,3d})^2}{1+\frac{1}{3}(L_u/L_{g,3d})^2} + \frac{1}{2}\exp\left[L_u/L_{g,3d} - \sqrt{3}\right]\right]^{-1}. \tag{1.18}$$

The presence of the bunching allows to reach saturation with very short undulators, L_u being only few gain lengths long. Anyway, even starting with such a large bunching factor, about two gain lengths are always required to reach the saturation power P_{sat}. When the bunching factor becomes comparable to that associated to the electron beam shot noise, the seed is not effective anymore in preparing the pre-bunched beam, resulting in SASE operation.

In the common case of a seed laser pulse shorter than the electron bunch, the output FEL pulse duration σ_τ^{FEL} depends strongly on the seed laser one

L_{seed}. Moreover, the harmonic conversion leads to a natural shortening of the output pulse; when the Bessel function of Eq. 1.17 is maximized, the FEL and seed pulse durations scale as

$$\sigma_\tau^{FEL} = \frac{L_{seed}}{\sqrt{n}} \ .$$

When the Bessel function is not maximized, the scaling is expected to be

$$\sigma_\tau^{FEL} = \frac{6L_{seed}}{7n^{1/3}} \ .$$

Furthermore, by increasing the argument of the Bessel function further after the value corresponding to the Bessel function for maximum bunching, over-bunching leads to pulse-splitting.

The limiting factor for the maximum practical harmonic up-shift ratio n for which reasonable microbunching values can be maintained over multiple radiators in a single-stage HGHG configuration is therefore the overall electron beam energy spread, given by the intrisic one and the induced energy modulation by the seed: $\sigma_\gamma^{tot}(\sigma_\gamma, \Delta\gamma) = \sqrt{\sigma_\gamma^2 + \frac{\Delta\gamma^2}{2}}$.
Both FEL gain and power are sensitive to the electron beam and undulator parameters (as current, σ_γ, a_u): for this reason, there is a maximum harmonic order n for which the HGHG output power can approach reasonably large saturation levels, beyond which the saturated power generally decreases exponentially with increasing n. High-gain seeded FELs typically feature around 100 keV of uncorrelated energy spread and a ρ parameter of about 10^{-3} or less, in which case the single-stage HGHG scheme is limited to harmonics up to n=15.

Shorter wavelengths can be achieved by minimizing the uncorrelated beam energy spread; however, its minimum value is limited by space charge effects in the gun and by the bunch compression.

Multi-stage harmonic cascades in which the micro-bunching or output radiation from one stage is used to seed a following stage, whose radiator is resonant at an integral harmonic of the previous one, were proposed to circumvent this limitation and extend the useful operating range of HGHG to short wavelengths [80]. In a two-stage example, if the first stage performs the harmonic up-shift ratio n_1 and the second stage n_2, the final output wavelength is $\lambda_{seed}/(n_1 n_2)$. In its simplest form, if high-power seeds are available and dispersive chicanes for harmonic bunching are not needed, a two-stage cascade can be configured by splitting the radiator of a nominally one-stage cascade into two consecutive sections, with the first resonant at λ_{seed}/n_1 and the second at $\lambda_{seed}/(n_1 n_2)$.

The HGHG sensitivity to energy spread is not improved, since the accumulated energy spread for each stage can degrade the performance of the final

radiator and is therefore the main problem. In particular, the energy spread induced by both the laser seed and the FEL interaction in the first-stage modulator and radiator, respectively, are sources of degradation for the FEL gain and final saturation power in the second stage. The short region toward the head of the seeded portion of the electron beam, where electrons not strongly energy modulated by the seed can be reached by the radiation "slipping" forward, can produce ultra-short pulses characterized by quite high peak power but low longitudinal coherence [70].

The "fresh-bunch" two-stage cascading scheme [81, 82, 83, 68] allows to preserve the coherence. In this scheme, seed pulses much shorter than the electron beam duration ($\tau_{seed} \ll \tau_{e-beam}$) are employed, and the second stage is separated from the first by a strong chicane that delays the electron beam by an amount $\tau_d \geq \tau_{seed}$ (of about few hundreds of fs), that allows the first-stage radiation to seed a "virgin" electron beam region for which the energy spread has not been heated by the previous light-electron interaction. Such a scheme features two identical HGHG stages separated by a delay line which lengthens the electron path with respect to the radiation straight path. In the final radiator, harmonic conversion factors up to 5–6 of the first-stage seed can be generated, providing a significant shortening of the final wavelength.
The energy spread is no longer a crucial limitation of this setup. In practice, the number of stages and final wavelength are limited by phase noise amplification problems, insufficient FEL gain at very short wavelengths (due to a very low resonant undulator strength parameter a_u) and the finite electron beam pulse length. Furthermore, since the entire process operates only locally with a slice of the bunch moving slowly from the tail to the head of the bunch, a small fraction of electrons contribute to lasing in the final radiator and the overall pulse energy is smaller than in SASE operation. So far, only two-stage cascades have been operated successfully.

Since the first experiments on HGHG, the production of pulses with improved energy and central wavelength stability, reduced spectral line-width and a larger longitudinal coherence, that can be a large fraction of the seed duration, has been demonstrated, thus showing the advantages of HGHG seeding over the SASE configuration. Besides providing the intensity amd spatial coherence of SASE FELs, the output radiation features a Fourier transform limited spectral bandwidth as well as temporal coherence, and the saturation length is reduced, leading to a more compact system. The first proof-of-principle experiments demonstrating the HGHG process were conducted at Brookhaven by L.H. Yu et al. at infrared [74] and UV wavelengths [84] employing harmonic up-shift ratios of three. Demonstrations at FERMI FEL-1 [83] have extended the output wavelength range down to the XUV regime with power saturation for harmonic ratios $n \geq 13$. Unconventional seeding methods at shorter wavelengths for the HGHG scheme, such as laser harmonics produced in gases (HHG), have been

also investigated and experimentally tested [73, 85, 15]; frequency mixing techniques applied on the pump laser or a chirp on both electron beam and laser pulse can be exploited to achieve tuneability.

Two-stage harmonic cascades have been experimentally studied at the SPARC_LAB facility, starting with an HHG source as a seed [86, 87] and at FERMI [88], for which the net harmonic up-shift value $n_1 n_2$ has been as large as 65. Fresh-bunch HGHG cascades made tremendous progress towards shorter wavelength down to 5 nm. The fresh-bunch injection technique has been demonstrated at SDUV-FEL [89] and at FERMI [80].

A similar process to HGHG occurs in an optical klystron [90, 91], a rather simple scheme consisting of two undulator sections for electron energy modulation and radiation amplification, tipically tuned at the same resonance and separated by a dispersive section for electron density modulation. Its main outcome is an enhancement of the gain process, and it has been also used in high-gain FELs to reduce the needed saturation length [92, 93].
The major difference compared to HGHG is the smaller energy modulation and the usual absence of harmonic conversion.

Variants of the HGHG configuration have been recently investigated for decreasing the seed peak power requirements and extend the operational range of a seeded FEL to even shorter wavelengths and higher repetition rates [94, 95, 96, 97, 98].
As discussed in Chapter 3, I propose few alternatives in this direction.

Echo-Enhanced Harmonic Generation (EEHG)

Echo-enabled harmonic generation was first proposed by G. Stupakov in 2009 [76] as a means to overcome the limitations posed by incoherent energy spread in the previously discussed HGHG scheme. Its ultimate goal is that of reaching extremely high harmonic numbers ($n > 100$) for generation of soft X-ray radiation when starting from an external UV seed laser.

It is a more complex configuration, sketched in Fig. 1.3, which relies upon multiple seed lasers, dispersive sections, modulator and radiator sections to first produce a coherent "shearing" of the longitudinal phase space followed by subsequent modulation that, via an echo-like effect, leads to a coherent density bunching exceeding the incoherent shot-noise background [68, 67].
At the beginning, a strong seed laser (seed 1) at wavelength λ_1 induces a moderate ($\Delta\gamma \sim 0.5\sigma_\gamma$), coherent energy modulation on the input electron beam in a short modulator. The following dispersive section is sufficiently strong such that $R_{56}\frac{\sigma_\gamma}{\gamma} \gg \lambda_1$, thus over-rotating the longitudinal phase space and, at a given phase, leading to multiple, alternating narrow bands of large and small density as a function of the energy. The purpose of this first part is

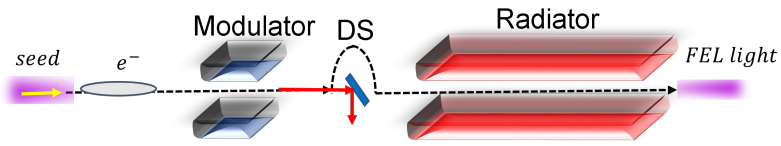

FIGURE 1.3: Schematic layout of an FEL in the echo-enabled harmonic generation configuration. The scheme consists in a double modulation-dispersion stages (Mod.1-DS1 and Mod.2-DS2 respectively) generating the density modulation at the desired wavelength via a harmonic frequency mixing of two seeding signals (seed 1 and seed 2, indicated by yellow arrows).

to over-compress the energy modulation well beyond maximum bunching with a strong magnetic chicane, rather than optimizing its harmonic content as in HGHG [68].
The second part, generating a current spike for each band, replicates an HGHG FEL: the electron beam passes into a second modulator section where it interacts with a second seed laser (wavelength λ_2), producing a new energy modulation of amplitude $\Delta\gamma_2 \sim \sigma_\gamma$ on top of the sheared bands produced in the first section. A second chromatic dispersion is then tuned in strength to rotate the longitudinal phase of these ripples by approximately $\pi/2$. The resulting phase space is rich in harmonic content and can be tuned, by choosing an appropriate seed laser and dispersion strength, to produce an echo effect whose maximum bunching appears at a net harmonic $n \gg 1$ relative to the initial seed wavelength.

The electron bunching at the final radiator can be expressed in terms of four parameters, the dispersion strengths of the two chicanes $R_{56,1/2}$ and the normalized electric fields $A_{1,2}$ of the seeds:

$$A_{1,2} = \frac{e a_u \lambda_O}{mc^2 \pi \sigma_{1,2}} \sqrt{\frac{P_{1,2}}{c\varepsilon_0 \pi}} \tag{1.19}$$

where $P_{1,2}$ and $\sigma_{1,2}$ are the peak power and the rms transverse dimension of the seeds, e and m the electron charge and mass, c the speed of light and ε_0 the vacuum dielectric constant.
The overall seed wavenumber can be defined as $k_{seed} = k_2/k_1$, where k_1 and k_2 are the wavenumbers of the two seed pulses respectively; the wavenumber of the density modulation after the second chicane is $k_E = ak_1 + mk_2$, where a and m are a negative, tipically small, and a positive, tipically large, integer numbers defining the harmonic number $n = m + a$.

The bunching at the n-th harmonic from EEHG can be calculated as [99]

$$b_{n,m} = |\exp(-\frac{1}{2}(aB_1 + (k_{seed}m + a)B_2))| \tag{1.20}$$

and is tipically maximized for $a = -1$, when the current spikes of all energy bands are spaced at the final radiation wavelength and add up coherently.

The first stage of the EEHG process artificially reduces the intrinsic energy spread per band due to the strong over-compression, which allows much higher harmonic conversion in the HGHG stage at the cost of a slight increase in the energy spread [75, 100].
Assuming a Gaussian distribution for the incoherent energy spread, in contrast to HGHG scheme that has the coherent bunching fraction b_n decaying exponentially as n^2 for high harmonic numbers, EEHG has b_n decaying only as $n^{1/3}$ in the absence of other effects such as incoherent intra-beam scattering.

Therefore, it is in theory possible to achieve very high harmonics with a bunching efficiency up to $b_n = 0.39/n^{1/3}$ [101]. The wavelength and pulse energy stability is also improved and less affected by energy chirps with respect to HGHG.
The ability to preserve the energy bands throughout the seeding line, together with the strong first chicane, is the limiting factor, which makes the bunches more susceptible to collective effects such as intra-beam scattering, incoherent and coherent synchrotron radiation.

Its potential for achieving very high numbers makes it an attractive alternative to HGHG methods, despite its intrinsic and complex coupling of two energy modulation and two chicane strengths. Experimentally, the scheme has been first investigated and confirmed from the optical to soft X-ray regions ($\lambda \sim 160 - 2$ nm) at harmonic numbers as high as 100 [47, 99, 102, 103]. The minimum wavelength produced by this scheme is 2.6 nm [104], while different methods are needed to reach higher frequencies. A cascaded configuration combining HGHG with EEHG has been recently investigated [105].

Self-seeding

The two previous methods require an external signal synchronized to the beam arrival time at the undulator location. To avoid shots with no overlap, the stability of the jitter in the seed signal and the beam arrival time needs to be less than the bunch length. In order to relax the arrival tolerance, most externally seeded FELs foresee a lower current: as a result, the FEL Pierce parameter and the power at saturation are reduced. In addition, the lower FEL bandwidth restricts the amount of energy modulation of the seeding schemes, thus reducing

the ability to scale to very short wavelengths in the 1 nm range [67].

In a self-seeding technique [78, 79] the seed signal is derived from the same bunch in a two stage configuration. Fig. 1.4 shows its schematic layout.

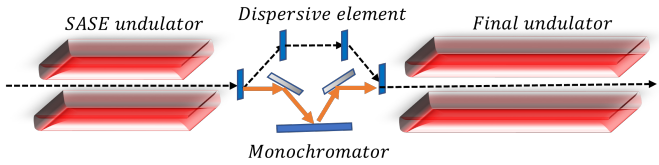

FIGURE 1.4: Schematic layout for a self-seeding configuration. The SASE FEL pulse is filtered by a monochromator to seed the electron beam in the final undulator. The bypass line (Dispersive element) for the electron beam matches its arrival time with the filtered signal.

The first stage of the self-seeding configuration operates as a SASE FEL before saturation, so that the beam preserves the ability to amplify an external signal to full saturation. Following the SASE FEL, the electron beam and radiation field are separated: the radiation is filtered by a monochromator transmitting only a narrow frequency band, thus confining the radiation in a small spectral bandwidth, and then recombined with the electron beam. The filtered signal and the electron beam are finally injected into the second stage of the FEL, operating as an FEL amplifier. The electron bypass is used to match the arrival time of the beam with the monochromatized signal and, secondarily, to remove the induced bunching by the momentum compaction factor of the chicane.

This technique produces a single-mode FEL radiation pulse, with a significantly increased peak brilliance, and is not limited toward shorter wavelengths. However, the process is internally synchronized but not stabilized to an external device. In addition, by selecting a single spike of the SASE spectrum, the intensity fluctuations of the FEL radiation increase.

The initial idea was proposed for the soft X-ray range by Feldhaus et al. [77] and its possible implementation was first considered at FLASH [106]. However, conceptual difficulties with the long electron bypass line, where the transport had to be controlled by a lot of quadrupole and sextuple magnets to preserve the electron beam properties, prevented its realization. A self-seeding scheme with the grating has been implemented at LCLS soft x-ray line [107].

A self-seeding scheme using Bragg reflection was proposed by Saldin et al. [108] for the hard X-ray regime, and has been successfully demonstrated at LCLS [109], where a narrowing of the FEL bandwidth by a factor 50 has been measured. A narrow-bandwidth filter can be used to stretch the short SASE spikes, characterized by a coherence length typically smaller than the bunch

length: this leads to a much longer coherence length, so that a well-defined radiation phase is spread over the entire bunch in the second stage. This effect is also achieved if the slippage is increased to over the entire bunch. Several methods were proposed [110] to artificially increase the slippage per gain length by either breaking up the undulator, and interleaving the modules with small chicanes delaying the bunch, or by operating on a sub-harmonic of the FEL, where the slippage is increased by the harmonic number. All methods reduce the FEL bandwidth up to a point where the bunch length is limiting the spectral width. These methods, equivalent to self-seeding methods but avoiding filters intercepting the radiation [67], are attractive alternatives if the heat load on the monochromator, mirrors or crystal is an issue.

Self-seeding has been successfully demonstrated down to the hard X-ray regime with the generation of narrow and single line spectra. The record for the shortest wavelength with self-seeding was done at LCLS at a wavelength of 1.5 Å. No apparent limitations occur in self-seeding schemes, assuming a sufficient filter exists to clean up the spectrum. The electron beam parameters are the same as for SASE operation and an increase in the FEL brilliance is achieved [67]. Its operation at high repetition rates is challenging due to the heat load of the crystals used.

1.4 Motivations & Outline of the Thesis

This cumulative thesis is focused on design studies and proposals for the development of compact and coherent novel FEL schemes at high repetition rates and short wavelengths.

External FEL seeding has increased the opportunities in high gain FELs due to its full coherence and stability. However, the seed laser limits

- Shortest wavelength that can be achieved.
- The tunability of the seeded FEL radiation.

The seeding schemes introduced so far are limited in harmonic conversion, so that it is desirable to start with a short wavelength seed laser source, as long as it provides sufficient peak power and stability.
Moreover, accelerators based on superconducting RF technology can provide electron bunches at MHz repetition rates. More and more burst-mode and CW accelerators are currently under construction, and there is a clear direction for increased repetition rate in future FELs.

The studies presented in this thesis aim at pushing the limits of the capabilities of FELs and improve them even further to accommodate the needs of multiple experiments of different purposes.

Both the high purity that seeding techniques offer and high statistics are often desired. Neither SASE nor external seeding can offer a good amount of statistics: on one hand, SASE radiation needs to be monochromatized, which leads to flux reduction and intensity fluctuations; on the other hand, seeded radiation is currently only available at a low repetition rate. Extending the wavelength range below 2 nm would allow new types of experiments that require higher resolution, such as imaging and diffraction, to take advantage of the unique properties of seeded radiation.

The main goal is to address the limitations described above and propose novel schemes that aim to combine the unique properties of externally seeded radiation with the high repetition rate of superconducting-based FELs.

The theoretical and numerical studies have been carried out in the framework of two main research projects, whose goal is the construction of compact facilities based on next generation light sources exploiting advanced and revolutionary techniques.

Chapter 1, as well as Appendix A and B, deal with FEL theory, the main principles and properties of FEL emission and some configurations that have been already proposed in literature for a coherent FEL source.

Possible directions for a compact FEL machine are outlined at the beginning of Chapter 2, followed by an overview of the projects at the basis of the performed investigations.

Chapter 3 of this thesis deals with simulation studies on the FEL oscillator configuration, as direct source of coherent pulses at high repetition rate and short wavelengths down to the X-rays, in different spectral regions of interest in its first part, followed by the proposal and investigation of two advanced schemes for an hybrid oscillator-amplifier configuration able to produce high repetition rate FEL photon pulses in the tender X-ray spectral range by means of harmonic up-conversion techniques.

Other numerical studies based on the innovative plasma-acceleration technique, carried out in collaboration with the Frascati section of INFN in the framework of the European ambitious project of a compact plasma-driven FEL user facility, are outlined in Chapter 4, while Appendix C gives a general overview of plasma acceleration techniques.

Finally, Chapter 5 draws some conclusions and outlooks.

Chapter 2

Towards a compact and coherent Free-Electron Laser

For both circular and linear machines, the dimensions of the accelerator are strictly linked to the needed particle beam energy, higher beam energies requiring longer accelerating structures. At the same time, also the economic investment for building an accelerator grows with its dimensions.

Regarding specifically the FEL light sources, the emission of higher frequencies up to the X-rays requires large GeV-scale electron beam energies, and single-pass FEL schemes need a km-long acceleration stage followed by a few tens to hundreds meters-long undulator chain. Therefore, the demanding FEL footprint derives from both the acceleration and the amplification lengths, limiting the use of these devices to few large-scale laboratories.

Studies toward a more compact FEL layout aim at being able to build and operate such machines in any environment, such as hospitals and universities, simultaneously reducing the needed investment efforts. This can be achieved by either shortening the electron linear accelerator (LINAC) or the FEL saturation length.

2.1 Shorter acceleration stage

The primary way to a more compact light source is that of shortening the electron acceleration stage. This research line is linked to the technological advancements in particle acceleration; few promising studies and applications of advanced acceleration techniques may pave the way to more compact accelerators.

Super-conducting (SC) accelerating cavities are the result of the application of superconductivity for particle acceleration: their performance depends on the intrinsic limitation of the critical field of the bulk material, which is tipically Niobium. However, thanks to improvements in fabrication methods and handling procedures, their improved features with respect to conventional

normal-conducting (NC) radio-frequency (RF) cavities have driven the design of large-scale SC accelerators for future applications [111]. Despite requiring a cryogenic system and being less tolerant against beam loss, SC cavities are free from the thermal problems of a NC structure, allow operation at higher gradients with smaller RF power levels and enable acceleration in continuous-wave mode at high MHz-scale repetition rates. Indeed, SC accelerating structures can be continuously powered on, thus saving in operational costs, while progress in simplifying production methods is expected to reduce them further.

As outlined in the next section, the acceleration length of a SC structure can be reduced by exploiting a specific feature of these cavities.

2.1.1 Two-pass two-way acceleration

A peculiar capability of SC cavities, not yet experimentally verified but already studied and considered for some projects, is that of sustaining standing waves that allow the acceleration of the beams in both directions [112, 113]. The concept of two-way acceleration, including beam recirculation and re-injection for a second pass in the accelerator, was proposed in Ref.s [114, 115], even if the beam dynamics of such a recirculation was not studied.

Due to the half length of the accelerating section, this two-fold operation of a SC LINAC allows to reduce the cost on cryogenics. On the RF side, the power required to accelerate the beam depends on its final energy and not on the LINAC length.

A critical point of the two-pass two-way scheme is related to the quadrupoles, whose behaviour is not symmetric for both directions and cannot be employed for beam focusing; SC solenoids can instead be used to contain beam envelopes.

If experimentally verified, this technique would reduce the net acceleration length of SC LINACs, thus leading to more compact layouts, compatible with real-estate availability, at high repetition rates.

2.1.2 Plasma acceleration

An important achievement in the field of accelerator physics is related to the use of plasmas for particle acceleration.

Plasma acceleration is a technique for accelerating charged particles using the large electric fields generated in a plasma. The possibility to accelerate electron beams to ultra-relativistic velocities over short distances by using plasma-based technology holds the potential for a revolution in the field of particle accelerators, including a tremendous reduction in size of accelerators used for research, medical and industrial applications that could allow the development of table-top machines accessible to a broad scientific community [116].
Thanks to their capability to sustain extremely large accelerating gradients,

plasma-based accelerators represent the new frontier for the acceleration of high quality electron beams.

There is no need for metallic or dielectric cavities, the accelerating medium being the plasma itself: for this reason, unlike conventional Radio-Frequency (RF) structures, plasma-based ones can sustain electron plasma waves with electric fields several orders of magnitude higher than those achievable with actual technologies. They can provide accelerating field gradients of some GeV/m compared to the maximum 100 MeV/m sustainable in RF-based machines limited by vacuum breakdown [117].

Its basic concepts and possibilities were originally conceived in 1979 by Toshiki Tajima and John M. Dawson [118].
The generation of plasma accelerating structures in a plasma target, i.e. a jet or confined channel of ionised gas, is initiated by a drive beam, either a laser pulse (laser-driven plasma wakefield acceleration, LWFA) or a relativistic electron beam (particle-driven plasma wakefield acceleration, PWFA), propagating through and inducing electron density oscillations. The excited wakefields feature high field strengths [119, 120]

$$E_0[V/m] \approx 96\sqrt{n_0[cm^{-3}]} \ .$$

A short electron beam, termed the witness beam, placed into this plasma wakefield with the correct phase, can be accelerated and focused to reach GeV energies over centimetre to metre distances.

Both techniques offer a way to build high-performance particle accelerators of much smaller size than conventional RF devices: current experimental devices show accelerating gradients several orders of magnitude greater than conventional particle accelerators over very short distances (1 GeV/m vs 0.1 GeV/m for an RF accelerator [117]). Therefore, plasma accelerators have immense promise for innovation of affordable and compact accelerators for various applications ranging from high energy physics to medical and industrial applications.

The main challenge is that of preserving the beam quality after acceleration in the plasma; advanced techniques able to preserve the beam energy spread or emittance have been demonstrated [121] and make applications based on plasma-accelerated electron bunches possible. Following such advancements, the research community focused on demonstrating that the beam qualities from plasma acceleration are able to trigger FEL emission. Proof-of-princile experiments of FEL lasing based on a laser-driven [122] and beam-driven [123] plasma accelerator were recently conducted.

An overview of the physics and implementation of plasma-based acceleration is given in more details in Appendix C.

2.2 Shorter amplification stage

The FEL amplification stage is the second important contribution to the overall footprint of any FEL machine. For a conventional single-pass SASE FEL scheme, it is basically a long sequence of few meters-long undulator modules, with the emission of higher frequencies requiring longer undulator chains to overcome the FEL lethargy regime and reach saturation. The required amplification length is therefore determined by the saturation length.

As already stated in Chapter 1, FEL seeding has the capability to shorten the FEL lethargy, thus reducing the saturation length with respect to a SASE FEL. The implementation of different FEL schemes also depends on the electron beam temporal structure. The electron temporal distribution from pulsed operation is well-suited for a single-pass configuration, where the footprint of the FEL amplification stage can be reduced by means of FEL seeding. The electron bunch trains at high repetition rate provided by CW SC accelerators is instead suitable for a multi-pass FEL oscillator configuration.

As remarked later, single-pass FEL seeding schemes are limited in both repetition rate and wavelength.

2.2.1 High repetition rate FEL seeding

Many experimental applications, such as time-resolved spectroscopy, would benefit from radiation pulses combining high coherence and repetition rate.

Although laser systems are continuously improving, their repetition rate is at the moment limited to 100 kHz, higher repetition rates featuring insufficient pulse energies for FEL seeding. Furthermore, the shortest attainable wavelength by conventional lasers falls in the UV-deep UV range, also making the shortest FEL wavelength dependent on the performance of harmonic upconversion mechanisms.

Thanks to a deeper knowledge of FEL science and the growing number of SC accelerators providing high repetition rate electron bunches, the interest in high repetition rate FEL seeding is recently rising.

As anticipated in the previous Chapter, seeding at high repetition rates is a challenging task and FEL seeding schemes have been widely studied and so far implemented only at low repetition rates. External laser seeding is intrinsically limited, the highly demanding laser parameters being not easily achievable at high repetition rates. In particular, the requirements put on conventional laser systems in terms of peak power limit their repetition rate to the kHz regime, and the maximum repetition rate of the seeded radiation is determined by the one of the seeding source.

The lack of seed laser systems operating at the repetition rate of a SC accelerator mainly comes from the heat loading due to the high peak powers they need to operate at, proportional to the pulse energy and repetition rate. Some of the electron bunches of a SC accelerator would therefore remain unseeded, limiting the average flux of the FEL pulses.

In order to address this limitation of the standard external laser seeding techniques, following the development in mirrors, simulation codes and the increased knowledge of possible FEL schemes, alternatives to increase the repetition rate of seeding schemes up to the MHz range of a SC machine have been recently studied [94, 95, 96, 97, 124, 98].

In a SC accelerator, more electron bunches per second are extracted from the cathode and this high repetition rate capability gives rise to a specific electron beam structure made of bunch trains with up to hundreds-meters separation. The temporal structure and higher repetition rate of the electron bunches generated and accelerated in a SC machine allow for a multi-pass FEL oscillator configuration [21]: FEL saturation is here reached through multiple passes of the electron bunches in the undulator, thus making the FEL footprint depending only on the required cavity length and potentially shortening it with respect to a single-pass scheme.

The oscillator configuration

In this scenario, I investigated the FEL oscillator configuration and the possibility to use it as seeding source at short wavelength and high repetition rate for a downstream FEL amplifier: this scheme, depending on the availability of suitable mirrors, can itself generate coherent and high brightness FEL pulses at short wavelengths or seed a FEL amplifier to reach even shorter wavelengths. Its theory and operation in different spectral regions are discussed in Chapter 3.

An oscillator–amplifier setup can generate both high peak brightness and high average flux FEL pulses compared to SASE and standard seeding schemes, by producing high repetition rate seeded radiation pulses. The repetition rate is here determined by the cavity, acting as a feedback system which recirculates the radiation pulses to seed the electron bunches in a bunch train, maintaining their peak power and pulse properties.

One may either use a low repetition rate seed laser pulse to initiate the modulation of the first electron bunch, or start from shot noise: in the former case, the laser source and mirror availability determine the shortest wavelength achievable; in the latter, the radiation peak power builds up with the number of passes and the shortest wavelength is determined by the mirrors only. Power amplification within the oscillator is needed to overcome the unavoidable cavity

losses and allows to reduce the seed laser power requirements, therefore increasing its repetition rate and giving the possibility to use shorter wavelength seed lasers, that are only available at low peak powers.

2.3 Design study of a compact X-ray Free-Electron Laser

This section gives an overview of the design project of two compact research infrastructure, including a seeded X-ray FEL facility at high repetition rate and its demonstrator, as well as the ambitious European project of a FEL facility driven by a plasma accelerator.

2.3.1 The MariX project

MariX [8, 125] (Multidisciplinary Advanced Research Infrastructure for the generation and application of X-rays) is the name of the project of a medium-size research infrastructure, designed by the INFN-Milan group for the future scientific campus of the University of Milan in the ex-EXPO area, with contributions from Politecnico di Milano and many other universities, institutions and laboratories in Italy and Europe.

It is a LINAC-based facility with a large energetic efficiency and a compact footprint, conceived for multi-disciplinary studies of matter based on an optimized source for ultrafast spectroscopy. It represents a new generation of X-ray sources, bridging between Synchrotron light sources and Free Electron Lasers (a brief history of light sources from Synchrotron radiation sources to FELs is given in Appendix A).
The designed machine shares common technologies (LINACs, undulators, optimized beam optics lattices, high power lasers) with different generations of light sources, but marryies them into a unique and unprecedented layout blending energy recovery LINACs with arc compressors and recirculated acceleration.

The main motivation behind the project design is to enable fundamental and applied research with photon beam performances tailored to linear spectroscopy and imaging experiments, with a temporal resolution at the femtosecond level and MHz-class pulse repetition rate. MariX scientific mission is pursued by a combined radiation source with two cutting-edge techniques for ultra-high brilliance X-ray generation, namely an Inverse Compton Scattering source (ICS) and a Free-Electron Laser, into a single machine.

The innovative machine layout, shown in Fig. 2.1 and developed directly from Beam Dynamics simulation results and site constraints, is compatible with the limits imposed by real estate availability, sustainable construction and operation costs, thus allowing the integration in highly urbanized areas or university

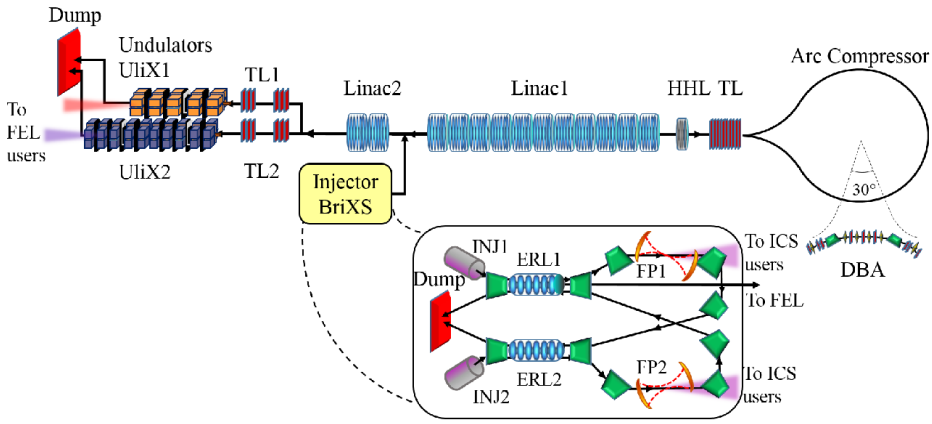

FIGURE 2.1: Conceptual layout for MariX, based on a two-pass Super-Conducting, CW and GeV-class LINAC driven by a folded push-pull Energy Recovery 100 MeV LINAC, from [125]. BriXS: injector. L1 and L2: superconducting LINACs. HHL: high harmonic cavity. AC: arc compressor, DBA: double bend achromat. TL: transfer lines, UliX1 and UliX2: undulators.

campuses [8]. In order to generate, accelerate, control, diagnose and deliver to the users an ultra-high phase space density electron beam with kA-class peak currents, very small transverse and longitudinal emittances, ultra low energy spreads, at an electron bunch charge in the tens to a few hundreds pC range, operated in CW mode, a LINAC-based scenario, operating with Superconducting Radio Frequency (RF) Cavities and a two-fold Energy Recovery scheme, has been conceived.

The whole infrastructure has a footprint about 500 m long and 100 m wide, mainly 8-10 m underground. MariX ultra-high flux and compact footprint come from the use of SC-LINACs supporting the CW mode. On the contrary, conventional X-ray FEL accelerators in operation (as EuXFEL [16]) or under construction (as LCLS-II [17]) are few km-long, with key services and experimental halls at the opposite ends. Furthermore, most operational FELs are driven by warm LINACs and support 100 Hz operation at maximum.

The MariX project is split in two main parts, named BriXS (Bright and compact X-ray Source) and MariX itself, working in series and sharing a common acceleration line. The injector and early acceleration section includes an energy recovery scheme based on a modified folded push-pull CW-SC twin LINAC ensemble (ERL1 and ERL2), allowing to handle very large beam powers (in the MW range) by smartly recovering most of the active power and reducing significantly its impact on electrical power consumption and radio-protection issues. It delivers a twin CW 100 MHz, 100 MeV electron beam to BriXS, depicted in

the enlarged box at the bottom of Fig. 2.1, for scattering the photons of optical laser pulses in two specular Fabry-Pérot cavities (marked as FP1 and FP2).

The second block of the MariX accelerator complex is a two-pass SC LINAC (Linac1 in Fig. 2.1) exploiting the two-way acceleration capability of the SC RF cavities. It is equipped with a bubble-arc compressor (AC) similar to a conventional Double Bending Achromat (DBA) magnetic lattice of a storage ring (e.g. Elettra-like [126]). A high harmonic cavity and a dedicated transfer line are placed between Linac1 and the arc for chirping and optimizing the matching of the electron beam to the compressor.

After a second short LINAC devoted to fine tuning of the beam energy (Linac2), the electron beam reaches a maximum 3.8 GeV energy, therefore allowing the FEL to radiate up to 8 keV actually operating only a 1.5 GeV LINAC (that also includes the BriXS ERL delivering the initial 0.1 GeV injection energy). The MariX FEL line includes two undulators: UliX1, with period $\lambda_u = 2.8$ cm and generating radiation from 200 eV to 4 keV, and UliX2, with period $\lambda_u = 1.2$ cm and delivering 2-8 keV. The FEL and ICS experimental halls are contiguous permitting a possible mutual interaction. Fig. 2.2 gives a perspective view of the buildings hosting the infrastructure [125].

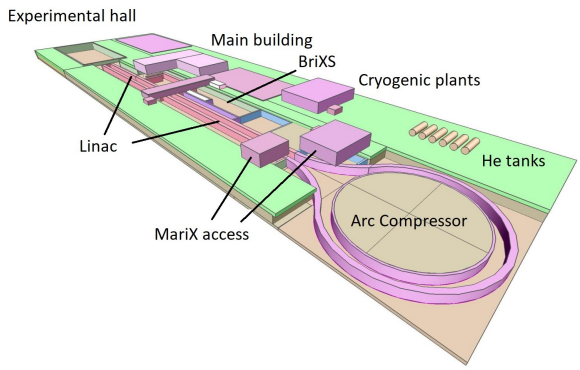

FIGURE 2.2: Schematic perspective representation of the buildings hosting the MariX infrastructure, from [125].

Table 2.1 summarizes the electron beam properties driving the two light sources.

The most peculiar characteristics of the project is the operation in CW mode at high repetition rate of the two radiators: around 93 MHz at high charge (200 pC) for the ICS and almost 1 MHz at lower charge (50 pC) for the FEL [8].

The ultimate goal is the generation of low intensity pulses, suitable for time-resolved experiments but not for multi-photon techniques, thus pointing at the soft and tender X-ray ranges. The main fields of research that can be explored

TABLE 2.1: MariX ICS and FEL working points. ϵ indicates the slice normalized transverse emittance.

Source rate (MHz)	Q (pC)	E (GeV)	$\Delta E/E$ (%)	ϵ (mm mrad)	I_{peak} (A)	Rep.
ICS	200	0.1	0.016	0.7-0.8	20	100
FEL	50	3.2	0.028	0.3-0.5	1600	1

by MariX are: imaging of proteins and nano-objects with nano-metric resolution, linear time-resolved femtosecond spectroscopy, new radiotherapy techniques that harness monochromatic hard X-rays, advanced multi-color X-ray based imaging. The lower number of photons per pulse would greatly mitigate the risk of space-charge effects distorting the spectra in high energy photoemission spectroscopy [8].

BriXS, an ICS X-ray source

BriXS constitutes the first block of the MariX accelerator complex and works as injector for the second block. It is a compact machine capable of generating high-brilliance, mono-chromatic and tunable X-rays with an energy in the range from 20 to 180 keV via Compton scattering.

Enabled applications by such a machine are medical oriented research, mainly in the radio-diagnostics and radio-therapy fields as well as material studies, crystallography and museology for cultural heritage investigations.

The main properties of the Compton X-ray beams produced by BriXS are summarized in Table 2.2.

TABLE 2.2: Summary of BriXS Compton X-ray beam specifications.

Output beam	Units	
Photon energy	keV	20 - 180
Bandwidth bw	%	1 - 10
# photons per shot within FWHM bw		0.05-1 x 10^5
# photons/sec within FWHM bw		$0.05 - 1x10^{13}$
Photon beam spot size (FWHM)	cm	40 - 4
Peak Brilliance	Photons/s/mm^2/mrad^2/bw	$10^{18} - 10^{19}$
Radiation pulse length	ps	0.7 - 1.5
Repetition rate	MHz	100
Pulse-to-pulse separation	ns	10

The CW SC Linac with folding Arc Compressor

After the common acceleration line, the 100 MeV bunches are separated via a fast kicker: one bunch (50 pC at 1 MHz) out of 100 is sent to the high energy (HE) MariX line where it is accelerated to about 3 GeV and compressed to 1.5-2 kA range peak current. The undeflected bunches (200 pC at about 100 MHz) travel to the ICS Interaction Point.

The High Energy MariX section starts at the entrance of the main LINAC (Linac1 in Figure 2.1), where the electrons are injected by a dedicated transfer line.

It consists of a SC-LINAC booster, composed of 11 cryomodules with 11 TESLA-like standing-wave (SW) cavities, accelerating the beam in the 0.9-1.8 GeV energy range, followed by few higher-harmonic SC Tesla cavities (giving the 20 m long HHL linearizer) to pre-correct the longitudinal phase space shape, which give an extra acceleration of about 50-100 MeV. This pre-correction is used to compensate for the arc-compressor coherent synchrotron radiation (CSR) effects[1]. Thanks to the standing-wave operation of the booster, an appropriate injection allows to accelerate electron bunches in both directions with an accelerating field gradient $E_{acc} = 16$ MV/m [112].

Arc compressors are tipically used in FELs to raise the peak current of the electron bunches, simultaneously compressing them, as they pass through dispersive paths characterized by the presence of bending magnets [127]. The MariX Arc Compressor (AC), shown in Fig. 2.3, is based on the arc described in Ref. [128], which uses the arc cells of the Elettra storage ring at Sincrotrone Trieste. The AC consists of 14 achromatic cells, called Double Bend Achromat (DBA) and often referred to as "Chasman-Green lattice", repeated in series.
10 DBAs have positive and 4 negative curvature radius for a smooth matching to the LINAC: it is able to re-inject the electro beam leaving the LINAC after being accelerated once, so to get boosted twice in energy.

Microbunching instabilities[2] may arise from the influence of the CSR emitted by the bunch tail on the upstream particles. This leads to an energy spread

[1] When a bunch of high current passes through a bending magnet it emits Coherent Synchrotron Radiation (CSR), a collective radiation emission phenomena by neighbouring particles responsible for the degradation of transverse emittance of the beam, whose power scales as $P_{CSR}[W] = 2.42 \times 10^{-20} \frac{N^2}{\sqrt[3]{r^2[m]\sigma_z^4[m]}}$, where N is the number of emitters, r the bending radius and σ_z the rms bunch length. CSR emission is strictly related to the bunch length, shorter bunches and higher peak currents emitting the greater power [8].

[2] In order to suppress the microbunching instability and its negative effects on the higher harmonic lasing in the FEL seeded operation, an upgrade of the layout may also include a laser heater (LH) after the cathode, used to induce a uniform heating of the electron beam, or a collimation system after the last two cryomodules and before the FEL lines.

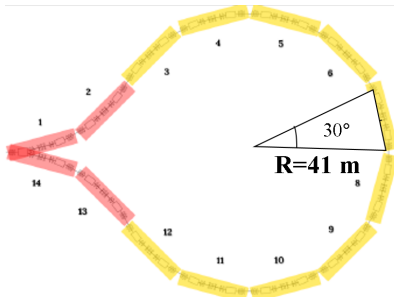

FIGURE 2.3: The AC layout, from [8]. It is composed by 2 DBAs that fold the beam to the left (in red), 10 DBAs that bend to the right (in yellow) and finally 2 DBAs that bend it left again bringing it back to the starting point (in red).

increase, that is then translated into transverse emittance dilution in the subsequent bending magnets. Moreover, due to non-uniform local energy losses, CSR emission tend to deform the longitudinal phase space of the bunch. The concept of the arc compressor preserving the high brightness of an electron beam has been re-elaborated consistently with the layout of a two-pass two-way acceleration in a SC LINAC, under the constraints of beam quality for X-ray FEL emission [112, 129]. The only use of quadrupoles inside the two-pass region deals with the AC beam matching. The combination of the dispersive strength of the ring with a suitable electron energy longitudinal chirp provides an ultrashort and high-current electron beam (the peak current increases from 16 A to 1.5 kA).

Downstream the arc compressor matching line, the returning bunch travels through the L1 booster for the second time. The beam is over focused to few tens of microns by a SC solenoid at the entrance of the line in the second passage. Then the bunch naturally defocuses and is partly kept under control by the RF focusing and the adiabatic damping focusing effect of the LINAC.

An advanced FEL source

The parameters of the electron beam at the exit of the acceleration stage, before entering the photon machine, are summarized in Table 2.3. A maximum 50 pC electron charge is allowed for energy dump need.

The photon machine area is constituted in sequence by undulators, radiation diagnostics and photon beamlines. The layout of the MariX X-ray Free-Electron Laser source, to be compared to the simple basic FEL scheme of Fig. 1.1, is shown in Fig. 2.4: a couple of quadrupole triples separated by a long drift constitutes the transport and matching lines (TL1 and TL2).
The goal of the MariX FEL is to radiate with continuity in a wavelength range

TABLE 2.3: Nominal MariX electron beam parameters for FEL operation

Electron beam	Units	
Energy E_e	GeV	1.6 - 3.8
Charge Q	pC	8 - 50
Peak current I_p	kA	1.5 - 1.8
Norm. rms emittance ϵ (slice)	mm mrad	0.4 - 0.6
Energy spread $\Delta E/E_e$ (slice)	%	0.02 - 0.04
rms pulse duration	fs	1.5 - 16

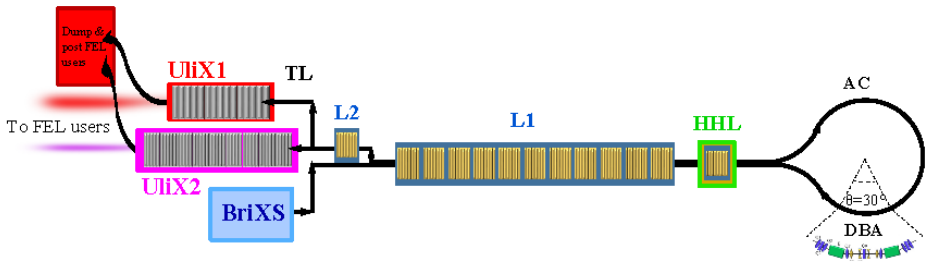

FIGURE 2.4: Layout of the MariX FEL source.

between about 10 nm and 1.5 Å. In order to remain within the bunker allocated dimensions, to satisfy the widest range of users and to balance risks and competitiveness, the selection of the FEL parameters, as well as the ones of the electron machine, has been done by minimizing the dimension of the device, maximizing the FEL performance in terms of versatility, power, coherence, stability and using technologies and techniques at the limit or just beyond the state of the art.

Fig. 2.5 shows the radiation wavelength mapped onto the undulator period and the electron energy for a maximum undulator magnetic field $B = 1$ T, for low (left panel) and high (right panel) photon energies.
For radiation wavelength in the nanometer range (left panel), there is a wide range of options for undulator period and type, all well within the limits of the state of the art. An undulator with period $\lambda_u = 2.8$ cm allows the MariX electron beam to emit from 1 nm to more than 12 nm with a magnetic field of 1 T (corresponding to a value of the undulator parameter $a_u = 1.9$) and to extend the range towards $\lambda = 0.5$ nm by lowering the magnetic field, although with less efficiency. As shown in the right panel, for a permanent magnet undulator (PM undulator), the shorter period undulator device has $\lambda_u = 1.4$ cm, which is a joint KYMA-ENEA project commissioned and tested at SPARC_LAB in

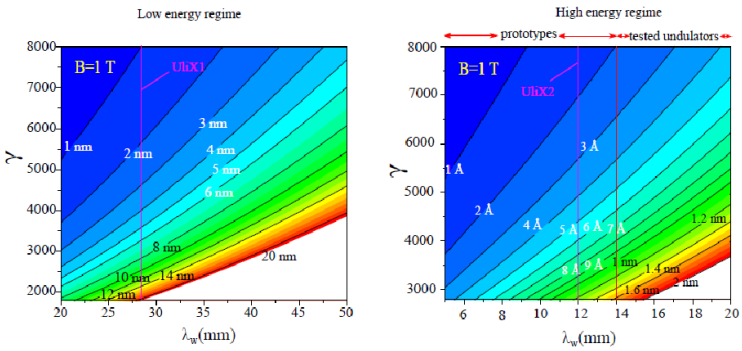

FIGURE 2.5: MariX FEL radiation wavelength λ mapped onto the undulator period λ_u and the electron Lorentz factor γ, from [8], for the undulator peak magnetic field in two different regimes, low (left panel) and high (right panel) photon energies.

the INFN National Laboratory of Frascati [130].
Fig. 2.5 also shows that the objective of radiating at 1.5 Åcan be attained only with undulator periods close or less than 1.2 cm. Considering a magnetic field of about 1 T and varying the electron energy, the wavelength domain of the high photon energy line ranges between $1 - 1.5$ nm and 1.5 Å.

TABLE 2.4: MariX undulator parameters

Parameter	**UliX1**	**UliX2**
Type	pern. mag.	perm.mag perm. mag. segmented
Radiation mode	SASE	SASE Seeded-Cascade
Period λ_w	2.8cm	1.2cm
a_w	< 2.5	< 0.8
Length L_w	$30 - 35$m	≈ 60m total ≈ 70m
Wavelength range	11 nm – 8 Å	$9 - 1.5$ Å $9 - 2.5$ Å
Polarization	linear	linear

The undulators for MariX, whose parameters are summarized in Table 2.4, are supposed to be two: a first undulator UliX1 (Undulator Light Infrastructure for X-rays 1), 30 m-long with undulator period $\lambda_u = 2.8$ cm and strength up to $a_u = 2.5$, and a second one, UliX2, with $\lambda_u = 1.2$ cm and strength up to $a_u = 0.75$ with length of about 60 m. In the last column of Table 2.4, the

second line refers to a possible sequence of modulators for the cascaded FEL option, operated with the UliX2 undulator as radiator (see section 3.2).

Fig. 2.6 shows a plot of the wavelength and photon energy domain covered by the two undulators UliX1 and UliX2 (in the not-segmented version) as function of the electron beam energy [8].

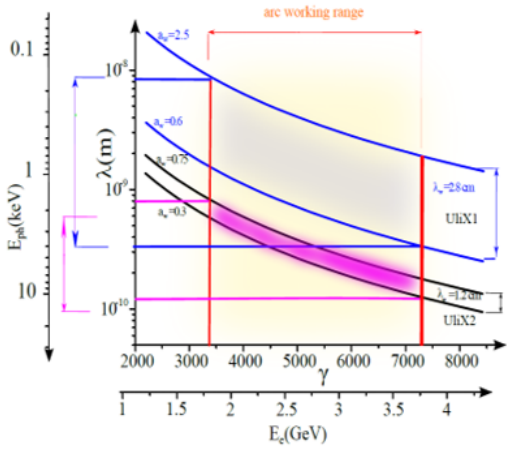

FIGURE 2.6: MariX operation wavelength (photon energy) vs electron Lorentz factor (electron energy) for the two undulators ULIX1 and ULIX2, from [8].

The yellow area delimits the wavelength domain (from 100 eV to 4 keV, soft X-ray range) produced in the undulator UliX1, whereas the red area is relevant to UliX2 (from 2 keV to 8 keV, tender-to-hard X-ray regime).

The MariX FEL lines are able to provide coherent X-rays tailored for time-resolved spectroscopies, with individual pulses not exceeding the linear response regime and space charge effects. This implies about 10^8 photons per 10 fs-long pulses, which is 3-4 orders of magnitude lower than the individual peak intensity of the current X-ray FELs. However the 4-5 orders of magnitude gain in repetition rate restores the high flux per second of the most advanced synchrotron sources, still having ultra-short pulses suitable for time resolved pump-probe methods in photoelectric effect and inelastic X-ray scattering experiments. Interesting energies in the soft X-ray range investigated by the low photon energy line UliX1 are the carbon K-edge (280 eV, 4.4 nm) and the domain of the water window (around ∼415 eV, 3 nm). Going toward higher energies, the oxygen (∼500 eV) and the silicon (1.8 keV) K-edges follow. The high energy line UliX2 can access to energies above 5 keV, thus enabling the analysis of key earth-abundant chemical elements and providing atomic resolution. The dynamics of molecular and atomic phenomena can be detected by soft X-rays with pulse

lengths of about 10-100 fs, whereas the electronic processes involving outer and inner shells develop on atto/femto-second scale and need therefore probes and methodologies in this duration range.
The trend for newest and future set-ups is that of increasing by orders of magnitude the repetition rate with respect to the 10-100 Hz available in the existing short wavelength FELs, thus reaching the high repetition rate capability of IR FEL facilities. A high repetition rate of 1 MHz and an uniform time structure should provide the possibility to collect more than 10^8 scattering patterns (or spectra) per day with sample replacement between pulses, enabling methodologies as the serial crystallography and the multidimensional X-ray spectroscopy. The availability of a high average coherent power in the soft-hard X-ray range, combined with reproducible pulses at high repetition rate, will enable studies of spontaneous ground-state fluctuations and heterogeneity at the atomic scale and femtosecond time-scales using powerful time domain approaches such as the X-ray photon correlation spectroscopy (XPCS).

The MariX extremely large repetition rate locates it among the sources with largest average flux worldwide. Moreover, the 200 fs down to 10 fs pulse durations coupled to the capability for double pulses with independent control of energy, bandwidth and timing open up experimental opportunities that are simply not possible on non-laser sources.

The project Conceptual Design Report (CDR) was funded by INFN and published in 2019. It has been successfully presented in national and international conferences and there has been interest from the scientific community; however, the needed investment effort prevented its construction.

Both SASE and seeded operation of the MariX FEL have been included in the CDR. More detailed studies on seeding techniques for the MariX high repetition rate X-ray FEL have been later investigated and are part of this thesis (see sections 3.1.2, 3.1.3 and 3.2 in Chapter 3).

2.3.2 BriXSinO

BriXSinO [131] (Brilliant source of X-rays based on Sustainable and innOvative accelerators) is the project of a high-flux dual X-ray and THz radiation source based on Energy Recovery Linacs (ERLs), conceived as a MariX demonstrator to be built at the LASA laboratory in Segrate, which is devoted to studies and applications of superconductivity and criogenics.

This section discusses the design and main components of the facility, whose primary goal is to study the physics and demonstrate the feasibility of the two-way acceleration and energy recovery in SC Linacs (ERLs) equipped with bubble arcs.

Fig. 2.7 shows the layout of the BriXSinO facility.

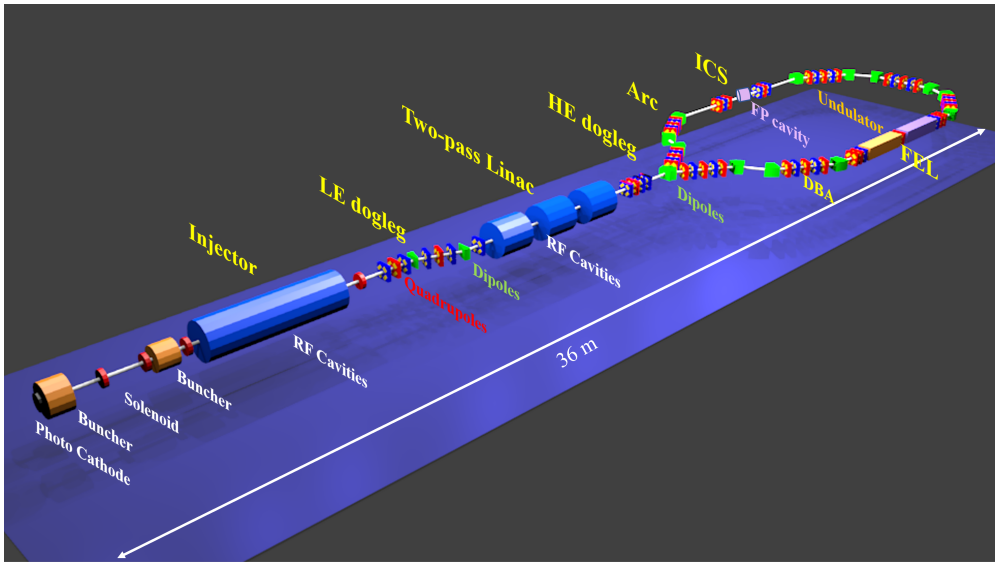

FIGURE 2.7: BriXSinO general layout, taken from [132]. From left: injector with DC gun, bunchers and radiofrequency cavities. Low-energy (LE) dogleg with quadrupoles in red and dipoles in green. Two-way (or ERL zone) SC Linac that can be operated in the two-pass two-way acceleration or ERL mode. High-energy (HE) dogleg. Recirculating loop (Arc), made by seven Double Bend Achromats (DBA), hosting the light sources and bringing back the beam to the two-way zone. Fabry-Perot (FP) cavity. Free-Electron Laser (FEL). Two different beam dumps for the low- and high-energy electron beams are foreseen beside the injector and are not sketched here.

The first element from left is the injector: the electron bunches, with 50-150 pC bunch charge per shot, are here generated by means of a DC gun (300 keV class, Jefferson Lab.-like) driven by an Ytterbium laser and extracted from a Cs_2Te photo-cathode, operating at a maximum repetition rate of ~ 92.8 MHz.

Downstream the gun and before injection in the main LINAC through a dispersive path constituted by a low energy dogleg [133, 134], two RF subharmonic bunchers operating at 650 MHz and three short SC cavities compress the beam and boost its energy up to ~ 4.5 MeV, respectively.

The main LINAC, where the beam passes twice with alternate verse, is constituted by a cryostat hosting two or three Standing-Wave SC seven-cell cavities.

The arc is the last element of the device, which has been designed as composed of 7 Double Bend Achromats (DBA): it allows the beam to come back to the two-way main LINAC and hosts two experimental stations in correspondence of its zero dispersion regions, namely the Inverse Compton Source (ICS) named

Sors and a THz FEL.

Two operating modes of the two-way LINAC are foreseen: the energy recovery mode, where the beam energy is recovered by the cavities, requires a delay system for synchronizing the return beam with the decelerating RF wave crest; in the two-pass two-way acceleration mode, first introduced in the framework of the MariX project [8, 112], the beam is accelerated two times by travelling the same Linac in opposite directions.
Two different dumps, located on the injector side of the complex, are used to dump the low-energy and high-energy electron beams respectively.

The injector

The injector of the BriXSinO complex, whose sketch is reported in Fig. 2.8, has been designed considering the typical goal of injectors and mergers for ERL machines, including high average beam currents and low injection energies, and to to provide high-brightness electron beams for experiments.

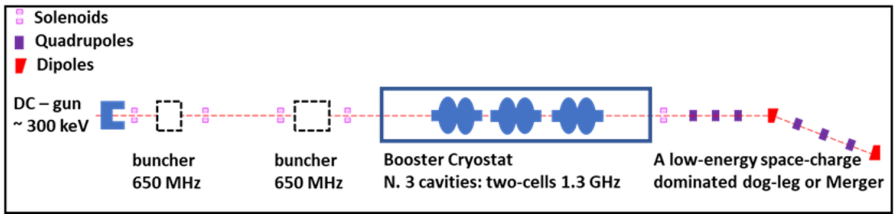

FIGURE 2.8: Sketch of the BriXSinO injector: The DC-gun, the two sub harmonic bunchers, the cryostat booster carrying three two-cells cavities and the low energy dogleg. The different phase velocities cause the different length of the two bunchers. Courtesy of A. Bacci.

The first component of the injector is the state-of-the-art 250-350 keV DC-gun, driven by a Ytterbium laser. The laser pulse characteristics are summarized in Table 2.5.

TABLE 2.5: Main characteristics of the laser pulse shape at the BriXSinO gun photocathode.

Parameter	**Value**
Flattop laser pulse	22.3 ps
Rise time	1.0 ps
σ_x transverse uniform	0.710 mm
Extracted bunch charge	50-150 pC

Following the 7 cm-long solenoid for emittance compensation, two normal conducting RF bunchers working at 650 MHz (the sub harmonic of the main RF machine frequency). guarantee both acceleration and compression downstream the gun.

The choice of operating the bunchers at a sub-harmonic is driven by the fact that a longer RF bucket allows a more linear accelerating field with relevant benefits in the bunch longitudinal compression and in the energy spread preservation: the performances of two frequencies (650 MHz vs 1.3 GHz) for bunch compressors have been compared with the Genetic optimization code GIOTTO [135] by varying the RF phase velocity, field and injection phase.
The best solution values are summarized in Table 2.6.

TABLE 2.6: Bunchers' best working parameters found using GIOTTO [135], minimizing the normalized bunch emittance, the energy spread and the bunch length.

	First-buncher	**Second-buncher**
RF phase velocity/c	0.740	0.906
RF E_{peak}	3.4 MV/m	3.4 MV/m
Injection Phase	-30°	-17°

It follows a cryostat with three two-cells SC cavities, with accelerating gradient up to 7.5 MV/m in CW, thus giving a low energy boost at 4.5 MeV.
The injector could achieve 100 MHz electron bunches. Conversely, the maximum sustainable average current of 5 mA in the cavities and on the dump may limit the single beam charge values at this high repetition rate, while higher amounts of single beam charge could be achievable at lower repetition rates.

After the injector, the electron bunches have good qualities and can enter the dispersive path: they are 1 mm-long, have a small-1 μm normalized transverse emittance and small energy spread. From a first evaluation, the dark current has been considered negligible: its maximum value (considering both the gun and the acceleration cavity) turns out to be below 1 nA.

The dispersive path

As shown in Fig. 2.9, the dispersive path is a standard dogleg.
The beam dynamics in this space charge-dominated dispersive path has been studied with GIOTTO [135].

The beam emittances are conserved.

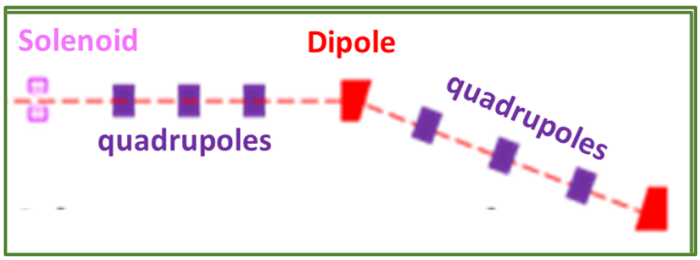

FIGURE 2.9: Sketch of the BriXSinO low-energy dogleg, composed of a solenoid, three quadrupole magnets and a couple of dipoles separated by another quadrupole triplet.

Energy recovery superconducting module

The energy recovery SC module is a two-way, energy recovery cryomodule where the energy of the electron bunches gets boosted to 45 MeV.

Its scheme, consisting of three 7-cells SC cavities, is shown in Fig. 2.10.

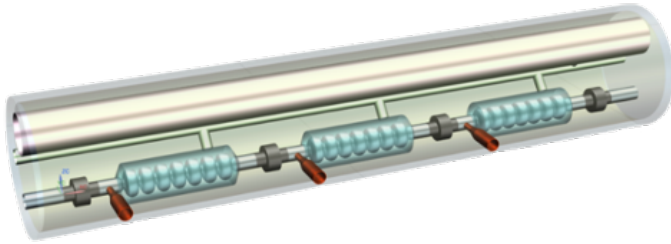

FIGURE 2.10: BriXSinO SC energy-recovery LINAC, composed of three 7-cells SC cavities.

The use of two or three 7-cell cavities in the cryostat was considered: the latter turns out to be more suitable, allowing a lower accelerating gradient and additional knobs for beam dynamics control.

The returing electron beam is either decelerated in the energy-recovery mode or re-accelerated in the two-way acceleration one: in the former case, it is dimmed to 5 MeV for the low-energy dump, while it is re-acceleration at lower current by phase matching in the latter case.
From beam dynamics simulation results, the good beam qualities are preserved both in the forward and in the backward direction, and the presence of two counter-propagating bunches within the Linac does not deteriorate them [8].

Table 2.7 summarizes the main beam properties in different sections of the facility: its third column presents the optimized working point after the first passage in the LINAC. The bi-directional dynamics and the presence of multiple

TABLE 2.7: BriXSinO electron beam characteristics during the various phases.

Property	After the injector	After the LINAC	Before the undulator
Energy	1.4 MeV	43 MeV	43 MeV
Energy spread	0.01 keV	145 keV	145 keV
Emittance in x	1.4 mm mrad	1.6 mm mrad	1.6 mm mrad
Sigma x	1.3 mm	0.23 mm	0.15 mm
Sigma z	1.3 mm	2.2 mm	1.8 mm

consecutive modules that can couple high order radiofrequency modes (HOMs), which perturb the beam dynamics, are still under investigation.

An optical system of four quadrupoles, placed downstream the SC LINAC, provides a flexible electron beam matching to the arc.

The arc

The BriXSinO arc is a feedback loop similar to the MariX bubble arc compressor and constituted by seven DBA sections (two 30-degrees dipole magnets and five quadrupoles).

Its layout is shown in Fig. 2.11.

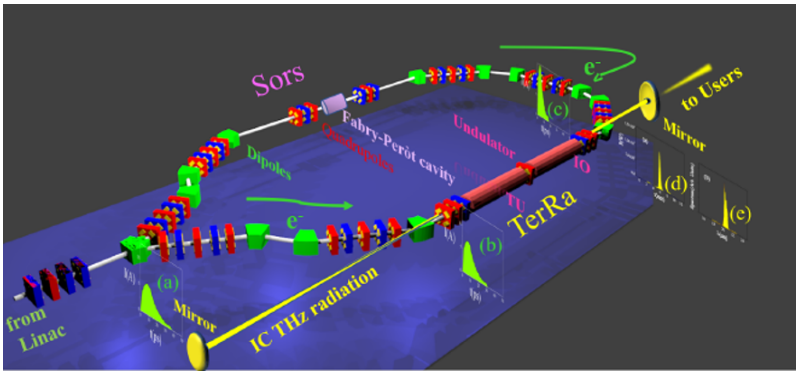

FIGURE 2.11: Layout of the BriXSinO arc, rendering of I. Drebot. The two radiation sources are pointed out: the X-ray ICS Sors and the THz FEL oscillator TerRa. In green: alternative paths of the electron beam, on the left or on the right of the arc. Quadrupoles are in red or blue, dipoles in green, the cavity mirrors in yellow. (a) Electron current at the entrance of the arc. (b) Current at the undulator entrance coming from right. (c) Current at the other edge of the undulator if the electron beam comes from left. (d) and (e) Intra-cavity (IC) power and spectral distribution of the THz radiation at the exit of the undulator.

Two light sources are placed in the zero-dispersion regions of its two opposite branches: the Inverse Compton scattering X-ray source Sors and the TeraHerz source TerRa.

The transport in the arc contributes also to compress the electron beam, as explained in Ref [136, 128, 127]: the 100 pC beam shortens from 2.2 mm to 1.8 mm, increasing its peak current from 5.5 A to about 7 A when passing through the two DBAs along the right branch of the arc, from the exit of the Linac to the FEL entrance.

Table 2.7, last column, presents the beam parameters at the undulator entrance. Fig. 2.12 presents the simulated longitudinal phase space of the electron bunch at the entrance of the undulator, showing the accumulation of the particles on the leading edge of the bunch producing coherent radiation, which is the seed of laser oscillation in the THz regime.

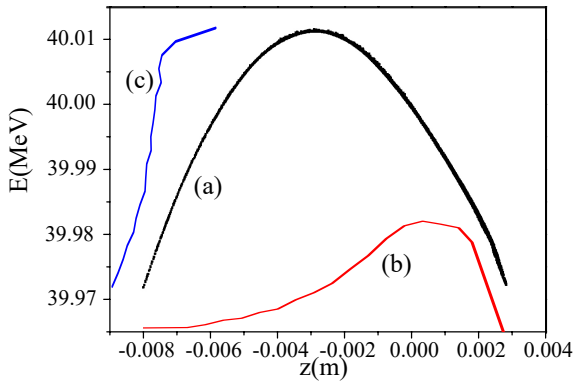

FIGURE 2.12: Simulated longitudinal phase space at the BriXSinO FEL entrance, from [132]: (a) longitudinal coordinates of the particles E(MeV) vs z(m). (b) Electron beam current in arbitrary units. (c) Energy density.

In alternative, the electron beam could run across the arc in the opposite direction, passing through 5 DBAs before reaching the other side of the undulator, allowing a further compress the beam down to 1 mm, with a corresponding peak current of 12 A. Operation with a slightly larger charge, up to 120-130 pC, could enhance the current to the value of 15-16 A and is under investigation.

BriXSinO will represent a multitasking device, different from any other project, where studies of the physics and feasibility of the two-pass two-way electron beam acceleration and energy recovery in SC LINACs equipped with

bubble arcs [8, 112] are foreseen. It exploits a different energy recovery scheme, where the beam either gains or give energy to the same SC cavities in the two directions, compared to the BriXS folded push-pull Energy Recovery 100 MeV LINAC scheme within the MariX project, where the beam is accelerated and decelerated in two different SC LINACs. Regarding the two-way acceleration mode, it is basically a demonstrative operating mode not exploited in the light sources.
Furthermore, the radiation sources driven by the electron beams exhibit huge potentialities for applications. This versatility makes BriXSinO attractive and complementary to the other THz FEL Oscillators.

The high repetition rate is a distinctive and essential characteristic of the device. Its compact footprint (maximum length of about 36 meters, see Fig. 2.7), sustainability and versatility make it a new paradigm for sources dedicated to experiments in various research fields in medium/small size laboratories, hospitals and university campuses.

The project has been funded by INFN and its Technical Design Report has been recently published. I contributed to the machine design study focusing on the THz FEL source: this is detailed in Chapter 3, section 3.1.1.
The bunker and the machine injector are now being built in the LASA laboratory.

2.3.3 EuPRAXIA

EuPRAXIA [116, 137] is a European project for the development of a distributed particle accelerator research infrastructure based on novel plasma concepts and laser technology.

This innovative and ambitious project involves links, knowledge exchange and synergies between the international laser community and accelerator science. Recent breakthroughs in laser technology and parallel advancements in plasma accelerators worldwide underpin the realisation of a plasma-accelerator-based user facility for science and research exploiting existing accelerator infrastructures in France, Germany, Italy and the UK.

The realisation of the first plasma user facility worldwide aims at demonstrating feasibility and gaining operational and user experience.
As anticipated earlier, a significant reduction in size and possible savings in cost over current state-of-the-art RF-based accelerators is offered by a electron accelerator using laser- and electron beam– driven plasma wakefield acceleration.

High-quality beam generation from a plasma accelerator is the fundamental stepping stone to possible future plasma-based facilities.

The plasma-based accelerator of the EuPRAXIA project [116, 137] envisions a beam energy of 1 to 5 GeV and a beam quality equivalent to RF-based LINACs: distributed and versatile user areas will exploit the inherent features of the plasma accelerator, e.g. multiple parallel user lines, the generation of ultra-fast electron and short photon pulse lengths, the quasi-point–like emission of X-rays inside plasmas for ultra-sharp imaging, and unique pump-probe configurations with the synchronised EuPRAXIA particle and laser beams.

The consortium will set up several plasma-accelerator beamlines providing pilot access to academic and industrial users at the different construction sites. Versatile applications in various domains, such as compact sources for medical imaging, table-top test beams for particle detectors, as well as deeply penetrating X-ray and gamma-ray sources for material testing, will be enabled by the EuPRAXIA energy range and performances.

Two different sites are supposed to host a user facility based on beam- and laser- driven plasma wakefield acceleration. The INFN national laboratories in Frascati will host the project headquarters and has been agreed as the construction site for a beam-driven plasma accelerator facility driving a FEL: EuPRAXIA@SPARC_LAB [138] is the name of this Frascati contribution to the EuPRAXIA project, including a beam-driven plasma accelerator based on the development and construction of a compact X-band RF accelerator, driving two FEL beamlines. Preliminary results towards the EuPRAXIA@SPARC_LAB project and its FEL beamlines are discussed in Chapter 4. Regarding the laser-driven construction site, it will be determined during the preparatory project phase.

EuPRAXIA will support and further position Europe as a world-leading competitor in accelerator innovation, also challenging and supporting the laser industry to further develop and improve their products on high-power pulsed lasers.
Its Conceptual Design Report was published in 2019, while R&D activities towards the EuPRAXIA@SPARC_LAB Technical Design Report are underway and will follow in the next 5 years.

I am involved in the FEL working package: as shown in Chapter 4, section 4.2, my still ongoing contribution to the preparation of the TDR concerns the design and simulation studies of the two FEL beamlines of the project baseline. Full operation is expected in 8–10 years.

Chapter 3

Free-Electron Laser Oscillator: numerical studies

This Chapter is devoted to numerical studies of the FEL oscillator (FELO) configuration and the design of advanced schemes for a seeded FEL source of high repetition rate X-rays.

The FEL Oscillator, being capable of generating stable and high-power FEL pulses at high repetition rate, plays an important role in the context of a compact and coherent FEL at high repetition rate.

Physics and design strategies

In this configuration, already introduced in Chapter 1, a sequence of high repetition rate electron bunches is driven inside an optical cavity hosting an undulator for FEL emission. The radiation field is thus generated by multiple passes of the electron bunches through the undulator[1].

The FELO works as a threshold system, whose successful operation is connected with the electron beam, the undulator length, the total losses as well as mirror properties. The field power needs to approach saturation and evolves with the number of cavity round-trips n as

$$P_{n+1} = (1 - R_{tot})(1 - \Gamma_{abs})P_n$$

where P_{n+1} and P_n are the peak power at pass n+1 and n respectively, R_{tot} is the total resonator reflectivity and Γ_{abs} accounts for absorption losses. The net gain of the system is

$$G = \frac{P_{n+1} - P_n}{P_n} \ .$$

[1] Basic concepts on the physics and operation of FEL oscillators can be also found in [139].

The FEL interaction in the undulator deteriorates the used electron bunch, which is sent outside the cavity and eventually driven to a dump after each pass. The field power in the first pass P_1 is stored and recirculated inside the resonator to seed a successive electron bunch. In the start-up regime, the net gain G is positive. Over a large number of passes, the electrons get bunched and emit coherently at the resonant wavelength; as the optical intensity increases, the EFL gain decreases until it is equal to the total cavity losses (G=0) and FEL power saturates. At saturation, the peak power remains constant as long as the pulse properties are stable (steady state regime).

The FELO output efficiency depends on the undulator efficiency, measure of the energy extraction efficiency from the electron beam to the optical pulse, the outcoupling Γ_{out} and total losses Γ_{loss}:

$$\eta = \left(\frac{\Gamma_{out}}{\Gamma_{out} + \Gamma_{loss}} \right) \frac{P_{FEL}}{P_{beam}} \ .$$

The emission process in the first pass can start either directly from the electron shot-noise or from an initial seed pulse spatially and temporally superimposed to the electron bunch at the undulator entrance. When starting from noise, the field power P_1 arises from incoherent spontaneous emission in the undulator and the emitted pulses are independent of seed laser systems both in terms of repetition rate and wavelength. In the second case, the external seed laser pulse provides precise control over the start-up conditions, shortening the transition to the steady-state. Its optical properties are retained in the feedback system, while the repetition rate is determined by the cavity. In addition, for advanced oscillator-amplifier setups, the induced energy spread in the undulator can be controlled and kept far from saturation by choosing the right undulator length and initial seed laser power for a given wavelength.

The optical resonator is an important and distinctive component of this configuration. It is used to increase the low repetition rate of seed lasers and to recirculate the radiation, which interacts with fresh electron bunches over many passes. The propagation can be in vacuum or in waveguide.

The primary step in the resonator design is the choice of cavity geometry, which depends on the wavelength requirement and space constraints of a specific facility. The simplest geometry for the resonator is made up of two concave mirrors: the high-reflective rear one is used to reflect the backward radiation field, while the front mirror (outcoupler) reflects the radiation and is also used for radiation outcoupling. FEL resonators may have different symmetries: in the most common near-concentric design, where the distance between mirrors is equal to two times their curvature radius ($D = 2R$), the optical field is focused in the middle and its size gets larger at the mirrors, so that the strong

beam divergence minimizes the risk of optical damage. In a two-mirror confocal resonator the mirrors are instead separated by a distance equal to their radius of curvature ($D = R$), and the optical beam diameter is much larger than the electron beam.

A method to estimate the stability of a resonator, inherited from laser physics, is given by the Fox-Li condition $g_1 g_2 \leq 1$, where $g_i = 1 - \frac{D}{R_i}$. Depending on the available dimension for the cavity and the mirror losses, other resonator geometries consisting of a larger number of mirrors are possible: an example is the bow-tie cavity layout, in which the field is reflected by four mirrors [140].

The most stringent stability requirements are posed by the cavity length and the electron-radiation transverse alignment. In order to let the process start and reach saturation, the opticaL pulses need to overlap with the electron bunches in N passes. For this reason, the round-trip cavity length L_{cav} (equal to two times the physical cavity length for a simple two-mirror cavity) is directly linked to the bunches' separation, represented by their repetition rate f_{rep}:

$$L_{cav} \simeq c/(m f_{rep}) \tag{3.1}$$

where the electron bunches are here assumed to move at the speed of light c, and m is an integer representing the number of round-trips before the radiation field meets a new electron bunch at the undulator entrance.

Therefore, the oscillator footprint is reduced either by considering high repetition rate electron bunches, as the ones accelerated in a SC machine, or by a factor equal to the number of round-trips in-between two consecutive bunches. On one hand, the electrons provided by SC machines can drive effective FELO schemes with reasonably compact cavities and low mirror losses; for example, the MHz repetition frequency of MariX corresponds to 300 m of bunch-to-bunch separation and needs a 150 m-long cavity at maximum. On the other hand, despite the reduced total resonator reflectivity and increased losses, a larger number of round-trips can allow to drive this scheme with the bunches provided by a NC accelerator, meeting the lower repetition rate requirements of some experimental applications (as the 100 kHz range of time-of-flight measurements).

Once the so-called cold cavity length in Eq. (3.1) is determined, the actual length needs to take into account the slippage of the optical pulses with respect to the slower electron bunches. As already stated, the slippage length accumulated in the undulator amounts to approximately $L_{slip} = N_u \lambda$, where λ is the pulses' resonant wavelength. Due to slippage effects, perfect synchronism is achieved for cavity lengths longer than the cold cavity length (with no slippage). Moreover, it can cause degradation of the output FEL pulses and needs to be compensated. For this purpose, it is convenient to operate with

long electron bunches, i.e. $\sigma_e \geq L_{slip}$.
Considering both the gain of the system and the slippage, the resonator length can be adjusted by using a technique called cavity length detuning [141], based on the fact that a change in cavity length changes the radiation pulse arrival time AND whose goal is to find an optimal cavity length for radiation-electrons overlapping after each round-trip. it is tipically performed by adjusting the position of one or more mirrors, the cavity detuning for maximum power gain being independent of the total reflectivity and only depending on the total slippage per pass.

The mirror choice plays another important role. First of all, it mainly depends on the spectral range of operation: cavity mirrors need to be suitable to the emission frequency range.
Their material should minimize absorption losses in that range. The mirrors' reflectivity and curvature radius are other two important parameters: the reflectivity needs to be as high as possible to avoid losing the radiated power and is the main challenge; the curvature radius determines the focusing properties and depends on the radiation beam size and divergence. Furthermore, their filtering properties instead depend on their spectral line-width and acceptance.

Resonators have at least two transportation mirrors, one highly reflective and the other one either translucent or containing apertures for outcoupling the radiation. Apart from simple transportation mirrors, the resonators can additionally include gratings (monochromators) and focusing optics.

Round-trip losses are the result of the radiation-electron overlapping, the absorption, the mirror losses (due to the limited reflectivity) and the outcoupling of the intra-cavity radiation. The latter can be accomplished by means of a partially transparent mirror, a reflective window and grating, or a hole in the end-mirror.

In the hole-outcoupling scenario, out-coupling losses per round-trip refer to the percentage of light outcoupled from the hole and are determined by the hole size with respect to the radiation beam size. The hole vs. radiation beam size ratio is the relevant parameter: for a certain hole radius, the radiation beam size at the holed front mirror must be large enough to guarantee a fraction of a few percent of extra-cavity radiation, and the Babinet theorem is used to treat the reflection [142].

A typical total round-trip loss is less than 10%, including the transmission and absorption from each mirror and the extraction efficiency.

Model and simulation

The numerical modeling of a FELO scheme requires the evaluation of radiation emission inside the undulator by means of a FEL code, followed by the extraction of the radiation and its transport within the cavity [143, 35, 144, 145, 39, 124], taking into account its interaction with all the optical elements, back to the undulator entrance where it is superimposed to the successive electron bunch for the second pass.

The first topic to deal with is the cavity design: its zero-detuning length (Eq. 3.1) must match the electron bunch repetition rate and be long enough to host the undulator for sufficient FEL gain, while the detuning length depends on the slippage length $N_u\lambda$ accumulated in the undulator. Mirrors with high reflectivity, good thermal and filtering properties in the spectral range of operation are selected, while the cavity geometry is mainly linked to the maximum number of mirrors allowed, determining the round-trip losses, and space constraints.

Following the resonator design, the simulation of the FELO operation begins with the FEL amplification for the first pass of the electron bunch in the oscillator undulator, and includes the radiation transport through the cavity, accounting for the effects of the optical line components, such as mirrors and filters, and propagation. During its propagation, the pulse gets reflected from the mirrors and moves back to the undulator entrance.

This simulation process is reiterated at each pass, until a steady state is reached. It can take from tens to thousands round trips before saturation, which makes the whole procedure time-consuming.

Different simulation tools, either one- or three- dimensional, can be employed for the FEL emission and optical propagation.
During my studies I developed a code written in Fortran, which strictly depends on the cavity configuration but performs all the required simulation steps automatically for each round-trip.

According to the optics' matrix formulation [146] (see Appendix B.1), each cavity component, such as drifts, mirrors and lenses, is described by a transfer matrix and the entire resonator is represented by a round-trip 2×2 matrix, given by the product of the various transfer matrices in reverse order.
FEL emission at each pass in the undulator is simulated by running the three-dimensional FEL code GENESIS 1.3 version 2 [147]; in order to simulate the interaction of the intra-cavity radiation with different bunches and the bunch-to-bunch fluctuations, the microscopic distribution and the relevant macroscopic properties of the electron bunch can be changed shot to shot by changing randomly the seed of the Hammerslay sequences of the electron phase space

distribution and the average beam characteristics within the jitter intervals respectively.

The amplified radiation $E(\mathbf{x})$, where $\mathbf{x} = (x, y, z)$, is extracted from the simulation over a three-dimensional grid, given as input to the code and recirculated through the optical line[2]. Mirrors reflect only a fraction of the incident light, which therefore gets attenuated, and the remaining part is dissipated through heating: for this reason, high reflective mirrors with a suitable damage threshold at the operating frequency are chosen.

The propagation of the radiation from the undulator exit back to its entrance can be evaluated either by treating each pathway separately or by considering the cumulative cavity transfer function, where attenuation and filtering effects from the different optical elements are included.
The effect of the mirrors on the radiation pulse is described by the convolution between the electric field E in frequency space and their reflectance R, whose profile is given as input to the code:

$$E(\mathbf{x}') = \int d\mathbf{k} R(\mathbf{k}) \int d\mathbf{x} E(\mathbf{x}) e^{i\mathbf{k}\cdot(\mathbf{x}-\mathbf{x}')}$$

where $\mathbf{k}$ is the wave vector of the radiation. As aforementioned, the reflectance can include all cavity mirrors at once, representing the whole cavity reflectivity, or each mirror can also be treated independently.

The propagation effect is then computed by means of the modified Huygens integral [146]: the field after the transport in the cavity is given by

$$E(\mathbf{x}') = \int dx dy \frac{iE(\mathbf{x})}{B\lambda} e^{-\frac{i\pi}{\lambda B}(A(x^2+y^2)-2(xx'+yy')+D(x'^2+y'^2))}$$

where A, B, C and D are the elements of the round-trip matrix describing the optical path and depending on the drift lengths and on the mirrors' focal lengths. As before, the propagation can be evaluated for each single drift length or for the cavity as a whole, depending on the presence of additional elements in-between the resonator mirrors. In the first case, the Huygens integral is extended from the end of the undulator up to the front mirror at first. Moreover, this case allows to monitor the radiation field transverse size after each component of the cavity.

[2] The GENESIS source code, written in Fortran in its second version, has been slightly modified by fixing a given name, i.e. input.in, for the input file name: such input file name is rewritten by using the Fortran code at each step and, by so doing, GENESIS runs do not ask for it anymore before execution. At the end of each simulation (passage in the undulator), the radiation is extracted over a three-dimensional grid, whose size is over-sampled in the Fortran code, before being propagated through the cavity.

If radiation focusing is important and the resonator includes a focusing system, such as a telescopic system, an alternative method based on the Gaussian optics formulation provides the beam spot size evolution within the cavity. The FEL pulse is approximated as a Gaussain field

$$E(x,y,z) = \frac{1}{q(z)} \exp\left[-ik\frac{x^2+y^2}{2}\frac{1}{q(z)}\right]$$

and described by its complex curvature radius $\frac{1}{q} = \frac{1}{R} - i\frac{\lambda}{\pi w^2}$, where R is the real beam curvature radius and w its spot size.

Along a cavity path $z_1 - z_2$, described by its transfer matrix M=(A,B,C,D), the beam complex curvature radius q evolves as $q_2 = \frac{Aq_1+B}{Cq_1+D}$. By separating the real and imaginary parts, the evolution of the spot size and real curvature radius is respectively

$$w_2 = \sqrt{\left(A + \frac{B}{R_1}\right)^2 w_1^2 + \left(\frac{\lambda B}{\pi}\right)^2 \frac{1}{w_1^2}} \tag{3.2}$$

$$\frac{1}{R_2} = \frac{\left(C + \frac{D}{R_1}\right)\left(A + \frac{B}{R_1}\right) + \left(\frac{\lambda}{\pi w_1^2}\right)^2 BD}{\left(A + \frac{B}{R_1}\right)^2 + \left(\frac{\lambda}{\pi w_1^2}\right)^2} \,. \tag{3.3}$$

The radiation at the undulator exit (point 1) will have assigned waist size w_1 and curvature radius R_1, functions of the radiation beam size σ provided by the FEL calculation: $w_1 = 2\sigma$ and $R_1 = \sigma/\theta_{div}$. If the second terms $\propto \lambda$ in Eq.s (3.2-3.3) are negligible, radiation diffraction can be neglected and the geometric optics' formulation can be employed.

3.1 Few example studies

This section contains a description and the main results of numerical studies I carried out on FEL oscillator schemes in different spectral ranges.

The example studies are here reported in descending order of wavelength.

3.1.1 THz

I studied and contributed to the design of a FELO scheme, named TerRa (TeraHertz Radiation source), for the THz FEL source of the BriXSinO facility (described in the last section of Chapter 2) [132].

THz waves are a powerful tool for a wide range of interesting applications in physics, chemistry, biomedical and material sciences. However, the so-called THz gap refers to the scarce availability of electron sources in this region of

the electromagnetic spectrum, where there are few low-frequency electronic and higher-frequency photonic sources. In particular, coherent THz sources of high average power and high repetition rate are scarce: on one hand, traditional microwave sources suffer from metallic wall losses and the need for higher static electromagnetic fields and electron beam current [148]; on the other hand, low-cost and compact electronic technologies, like IMPATT-diodes, can achieve only moderate power levels [149]. Moreover, sources based on the interaction of electron beams with targets [150] are characterized by extremely low repetition rates (tens Hz). The scientific community is therefore putting big efforts towards the development of novel sources which could fill this gap, and accelerator-based sources have the potentiality of achieving high peak and average powers.

Versatile and tunable sources combining high-power and excellent output performances are required by a rising number of advanced applications. Free-Electron Laser sources produce widely tunable pulses in this relatively short frequency range and satisfy the requests of energy stability, polarization, spectral and spatial distribution posed by the most advanced applications. For example, FEL pulses in this spectral region can be exploited to excite and test strongly correlated quantum systems, magnetic states in complex structures, to study the functioning and transition dynamics in various molecular, atomic and electronic systems, as well as to analyse impurities in semiconductors and vibrations in crystalline and amorphous materials [151, 152].

Operating THz FELs in this wavelength domain produce fully coherent radiation with very short (ps-range) pulse lengths, MW-level peak intra-cavity powers, continuously tunable wavelengths from 10 μm to 0.2 mm (0.1-30 THz), available in both continuous wave (CW) and pulsed form. Infrared (IR) and far-IR FELs mainly operate as oscillators: among the operating FEL oscillators in this spectral range, FELBE [28], based on a superconducting RF LINAC operated in CW mode, and UCSB-FEL [29], based on an electrostatic Van de Graaff accelerator with energy recovery operated in a long pulse mode, are characterized by the highest power yield. NovoFEL [27], which consists of a series of 180 MHz normal-conducting RF cavities and an energy recovery system operated in CW mode, can generate an average power of 400 W and a micropulse energy of 50 μJ.

As outlined earlier in Chapter 2, BriXSinO [131, 153] is composed by a SC Energy-Recovery LINAC operating in CW mode and delivering about 100 MHz electron bunches; a recirculating ring hosting a Fabry-Perot cavity for inverse Compton scattering in its top branch and a THz FEL source in the bottom one (see Fig. 2.11) follows the accelerator. The 100 MHz-class SC LINAC combines the SC technology of FELBE [28] with the energy recovery concept of UCSB-FEL [29] and NovoFEL.[27]. The range of wavelengths explored and

the structure of the undulator differentiate the BriXSinO THz FELO from similar operating devices.

In this framework, TerRa is conceived to be a FEL source of stable, high repetition rate (multi-MHz-class) short-THz beams for user applications.
The main properties of the electron beam delivered by the BriXSinO SC accelerator line and driving the FEL are reported in Table 3.1. Due to the 5 mA

TABLE 3.1: Properties of the electron beam delivered by the BriXSinO SC LINAC at the THz FEL oscillator.

Property	**Unit**	
Energy	MeV	22-45
Bunch charge	pC	100
Repetition rate	MHz	46.4
Transverse size σ_x (rms)	mm	0.15
Bunch length σ_z (rms)	mm	1.8
Peak current	A	7-10
Slice energy spread	keV	145
Slice emittance in x	mm mrad	1.6

threshold, higher charge values (up to 150 pC) are available at lower repetition rates.

Layout of the THz FEL source TerRa

The motivation behind the design of a FEL oscillator scheme for the THz source of the BriXSinO project comes from the lack of alternative THz sources exploiting its high repetition rate, the electron beam properties provided by the SC accelerator, such as the high repetition rate as well as stability in energy and low peak current, and the limited space allocated in the facility bunker [131].

TerRa, alimented by 100 pC electron bunches at about 50 MHz, has been conceived as composed by two undulator modules of different periods, named TU (TeraHertz Undulator) and IO (Infrared Oscillator), separated by a drift where optical elements and diagnostics can be allocated and embedded into a two-mirror near concentric cavity based on metal-coated mirrors. Fig. 3.1 (see next page) shows its layout, while Table 3.2 summarizes the main parameters of the undulator sections.

Operation at IR-THz wavelengths is characterized by a transversely large electron beam exciting a highly diffracted radiation: electrons and photons may interact with the undulator chamber wall if short period undulators with tiny

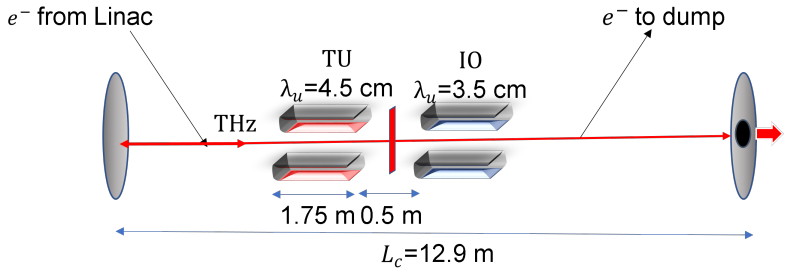

FIGURE 3.1: The undulator TU&IO of the TerRa@BriXSinO FEL. The electron bunches from the LINAC produce short-THz radiation through their passage in two short undulator sections with different periods (TU, Terahertz Undulator, and IO, Infrared Oscillator) separated by a quadrupole (indicated in red) and embedded in a two-mirror near concentric cavity (whose length L_c is equal to four times the bunch-to-bunch separation). The front mirror is holed for radiation out-coupling. After the FEL interaction, the used electron bunch is driven to the dump by means of a dipole. The elements are not in scale.

TABLE 3.2: TU (TerRa FEL: TeraHertz Undulator) and IO (Infrared Oscillator) undulator parameters. VG: variable gaps, LP: linear polarization. The last row specifies the peak on-axis magnetic field strength.

Parameter	Unit	**TU**	**IO**
Gap	cm	$\sim$ 1 -VG	$\sim$ 1 -VG
Polarization		LP	LP
Period λ_u	cm	4.5	3.5
Length L_u	m	1.75	1.75
Magnetic field B	T	0.6-1.2	0.6-1.2

gaps are used. For this reason, undulator gaps of the order of 1 cm or larger are required. Undulator periods shorter than 3 cm require gaps smaller than 5-7 mm for emission beyond 25 μm; on the other hand, periods larger than 3.7 cm do not allow operation at wavelengths smaller than 30 μm.
A period of 4.5 cm is a good compromise for the TU undulator, while a shorter period of about 3.5 cm can be considered for the IO module, tuned at shorter wavelengths. Variable gap undulators allow to extend the radiation spectral domain and have a more tunable source.

The symmetric cavity is composed by two metal-coated (e.g. gold on copper) mirrors with a total reflectivity of the order of 93-97% in the short THz frequency range of operation. As mentioned earlier in this Chapter, the mirror

choice needs to guarantee the maximum efficiency on the largest range in the considered emission interval, which is $25-50$ μm (long-IR / short-THz frequencies) in this case.
The cavity length, $L_c = 12.92$ m, is suitable for hosting the undulator sections, the required diagnostics and for permitting the divergence of the MW-class intra-cavity radiation on the cavity mirrors. Moreover, the round-trip length L_{rt}=25.84 m corresponds to 4 times the bunch-to-bunch separation: therefore, starting from the 46.4 MHz bunch repetition rate of the 100 pC electron beam, the oscillator can operate down to a repetition rate of 11.6 MHz without the need to increase the number of reflections and the radiation losses.

The radius of the 15 THz optical mode is about 2 mm at the undulator center, compared to the matched electron beam radius of 0.2 mm. The radiation is Fourier transform limited and diverges from 2 mm up to about 1.5 cm rms downstream the undulator. Besides, its Rayleigh length Z_R should be approximately one undulator module-long and the radiation beam size turns out to be greater than the electron beam size σ_e, i.e. $\sigma_r \simeq \sqrt{\frac{Z_R \lambda}{2\pi}} >> \sigma_e$. A good coupling between the electron bunch and the radiation is guaranteed, at the cost of quite high radiation losses, while the mirror radius of curvature is designed to be about 15-25 m.
The front end-mirror needs to be translucent or have an out-coupling hole with losses close to 5%. A total round-trip loss of 7%, including 1.5% transmission from each mirror and resulting in an extraction efficiency of 4%, energy jitters of 0.3% and pointing instability of 100 μm are here assumed [132].

TerRa FEL Oscillator working points

This section discusses the choice of the radiation working points, focused mainly in the short-THz frequency range ($6-30$ THz, corresponding to $15-100$ μm).

At a fixed beam energy γ, the two undulators (TU and IO in Fig. 3.1) can either deliver the same radiation frequency or be tuned independently, thus enabling two-color operation in the latter case. Fig. 3.2 from [132] shows the resonant wavelengths λ_1 (blue region, $\lambda_{u_1} = 3.5$ cm) and λ_2 (red region, $\lambda_{u_2} = 4.5$ cm) as function of the electron beam Lorentz factor $\gamma = E/mc^2$, estimated from the FEL resonance relation $\lambda_{1,2} = \lambda_{u_{1,2}}(1 + a^2_{u_{1,2}})/(2\gamma^2)$, where $a_{u_{1,2}} = eB\lambda_{u_{1,2}}/(\sqrt{2}2\pi mc)$ represent the undulator strengths of the two modules and considering magnetic fields B ranging from 0.6 to 1.2 T for the two undulators.
The intersection between the two regions of the graph corresponds to the wavelength range where the two undulator segments generate the same color on the whole magnetic length, while the two-color working points are defined by the adjacent areas. For instance, for an electron energy of $E = 40$ MeV ($\gamma = 80$),

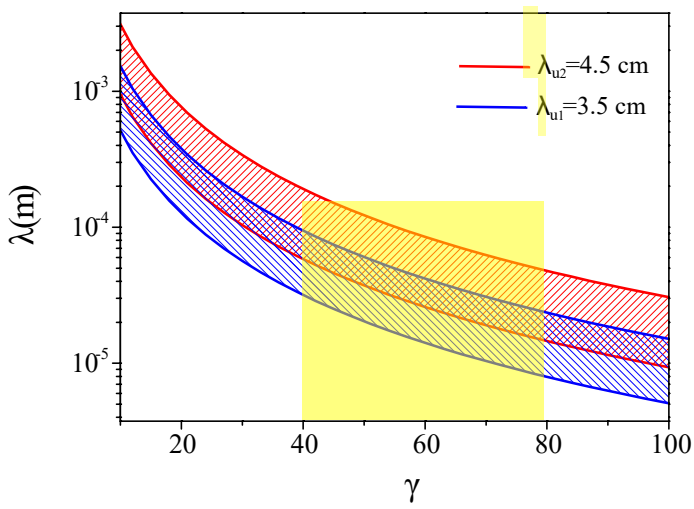

FIGURE 3.2: Radiation wavelength λ(m) as function of electron Lorentz factor γ, from [132]. λ_1 achieved with $\lambda_{u,1} = 3.5$ cm in blue, λ_2 achieved with $\lambda_{u,2} = 4.5$ cm period in red. Undulator magnetic fields range from B=1.2 T (upper curves) to B=0.6 T (lower curves). The intersection between the two regions corresponds to the two modules being tuned at the same wavelength. The region related to the beam energies provided by the SC LINAC is enlightened in yellow.

the two modules can operate in the interval 20-30 μm at the same wavelength, or can cover the range 10-30 μm and 20-50 μm respectively, thus producing two-color radiation.

As already mentioned in Chapter 1, an inherent feature of the FEL instability is the slippage of the radiation pulses along the propagation direction, by one radiation wavelength every undulator period, with respect to the electrons. The radiation beam needs to overlap with the electron bunches for a strong interaction, and slippage effect is more pronounced at long wavelengths.
In order to avoid the large slippage effect in the THz spectral range and the pulse deterioration into deep saturation, an optimal value for the electron beam rms length σ_e is of the order of two times the slippage length $L_s = N_u\lambda$ (N_u being the number of periods of the undulator module), which lowers its peak current and the gain in the single pass. In two-color operation, when the two undulators are tuned at different wavelengths, the electron beam length should exceed the longest slippage length. As shown later, also the cavity length can be optimized for optimal gain and slippage compensation. At the same time,

long wavelengths are also affected by strong radiation diffraction, which limits the achievable peak current and output radiation quality.

To overcome these limitations, FEL facilities make use of the oscillator configuration, in which the gain builds up over hundreds of micropulses within a single macropulse; in this case the challenges are the output pulse length and the availability of electron sources with high peak brightness and high repetition rates.

Apart from the round-trip losses, the threshold of operation also depends on the undulator length: when the electron beam is much longer than the cooperation length (i.e. when $\sigma_e >> L_c = \lambda/(2\pi\rho)$), a stable condition is given by $0.27(4\pi\rho)^3 {N_u}^3 >$ Loss, where ρ is the Pierce parameter [4, 41] and Loss is the percentage of energy lost by the light during the round-trip from the end to the undulator entrance [154]. The opposite limit leads to a slightly different threshold, i.e. $0.608(4\pi\rho)^3 {N_u}^3 >$ Loss.
The BriXSinO electron beam length is about 5-10 times the cooperation length, so that it lays in an intermediate region between the two limiting cases ruled by the short ($\sigma_e \approx L_c$) and the long-bunch models [132].

As already mentioned, the radiation beam size is greater than the electron beam one: for this reason, despite the moderate radiation losses due to the pulse cycling and extraction along the trajectory outside the undulator, the electron beam-radiation coupling at the undulator entrance is scarce. Assuming large losses and considering the reported threshold for both bunch limits, a conservative choice of the number of undulator periods N_u satisfies the constraint $N_u > \frac{1.54}{4\pi\rho}$ in the long bunch scenario or $N_u > \frac{1.18}{4\pi\rho}$ with a short electron beam.

Based on these formulae, the graph in Fig. 3.3 represents the required undulator period number N_u as function of the beam peak current I(A) in four cases: $\lambda = 20$ μm (black curve, with $\lambda_u = 3.5$ cm), $\lambda = 35$ μm (blue curve, with $\lambda_u = 4.5$ cm), $\lambda = 40$ μm (magenta curve, with $\lambda_u = 3.5$ cm) and $\lambda = 50$ μm (red curve, with $\lambda_u = 4.5$ cm) where three-dimensional and inhomogeneous effects have been taken into account in the calculation of the Pierce parameter [9]. Both long (solid lines) and short (dashed lines) electron beam cases are reported.

The resulting undulator lengths ($L_u < 4$ m) are in agreement with the constraints of the allocated space in the BriXSinO bunker, and reasonable peak currents ($7\text{A} < I < 15$ A) are needed, in the range attainable by the BriXSinO accelerator.

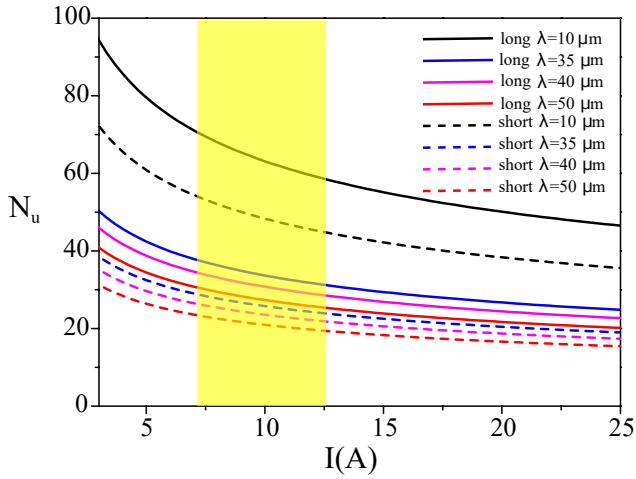

FIGURE 3.3: Required number of undulator periods N_u versus electron beam peak current I(A), from [132]. Black curve: $\lambda = 20$ μm, $\lambda_u = 3.5$ cm, γ=80. Blue curve: $\lambda = 35$ μm, $\lambda_u = 4.5$ cm, γ=80. Magenta curve: $\lambda = 40$ μm, $\lambda_u = 3.5$ cm,γ=40. Red curve: $\lambda = 50$ μm, $\lambda_u = 4.5$ cm,γ=40. Three-dimensional and inhomogeneous effects are taken into account. The region corresponding to the peak current values of the BriXSinO electron beam is enlightened in yellow.

TerRa FEL operation & performances

The numerical modelling of the TerRa FELO has been carried out by implementing the iterative procedure described above. The front end-mirror is supposed to be holed for radiation out-coupling: the reported simulation results consider an out-coupling hole with losses of about 4%.

The accelerated electron bunches, whose nominal parameters are listed in Table 3.1, are injected into the undulator and FEL emission is simulated with the three-dimensional, time-dependent FEL code GENESIS 1.3 [147]. The radiation field co-propagates with the electron bunches inside the undulator, slipping ahead by approximately one radiation wavelength per undulator period.

Taking into account both slippage and propagation, the radiation field needs to be delayed by an amount of the order of the total slippage length at the successive round-trip. A cavity shortening (detuning of the cavity length) of hundreds-μm allows to synchronize the radiation with the following bunch at the undulator entrance at each pass: the FEL emission is thus optimized by maximizing the FEL output power as function of the detuning length [141, 155]. The achieved intra-cavity energy level, at λ=20 μm and in the case of a single undulator module (L_u=1.75 m), is shown in Fig. 3.4 for different mirror losses, as function of the detuning with respect to the zero-detuning cavity length L_c.

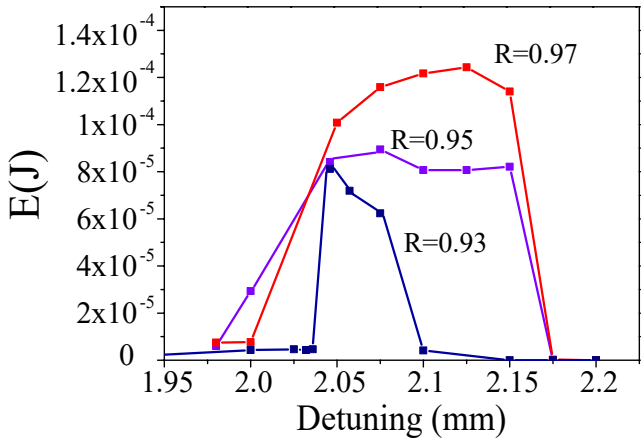

FIGURE 3.4: Intra-cavity radiation energy of a single shot at saturation E(J) vs. detuning length (mm) for various values of mirror reflectivity R, from [132]. Emission at $\lambda = 20$ μm with an undulator length of $L_u = 1.75$ m is considered.

The expected temporal and spectral pulse profiles, as well as their transverse distributions, for each output wavelength and undulator length are characterized by shortening the cavity length to the value corresponding to the maximum energy.

In the case of a 40 MeV ($\gamma = 80$) electron beam, the undulators can both be tuned at $\lambda = 20$ μm by setting the following peak on-axis magnetic fields: B_{TU}=0.73 T for the 4.5 cm period undulator and $B_{IO} = 1.09$ T for the other one with $\lambda_u = 3.5$ cm.
Fig. 3.5 (see next page) shows the intra-cavity radiation energy growth as function of the number N of shots for an undulator length $L_u = 1.75$ m, corresponding to the use of IO only (yellow curve, a), and for the value $L_u = 4$ m corresponding to the use of both sections (blue curve, b), including the 3.5 m magnetic length and the 0.5 m drift between the two modules. As aforementioned, the cavity length is optimized for both undulator settings.
The achieved temporal (left), spectral (middle) amplitudes and transverse distribution (right) of the radiation at saturation at the end of the undulator are reported in Fig. 3.6 for $L_u = 1.75$ m, top line, and for $L_u = 4$ m, bottom line.

The short-wavelength radiation saturates at low energy in more than 800 round trips when $L_u = 1.75$ m (case a, top line in Fig. 3.6): this case, with the total slippage length smaller than the electron beam width, results in a long

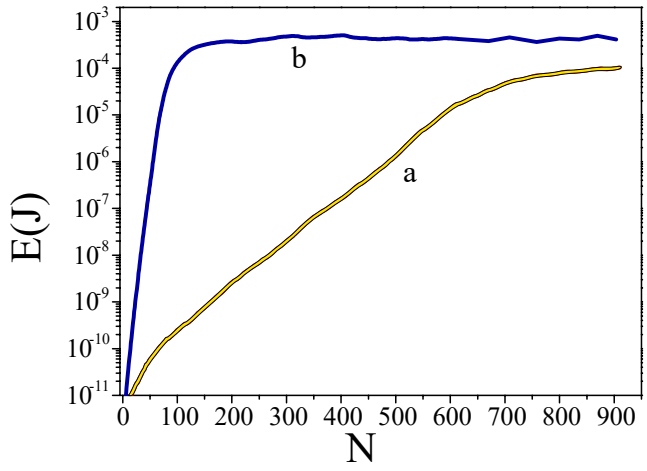

FIGURE 3.5: Intra-cavity radiation energy growth E(J) vs. number of shots N for $\lambda = 20$ μm, with undulator length $L_u = 1.75$ m (yellow curve, a) and $L_u = 4$ m (blue curve, b).

single-spiked pulse and narrow spectrum. On the other hand, post saturation intensity oscillations at few percent level after only 100 shots are present when operating with $L_u = 4$ m (case b, bottom line), leading to higher energy, shorter pulse lengths with noisy background[3] and wider spectrum with occurrence of small sidebands. In both cases, the larger transverse dimension of the radiation field with respect to the electron beam limits its divergence due to diffraction [132].
An intra-cavity energy level up to few hundreds of μJ leads to 3-20 μJ of extra-cavity energy and 0.1-1 kW of output average power.

According to these results, the oscillator lasing behaviour stands in an intermediate regime between a long bunch and a short superradiant bunch. Figures 3.7-3.8 show the energy growth and the pulse temporal, spectral and transverse distributions for emission at 35 μm respectively, obtained with $\gamma = 60$, $B_{IO} = 1.08$ T and $B_{TU} = 0.72$ T. Also in this case, the cavity length is adjusted to its optimal value through cavity length detuning; such longer-wavelength radiation exhibits spectral sidebands leading to a broadband and less performing behavior.
When $L_u = 4$ m (case b, bottom line of Fig. 3.8), a structure of equidistant spikes, stable from shot to shot, appears and could be exploited in stroboscopic

[3] The rms pulse length appears to be larger than the previous case, but the FWHM length is quite lower.

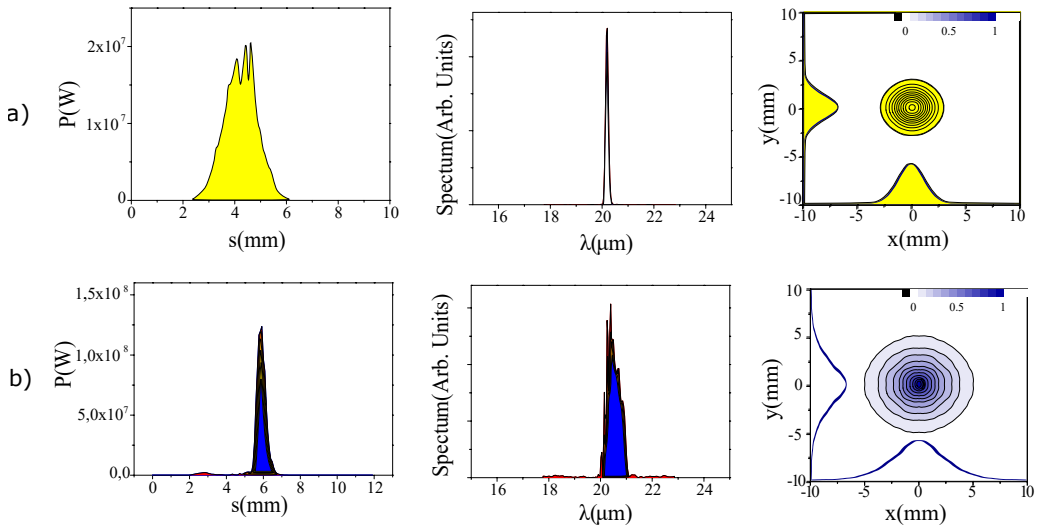

FIGURE 3.6: Output pulse at saturation at the undulator exit for emission at $\lambda = 20$ μm: radiation power profile P(W) vs coordinate s(mm) on the left, spectral distribution in arbitrary units vs $\lambda(\mu$m) in the middle and transverse distribution on the right. Case a (top line) refers to $L_u = 1.75$ m, case b (bottom line) to $L_u = 4$ m.

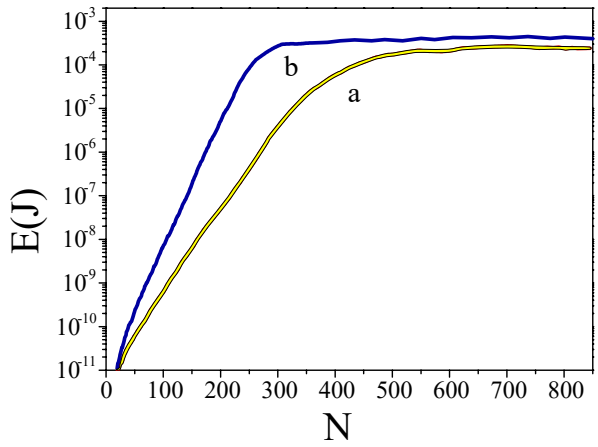

FIGURE 3.7: Intra-cavity radiation energy growth E(J) vs. number of shots N for $\lambda = 35$ μm, with $L_u = 1.75$ m (curve a) and $L_u = 4$ m (curve b).

measurements [156, 157]. Also in this case, few hundreds of μJ of intra-cavity

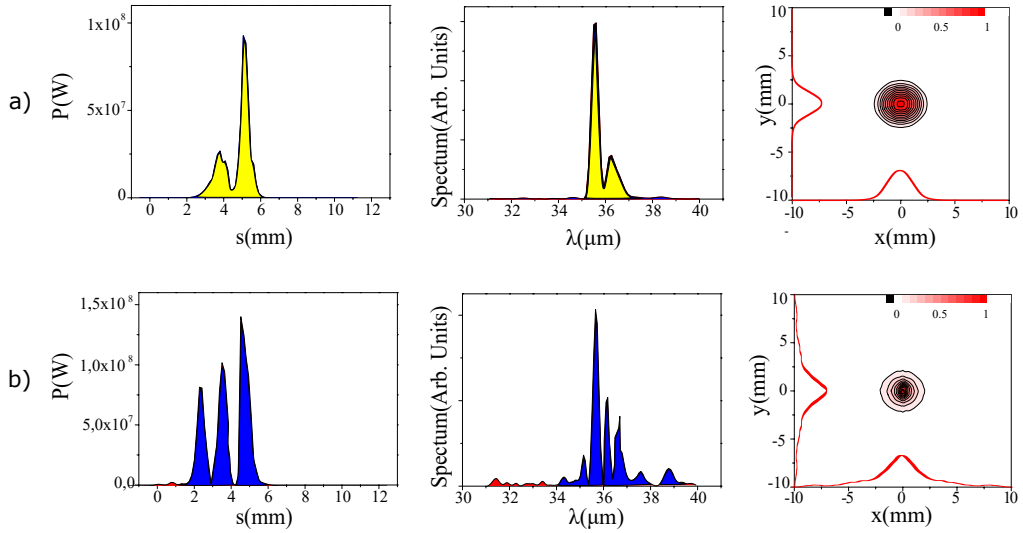

FIGURE 3.8: Output pulse at saturation at the undulator exit for emission at $\lambda = 35$ μm: radiation power profile P(W) vs coordinate s(mm) on the left, spectral distribution in arbitrary units vs $\lambda(\mu m)$ in the middle and transverse distribution on the right. Case a (top line) refers to $L_u = 1.75$ m, case b (bottom line) to $L_u = 4$ m.

energy guarantee tens of μJ of extra-cavity energy and up to 1 kW of average power. A slight component of higher order transverse modes is revealed by the pulse transverse distribution (bottom right window of Fig. 3.8).

When the total slippage is of the order of the electron beam length, shorter pulses with an accordingly broader spectrum are produced (Fig.s 3.6-Fig 3.8, top line), while subsequent spikes in the trailing edge begin to develop.
At longer wavelengths and magnetic lengths ($L_u = 4$ m), corresponding to total slippage larger than the beam length, the system enters a quasi-stationary superradiant regime characterized by frozen multiple spikes [156] (Fig. 3.8, bottom line) similar to the one observed in the JAERI experiment [132, 155]. FEL oscillators can exhibit unstable behavior in the superradiance regime. Problems associated with the dynamic behavior of superradiant oscillators, such as the energy fluctuations, are here mitigated by the very short FEL pulse bandwidth[4].

[4]Such unstable behaviour can be also mitigated by assuming a realistic spectral response for the cavity mirrors, which would limit the cavity spectral acceptance, or by inserting a band-pass filter within the cavity.

Other important characteristics of the amplified radiation are its polarization, as well as its longitudinal and transverse coherence and stability. The polarization is about the same of the undulator's, which is supposed to be linear in the vertical direction at 100%. Table 3.3 summarizes the main properties of the amplified pulses, including the values of self and mutual coherence rms lengths evaluated through the corresponding correlation factors (see Eq. 1.9) [10, 12][5].

TABLE 3.3: Characteristics of the TerRa FEL radiation at $\lambda = 20$ μm and $\lambda = 35$ μm at the undulator exit. IC: intra-cavity, EC: extra-cavity. Round trip losses 7%, extraction efficiency 4%. Repetition rate= 46.4 MHz. The rms pulse coherence (coh.) lengths are reported in the last three rows.

Wavelength	**20 μm**	**20 μm**	**35 μm**	**35 μm**
Undulator length	**1.75 m (IO)**	**4 m (TU&IO)**	**1.75 m (IO)**	**4 m (TU&IO)**
Single-shot IC energy	84 μJ	420 μJ	250 μJ	420 μJ
Single-shot EC energy	3.36 μJ	16.8 μJ	10 μJ	17 μJ
Average power	0.156 kW	0.78 kW	0.46 kW	0.8 kW
Bandwidth	0.65 %	2.5%	1.85%	4.2 %
Size	2 mm	2.6 mm	2.4 mm	2.8 mm
Divergence	2.8 mrad	4 mrad	4.2 mrad	5 mrad
Pulse rms length	635 μm	830 μm	749 μm	1000μm
Self coh. length	755 μm	1330 μm	800 μm	1300 μm
Mutual coh. length	700 μm	1000 μm	600 μm	1000 μm
Transverse coh. length	1.48 mm	2.98 mm	2.42 mm	4. mm

TerRa FEL: two-color radiation

The two undulator modules of TerRa@BriXSinO can be tuned at different wavelengths, thus producing two-color radiation in the wavelength range indicated in the intersection between the two coloured regions of Fig. 3.2. The frequency tuning of two-color sources based on FELs is operated either by changing the undulators' magnetic field, which requires small adjustments of their gaps, or by choosing a different electron beam working point, which allows for a larger shift of the radiation frequency but needs an ad-hoc preparation and transport of the electrons.

Following the line of the pivotal experiment reported in [158], systematic two-color operation [157] is expected to widely increase the number and interest of the possible applications of THz radiation.

[5]The coherence degree is a property connected with the radiation electric field: for this reason, the coherence length could be larger than the width of the pulse power profile.

Regarding specifically the designed FELO, the FELO could be in principle fed by both sides by circulating the electron beam clockwise or counterclockwise in the BriXSinO arc: the order of both the two colours and undulators could therefore be shifted.
In the set-up shown in Fig. 3.1, the first longer wavelength color (pump) is generated by driving the electron beam in the first undulator module TU. The second color (probe) is emitted by the same electron beam proceeding along the second module IO, tuned at a shorter wavelength. The same electron bunch is driven in the two different undulators: different matching conditions are possible, and the electron bunch is here matched to the second undulator module tuned at the shorter wavelength[6]. Simulations indicate that the induced energy spread by the emission in the first module does not affect the radiation in the second module.

The two produced photon pulses are temporally synchronized, apart for the slippage $\Delta_z = N\lambda_1$ accumulated from the first radiation pulse with respect to the electron beam in the first module, a time delay of the order of 1 ps that can be recovered in the transfer line to the user station downstream the FEL source.
The relation $\lambda_1/\lambda_2 \sim \lambda_{u,1}/\lambda_{u,2}$ identifies the cases where the slippage of the pulses in the two undulator modules is similar and the optimization of the cavity shortening efficiently compensates the delay between electrons and radiation for both colors [132]. Table 3.4 shows two different combinations of two-color radiation for which cavity length detuning works efficiently[7].

TABLE 3.4: Characteristics of the TerRa@BriXSinO two color FEL radiation. IC: intra-cavity, EC: extra-cavity. Extraction efficiency 4%. Repetition rate = 46.4 MHz.

Undulator	**IO**	**TU**	**IO**	**TU**
Electron energy	**40 MeV**	**40 MeV**	**20 MeV**	**20 MeV**
Wavelength	**20 μm**	**35 μm**	**40 μm**	**50 μm**
Single shot IC energy	84 μJ	305 μJ	340 μJ	46 μJ
Single shot EC energy	3.36 μJ	12.2 μJ	13.6 μJ	1.84 μJ
Average power	0.156 kW	0.6 kW	0.63 kW	0.085 kW
Bandwidth	0.65%	0.7%	0.49%	0.46% 0.5%
Size	2 mm	2.5 mm	2.5 mm	2.2 mm
Divergence	2.8 mrad	3.8 mrad	5 mrad	6.3 mrad
Pulse rms length	635 μm	830 μm	720 μm	1200μm
Self coherence rms length	755 μm	1000 μm	1300 μm	1500 μm
Mutual coherence rms length	700 μm	900 μm	1000 μm	1200 μm
Transverse coherence rms length	1.48 mm	2.63 mm	2.44 mm	2.9 mm

[6] This is a typical choice in cascaded undulator setups and is driven by the fact that beam matching is more and more important at shorter emission wavelengths.
[7] An equal value of mirror reflectivity for the two colours is here assumed.

In the second and third columns, an electron beam energy of 40 MeV is considered, with the two undulator modules tuned at 20 μm with $B_{IO} = 1.09$ T and at 35 μm with $B_{TU} = 1.02$ T respectively. A different case with 25 MeV electron beam energy and the two undulators tuned at 40 μm ($B_{IO} = 0.94$ T) and at 50 μm ($B_{TU} = 0.72$ T) is outlined in the forth and fifth columns respectively.

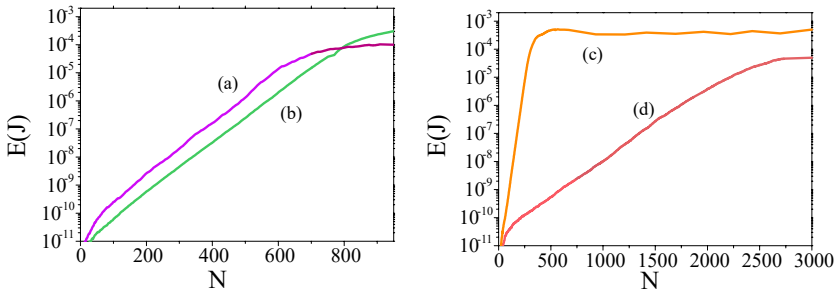

FIGURE 3.9: Energy growth of two-color radiation as function of the number of shots N, from [132]. (a) $\gamma = 80$, $\lambda = 20$ μm; (b) $\gamma = 80$, $\lambda = 35$ μm; (c) $\gamma = 50$, $\lambda = 40$ μm; (d) $\gamma = 50$, $\lambda = 50$ μm.

These two possible two-color working points are highlighted in Fig. 3.9 and Fig 3.10, showing the radiation energy growth as function of the number of round-trips, and the temporal and spectral amplitudes at the end of the undulator line respectively.
The intra-cavity energy reaches a level of 50-300 μJ, delivering to the users 1-20 μJ, meaning 0.06-1 kW of average power in each color. The spectra in the right windows of Fig. 3.10 feature two narrow, tunable and well separated spikes: in case (c), at 40 μm and done with the 3.5 cm period, the radiation presents superradiance, with two temporal and spectral frozen peaks.
The transverse distribution of both pulses at the end of the emission process is reported in Fig. 3.11, the top line showing the cases $\lambda = 20$ and 35 μm while $\lambda = 40$ and 50 μm in the bottom one. Deviations from the single spike structure in the spectral domain (as in the bottom right plot of Fig. 3.10 at $\lambda = 40$ μm) are connected to slight occurrence of higher order transverse modes.

The designed FELO is based on a compact, rather simple THz cavity and features interesting characteristics; the inclusion of two short undulator modules may facilitate a modular realization of the source.
The reported simulation results assess the capability of this scheme for typical wavelengths of interest (in the $10-50$ μm range). In view of a Technical Design and its future implementation, deeper studies of its two-color operation, including the influence of slippage and its dependence on the undulators' ordering, as well as further investigations on the radiation out-coupling, would be required.

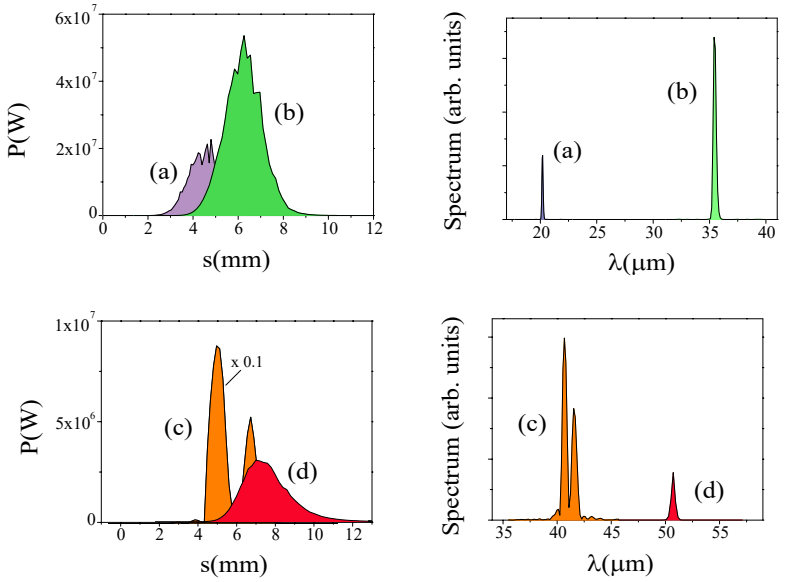

FIGURE 3.10: Two color radiation at TerRa@BriXSinO, from [132]. Top line: single-shot power distribution P(W) at saturation vs coordinate z(mm) on the left and corresponding spectral amplitude (arbitrary units) vs $\lambda(\mu m)$ on the right for (a) $\gamma = 80$, $\lambda = 20$ μm; (b) $\gamma = 80$, $\lambda = 35$ μm; Bottom line: the same as in top line for (c) $\gamma = 50$, $\lambda = 40$ μm; (d) $\gamma = 50$, $\lambda = 50$ μm.

The foreseen performances of TerRa@BriXSinO, reaching $0.1 - 1$ kW average power levels between 20 and 50 μm wavelength (frequency $\nu = 3 - 15$ THz), are comparable to the ones achieved by only a few devices worldwide and may open the way to many novel experiments and studies.

These studies contributed to the BriXSinO Technical Design Report [131]. A similar THz FELO was also considered for the design study of a dual source of THz and soft X-ray pulses [159], generated in sequence through FEL lasing and Compton/Thomson back-scattering by two successive bunches of the electron beam train and therefore naturally synchronised within the characteristic temporal jitters of the SC accelerator. In this case, the need to have a THz beam focused down to hundreds-μm leads to a slightly modified cavity geometry composed by four mirrors.

3.1.2 Extreme-UV

In the framework of the MariX project [8] (introduced in Chapter 2) and its seeded FEL source, I studied an FEL oscillator working in the Extreme-UV

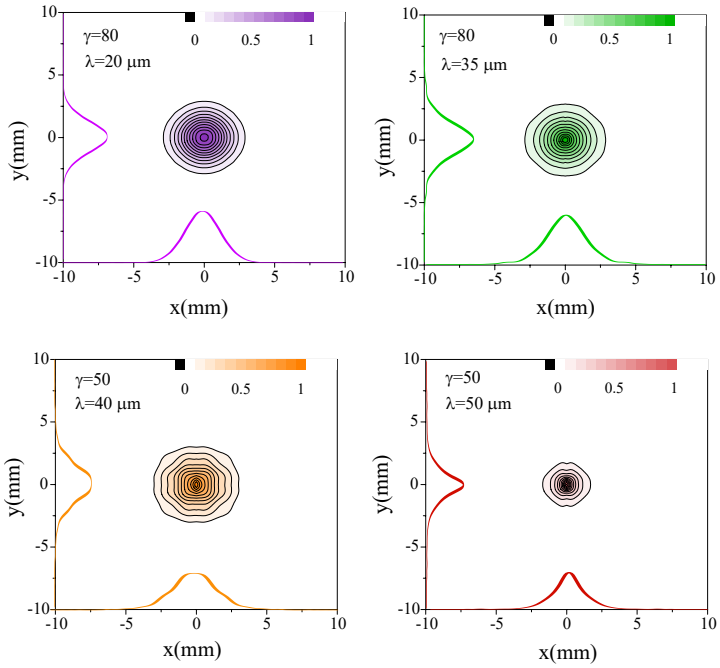

FIGURE 3.11: TerRa@BriXSinO two-color radiation: transverse distribution of single-shot radiation at saturation, from [132]. Top line: electron beam with $\gamma = 80$. Left: $\lambda = 20$ μm, right: $\lambda = 35$ μm. Bottom line: electron beam with $\gamma = 50$. Left: $\lambda = 40$ μm, right: $\lambda = 50$ μm.

(EUV) range at λ_O=13.6 nm to be used as seed for a downstream FEL amplifier [124, 160]. The FEL oscillator-amplifier schemes I investigated are discussed in the next section.

As mentioned in Chapter 2, the injector of the MariX project is able to deliver 100 MHz electron bunches for the Inverse Compton Scattering source BriXS, and 1 out of 100 is driven to the main booster and high energy part of the complex. The MariX electron beam parameters for FEL operation, after compression in the arc and the double acceleration in the LINAC, are summarized in Table 2.3 of the previous Chapter.

Another injection working point has been considered for the FEL oscillator. The injector can also produce trains of four electron bunches spaced by 2 μs (repetition rate of 0.5 MHz) with a spacing of 10 ns between electron bunches. The designed oscillator is alimented only by the front electron bunch (b_1 in Fig. 3.12), at the head of each train; the other three bunches are sent to the subsequent FEL amplifier.

EUV FELO layout and mirror choice

The layout of the FEL oscillator to be employed as seeding source of the MariX FEL is sketched in Fig. 3.12: only the front bunch of each train drives the oscillator and is here reported and indicated as b_1. The decreased repetition rate in this injector working point of the MariX LINAC, providing 0.5 MHz electron bunches at 2.04 GeV (see Table 2.3 for more details on the beam properties), and the need to limit its longitudinal dimension lead to a more complex, four-mirror resonator design.

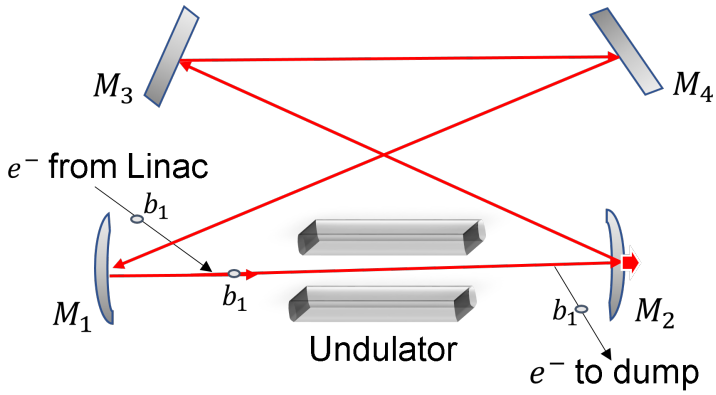

FIGURE 3.12: EUV FEL Oscillator scheme: b_1 represents the electron bunch driving the oscillator, which is dumped after each passage in the undulator. M_1,...,M_4 are the mirrors of the oscillator (M_3, M_4 spherical mirrors).

The EUV FELO is constituted by an undulator segment with period $\lambda_u = 5$ cm and $a_u = 2.77$, embedded into a folded etalon with a minimum of four mirrors, of which two are assumed bent and focusing.

The length of the optical round-trip is given by the recirculation distance of 600 m, matching the 0.5 MHz bunches' repetition rate, minus the rather short slippage length accumulated in the undulator. The detuning-length, giving the correction of the round-trip length, is of the order of 1 μm. Its optimal value is determined through a scan of the detuning length as function of the accumulated slippage length between the radiation and the electron beam at the undulator entrance. In order to ensure sufficient electron-radiation overlapping, compensating small shifts, and stabilize the output, the mirrors are supposed to be micrometrically movable and turnable [124].

The emission wavelength, λ_O=13.6 nm, corresponds to the optimum wavelength for Mo/Si multilayer mirrors [32, 161]. As shown in Fig. 3.13 from [124], the y of these mirrors in normal or quasi-normal incidence exceeds R=0.75. Moreover, the width of the transfer function of the optical line is much larger

than the SASE or seeded radiation spectra [161], so that the spectral filtering of the mirrors is inessential and can be neglected. The angular filtering is also ineffective, since the mirror acceptance, exceeding 0.15 rad [162], is extremely larger than the pulse divergence of the order of tens-hundred μrad.

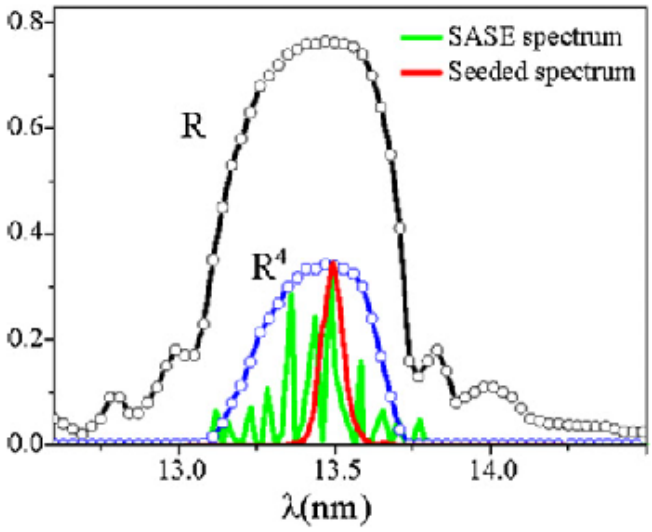

FIGURE 3.13: Reflectance of the Mo/Si multilayer mirrors as function of the wavelength λ, from [124], for one mirror (R) and four mirrors (R^4), compared with the first-pass SASE oscillator spectrum (green curve) and multi-pass seeded spectrum (red curve) at saturation in the oscillator. Incidence angle: 3° from normal.

The purification of the pulses' spectral and temporal distributions occurs via the reiterated amplification of the best SASE spike [124]. The reflectivity after four reflections is about R^4=0.3, while the fraction coupled to the line matching the seed to the amplifier, characterized by two more mirrors, consists of 25% of the oscillator yield.

EUV FELO operation: undulator length optimization

The simulation of the oscillator is performed by means of GENESIS 1.3 [147] and the cycling technique previously described.

Fig. 3.14 reports the energy loading as function of the number of round-trips for different values of the undulator length L_u. Best FEL operation should be at about $L_u = 2\pi Z_R$, where Z_R is the Rayleigh length: for an electron beam with $\sigma_{x,y} \approx 35\,\mu m$ transverse dimensions, the Rayleigh length is about 1.1-1.2 m and L_u turns out to be of the order of 7.5 m. Various undulator lengths from 6 to 10 m are explored in Fig. 3.14, whereas cavity detuning is here neglected.

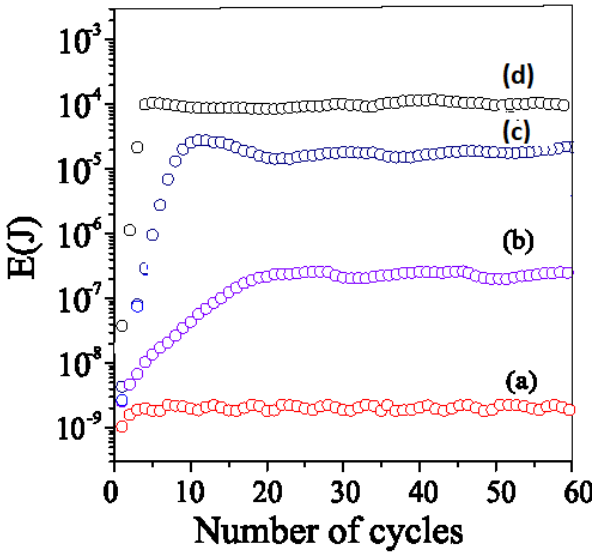

FIGURE 3.14: FEL oscillator at 13.6 nm, from [124]. Radiation energy growth E(J) as function of the round-trip number. (a) $L_u = 6\,\mathrm{m}$, (b) $L_u = 7\,\mathrm{m}$, (c) $L_u = 8\,\mathrm{m}$, (d) $L_u = 10\,\mathrm{m}$.

Depending on the undulator length L_u, saturation is reached in about 10-50 passages and the amplified radiation presents slight intensity oscillations around the average saturation value E_{sat}, a sort of breathing of the system already observed in Ref. [39]. A general irregularity deriving from the different microscopy of the successive electron beams flowing in the oscillator is superimposed to the natural oscillations: this is more evident in the shorter undulator cases and tend to delay the saturation. This effect is assumed to be stronger if other beam fluctuations, such as energy or current, were included.
Fig. 3.15 highlights the dependence of the saturation energy with respect to the undulator length.
The radiation yield saturates at a very low level (E$\sim$1 nJ) in the case of shorter undulators (L_u<7 m), in which case the coherence stage is not reached; moderate energy values (E$\sim$10 nJ -10 μJ) and high coherence levels are achieved in 30-50 cycles for intermediate states with 7 m< L_u<9 m, while tens-hundreds μJ with moderately good longitudinal coherence are emitted in few tens cycles for undulators larger than 9 m. The coherence degree gets deteriorated due to non linear saturation effects in the case of longer undulators ($L_u \geq$9 m). This analysis indicates an emission threshold around 7 m [124].

Fig. 3.16 reports the pulse temporal and spectral densities at saturation for various undulator lengths.

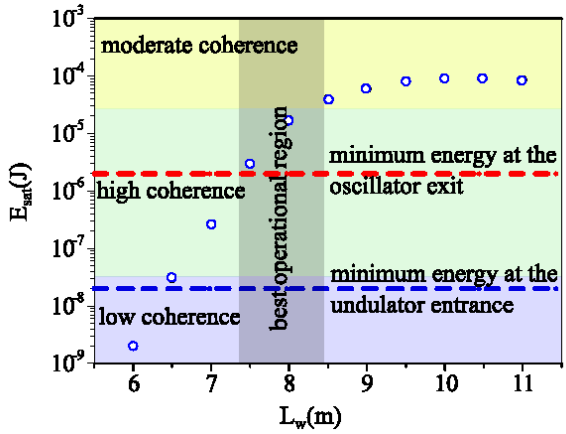

FIGURE 3.15: FEL oscillator at 13.6 nm. Saturation energy E_{sat}(J) vs undulator length L_u(m), from [124]. The coherence level for each case is specified.

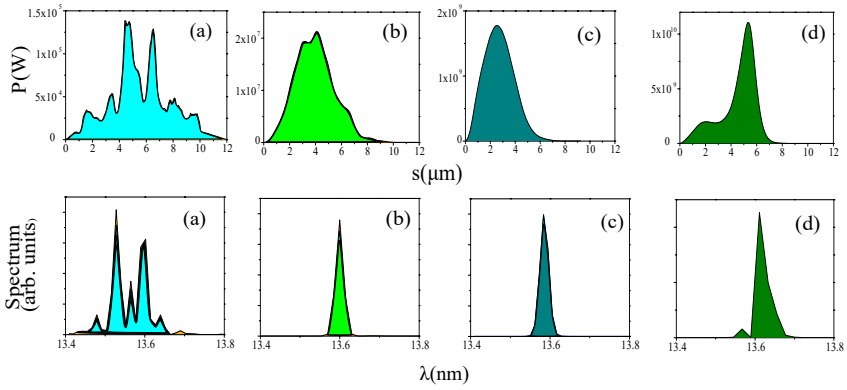

FIGURE 3.16: EUV FELO output pulse profiles. Top row: temporal distribution of the oscillator output. Bottom row: output spectral density at the exit of the oscillator for (a) $L_u =$ 6 m, (b) $L_u = 7$ m, (c) $L_u = 8$ m, (d) $L_u = 10$ m.

The undulator length is chosen by searching the optimal intensity of the output pulse for FEL seeding: on one side, the oscillator seed must overcome the undulator spontaneous emission in the following FEL amplifier; on the other side, a too intense seed might produce very strong non linear effects in the electron beam with not-controllable harmonics' production. The seed energy should fall between few tens and hundred nJ at the entrance of the FEL

amplifier (i.e. 20-100 nJ).

EUV FELO cavity

The EUV FELO optical line is composed by two plane (M_1, M_2 in Fig. 3.12) and two spherical (M_3, M_4) mirrors with curvature radius $\mathcal{R}$, all interspersed by drifts. The distance between the second focusing mirror M_4 and the undulator entrance is about 225 m and, in order to have the maximum radiation focusing around the undulator center and stable operation of the oscillator, mirror focal lengths of $f = \mathcal{R}/2 = 225.7$ m were assumed.

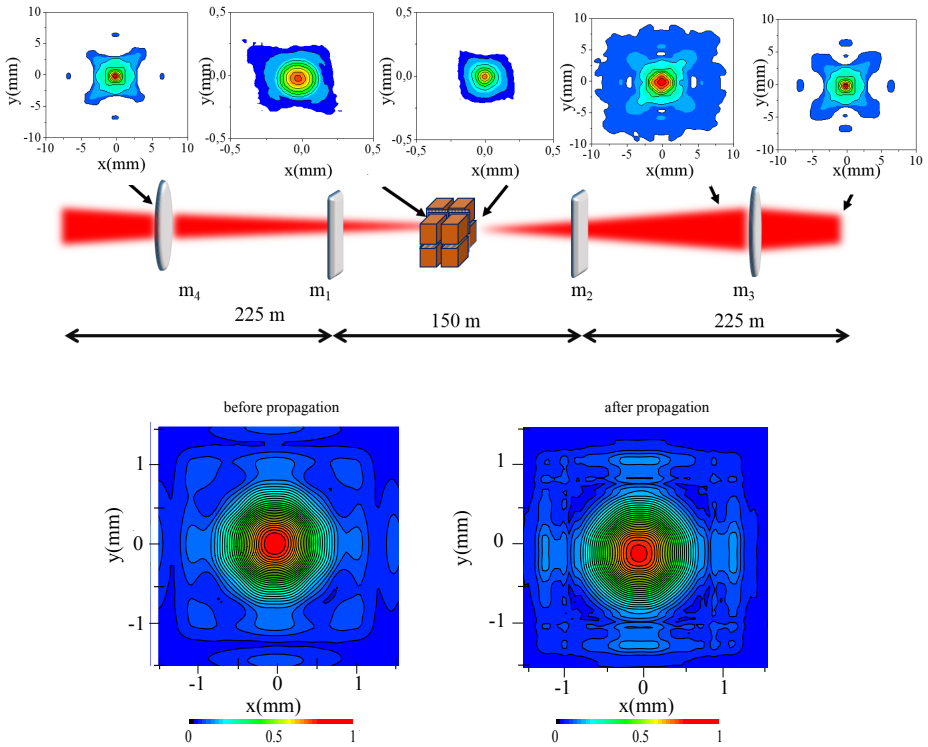

FIGURE 3.17: Top plot: transverse field pattern of the oscillator pulse at saturation along the propagation in the cavity, from [124]. Bottom plot: enlarged view of the transverse power pattern before (left) and after (right) the propagation in the cavity.

The structure of the field can be analyzed in terms of the cavity modes: as shown in the top plot of Fig. 3.17, a field with a transverse structure substantially constituted by the fundamental mode develops, while the higher transverse FEL modes get soon depleted in the undulator by the FEL interaction itself, and such structure is not deteriorated by the transport line. An enlarged

view of the transverse field power patterns after the undulator and at its entrance, after the propagation in the cavity, is also shown in the bottom plot of Fig. 3.17.

The radiation hits the mirrors with a maximum transverse rms dimension of $\sigma_{x,y} \sim 1$ mm and enters the undulator with $\sigma_{x,y} \sim 150 - 200\ \mu m$. It is then further focused by the FEL amplification process, till about 100 μm [124].

Hundreds nJ–tens μJ are obtained with undulator modules of the order or longer than 7.5 m for the oscillator, confirming the best operational points given by undulator lengths in the range $L_u = 7.5 - 9$ m. Given the rather low reflectivity of state-of-the-art multilayer mirrors, radiation out-coupling is here performed by means of the mirror transmission: the light transmitted from the front cavity mirror (M_2 in Fig. 3.12), also taking into account EUV power losses from absorption, therefore constitutes the out-coupled radiation. The resulting coherent and high-power pulses from the EUV FELO, whose main properties are summarized in Table 3.5, can seed a FEL cascade scheme for the production of shorter wavelengths down to the X-rays (see section 3.2 of this Chapter).

TABLE 3.5: Main properties of the 13.6 nm pulse, generated by the EUV FEL oscillator with undulator length L_u=8 m (case c in Fig. 3.16). The repetition rate of the source is 0.5 MHz. \$=Photons/s/mm^2/$mrad^2$/bw(0.1%).

λ_O (nm)	13.6	E (μJ)	20
N_{ph}/shot	1.3×10^{12}	N_{ph}/s	0.05×10^{18}
bw	1.7×10^{-3}	duration (fs)	6.6
div (μrad)	50	size (μm)	80
peak brilliance (\$)	0.7×10^{31}	average brilliance (\$)	2.3×0^{22}

The design study of this EUV FELO, based on the capabilities of the MariX complex, relies upon state-of-the-art technologies. Higher repetition rates of the accelerator would allow to conceive more compact, easier-to-realize cavity lengths. Moreover, further studies on this configuration are foreseen prior to its possible implementation, including feasibility and tolerance studies of the considered multi-layer mirrors[8] and the inclusion of other relevant electron beam fluctuations as well as its full phase space distribution [9].

[8] Useful simulation codes already exist and are currently used for this purpose.

[9] A preliminary simulation campaign in this direction has shown good agreement between the FEL performances starting from the average beam parameters and the complete distribution arising from beam dynamics simulations.

3.1.3 X-ray FELO

In the framework of the MariX project and in collaboration with Politecnico di Milano, I also investigated the possibility to use a FEL Oscillator based on an X-ray cavity (XFELO) as direct source of coherent X-rays in the 5–2 Å wavelength range [163].

My analyses rely on the electron beam foreseen by the accelerator of the MariX project [8], whose main characteristics were evaluated through start-to-end simulations from the injector to the undulator entrance and are listed in Table 2.3. A beam charge of 50 pC has been considered for driving the XFELO.

The XFELO configuration requires a single short undulator module equipped with a sequence of X-ray crystal mirrors. Considering the moderate electron energy provided by the MariX accelerator (3.8 GeV at maximum), production of radiation pulses in the desired wavelength range (5–2 Å, or in energy 2–5 keV) can be achieved by a short-period undulator: from the resonance relation, a 2.4 GeV electron beam emits at 3 keV in an undulator with period $\lambda_u = 1.2$ cm and with a peak on-axis magnetic field B=0.93 T.

XFELO layout and mirrors

As shown in Fig. 3.18, the scheme of the coherent source is constituted by a short (about 7–10 m-long) undulator module with period $\lambda_u = 1.2$ cm, embedded within a ring cavity, similar to the one designed for the EUV FELO (see Fig. 3.12) but based on X-ray mirrors.
For an electron beam repetition rate of 1 MHz, the round-trip length of the cavity must be 300 m[10]. The sequence of the accelerated beam packets entering the undulator is synchronized with the radiation reflected and recirculated by hard X-ray mirrors. Moreover, due to the very short emission wavelengths, radiation slippage is very low and the zero-detuning cavity length can be considered.

Three Diamond mirrors and one beam splitter, made by Zincblend perfect single crystals (lattice parameters: a=b=c=3.566 Å, $\alpha = \beta = \gamma = 90$) operating in the 3.0–3.5 keV range, namely 3.6–4 Å, have been considered. At least two of the mirrors are assumed to be bent and focusing [163]; focusing of the intra-cavity X-rays could also be performed by adding compound refractive lenses in the radiation transport line through the cavity.

The mirror and beam splitter reflectivities have been simulated with the XOP (X-ray Oriented Programs) code [164]. Fig. 3.19 presents the cavity transfer function T, including all cavity mirrors, as a function of the photon energy for a central energy of 3.015 keV and a quasi-orthogonal reflection (incidence angle $\theta_0 = 3°$), compared with the natural SASE spectral line.

[10] Also in this case, higher repetition rates of the SC accelerator would shrink the needed cavity dimension.

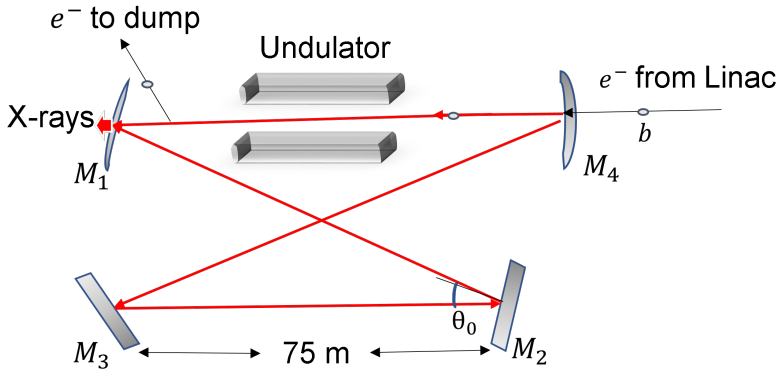

FIGURE 3.18: Scheme of the X-ray FEL Oscillator: short undulator module embedded in a ring cavity made of three Diamond mirrors (M_2, M_3, M_4) and one beam splitter (M_1) for radiation out-coupling. The X-ray radiation is emitted from right to left. θ_0 is the incidence angle on the cavity mirrors with respect to the normal. The distance $M_{1,4} - M_{3,2}$ between two mirrors is 75 m, giving a cavity round-trip length of 300 m, equal to the distance between two successive electron bunches.

The mirror transfer function is narrower than the natural FEL spectral line,

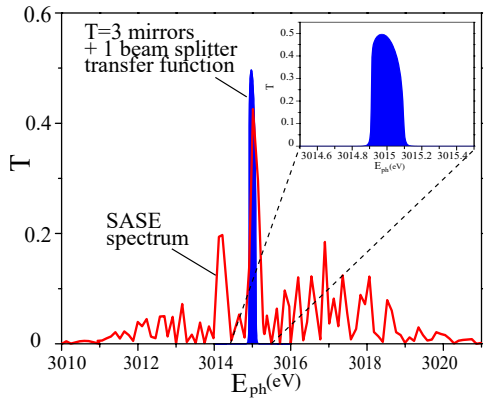

FIGURE 3.19: Transfer function T of an optical line made by three Diamond mirrors and one beam splitter (in blue), compared with the SASE spectrum in arbitrary units (in red) vs. the photon energy for an incidence angle Θ_0 of 3° with respect to the normal, from [163]. . The reflectivities were simulated with the XOP code [164].

so that the spectral filtering of the mirrors is the dominant effect in the spectral width reduction. On the contrary, the angular width of the transfer function

(about 2 mrad) is much larger than the SASE divergence of 25 μrad and the angular filtering is inefficient and negligible.

XFELO performances

As a reference case, SASE emission at 4.16 Å is illustrated in Fig. 3.20.

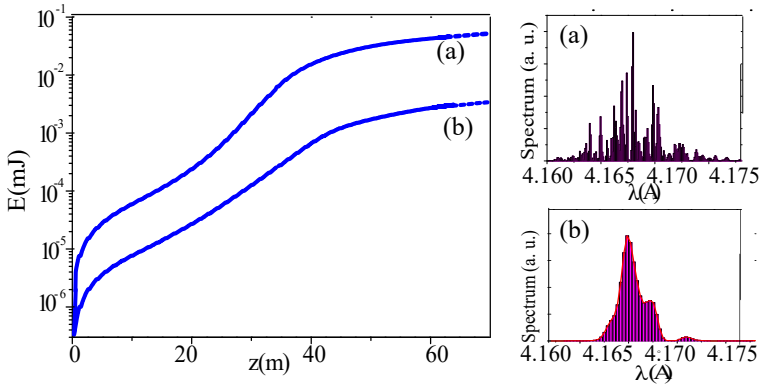

FIGURE 3.20: SASE emission at 4.16 Å from the MariX electron beam. SASE energy growth for the high-charge SASE (a) and low-charge single-spike (b) working points (left window) and corresponding spectral profiles at saturation (right boxes).

The energy growth along the undulator is shown on the left for (a) high (50 pC) and (b) low (8 pC) charge cases: saturation is reached in about 50 m with a level of (a) 8×10^{11} and (b) 4×10^{9} photons/pulse, respectively. The windows on the right report the spectral profiles, showing the SASE fluctuations in the high charge case (a) and the single-spike features in the low charge one (b).
Fig. 3.21 from [163] shows the patterns of the SASE power (a) and spectral distribution (b) as a function of the number of shots, highlighting the modest size of the coherence areas and the poor stability of the SASE process.

As already anticipated, the XFELO operation was analysed by considering the 50 pC electron beam. The left window in Fig. 3.22 shows the intra-cavity radiation energy as a function of the number of round-trips: saturation is reached in about 50 cycles, with an intra-cavity energy level of about 20 μJ; jitters due to the different microscopy of the successive electron bunches occur.
Due to the short undulator and wavelength, the slippage is very low: for this reason, the simulated time window (12 μm) is adjusted to the electron beam

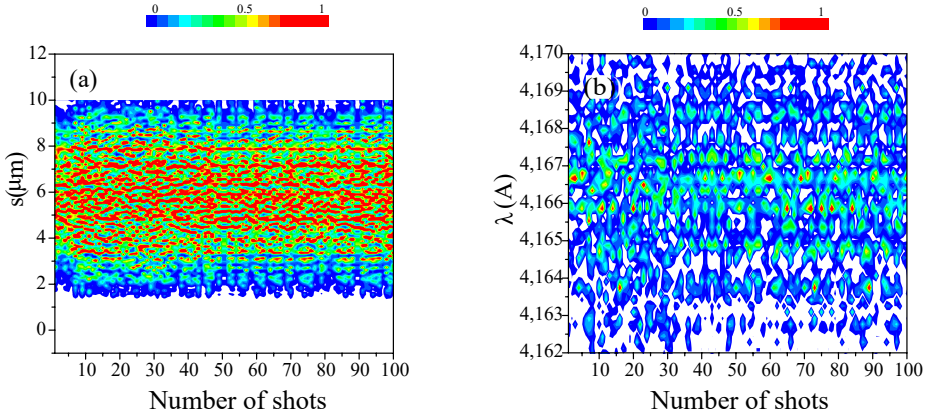

FIGURE 3.21: SASE emission at 4.16 Å from the MariX electron beam. SASE (a) power vs. s=ct and (b) spectral amplitude vs. λ as a function of the number of shots, from [163]. Logarithmic scale.

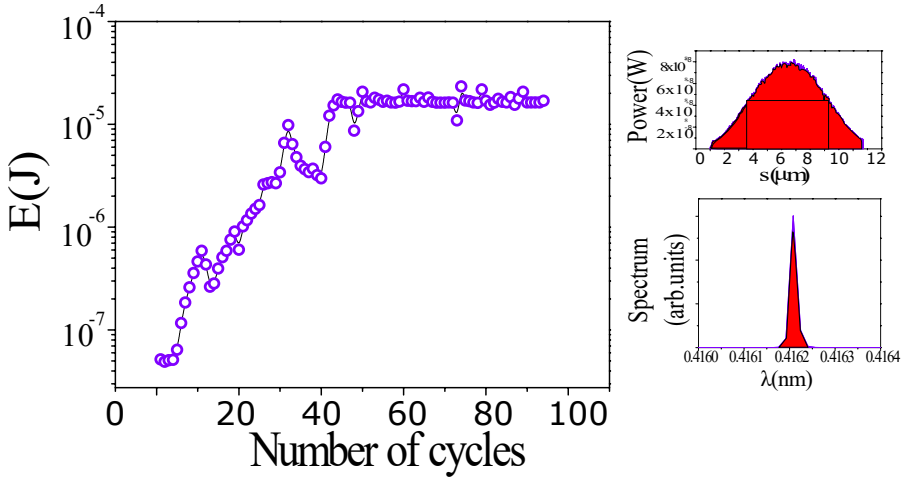

FIGURE 3.22: X-ray FEL Oscillator at 4.16 Å. Left window: intracavity energy growth as a function of the number of cavity round-trips. Right windows: temporal (top box) and spectral (bottom box) distributions at saturation.

and reported in the right windows of Fig. 3.22, which present the pulse temporal and spectral distributions at saturation.

The power longitudinal distributions along $s = ct$ (a) and the spectral amplitude structure (b) resulting from the XFELO are shown in Fig. 3.23 as a function of the round-trip number in the X-ray cavity.

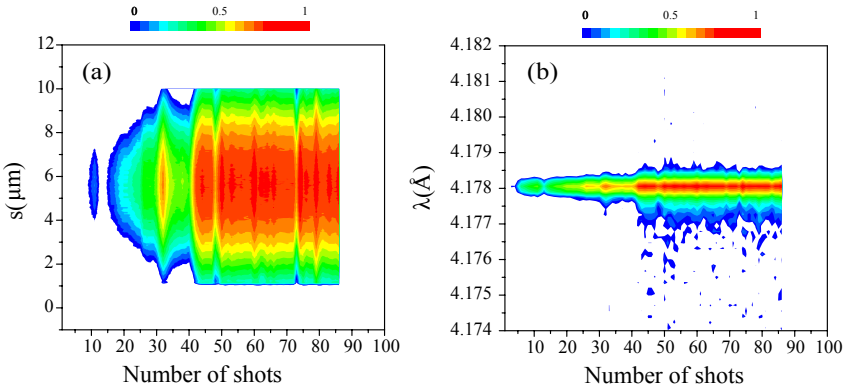

FIGURE 3.23: XFELO at 4.16 Å: intra-cavity power (a) vs. $s = ct$ and spectrum (b) vs. λ as a function of the round-trip number in logarithmic scale, from [163].

The enhanced stability, as well as monochromaticity, of the XFELO with respect to the SASE radiation are pointed out by comparing the radiation patterns of Fig. 3.23 and 3.21 respectively, whereas Fig. 3.24 shows the coherence degrees, evaluated from the correlation function between two different generic pulses ($\Gamma_{1,2}$) or for one single pulse (Γ), for both the SASE (left) and XFELO (right) radiation.
The SASE mode (case (a)) is characterized by both poor phase coherence in one single pulse and shot-to-shot stability, with a coherence length less than 1 μm over a 10 μm-long pulse and an equal time coherence degree of about 4×10^2. In the single-spike mode (case (b)), the coherence length coincides with the pulse length, but the shot-to-shot stability is low and the equal time coherence is about 2×10^1.

Table 3.6 reports the main properties of SASE (third column) and XFELO (fourth column) radiation.
As shown in the bottom right windows of Fig. 3.22-3.20, the spectral profile of the X-ray radiation from the oscillator is narrower than the SASE spectrum; the large rms bandwidth of the XFELO radiation in Table 3.6 is determined by the phase fluctuations[11].

[11] These fluctuations are about 10% and such noise is not detected by measurement systems. For this reason, in order to compare the simulated value with experimental results, a cut of about 4% of the spectra is tipically performed.

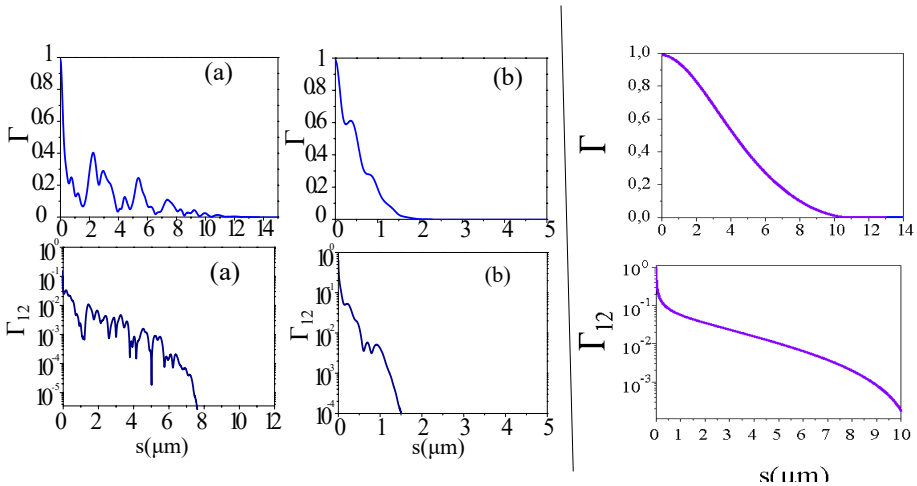

FIGURE 3.24: Left plots: SASE self (Γ, upper row) and mutual ($\Gamma_{1,2}$, lower row) coherence degrees vs. $s = ct$ for the (a) high-charge and (b) low-charge working points. Right plots: XFELO coherence factors vs. $s = ct$.

TABLE 3.6: Main properties of the tender X-ray pulses at 4.16 Å (3 keV) from the MariX FEL, alimented by 50 pC electron bunches in SASE and XFELO modes. The repetition rate of the source is 1 MHz. \$=Photons/s/mm^2/$mrad^2$/bw(0.1%).

Property	Unit	**SASE**	**XFELO**
Photon/shot	10^{10}	80	4.4
Photon/s	10^{16}	80	4.4
Pulse energy	μJ	55	21
Bandwidth	0.1%	2.1	4
Pulse length	fs	10	16
Pulse divergence	μrad	25	14
Pulse size	μm	130	35
Peak brilliance	10^{30}\$	3.6	3.8
Average brilliance	10^{22} \$	3.6	4

Highly stable and collimated pulses, even if characterized by a lower number of photons with respect to the SASE case, are produced with the designed and simulated XFELO configuration. The studied X-ray FEL Oscillator configuration, based on diamond mirrors, is able to produce $10^7 - 10^{10}$ coherent photons per pulse at 3–3.5 keV at 1 MHz, characterized by a very small spectral bandwidth.

Such design study contributes to the ongoing efforts for the study and development of light sources based on X-ray cavities. The choice of crystal mirrors relies on studies [36, 37] and is supported by preliminary experiments [165].

3.2 Investigation of advanced schemes for a coherent X-ray FEL

In the framework of the MariX project and in order to conceive a seeded FEL source of high repetition rate and coherent pulses down to the X-ray range, I studied and investigated two different cascaded FEL schemes, seeded by the EUV FELO described in section 3.1.2. The FEL oscillator-seeding scheme described in this section allows to operate any FEL amplifier at the high, MHz-class repetition rates of SC LINACs, thus overcoming the limitation of single-pass seeding schemes in delivering FEL pulses at high repetition rate.

The oscillator recirculates the spontaneously emitted radiation to seed the next head electron bunch in the bunch train, or can also helps in increasing the low repetition rate of a laser source seeding the electron bunch in the first pass.

Here two cascaded FEL schemes are discussed, namely a three-stage harmonic FEL cascade and an echo-enabled harmonic generation FEL: the oscillator provides the seeding pulses for the following amplifier and accomplishes both the transport of the radiation emited by the electron bunches back to the undulator entrance, where it interacts with the next, fresh electron bunch, and the attenuation of the pulse energy to the correct seed power.

Compared with conventional external seeding techniques, the advantage of this scheme is twofold: the oscillator operation increases the repetition rate by many orders of magnitude, thus allowing to exploit the high repetition rate of SC machines, and, thanks to the higher oscillator frequency and peak power, allows to more easily reach the soft-hard X-ray range with a lower harmonic up-conversion by means of cascaded FEL amplifiers.

Strarting from the proposed schemes, another possibility that has been studied is that of using the oscillator as first stage of the FEL amplifier [94].

3.2.1 Multi-stage harmonic cascade seeded by the EUV FELO

At first, I investigated an advanced oscillator-amplifier set-up, where the amplifier consists of a three-stage harmonic FEL cascade (introduced in Chapter 1). For this purpose, the MariX injector working point I considered is the one delivering electron bunch trains at 0.5 MHz, in which case only the front bunch of each train drives the FEL emission in the oscillator; the other three electron bunches are instead driven to the FEL cascaded amplifier.

In order to meet the successive electron bunch of each train at the cascade entrance, the EUV oscillator seed needs to be retarded by 1 μs, corresponding to a distance of about 300 m.

The radiation transfer line from the oscillator to the cascade provides the needed radiation focusing and is constituted by 2n mirrors, so that its attenuation amounts to $R^{2n} \sim 0.56^n$ (with n = 1–3) [124]. Spherical mirrors for the transport line might focus the radiation beam further and deplete the remaining high-order modes, while multi-purpose stations and beam stabilization systems (as the ones described in Ref.s [166, 167, 168]) can be used to check and adjust the oscillator seed pointing stability and transverse overlap with the electron bunches after the transport line.

FELO seed pulses of the order of 1 μJ allow to reach seed energies of tens to hundreds nJ at the cascade entrance.

In a multi-stage harmonic cascaded technique, the high-power seed pulse excites non-linear electron beam phase space motions and the amplification of harmonics of the seed pulse along different undulator stages, obtaining a coherent FEL pulse at higher photon energies.
The seeded FEL cascade considered for MariX is shown in Fig. 3.25.

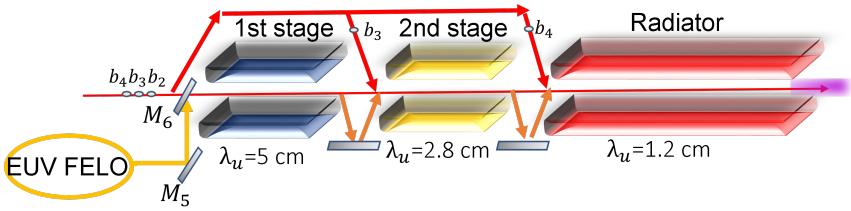

FIGURE 3.25: Scheme of the three-stage harmonic cascade driven by the EUV FEL oscillator: M_5 and M_6 are mirrors of the transport line, b_2,b_3,b_4 are the three successive electron bunches of the bunch train, spaced by 3 m and delivered to the three cascade stages, two long period modulators and a short period radiator, connected by two small delay lines for the radiation (indicated by orange lines). The different modules of the undulator stages are separated by quadrupoles and other radiation diagnostics. The elements are not in scale.

The segmented undulator scheme consists of two stages of longer period undulators (respectively of period λ_u = 5 cm and 2.8 cm), where electron energy modulation and generation of high-order harmonics of the seed fundamental wavelngth occur, and a third shorter period (λ_u = 1.2 cm) undulator as radiator, in which the desired harmonics is amplified.

The oscillator seed forces the electron beam in the first undulator segment to coherently emit the seed frequency itself and its higher harmonics. The n^{th} harmonics is extracted at the end of this first stage, and seeds the second stage,

which is tuned at this harmonics. In the second undulator, the m^{th} harmonics of the seed is generated and extracted. The radiator, tuned at the $(n \times m)^{th}$ harmonics of the seed, then forces the electron beam to emit this resonant frequency (namely λ_0/nm).

In order to avoid deteriorating the electron beam and the FEL pulse quality, the high repetition rate operation and the modest electron bunch duration (up to tens of femtoseconds) allow to consider a variant of the fresh-bunch injection technique [81] (see Chapter 1): three different transport lines deliver the other three electron bunches (b_2,b_3,b_4 in Fig. 3.25), belonging to each bunch train and following the head electron bunch alimenting the oscillator, to the different cascade stages. The electron arrival time and the radiation from the different stages are synchronized by means of two small delay lines of about 3 m between the first two stages and before the radiator.

The electron envelope is confined by the natural focusing power of the undulators and the use of quadrupoles in-between the undulator modules.

Table 3.7 reports various resonance options from 9 Å to 2.7 Å, resulting from a double harmonic up-conversion of two odd integers.

TABLE 3.7: Possible operational working points of the harmonic FEL cascade, seeded by the EUV FEL oscillator at 13.6 nm. The left column indicates the required electron beam energy E and the considered harmonic up-conversion, while the second column indicates the required undulator field strength a_u and the emitted wavelength λ for each cascade.

	λ_u (cm)	1^{st} Mod. 5	2^{nd} Mod. 2.8	Radiator 1.2
E=1.8 GeV	a_u	2.39	1.18	0.93
5×3	$\lambda(nm)$	13.6	2.72	0.906
E=2.04 GeV	a_u	2.77	1.1	0.85
7×3	$\lambda(nm)$	13.6	1.94	0.647
E=2.04 GeV	a_u	2.77	1.45	0.67
5×5	$\lambda(nm)$	13.6	2.72	0.544
E=2.45 GeV	a_u	3.31	1.48	0.701
7×5	$\lambda(nm)$	13.6	1.94	0.388
E=2.66 GeV	a_u	3.61	1.66	0.5
7×7	$\lambda(nm)$	13.6	1.94	0.277

I investigated two example cases of interest for linear spectroscopic applications, namely a 5×5 cascade down to about 5.4 Å and a 7×5 cascade down to 3.8 Å.

The spectral profiles from SASE FEL emission at 5.44 Å at saturation (after about 40 m in the undulator), corresponding to the 5×5 cascade and driven by the 50 pC (case (a)) and 8 pC (case (b)) electron beam of Table 2.3, are presented in Fig. 3.26.

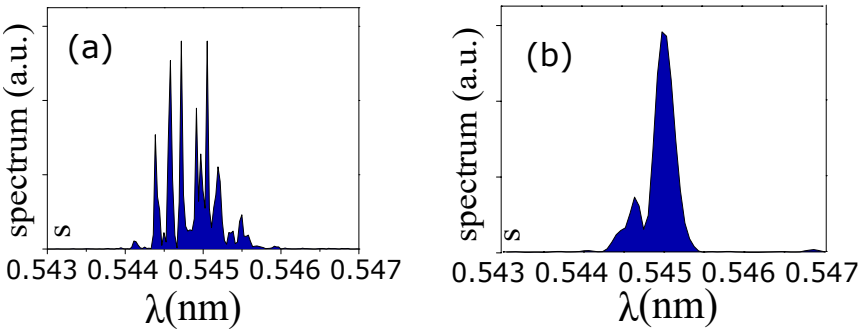

FIGURE 3.26: SASE radiation from the MariX FEL at saturation at 5.44 Å: spectral distributions in arbitrary units for (a) 50 pC (SASE) and (b) 8 pC (single-spike SASE) mode.

The output pulses at saturation achieve peak powers of about 2 GW and 0.3 GW in the high-charge SASE and single-spike SASE regimes, respectively.

In the case of the 5×5 cascade operation mode, as can be seen in Table 3.7, the second modulator (a_u=1.45) is resonant with the 5th harmonics of the first module, $\lambda = 2.72\,\text{nm}$, while the radiator ($a_u$ =0.67) resonates at about 0.54 nm, corresponding to the 5th (25th) harmonics of the second (first) modulator. The output pulse of the cascade performing a 5×5 frequency up-shift is shown in Fig. 3.27: its temporal and spectral distributions at the extraction point after 10 m of radiator are here reported.
The radiation features single spiked temporal and spectral profiles up to the onset of saturation, occuring in a total undulator length of 35 m, made of 8 m for the first modulator, 12 m for the second one and other 10 m of radiator. The output consists in 2×10^{10} photons per shot in a relative bandwidth of about 1.7×10^{-4}.

The enhanced coherence and stability of the seeded output with respect to SASE and single-spike modes can be noticed by comparing the coherence factors in Fig. 3.28.
In the cascaded case, the factor Γ decays much more slowly, and the equal-time mutual coherence factor $\Gamma_{12}(0)$ is 1 compared to 10^{-1} in the high charge SASE and to 2×10^{-1} in the single spike case.

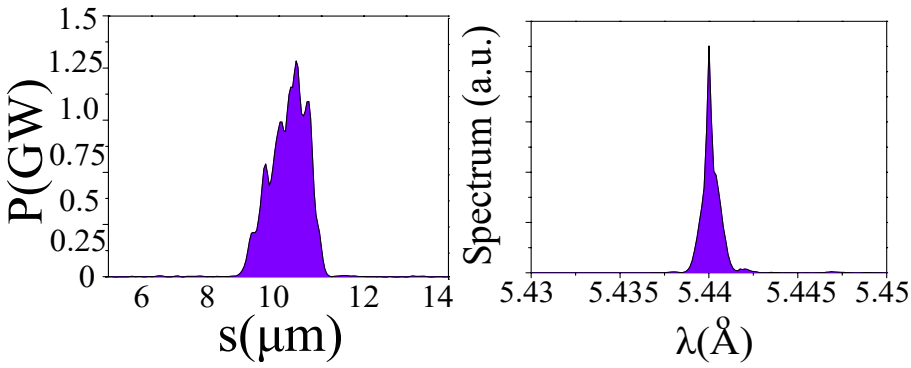

FIGURE 3.27: Performance of the 5x5 harmonic cascade seeded by the EUV FELO. Left window: temporal distribution; right window: spectral distribution of the radiation at 10 m in the radiator (32 m total).

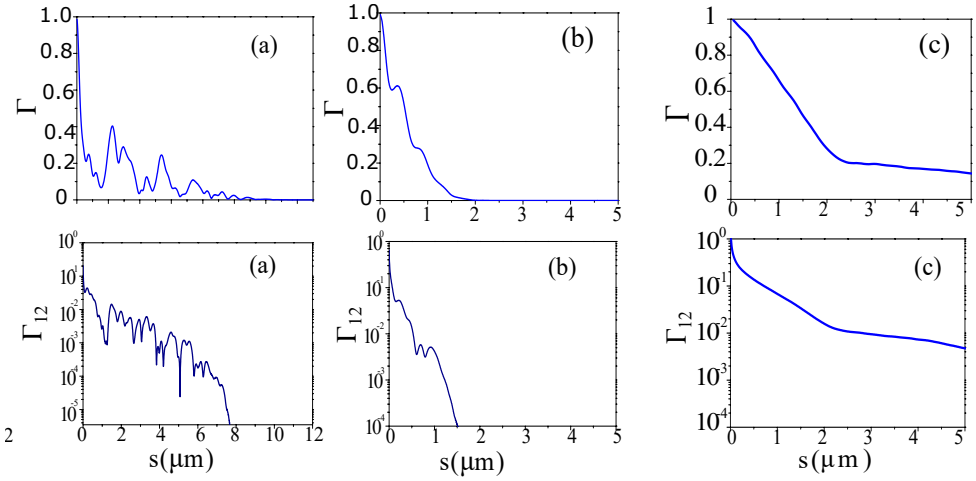

FIGURE 3.28: Performance of the 5x5 harmonic cascade seeded by the EUV FELO. Degree of self-coherence Γ (top plots) and mutual coherence Γ_{12} (bottom plots) of the output pulse vs $s = c\tau$ for (a) high-charge SASE, (b) low-charge single-spike regimes on the left and (c) cascaded mode on the right.

A more energetic, 2.4 GeV, electron beam allows to deliver radiation at 3.88 $\mathring{A}$ through a 7×5 cascade. The values of the undulator parameters are reported in Table 3.7, while the undulator lengths are the same of the other cascade. The temporal and spectral amplitudes at saturation and the coherence factors are presented in Fig. 3.29.
The 7×5 cascade ($\lambda = 3.88$ Å) results in 2.1×10^9 photons per shot in a bandwidth of 3.2×10^{-4}. The main radiation properties of the high charge and

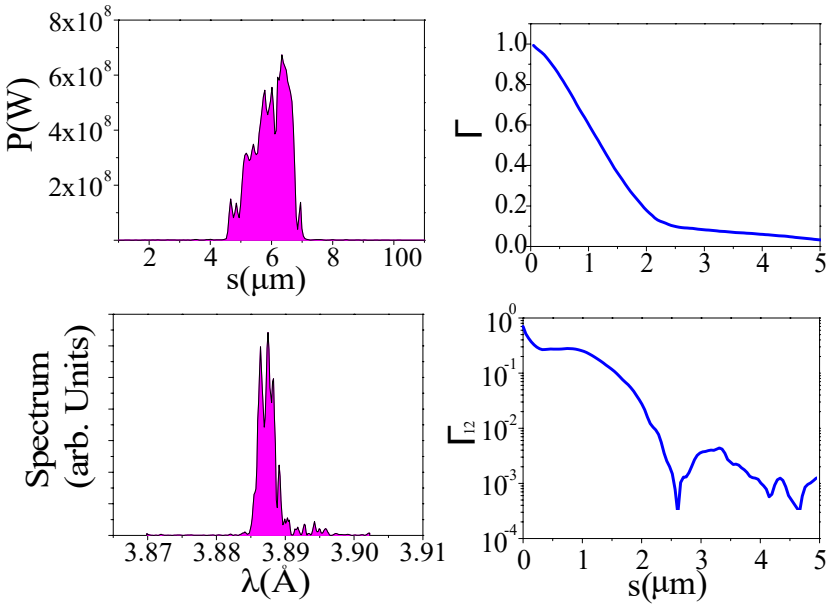

FIGURE 3.29: Performance of the 7x5 harmonic cascade seeded by the EUV FELO. Left windows: temporal distribution of the radiation (top line); spectral distribution at 10 m in the radiator and 32 m total (bottom line). Right windows: degree of auto-coherence Γ and mutual coherence Γ_{12} vs $s = c\tau$.

low charge SASE case, as well as the outputs of the 5×5 and 7×5 cascades, are respectively presented in the third, forth and fifth columns of Table 3.8.

This study demonstrates that the radiation from a EUV FEL oscillator can be used as seed for a cascaded FEL amplifier, performing a frequency up-shift conversion factor of 20-40, thus generating about $10^{10} - 10^9$ fully coherent photons per shot in the tender X-ray range. The described amplifier has a rather complex configuration, compatible with the MariX electron beam characteristics, that would require further feasibility studies for a future experimental realization: in particular, the operation of the transfer lines and synchronization with the radiation field at the end of each stage may be hampered by the jitters of the electron bunches and should be studied in more details.

3.2.2 EEHG cascade seeded by the EUV FELO

Another option of FEL amplifier, seeded by the same Extreme-UV FEL oscillator and driven by the MariX electron beam (see Table 2.3), is an Echo-Enabled Harmonic Generation FEL cascade (introduced in Chapter 1) [160].

I studied this amplifier option for the MariX FEL seeded by the EUV FEL oscillator considering the conventional injector working mode, in which 1 MHz

TABLE 3.8: MariX FEL characteristics of the analyzed working points, namely SASE, single-spike and two different frequency up-conversions using the harmonic cascade seeded by the EUV FELO. The SASE results are reported at 40 m for the high and low charge case. The repetition rate of the source is 1 MHz (SASE) and 0.5 MHz (seeded). \$=Photons/s/mm^2/$mrad^2$/bw(0.1%).

Radiation mode		SASE-Single spike	5x5	7x5
Electron charge	pC	50-8	50	50
Photon energy	keV	2.27	2.27	3.22
Radiation wavelength	Å	5.44	5.44	3.88
Photon/shot	10^{10}	3.5-0.21	1.9	0.21
Bandwidth	0.1%	5-7.5	0.17	0.32
Pulse length	fs	10-2	3	4.5
Pulse divergence	μrad	39-48	3.6	5
Photon/s	10^{16}	3.5-0.21	0.95	0.11
Average brilliance	10^{20} \$	3.5×10^{-3}-1.2×10^{-4}	200	10
$\Gamma_{12}(0)$		0.1-0.2	1	0.94

electron bunches are produced and, after acceleration in the main booster, alternatively driven in the oscillator or matched to the amplifier. The electron beam alimenting the oscillator is extracted at an energy of about 2 GeV upstream the LINAC end, while, depending on the beam energies required in the amplifier, the ones driving the EEHG device may have the same energy or be further accelerated.

The intra-cavity seed pulse temporal and spectral densities at saturation are shown in Fig. 3.30 (corresponding to the output oscillator pulse in the window (c) of Fig. 3.16), while Fig. 3.31 presents the EEHG cascaded scheme for the FEL amplifier.

The oscillator seed pulse is split in two different pulses by an optical transport line and synchronized to the electron bunches at the beginning of both modulators. The two seeds, with the same wavelength of 13.6 nm, interact with the electron bunches and modulate them in energy along the two short modulators, followed by the two dispersive chicanes. A short period radiator, i.e. $\lambda_u = 1.5$ cm, allows emission at $\lambda = 5 - 2$ Å, namely $2 - 5$ keV, with the MariX's moderate energy electron bunch (2–3.8 GeV).

In order to generate and amplify 5-2 Å radiation starting from the 13.6 nm seed, significant electron bunching (at few percent level) on harmonics' order n

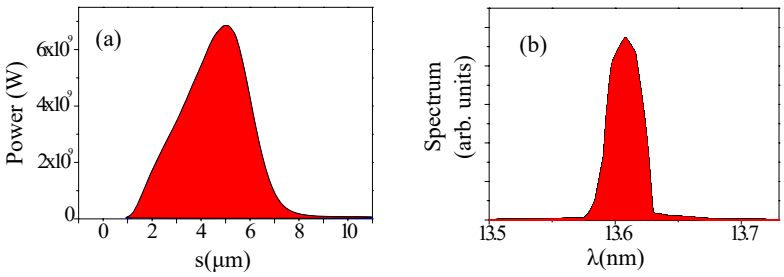

FIGURE 3.30: Signal (a) and spectrum (b) of the intra-cavity EUV oscillator seed pulse at saturation.

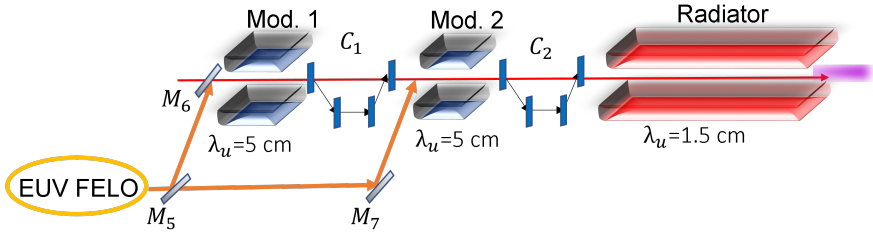

FIGURE 3.31: Scheme of the echo-enabled harmonic generation FEL driven by the EUV FEL oscillator. M_5,M_6,M_7 are mirrors of the optical line splitting and coupling the seed to the modulators Mod. 1,2, with a period $\lambda_u = 5$ cm and respectively 1.6 m and 1.5 m-long. The two dispersive chicanes ($C_{1,2}$) are both 0.45 m long and their dipoles are indicated in blue. The radiator, composed by a sequence of undulator modules with a period $\lambda_u = 1.5$ cm, is about 20 m long. The elements are not in scale.

from 25 to 70 is required.
By following the uni-dimensional model exposed in Ref.s [76, 169], the electron bunching is expressed in terms of the dispersion strengths $R_{56,1}$ and $R_{56,2}$ of the two chicanes and the normalized electric fields $A_{1,2}$ of the seeds (see Eq. 1.17 in Chapter 1). Assuming to split the oscillator pulse in two pulses of peak power $P_{1,2} = 100,200$ MW (0.86 and 1.72 μJ of total energy) respectively, and keeping the longitudinal lengths of the two chicanes constant, the dispersion strengths have been optimized by tuning the dipole's fields to maximize the electron bunching on the desired harmonics of the seed.

For an electron beam with 2.66 GeV energy and a slice relative energy spread of $\Delta E/E = 3 \times 10^{-4}$, the needed dispersion strengths of the two chicanes to provide proper bunching at n=25 at the end of second chicane, corresponding to $\lambda = 5.44$ Å, are respectively $R_{56,1} = 132$ μm and $R_{56,2} = 4.7$ μm.
The electron beam phase space evolution in different points along the line is

shown in Fig. 3.32, showing the electron phase spaces (a) after the first modulator, (b) after the first chicane, (c) after the second modulator and (d) at the radiator entrance.

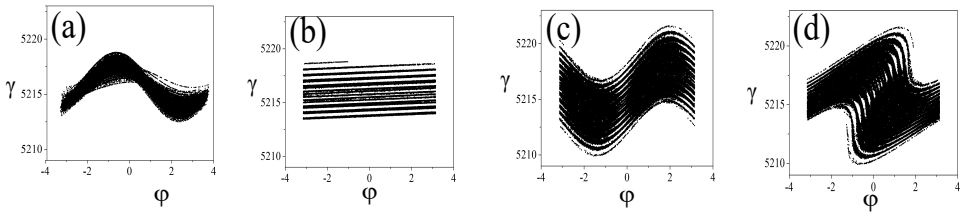

FIGURE 3.32: Evolution of the electron beam longitudinal phase space along the MariX EEHG amplifier, seeded by the EUV FEL oscillator. Windows (a), (b), (c), (d): electron phase space, electron Lorentz factor γ vs seed phase ϕ, at the (a) end of first modulator, (b) end of first chicane, (c) end of second modulator and (d) end of second chicane.

Fig. 3.33 reports the result of the EEHG FEL cascade, performing an up-shift frequency factor n=25.
The bunching on 5.44 Å (in violet in the left window) reaches a peak of 4.5% on the bunch at the radiator entrance, while the rms energy spread increases from 0.03% to 0.045% in the modulators and in the chicanes. These parameters are sufficient to trigger a consistent FEL emission in the radiator.
The radiation is extracted at the minimum bandwidth position, occurring after 12 m of radiator (about 16 m of the total device). The resulting single-spike structures in power and spectral amplitudes at the end of the undulator are shown in the top line, in blue and red respectively, compared with the corresponding SASE profiles extracted after 40 m of undulator.
The EEHG coherent source provides an ultra-short pulse with 5 μJ of energy per shot at $\lambda = 5.44$ Å, corresponding to 1.4×10^{10} photons/shot at 0.5 MHz (0.7×10^{16} photons/s), while the SASE source reaches 14.7×10^{16} photons/s at 1 MHz. Even if characterized by a smaller number of photons, bandwidth, coherence and collimation of the EEHG result in quite high average brilliance, only a factor 5 smaller than the corresponding SASE's.

The auto- and mutual correlation functions, assessing the pulses' coherence properties, are shown in the bottom-right windows of Fig. 3.33: the FWHM coherence length of the EEHG pulse (0.67 μm) is about 4 times the corresponding SASE's; the equal-time coherence between different pulses $\Gamma_{i,j}(0)$ is close to 1, differently from the SASE's of 10^{-1}, and the FWHM mutual coherence length, quantifying the shot-to-shot stability, is 0.1 μm, compared to 0.015 μm of the SASE one [160].

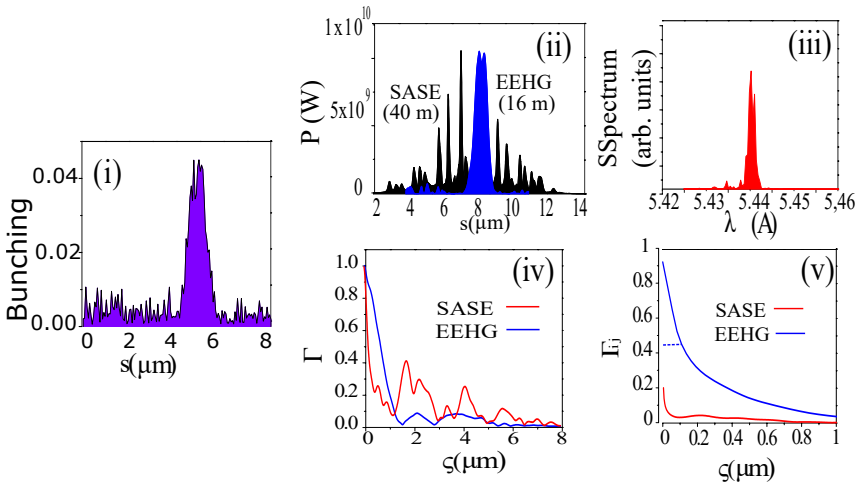

FIGURE 3.33: Radiation pulse at $\lambda = 13.6/25$ nm $= 5.44$ Å from the EEHG cascade seeded by the EUV FEL oscillator: (i) bunching on the 25th harmonics at the end of the second chicane, (ii) EEHG (blue) vs SASE (black) power density profile and (iii) EEHG spectral amplitude at saturation (at the radiator exit, after 16 m), (iv)-(v) SASE (red) and EEHG (blue) coherence degree for one pulse Γ and for different pulses $\Gamma_{i,j}$ vs. $\xi = c\tau$ (dotted segments indicate the FWHM coherence lengths).

Shorter wavelength radiation is generated by electron beams with progressively larger energies: working points covering the range between 5.44 and 2.7 Å, namely n=25, 35, 45 and 50, are summarized in Table 3.9 and compared to similar cases simulated with the previously discussed harmonic cascaded scheme (here referred to as HGHG for brevity) and SASE cases after 40 m of undulator. The coherence length is from 5 (n=35) to 3 (n=50) times the corresponding SASE's, while the stability is larger by a factor from 10 (n=35) to 20 (n=50) [160]. Fig. 3.34 presents powers and spectral amplitudes for both SASE (black) and EEHG (red) cases for n=35, 45 and 50.

The comparison between the results of the EEHG technique and those of the fresh-bunch harmonic cascade, performed with a similar electron beam and with the same oscillator as seeding source, shows a substantial equivalence in terms of number of emitted photons for n=25 (down to 5.4 Å). For higher harmonic numbers (n>35), the induced energy spread limits the EEHG radiation, while the HGHG efficiency decreases very rapidly and radiation levels comparable with the EEHG ones cannot be achieved.

The fresh-bunch technique is performed with a total of four different electron bunches per shot, while only two, one bunch for the oscillator and one for the

TABLE 3.9: Performances of the EEHG FEL at saturation at different harmonic orders of the 13.6 nm seed from the EUV FELO, compared with similar cases obtained with the fresh-bunch harmonic cascade (HGHG) and with the SASE FEL at saturation. The average brilliance is specified. \$=Photons/s/$mm^2/mrad^2$/bw(0.1%).

	SASE	EEHG-HGHG	SASE	EEHG-HGHG	SASE	EEHG	SASE	EEHG
Harmonic #	**25**	**5x5**	**35**	**7x5**	**45**	**45**	**50**	**50**
λ (Å)	5.44	5.44	3.88	3.88	3.02	3.02	2.72	2.72
E_{ph} (keV)	2.27	2.27	3.22	3.22	4.13	4.13	4.6	4.6
γ	5216	5216	6151	6151	6991	6991	7352	7352
$R_{56,1}$ (μm)	132		184.7		281.6			
$R_{56,2}$ (μm)	4.72			4.87		6.58		
Pulse energy (μJ)	58	5.1-7	58	0.9-3.2	46	0.9	42	0.18
Photons/shot (10^9)	158	13.9-19	112	1.74-6.2	69	1.36	57	0.245
Photons/s (10^{15})	158	7-4.7	112	0.87-3.1	69	0.67	57	0.09
Bandwidth (0.1%)	1	0.37-0.17	0.9	0.4-0.32	0.6	0.3	0.5	0.35
Duration (fs)	10	1.5-3	10	0.8-4.5	10	1	10	1
Divergence (μrad)	3.7	3.9-3.6	2.7	3.2-5.1	2.2	2.5	2.05	2.3
Size (μm)	35	27-24	32	25-29	27	25	27	30
Brilliance (10^{23} \$)	94	17-37	151	3.39-5.51	325	5.71	251	0.51
Coh. length (μm)	0.17	0.67-1.3	0.08	0.3-1	0.07	0.21	0.1	0.3

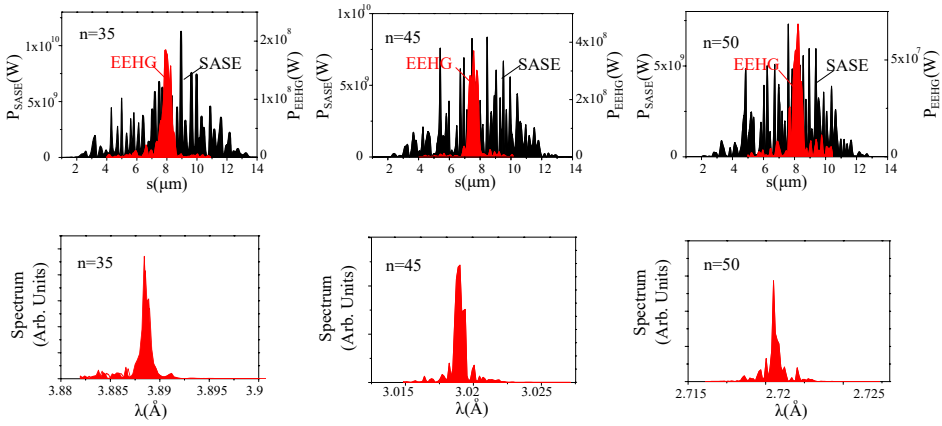

FIGURE 3.34: Performances at shorter wavelengths of the MariX EEHG cascade seeded by the EUV FELO. Top line: SASE (black) and EEHG (red) power profiles (SASE power vs $s = ct$ is on the left axis, EEHG power on the right), bottom line: corresponding EEHG spectral radiation profiles (in arbitrary units) for n=35 (3.8 Å, with $R_{56,1} = 184.7$ μm and $R_{56,2} = 4.86$ μm), 45 (3 Å, with $R_{56,1} = 281.6$ μm and $R_{56,2} = 6.58$ μm) and 50 (2.7 Å, with $R_{56,1} = 293.2$ μm and $R_{56,2} = 6.07$ μm).

FEL, are required in the EEHG case, doubling, in proportion, the radiation repetition rate. Regarding coherence, the more direct transfer of the coherence

properties from the seed to the radiation in the fresh-bunch harmonic cascade leads to a generally better performance.

The advantage of the EEHG cascade is a larger tunability and versatility of the source, that permits to generate intense ($10^{10} - 10^{8}$ photons/shot), ultra-short (down to 1 fs) pulses at all the harmonics n of the seed up to n=50 and not only at those corresponding to the product of two odd integer numbers [160].

The reported simulations of both the XFELO (section 3.1.3) and FELO-seeded cascaded schemes (section 3.2) for the MariX FEL do not take into account possible degradations due to errors, misalignment, pointing as well as temporal jitters and the losses dealing with the transport of the photon beams to the experimental stations: however, the estimations widely exceed the target values set by the MariX scientific case and should therefore be capable to satisfy the conditions requested by the envisaged experiments.

Chapter 4

Advancements for a plasma-based FEL

I collaborated with the SPARC_LAB laboratory of INFN in Frascati [170] on studies and the implementation of a plasma-based FEL. The Frascati laboratories of INFN will host the future plasma beam-driven FEL user facility of the EuPRAXIA project [116, 137]. This Chapter is dedicated to the description of the SPARC_LAB laboratory, its FEL test facility as well as the recent results on plasma-driven FEL lasing towards the implementation of the EuPRAXIA@SPARC_LAB project [138].

The design and simulation study of its FEL beamlines, also highlighted in this Chapter, contribute to the ongoing activities towards the EuPRAXIA Technical Design Report.

4.1 SPARC_LAB

This section gives an overview of the SPARC_LAB test facility at the INFN laboratories in Frascati, followed by recent studies paving the way to the implementation of the EuPRAXIA infrastructure.

SPARC_LAB (Sources for Plasma Accelerators and Radiation Compton with Laser And Beam) was born from a collaboration among ENEA, INFN, CNR, University of Rome Tor Vergata and Elettra Sincrotrone Trieste and was approved in March 2002. Its mission is to explore both the feasibility of a ultra-brilliant photo-injector and to perform FEL experiments.
In the following years, the development of a photo-injector using the "velocity bunching" and of beamlines for THz and Thomson sources improved the laboratory [171].

At present, research at SPARC_LAB aims at very high gradient acceleration with plasma, in the framework of the EuPRAXIA [116] collaboration, and with RF LINACs, in the Compact-Light [172] collaboration.

Photo-injector and linear accelerator

The SPARC_LAB photo-injector is a radio-frequency (RF) gun operating at high gradient, 120 MV/m, after which the electron beam is focused by a solenoid and enters the RF LINAC structures, whose entrance is placed at 1.5 meters from the cathode. The electrons stand on the crest of the accelerating wave, where the beam has the maximum energy gain from the RF.

The LINAC is composed by 3 SLAC-type traveling wave (TW) high gradient (22 MV/m) sections reaching about 180 MeV of energy and followed by an higher gradient (>40 MV/m) section (at 5.712 GHz); the remaining space is occupied by the experimental chamber for plasma acceleration.

Velocity bunching [173, 174, 175] is a technique that uses the RF structure also to compress the beam, by exploiting the difference between the RF wave phase velocity and the beam mean velocity. A low energy beam (3-5 MeV), injected in a TW accelerating cavity close to the zero-crossing phase (no acceleration), accumulates RF-induced correlated velocity spread that tends to compress the beam, giving higher velocities to the slower trailing particles. Differently from the ballistic bunching, acceleration and compression take place simultaneously.
Around the first two LINAC sections, two long solenoids composed by a long iron joke containing 13 coils are used to prevent beam blow up during compression. By so doing, the amplitude of the on-axis magnetic field can be shaped longitudinally to optimize the beam envelope along the LINAC.

The photo-cathode is capable of generating a comb beam, composed by two or more bunches at picosecond or less temporal separation [176]. Such an operation can be very useful for many applications, like plasma acceleration or two-color FEL. In this injector operating mode, the photo-cathode is illuminated by a comb-like laser pulse (characterized by two or more short pulses spaced by a few picoseconds) in order to produce a train of sub-picosecond high-charge density pulses within the same RF accelerating bucket. For this purpose, a possible technique relies on a birefringent crystal, where the input pulse is decomposed in two orthogonally polarized pulses with a time separation proportional to the crystal length. Another technique involves the use of a split and delay line with polarizing beam-splitter and remote controlled delay lines, that allow a fine tuning of the intensity and the separation of the pulses.

Downstream the gun exit, the space charge force produces a linear energy chirp along each pulse, which can be exploited to compress the initial charge profile by means of the velocity bunching. The resulting electron pulse trains have some hundreds-pC charge, a sub-picosecond length and a repetition rate of some terahertz.

Plasma stage

After the LINAC and upstream the SPARC FEL, a plasma acceleration stage was installed. SPARC_LAB is involved in the scientific and technological development of an experimental setup for plasma-based acceleration (see Appendix C for more details on plasma acceleration).

Plasma acceleration requires reliable and well known plasma sources. The plasma properties of any plasma-based acceleration experiment have to match the requirements of the experimental conditions. The ionization of the neutral atoms to produce plasma is the first problem to take into account: while for laser-driven acceleration the laser is usually intense enough to ionize the gas up to a degree in which the ionization is no more a problem for pump depletion, in the beam-driven case this is not necessarily true.

Given a prepared plasma structure, a fine external tuning of the plasma parameters is one of the main requirements. Those parameters include: radial and longitudinal plasma density distribution, plasma composition and degree of ionization, the plasma channel spatial dimensions and temporal dynamics, the plasma temperature: they are very important for injection and propagation of the laser/electron beams in the plasma channel, in particular for matching the accelerated electrons phase to the wakefield along the entire acceleration path, which may require several centimeters of plasma. An easy online control of the most of these parameters is possible in a multi-stage capillary discharge scheme, allowing to fit all the plasma characteristics to the different acceleration stages.

External injection schemes, both laser- or beam- driven, require a uniform, low (10^{16}~10^{17} cm^{-3}) plasma density for centimeter scale length, with sufficient transverse uniformity and relatively low temperature (<10 eV). On the other hand, self-injection schemes require a long and uniform distribution with an higher density (10^{19} cm^{-3}). In order to control the plasma acceleration process and the particle bunch properties, very reliable plasma sources are mandatory.

The study and work at SPARC_LAB was mainly devoted to the research on hydrogen filled capillaries as plasma source [177, 178]. Gas-filled capillary sources can provide a pre-ionized plasma channel for plasma-based acceleration experiments. In these devices, a current pulse of several amperes, passing through the capillary filled with gas at pressure of few tens of millibar, ionizes the gas and preforms the plasma channel before interacting with the driver beams. Capillaries allow for long and almost constant density profile up to centimeter scale and are used to extend the interaction length of the drivers with the plasma.

This kind of capillaries has been primarily used for laser-driven plasma acceleration: the typical parabolic transverse density profile indeed allows to

guide the laser radiation for distances longer than the Rayleigh length. Nevertheless, the high ionization level tipically reached by the discharge reduces the ionization losses acting on the driver(s) and is particularly suitable for low energy particle drivers.

These capillaries are usually made of hard materials, like alumina, quartz, diamond or sapphire. The SPARC research group has also investigated the possibility to produce 3D printed plastic capillaries: their use significantly reduces the cost and time for prototyping, allowing to easily manipulate their geometry. Compared with other plasma sources, gas filled capillaries allow to locally control the plasma channel properties by varying the capillary shape or by timing the discharge with the beams. Homogeneous plasma profiles at low densities of the order of $10^{16} - 10^{17}\ cm^{-3}$ were obtained. The characterization of a gas-filled capillary discharge, including its temporal as well as spatial evolution, must be always performed experimentally [179, 180]. Some useful diagnostic tools are reported in Appendix C.

The system implemented at SPARC can detect the spatial and temporal evolution of the plasma online in single shot analysis inside and even outside the capillary, allowing to study the interaction of the electron beam with the entire plasma profile. Plasma wakefield acceleration experiments were performed at the SPARC_LAB test facility by using a gas-filled capillary plasma source composed of a dielectric material. Electrons can reach GeV-level energy in a few centimeters. In this acceleration scheme, wakefields produced by passing electron beams through dielectric structures can determine a strong beam instability with the capability to focus high-current electron beams in the transverse plane. For these reasons, the estimation of the transverse wakefield amplitudes plays a fundamental role in the implementation of the particle wakefield acceleration [181, 182]. The experimental set-up uses cylindrical hydrogen-discharge plasma capillaries; the plasma channel achieved inside the capillary is 30 mm long with a radius of 0.5 mm. Two gas inlets with a radius of 0.3 mm feed the plasma channel with hydrogen gas.

A RF-Deflector and a magnetic spectrometer, with a Ce:YAG screen after the spectrometer bending magnet downstream the plasma, are used to characterize the time and energy profiles of the accelerated beam. Advanced methods for the stabilization of the plasma acceleration have been successfully investigated and implemented at SPARC [178, 183, 121, 184].

Free-Electron Laser and diagnostics

The SPARC_LAB FEL is the result of a collaboration between INFN and the Free Electron Laser research group of the ENEA research center in Frascati. It is a single pass FEL, initially designed to produce radiation mainly in the

visible region of the electromagnetic spectrum, that can be operated in both SASE and seeded configuration.

In this test facility, different operational schemes and configurations providing radiation between 800 nm and 40 nm with very short radiation pulse duration down to few tens of femtoseconds have been tested, ranging from pure SASE [42] to HGHG [185, 186, 187], seeding with High Harmonics Generation in gas [86, 188, 189, 87], two-color configuration in SASE and seeded mode by using a comb electron beam [190].

In order to optimize transport and maximize the FEL performances, the electron beam is properly matched to the following undulator by two triplets of quadrupoles. The undulator line consists of six permanent magnet undulator modules, 2.15m-long and made by 75 periods (77 including two termination periods) with λ_u=2.8 cm [130]. Each module allows a variable gap in the range from 25 to 8.4 mm, and the achievable undulator strength parameter at the minimum gap is limited by the presence of a vacuum chamber for the propagation of the electron beam. Quadrupoles for horizontal focusing and radiation diagnostic stations are placed in the intersections between the undulator modules. Each station is equipped with actuators allowing the insertion of screens to monitor the electron beam size and position, and in-vacuum metallic mirrors to extract the radiation and send it to a calibrated photo-diode.

A short period 1.5 m-long undulator with λ_u =1.4 cm, developed by ENEA and made by KYMA [130], has been tested and can act as an afterburner to have emission of radiation tuned at harmonics of the main resonance wavelength.

An in-vacuum imaging spectrometer is used to measure the output radiation at the end of the last undulator. The instrument is a 1 m normal incidence grating spectrometer with a Princeton UV-grade CCD camera, allowing the detection of spectra both in single shot and in integrated mode. The spectrometer spectral range covers the interval 35 – 800 nm with three different gratings operating at different wavelengths. The CCD camera and the necessary upstream optics were calibrated in energy. The spectral image permits the reconstruction of the total pulse energy together with the spectral parameters as central wavelength, linewidth, and the spot size and position of the radiation beam in the vertical direction. Different filters, mounted on two filter wheels, are available along the radiation beam line. Neutral density filters allow the attenuation of the radiation intensity at the CCD for wavelengths longer than 350 nm, and band-pass filters may be used to remove intense signals from long wavelengths while observing the higher order harmonics of the FEL [191]. Other diagnostics include photodiodes and energy meters, CCD cameras, a broad-band fiber spectrometer and a commercial IR FROG.

4.1.1 Plasma-driven FEL experiment

The first proof-of-principle experiment demonstrating SASE emission in a FEL driven by a centimeter-scale plasma accelerator was recently conducted at SPARC_LAB [123].

The beam-driven plasma acceleration scheme has been used: the driver is a relativistic electron bunch generating the accelerating field, which is then used to accelerate the trailing witness bunch. The experimental setup is shown in Fig. 4.1.

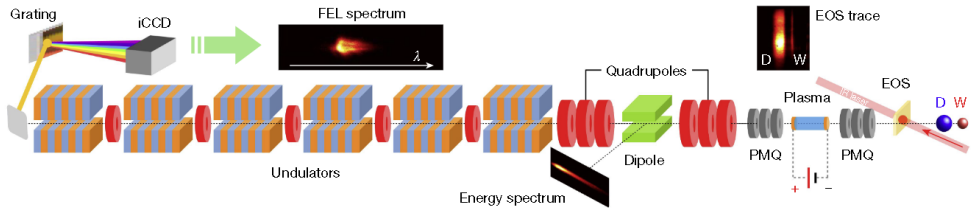

FIGURE 4.1: Beam-driven plasma acceleration and FEL beamline at SPARC_LAB, from [123]. The photo-injector produces the driver (D) and witness (W) electron bunches and a non-intercepting, single-shot Electro-Optical Sampling (EOS) diagnostics monitors their temporal separation. The bunches are focused by a triplet of movable permanent-magnet quadrupoles (PMQs) in a 3-cm-long capillary containing the plasma produced by ionizing hydrogen gas with a high-voltage discharge. The accelerated witness is extracted by a second triplet of PMQs and transported using six electromagnetic quadrupoles. A dipole spectrometer measures its energy with a scintillator screen. The FEL beamline consists of six planar undulators with tunable gaps and five quadrupoles in-between to transport the beam. An in-vacuum metallic mirror collects the emitted FEL radiation, while an imaging spectrometer equipped with a diffraction grating and a cooled intensified camera (iCCD) is used to measure it.

In this case, two short driver and witness bunches, separated by about 1.2 ps, were generated through the photo-emission of a copper cathode illuminated by two UV pulses. The first accelerating sections were properly tuned to compress them down to few tens of femtoseconds. The plasma module consists of a 3D-printed capillary, with a length of 3 cm and 2 mm diameter, filled with Hydrogen gas; the gas is pre-ionized with a Nd:YAG laser focused at the capillary entrance for reducing the discharge timing jitter from tens to few nanoseconds and the plasma density fluctuations from 12% to 6%, thus improving the stability and repeatability of the plasma formation, and ionization is achieved by means of two electrodes providing a high-voltage (5 kV) discharge. The beam

is focused into the plasma and extracted after acceleration by two triplets of movable permanent-magnet quadrupoles installed upstream and downstream the capillary [182].

At the capillary entrance, the driver bunch is 215 ± 5 fs-long (rms) and characterized by an energy of 88.5 ± 0.1 MeV (its core losing about 8 MeV in the plasma) with 0.23 ± 0.01 rms energy spread, a charge of 200 ± 5 pC and 2.5, 1.7 ± 0.2 μm normalized emittance in x, y respectively. The main parameters of the witness bunch before and after the plasma are instead summarized in Table 4.3.

TABLE 4.1: Plasma-driven FEL at SPARC_LAB: witness bunch at the plasma and undulator entrance. The reported values after acceleration, at the undulator entrance, are averages over 500 consecutive shots. The normalized emittance is here reported. All the quantities are quoted as rms.

	Plasma entrance	**Undulator entrance**
Charge (pC)	20 ± 2	20 ± 2
Duration (fs)	30 ± 3	30 ± 3
Energy (MeV)	88.1 ± 0.1	93.9 ± 0.3
Energy spread (MeV)	0.31 ± 0.02	0.31 ± 0.08
Emittance (μm)	$1.4(\mathrm{x}), 1.2(\mathrm{y}) \pm 0.5$	$2.7 \pm 0.7(\mathrm{x}), 1.3 \pm 0.2(\mathrm{y})$

The witness gains about 6 MeV over the 3 cm-long plasma, corresponding to ~ 200 MV/m accelerating gradient, and has FEL-graded properties: it is indeed reproducible with about 0.3% of energy spread and few microns of emittance [184]. Its positive energy chirp (higher energy particles on the head) compensates for the plasma wakefield slope; the achieved 0.3 MeV energy jitter is mainly due to the fluctuations of the witness-driver distance and plasma density. The energy spread of the accelerated witness is preserved, while its higher normalized emittance indicates a transverse mismatch of the beam in the plasma.

The witness is located in the positively charged region produced by the driver: its energy spread progressively reduces along the capillary longitudinal coordinate z, until a minimum is reached in the middle of the capillary, and then grows during the acceleration process in the second half owing to the phase-space rotation.
The beam is extracted from the capillary by means of the second triplet of permanent quadrupole magnets and matched into the SPARC_LAB FEL beamline. Both driver and witness bunches are transported through the undulators, even if the former has a much larger energy spread and is optically mismatched

to the FEL focusing-defocusing (FODO) lattice.

FEL radiation with spectrum peaked at a resonance wavelength $\lambda \approx 830$ nm is produced by the beam passing through the undulators. After each undulator, the photodiodes collect the light emitted, thus measuring the growth of the pulse energy. By comparing the photodiode signals with and without the witness bunch, it was possible to verify that the mismatching and poorer quality of the driver beam prevent light amplification from the driver alone. For each photodiode, 200 consecutive shots were acquired, and the average energy of the 10% most intense pulses has been measured. An average background signal resulting from the energy-depleted driver was also measured by turning off the witness and then subtracted.

The energy growth along the FEL beamline is reported in Fig. 4.2: the numerical fit computed on the measured energies according to the exponential law $E \sim exp(z/L_g)$, in which $L_g^{exp} = 1.1 \pm 0.1$ m is the experimental gain length, is shown.

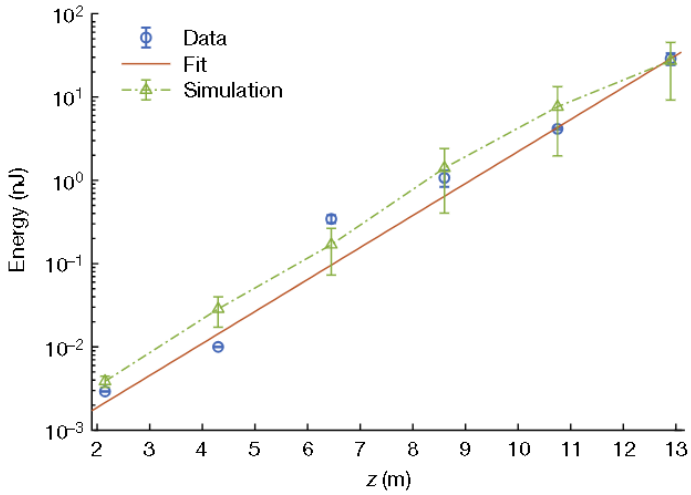

FIGURE 4.2: Exponential energy gain of the amplified light along the six SPARC undulators, measured with the photodiodes (blue circles), from [123]. The red line shows the computed exponential fit over the experimental data. The resulting FEL simulation (green triangles) is also reported. The error bars are computed as the standard deviation of the signal amplitudes measured at each point.

I contributed with the simulation of FEL amplification by the witness beam.

A set of 100 independent runs of the code GENESIS 1.3 [147] was processed similarly to the measured data, by statistically varying the electron beam macroscopic parameters (charge, emittance, energy spread and duration) within the experimental errors to estimate the energy fluctuations.
The simulated energies, reasonably matching the measured ones, are also reported in Fig. 4.2: the resulting gain length, computed on the 10% most energetic shots, amounts to $L_g^{sim} = 1.26 \pm 0.13$ m. Due to the large cooperation length with respect to the short electron beam, this FEL operates in the single-spike SASE regime: as already discussed in Chapter 1, large shot-to-shot fluctuations are expected and effectively observed in both the experiment and the simulations [11].

The imaging spectrometer at the end of the beamline was used for spectral measurements. Fig. 4.3 reports the spectral distributions of the 20 shots with the largest intensities (out of a distribution of 200 samples), together with the statistical analysis in the bottom windows.

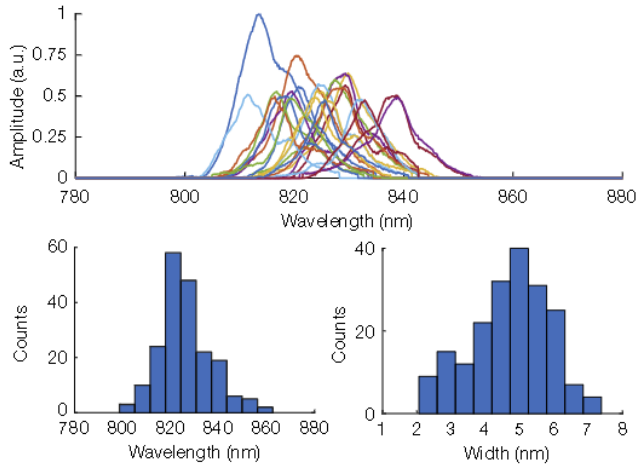

FIGURE 4.3: Spectral analysis of the amplified light at SPARC, from [123]. Top line: spectral distributions of 20 shots, selected out of 200 for the highest pulse energy. Bottom line: histograms of 200 consecutive experimental spectra, reporting the central wavelength (left) and bandwidth (right) of the radiation.

The radiation is centred at $\lambda_r = 826 \pm 9$ nm with bandwidth $\sigma_\lambda = 4.7 \pm 1.1$ nm (corresponding to $\approx 0.6\%$).

Fig. 4.4 shows a single shot of the FEL radiation measured with the imaging spectrometer. Good agreement between the simulations and the experiment is confirmed by looking at the simulated spectrum at the bottom. Both plots also report the respective spectrum traces obtained by projecting the images over the horizontal axis.

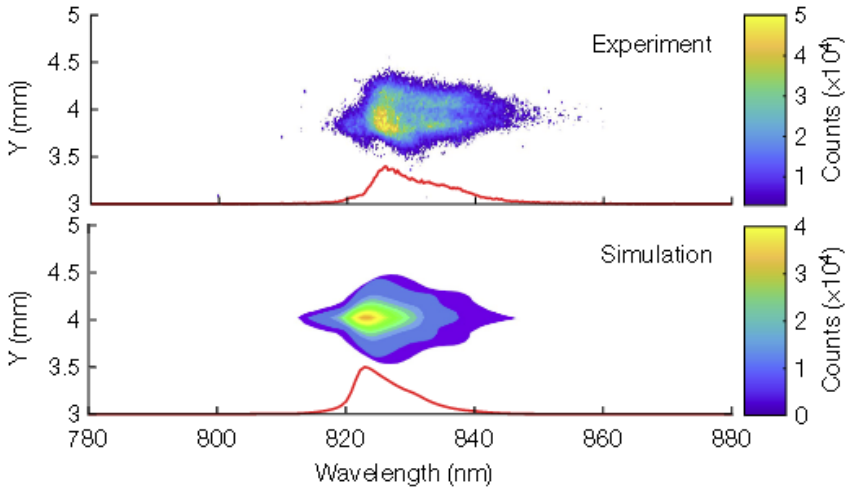

FIGURE 4.4: Single-shot radiation spectrum from the plasma-driven FEL at SPARC, from [123]. 2D traces of single-shot spectra retrieved from experiment (top graph) and simulation (bottom graph). The horizontal axis maps the wavelength dispersed direction and the vertical axis corresponds to the vertical position on the spectrometer CCD. The spectrum projection on the horizontal axis is represented by the red traces in both panels.

The first lasing of a FEL driven by a plasma beam-driven wakefield accelerator has been demonstrated in this experiment. The high quality of the plasma-accelerated witness beam, together with the high stability and reproducibility of the acceleration process, allowed to transport the beam along a segmented undulator beamline and amplify FEL light in the near-infrared range. The observed FEL performances closely match the theoretical expectations.
The scalability of this methodology to larger photon energies is enabled by a precise knowledge of the beam phase space from injection and propagation in the plasma up to the capture at its exit.

A limiting factor of this experiment is the small achieved transformer ratio (see Appendix C for its definition), mainly linked to the characteristic production of the bunches. Possible improvements are under investigation and may arise from the optimization of the bunches used in plasma acceleration such as their shaping.

Nevertheless, this is a promising result in view of EuPRAXIA [192], and indicates an alternative way to similar results achieved with a plasma driven by a laser source [122]: the generation of electron beams with sufficient quality to

induce light amplification in a single-pass FEL has been demonstrated by both techniques. Such results represent an important milestone for next-generation, compact and multidisciplinary user facilities.

This experiment paved the way to a second experiment at SPARC_LAB [193], which uses a fraction of the photo-cathode laser for seeding the plasma-accelerated electron beam with the aim of improving the stability of the amplified FEL radiation pulses with respect to the reported SASE performances.

4.1.2 Seeded plasma-driven FEL

As seen in section 4.1.1, the good qualities of the accelerated witness beam allowed to drive the SPARC_LAB FEL starting from shot-noise [123]. The instability of the pulses is due to the plasma acceleration process, leading to fluctuations of the particles' macrosocopic properties, as well as to the intrinsic fluctuations of the single-spike SASE emission.

A second experiment aimed at improving the stability of the FEL and demonstrating stable generation of intense amplified radiation from a FEL driven by a centimeter-scale plasma accelerator has been carried out. In this case, the plasma-accelerated witness bunch gets seeded by a fraction of the photo-cathode laser, namely a conventional Ti:Sa laser at about $\lambda = 795$ nm.

The Ti:Sa system delivers ≈ 20 mJ energy pulses with ≈ 100 fs duration at 10 Hz repetition rate. The main infrared pulse is sent to two different lines: in the first one, carrying most of the energy (tens of mJ), the signal is converted to UV and used to generate the driver and witness bunches on the photo-cathode; the low energy (hundreds of nJ) line is used both to drive an Electro-Optical Sampling diagnostics and as seed laser for the FEL beamline.
After laser adjustments in terms of temporal duration, transverse size and energy (1-100 nJ), the transfer line injecting the seed laser consists of two motorized in-vacuum high-reflective mirrors. Sufficient temporal overlap with the ultra-short witness is ensured by means of a 15 cm glass material stretching the pulse and inducing a group-delay-dispersion of about 187 fs^2/mm, while a motorized delay-line allows to tune the delay between the seed laser and the electron bunches.

The main characteristics of the seed laser are summarized in Table 4.2.
The seed pulse is much larger than the electron bunches and its size corresponds to a Rayleigh length of about 30 m: for this reason, the pulse dimensions renain almost unaltered from the entrance to the end of the SPARC undulator line. The divergence angle is about 0.2 mrad and the angular jitter is computed to be 0.15 mrad.
Apart from the seeding portion, featuring a transfer line for the seed pulses and a magnetic chicane used to horizontally displace the beam and allow the

TABLE 4.2: Characteristics of the seed laser for the plasma-driven FEL experiment at SPARC_LAB.

Seed parameter	Unit	
Wavelength λ_L	nm	797 ± 3
Bandwidth σ_λ	nm	7 ± 1
Pulse energy E_L	nJ	24.2 ± 0.2
Pulse duration τ_L (rms)	fs	≈ 250
Pulse size σ_L	μm	> 500
Transverse jiter	μm	≈ 25

injection of the seed laser on the same path, the experimental set-up is the one already shown in Fig. 4.1.

The bunch properties for the driver and witness bunches are similar to the one of the previous experiment: the driver bunch at the capillary entrance is 215 ± 5 fs-long (rms) and characterized by an energy of 87 ± 0.1 MeV with 0.23 ± 0.01 rms energy spread, a charge of 200 ± 5 pC and 2.5, 1.7 ± 0.2 μm normalized emittance in x, y respectively. Its core loses about 8 MeV in the plasma. The main parameters of the witness bunch before and after the plasma are instead summarized in Table 4.3.

TABLE 4.3: Plasma-driven FEL at SPARC_LAB: witness bunch at the plasma and undulator entrance. The reported values after acceleration, at the undulator entrance, are averages over 500 consecutive shots. The normalized emittance is here reported. All the quantities are quoted as rms.

	Plasma entrance	Undulator entrance
Charge (pC)	20 ± 2	20 ± 2
Duration (fs)	30 ± 3	30 ± 3
Energy (MeV)	86.6 ± 0.1	92.5 ± 0.3
Energy spread (MeV)	0.31 ± 0.02	0.31 ± 0.08
Emittance (μm)	$1.4(\mathrm{x}), 1.2(\mathrm{y}) \pm 0.5$	$2.7 \pm 0.7(\mathrm{x}), 1.8 \pm 0.2(\mathrm{y})$

At the entrance of the first undulator, the witness beam size is ≈ 200 μm, with a transverse jitter of ≈ 20 μm. The results are obtained in the quasi-nonlinear (QNL) regime, where the driver bunch density exceeds the plasma one and induces blowout but, due to its relatively small charge, the produced disturbance is linear.

The resonant wavelength of the FEL (≈ 827 nm) is set to be slightly different with respect to the seed one to be able to discriminate the two contributions

from the retrieved spectrum traces: the FEL pulse energy may reduce to the SASE one for large wavelength separations, but this does not prevent the FEL light amplification and stabilization provided by the seed.
The light is collected by using the calibrated photo-diodes downstream each undulator: Fig. 4.5 shows the measured energies of the FEL radiation detected with the photo-diode downstream the last undulator.

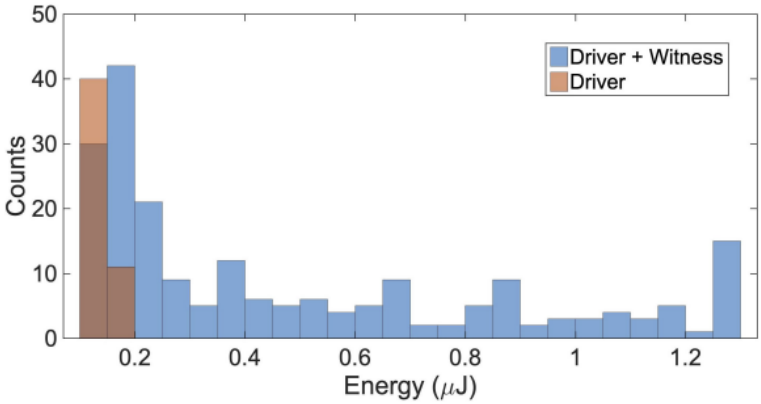

FIGURE 4.5: Seeded plasma-driven FEL experiment at SPARC, from [193]. Energies of the detected FEL radiation downstream the last undulator. The total signals, coming from both driver and witness bunches, are reported.

The total energies coming from both driver and witness bunches, as well as the background induced by the unamplified driver only are reported.
The detected radiation energies (E_{pd}) after each undulator are plotted as a function of the longitudinal coordinate (z) in Fig. 4.6, with (seeded regime) and without (SASE regime) the seed laser [193].
The reported energy values correspond to the average of the 30% more intense pulses out of 200 consecutive shots. The average background signal resulting both from the seeding laser and the energy-depleted driver was measured by turning off the witness, and then subtracted.

The dashed lines show the numerical fit computed on the measured energies according to the exponential law $E_{pd} \sim \exp(z/L_g)$. SASE operation results in a gain length of $L_g^{SASE} = 1.1 \pm 0.1$ m and a maximum energy gain $E_{pd}^{SASE} \approx 30$ nJ, while $L_g^{seeded} = 1.03 \pm 0.1$ m and $E_{pd}^{seeded} \approx 1.1$ μJ in the seeded configuration. An exponential growth of about four orders of magnitudes is observed in both regimes.

The observed amplification is confirmed by simulation results, also shown in Fig. 4.6: a set of 100 independent runs were simulated with the code GENESIS 1.3 [147] and processed similarly to the measured data, by statistically varying the beam macroscopic parameters (charge, emittance, energy spread and duration).

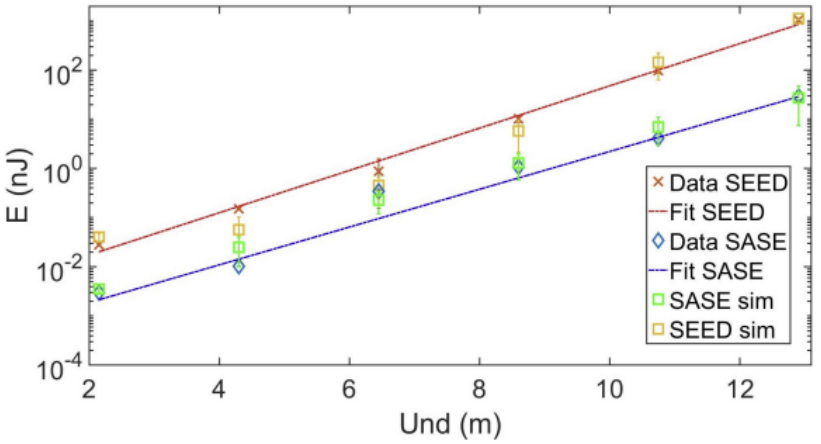

FIGURE 4.6: Seeded plasma-driven FEL experiment at SPARC, from [193]. Energy gain obtained with the seed laser on and off along the undulators (red crosses and blue diamonds, respectively). The dashed lines show the exponential fit of the experimental data. The resulting FEL simulations (green and purple stars) are also reported. The error bars are computed as the standard deviation of the signal amplitudes measured at each point.

The simulation includes the propagation of the seed laser pulse: the best agreement of the simulated exponential gain with the experimental data is obtained by delaying the seed laser pulse by 100 fs with respect to the witness bunch. Such delay mimics the average spatio-temporal misalignment between the seed laser and the electron bunch paths that occurred experimentally.

The energy fluctuations are mainly due to the jitters of the macroscopic witness beam parameters (in terms of energy, spread and emittance) and the microscopic shot noise initiating the amplification process. The 100% intensity fluctuations observed in a FEL amplifier starting from shot noise and supporting a single longitudinal mode are reduced by the seed pulse [193]. The radiation reproducibility is enhanced, resulting in a stability of $89 \pm 3\%$, compared to $27 \pm 5\%$ in SASE mode.

Spectral measurements were carried out with the imaging spectrometer at the end of the undulator sequence. Fig. 4.7 shows 100 consecutive shots acquired in SASE (left) and seeded (right) configuration, with the seed laser turned off or on respectively.
By averaging the acquired signals, the resulting central wavelength is $\lambda_r = 827 \pm 7$ nm, with a bandwidth $\sigma_\lambda = 4.5 \pm 1.2$ nm (corresponding to $\approx 0.6\%$). A similar result is obtained in the SASE configuration ($\lambda_r = 826 \pm 9$ nm with

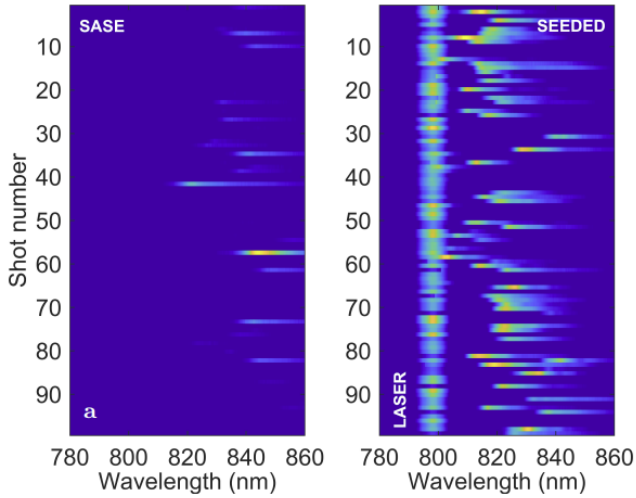

FIGURE 4.7: Seeded plasma-driven FEL experiment at SPARC, from [193]. Comparison between 100 shots acquired in SASE and seeded FEL configurations with the seed laser turned off and on, respectively.

$\sigma_\lambda = 4.7 \pm 1.1$ nm): therefore, the seeded emission occurs at close to the undulator resonance and there is a redshift with respect to the seed laser wavelength (see Table 4.2), similarly to what observed in [194]. Comparing the two regimes, the pulse energy rms fluctuation is 17% in SASE and it reduces to 6% in the seeded scheme.

Fig. 4.8 shows a single-shot of the seeded FEL radiation measured with the imaging spectrometer (left), to be compared to a simulated single-shot of the seeded FEL radiation (right); the respective spectrum trace obtained by projecting the images over the horizontal axis is also reported.
Also in this case, the redshift from the seed wavelength is confirmed.

This is the first proof-of-principle experiment demonstrating stable and reproducible generation of coherent amplified FEL radiation driven by a centimeter-scale plasma accelerator. The results indicate that the use of an external laser allows to seed the emission process from a plasma-accelerated bunch and stabilize its amplification along six undulators, strongly suppressing the fluctuations observed in previous experiments operating in the SASE regime. Further improvements of the stability of the emitted radiation from the witness beam could only be available by stabilizing the plasma formation and acceleration process, thus depend on the intrinsic electron beam fluctuations.

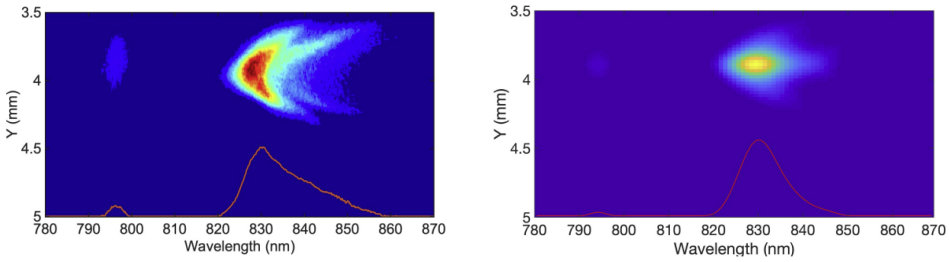

FIGURE 4.8: Seeded plasma-driven FEL experiment at SPARC, from [193]. Snapshot of the radiation spectrum. Two-dimensional traces of single-shot spectra retrieved from the experimental (left) and simulated (right) data in the seeded configuration. The horizontal axis reports the wavelengths and the vertical axis corresponds to the vertical size of the radiation. The orange line shows the spectrum projected along the horizontal axis.

4.2 EuPraXiA@SPARC_LAB: FEL beamlines

A short introduction to the EuPRAXIA project was given at the end of Chapter 2. This section is dedicated to EuPRAXIA@SPARC_LAB [138], the Italian contribution to the project.

As aforementioned, the R&D activities and experiments at SPARC_LAB are fundamental steps towards the implementation of the plasma beam-driven FEL concept in Frascati. For this reason, the study and development of the X-band RF LINAC, the beam-driven plasma module and the FEL beamlines fall under the name EuPRAXIA@SPARC_LAB, the Frascati beam-driven plasma accelerator and related applications of the EuPRAXIA project.

This facility, to be built in the INFN laboratories in Frascati, includes an X-band normal-conducting RF LINAC [195] combined to the beam-driven plasma accelerator to drive two FEL beamlines, discussed in the next sections.
The design of the layout of both the acceleration stages and FELs is still in progress: the preliminary up-to-date layout of the compact accelerator driving the FEL sources is shown in Fig. 4.9.
The design aims at a slice energy spread of 0.05% or lower [121], keeping the energy spread and transverse quantities under control by operating at 0.85 GeV/m accelerating gradient.

The space allocated in the bunker for the gun, S-band, X-band LINAC and the plasma module amounts to about 130 meters, followed by about 25 meters for the undulators.

In conjunction with the optimization and experimental realisation of the

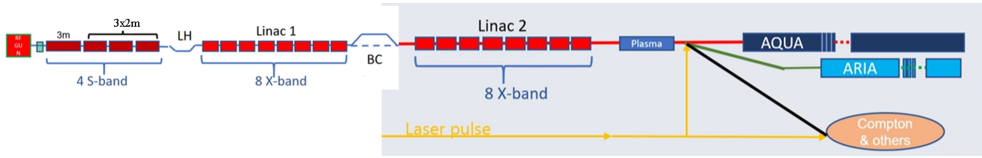

FIGURE 4.9: Sketch of the preliminary EuPRAXIA@SPARC_LAB acceleration and undulator chain, currently under study: two pairs of eight X-band accelerating cavities, separated by a magnetic bunch compressor (BC) and followed by the plasma module; the accelerated electron bunches are driven in two parallel FEL beamlines (AQUA and ARIA).

acceleration stages, two different FEL beamlines have been proposed and are still under study.

The main FEL source in the project baseline is a soft X-ray SASE FEL, named AQUA and aiming at the water window around 3-4 nm [196]. Recently, a second seeded FEL beamline in the VUV range, named ARIA, has been proposed and included in the project baseline [197].

4.2.1 AQUA FEL beamline

The AQUA beamline is the baseline and fully-funded FEL of the EuPRAXIA@SPARC_LAB infrastructure: it is a SASE FEL facility driven by 1 GeV electron bunches, accelerated in the X-band LINAC and the plasma wakefield acceleration stage, and working at $3-4$ nm ($310-410$ eV photon energy) [196, 198].

Its goal is to deliver highly brilliant photon pulses with variable polarization photons for user applications in the water window, where 3D images of biological samples, viruses or cells in their native environment can be obtained processing several X-ray patterns by means of coherent diffraction imaging experiments.
The switchable FEL polarization would allow to study chemical properties of materials.

Table 4.4 shows the electron beam parameters expected from the EuPRAXIA@SPARC_LAB accelerator at the repetition rate of 100 Hz and assumed for evaluating the AQUA FEL performance in [198]. A maximum repetition rate of 400 Hz could be sustained and an upgrade in this direction is planned.
The high-frequency operational range of the source and the limiting space constraints lead to demanding requests in terms of both electron beam quality and undulator technology. The requests to the undulator configuration include selectable linear and circular polarization, high deflection strength ($K \approx 1$) and flexibility in the wavelength tuning range.

TABLE 4.4: EuPRAXIA@SPARC_LAB electron beam parameters for the AQUA FEL operation. The normalized emittance is here reported. Repetition rate of 100 Hz.

Charge	30 pC
Bunch length (rms)	2 μm
Energy	1 GeV
Peak current	1.8 kA
Proj. energy spread	0.95 %
Slice energy spread	0.05 %
Proj. x,y emittance	1.7 mm mrad
Slice x,y emittance	0.8 mm mrad

Two undulator options are considered for the AQUA FEL: a 16 mm period length super-conducting undulator and an APPLE-X variable polarization permanent magnet undulator with 18 mm period length. APPLE-type undulators provide variable polarization, and the APPLE-X geometry is foreseen for its higher magnetic field strengths.

The undulator chain is about 25 m-long and constituted by an array of ten 2 m-long undulator sections, separated by drift lengths of 60 to 80 cm for the matching quadrupole magnets and diagnostics.

Few 10^{11} photons/pulse at $3-4$ nm wavelength are expected from preliminary simulations [196, 198].

4.2.2 ARIA FEL beamline

ARIA is the name of the second FEL beamline of the EuPRAXIA@SPARC_LAB project [197]. As sketched in Fig. 4.9, it could be placed in a parallel line with respect to AQUA.
It has been recently included in the project baseline, although not yet fully funded.

Layout and operationg modes

ARIA is a VUV seeded FEL source, whose layout and operational range is similar to the original ones of FERMI FEL-1 [71]. It features the standard High-Gain Harmonic Generation (HGHG) configuration [82] (introduced in Chapter 1) and operates between 50 and 180 nm, thus extending the FERMI FEL-1 wavelength domain to longer wavelengths and being the only source to cover this full spectral range in Europe.

Its layout is shown in Fig. 4.10 [199].
The electron bunches are energy modulated by the laser seed pulse, realised

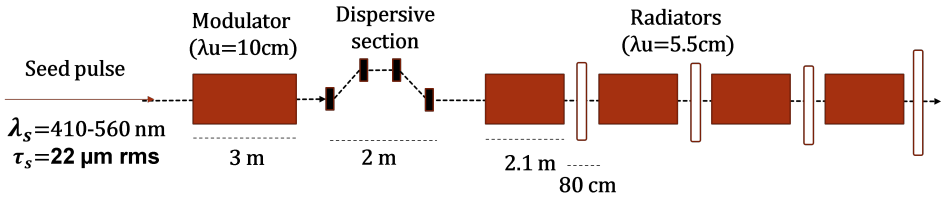

FIGURE 4.10: Layout of the ARIA HGHG FEL. The modulator is a short undulator segment (in orange), where the electron beam interacts with the external seed pulse and is modulated in energy. The dispersive chicane (whose four bending dipoles are sketched in black) converts the energy modulation into a spatial one, therefore providing electron bunching at certain harmonics of the seed. The radiation is amplified in the radiator stage, composed by four undulator modules (in dark red) separated by a quadrupole magnet (in white), properly tuned at the desired harmonics.

with commercial optical-parametric amplifiers in the range 410-560 nm, in a short modulator; the following dispersive section is a four-dipole chicane used for electron density modulation at higher harmonics of the seed, and the desired harmonics is amplified in a final amplification stage made up of four radiators. The specifics of the undulators and seed pulse are summarized in Table 4.5.

TABLE 4.5: ARIA line: undulator (top) and seed laser (bottom) specifications.

Undulator	**Modulator**	**Radiator**
Length (m)	3	4 x 2.1
Period length (cm)	10	5.5
Type	Apple-II	Apple-II
Seed	**Range**	**Simulated**
Wavelength (nm)	410-560	460
Pulse energy (μJ)	1-30	6-30
FWHM Duration (fs)	150-200	170

A long seed pulse with quite low intensity can be employed.

It is a compact beamline, based on consolidated undulator technology, where the use of APPLE-II undulators leads to the amplification of pulses with variable polarization. Furthermore, it can operate with non excellent electron beam qualities, making it potentially ready for user experiments since the first commissioning phase of the project.

Its high flexibility allows operation with either plasma- or LINAC-driven electron beams, characterized by poorer beam qualities and at an energy even lower than 1 GeV. If plasma-acceleration is employed, a dogleg for the electron transport or a second plasma stage can be foreseen.

Plasma acceleration provides low-charge short electron bunches, while the LINAC can also deliver high-charge long electron bunches. It can therefore work in two different beam modes: a short beam mode, where low-charge and short electron bunches from plasma are seeded by the long seed pulse, resulting in very short FEL pulses with a large gain bandwidth, and a long beam mode, with high-charge and long electron bunches combined to the long seed, resulting in narrow line-width FEL pulses which can be exploited for spectroscopic studies and further reduced by using a monochromator. These modes are complementary to the conventional seeded regime used at FERMI [83], where an ultra-short laser pulse seeds long electron bunches, leading to narrow-bandwidth FEL pulses whose properties can be tuned by laser pulse shaping. The synchronization with high harmonic generation sources or external lasers enables multi-color multi-pulse pump and probe operation.

The main electron beam properties in the two operation modes are summarized in Table 4.6.

TABLE 4.6: EuPRAXIA@SPARC_LAB electron beam parameters provided by the X-band LINAC and by the plasma wakefield acceleration (PWFA). The normalized emittance is here reported.

	LINAC	**LINAC+PWFA**
Charge (pC)	200	30
Bunch length (rms, μm)	34	2
Energy (GeV)	1	1
Peak current (kA)	0.7	1.8
Slice energy spread (%)	0.01	0.05
Slice emittance (mm mrad)	0.5	0.8

Due to the much longer seed duration, jitter issues are moderate.

When starting from shot-noise, without the seed, the FEL operates in single-spike SASE mode [50] (see Chapter 1), characterized by first-order coherent pulses with 100% intensity fluctuations: considering undulator modules similar to the radiators, FEL saturation requires three to five more undulators and FEL pulse lengths of the order of the cooperation length, dominated by the bunch duration, are achieved.

In the seeded case, the short electron bunches lead to the single spike, while the seed stabilizes the output by producing electron bunching for each

pulse. Operation with a long seed and short electron bunch has not been widely investigated.

Simulations and expected performances

This section deals with the expected and simulated performances of this FEL source [199].

The expected pulse energies can be estimated according to the Xie model [9], in both linear and circular polarization. Fig 4.11 show the results of this analysis when the line is driven by the low-charge electron beam.

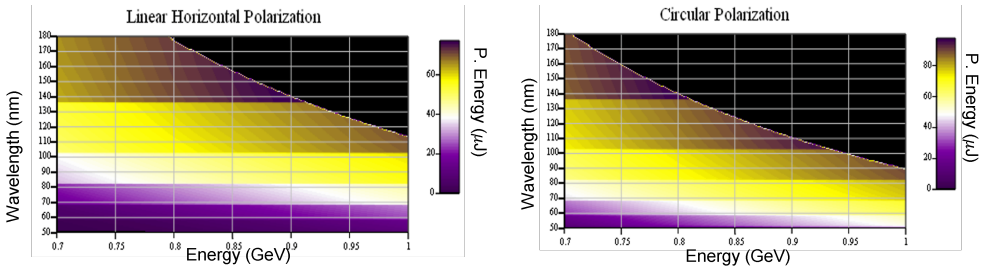

FIGURE 4.11: Low-charge beam mode from LINAC+PWFA at EuPRAXIA@SPARC_LAB: expected pulse energy of the ARIA FEL (μJ) vs electron beam energy (GeV) from Ming-Xie relations in linear (left) and circular (right) polarization. From [197].

In the analyzed electron beam energy range, pulse energies below 20 μJ are achieved in linear polarization between 50 and 70 nm, while slightly larger energies are obtained at longer wavelengths. The circular polarization enables larger photon energies for medium wavelengths around 100 nm.

The performance with high-charge long electron bunches is shown in Fig. 4.12.
In this case higher, hundreds-μJ pulse energies are obtained in both linear and circular polarization.

The expected pulse durations can be calculated as the Fourier Transform-limit of the bandwidth resulting from Xie scaling relations: for a Fourier Transform-limited pulse, the pulse duration is inversely proportional to the gain bandwidth. Gain bandwidth is itself proportional to the FEL Pierce parameter ρ, corrected for three-dimensional effects through the Ming-Xie formulas [9] (see Appendix B), and to $\sqrt{\frac{L_{sat}^{SASE}}{L_u}}$: it is therefore larger for undulators shorter than the length needed for saturation in SASE mode.

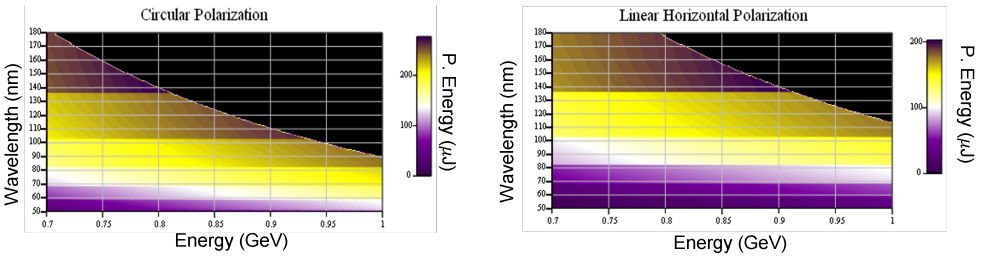

FIGURE 4.12: High-charge beam mode from LINAC at EuPRAXIA@SPARC_LAB: expected pulse energy of the ARIA FEL (μJ) vs electron beam energy (GeV) from Ming-Xie relations in linear (left) and circular (right) polarization. From [197].

A large ρ parameter in the long wavelength range and the presence of the seed, together with short and high-current electron bunches, enable the generation of ultra-short pulses. Short pulses feature large bandwidths; the goal is going around or below 15 fs FWHM with the pulse duration.

Fig. 4.13 shows the expected pulse duration in the low-charge operation mode.

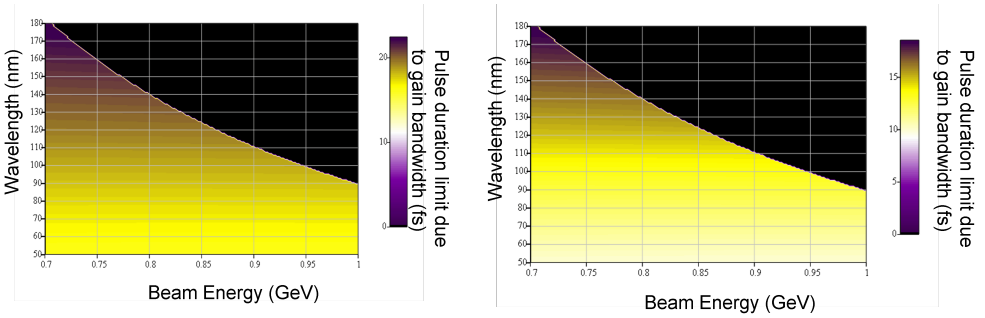

FIGURE 4.13: Expected pulse duration (fs), calculated as the Fourier-Transform limit of the bandwidth in the low-charge working point, vs electron beam energy (GeV) for a 15 fs-long (left) and 8 fs-long (right) electron bunch in circular polarization.

For a 15 to 8 fs-long bunch duration in circular polarization, 5-20 fs pulses are produced in the wavelength range of operation.

Three-dimensional and time-dependent simulations have been carried out by using GENESIS 1.3 version 2 [147] with the maximum available precision, considering an ideal electron beam, with a Gaussian current profile and the average properties listed in Table 4.6 at a maximum energy of 1 GeV, and a

Fourier Transform-limited long seed pulse at 460 nm and tens-μJ pulse energies (see the bottom part of Table 4.5 for the seed specifications).

The harmonic emission has been optimized by tuning the seed intensity and the dispersion strength, so as to reach saturation at the end of the radiator; the dispersion strength R_{56} is tuned by varying the dipole magnetic fields [199]. Fig. 4.14 shows a plot of the needed seed energy (left axis) and dispersion strength (right axis) to efficiently amplify different harmonic numbers HN, when starting from the 460 nm seed.

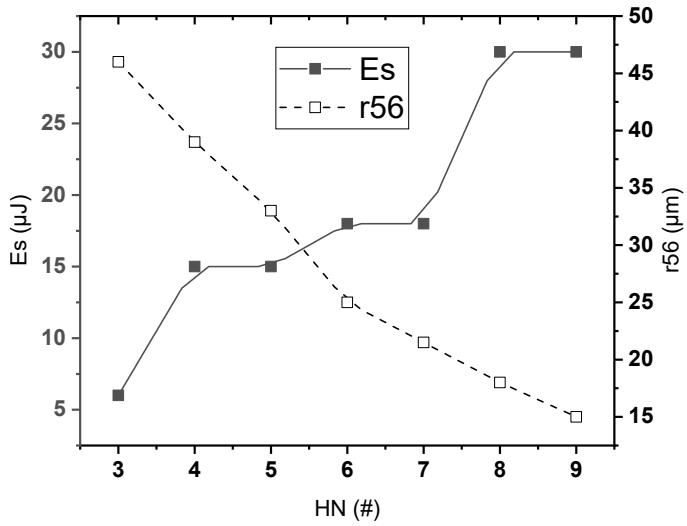

FIGURE 4.14: Required seed energy (μJ, left axis) and dispersion strength (μm, right axis) as function of the amplified harmonic number HN of the 460 nm seed pulse, from [199].

The result is independent of the two beam modes. In order to avoid early saturation, seed intensity and electron bunching should be as minimum as possible, exspecially at long wavelengths.

The simulated pulse energies at saturation are shown for the different amplified harmonic numbers and in both low-charge and high-charge beam modes in Fig. 4.15. The plots show the achieved FWHM pulse duration on top of each data point.
The numerical results presented in Fig.s 4.15 about pulse energy and duration agree with the theoretical estimations described above (see Fig.s 4.11-4.12-4.13).

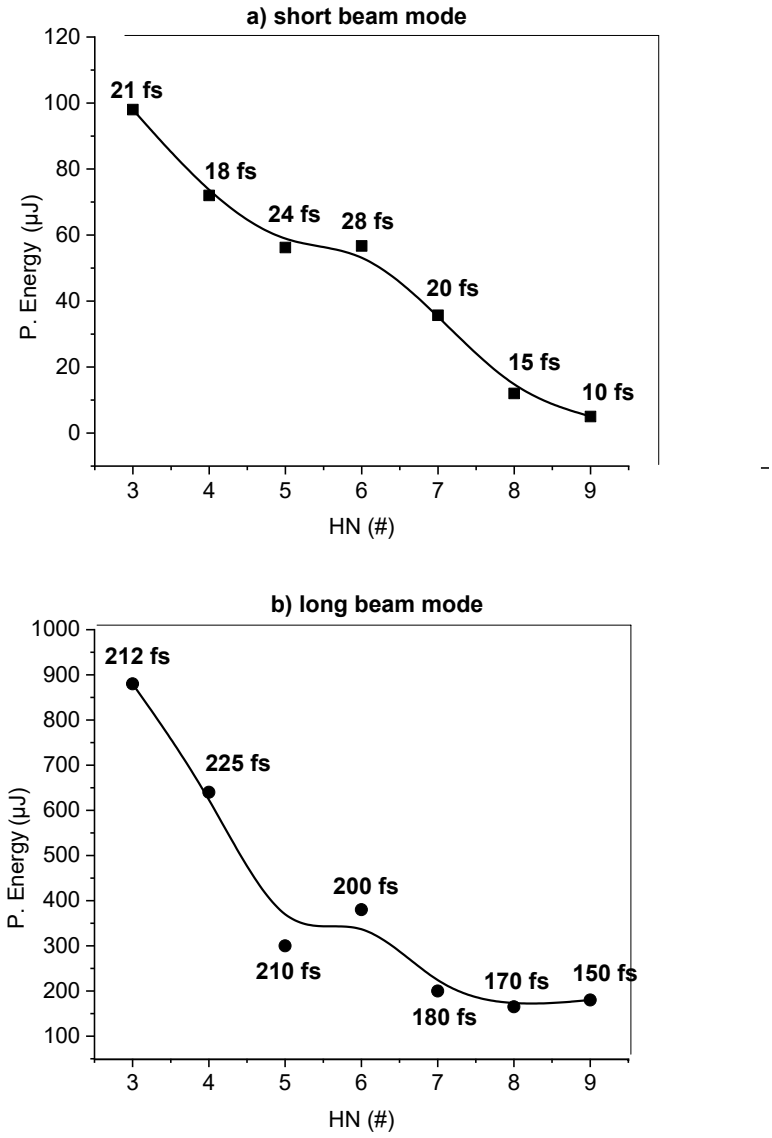

FIGURE 4.15: a) Low-charge beam mode from LINAC+PWFA, b) High-charge beam mode from LINAC: achieved pulse energies (μJ) at saturation for the various harmonic numbers of the 460 nm seed, from [199]. The FWHM pulse duration is also specified for each data point.

Regarding FEL emission at the third ($\sim$ 153 nm) and nineth ($\sim$ 51 nm)

harmonics of the seed, Fig. 4.16 (see next page) shows the temporal and spectral amplitudes of the FEL radiation obtained at saturation with the low-charge (left) and high-charge (right) beam mode, respectively.
The final FEL pulses have a GW-peak power level and are quite narrow.

The radiation pulse properties of the two reported harmonic orders in the short (a) and long (b) beam modes are summarized in Table 4.7.

TABLE 4.7: Radiation properties at about 153 and 51 nm (harmonics orders 3 and 9, respectively) at saturation, in the short (a) and long (b) pulse mode. *=saturation after 3 radiators.

Radiation properties / HN	3a*	3b	9a	9b
Wavelength (nm)	153	153	51	51
Pulse energy (μJ)	100	880	5	180
FWHM Duration (fs)	21	212	10	150
Time-BW Product (#)	2	2.7	0.69	3.8
Pulse size (mm)	0.74	0.85	0.43	0.35
Pulse divergence (mrad)	0.1	0.26	0.04	0.11

The lowest wavelength radiation pulses provided by the ARIA FEL feature small bandwidths close to the Fourier limit. The FEL pulses can be further narrowed by considering larger seed intensities and opening one radiator module, which can then be used for pulse gymnastics or to generate double pulses.

The source could also operate in other interesting beam configurations, already investigated at SPARC [190] and FERMI [200]. For example, double electron bunches and a common long seed pulse can be used to produce multiple phase-locked pulses, and change the relative electric field phase by using the phase shifter in-between radiator modules. A chirped laser pulse as seed of the double bunches could allow to amplify different colors. The radiators can be also tuned at different harmonics.

The ARIA FEL beamline, seeded by a near UV/blue laser, is a promising resource to build a user community from the early start-up of the facility. Tolerance studies of the electron beam parameters and their fluctuations, including the influence of the full 6D electron beam phase space distribution in the simulations, are foreseen; preliminary results obtained with the inclusion of the electron phase space from plasma acceleration show comparable performances to the one reported here.

Scientific goals

Different experimental opportunities in the fields of atomic, molecular and cluster physics are envisioned with the ARIA FEL beamline [197].

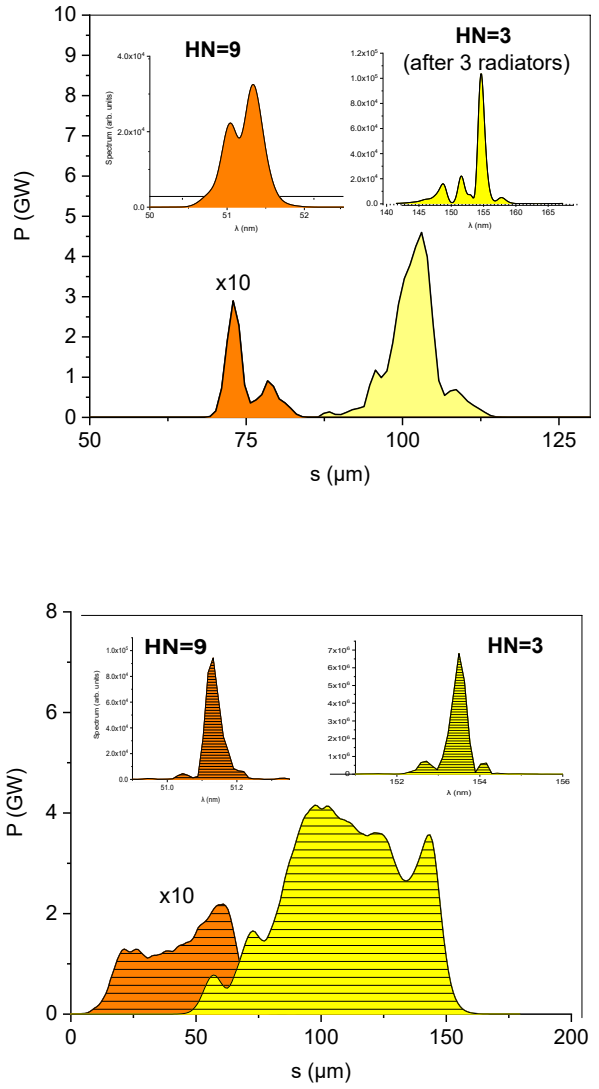

FIGURE 4.16: Low-charge, short beam (top) and high-charge, long beam (bottom) mode: temporal (bottom part of the graph) and spectral (on top) distributions at saturation for the third ($\lambda = 153$ nm, in yellow) and nineth ($\lambda = 51$ nm, in orange) harmonics of the seed pulse. The power profile for the shorter wavelength case in the low-charge beam case has been shifted and amplified for a better visualization.

Its photon energy range will give access to the photo-ionization thresholds and to the valence ionic states of atmospheric constituents, and its pulsed time structure makes it an ideal source for spectroscopy and to study dynamics induced by light in such complex media.

Such a VUV-FEL would enable the production of tunable radiation pulses from the visible into the deep UV, suitable to probe new electronic transitions within the 7–20 eV range for classes of cluster materials, such as nano-carbons. Due to the extremely low number of target particles in cluster experiments, great advances are expected at a VUV-FEL; studies on aggregates of elements with high vaporization temperatures, whose main goal is to look at the formation of free clusters of varying chemical nature [201] by means of resonant techniques, would be possible.

The variable polarization of the light pulses allows to obtain important information on correlating chirality and natural dichroism in biotic media. Moreover, the high brightness of this FEL source could enable the first direct analysis of systems with low density, as well as spectroscopic studies of exotic species.

The photo-dissociation of molecules by the bright and tunable FEL pulses and subsequent analysis of the fragment by time-of-flight spectroscopy, as already performed at the Dalian coherent light source [202] in the same photon energy range covered by ARIA, would also be possible.

In the time-resolved pump (external laser) and probe (FEL) configuration, this FEL beamline provides a powerful tool for the investigation of excited states, such as excitons and polarons.

The ARIA FEL has raised interest from the scientific community, efforts to get fundings and more detailed studies in the framework of the EuPRAXIA@SPARC_LAB Technical Design Report are ongoing.

Chapter 5

Conclusions and Outlooks

The studies reported in this thesis aim at exploring possible solutions to two main topics at the frontier of Free-Electron Laser (FEL) physics: new advanced sources and schemes for external seeding techniques are required to overcome the intrinsic limitations of conventional laser systems in terms of maximum repetition rate and minimum wavelength, thus simultaneously providing coherent and high repetition rate pulses to enable high resolution and statistics in experiments; new acceleration schemes, possibly combined to the newly conceived seeding set-ups, have the potential to decrease the demanding footprint of a FEL machine, paving the way to more compact schemes and making its high-quality pulses available to a broader community. These research lines have been here addressed in the framework of two projects, introduced in Chapter 2: on one hand, MariX is the project of a medium-size research infrastructure exploiting the two-pass two-way acceleration in a super-conducting LINAC to drive a seeded and high repetition rate X-ray FEL; on the other hand, EuPRAXIA is the European project of a compact FEL user facility driven by a plasma-based accelerator.

Chapters 3-4 showed simulation results that have been already published and contributed to the design studies of both MariX and EuPRAXIA. As outlined in Chapter 3, the FEL Oscillator configuration has been modelled, designed and its operation analysed in the THz, Extreme-Ultraviolet (EUV) and X-ray spectral range, starting directly from the electron shot-noise and pointing out the possibility to use the produced radiation pulses as a coherent seed at high repetition rate and short wavelength.
An oscillator scheme based on a THz cavity has been studied in the framework of the BriXSinO project, originally conceived as MariX demonstrator and composed by a super-conducting energy-recovery LINAC equipped with a recirculating arc: suitable working points have been determined, focusing on the main constraints posed by FEL operation in this long wavelength domain.

A slightly more complex cavity, exploiting a secondary working point of the MariX injector and equipped with multi-layer mirrors for delivering EUV pulses at about 13.6 nm, has been also designed and investigated. The reduced electron beam repetition rate of this injection mode results in a long optical

cavity with a four-mirror bow-tie configuration: the needed cavity length is inversely proportional to both the electron beam repetition rate and the number of round-trips performed by the radiation in-between two consecutive electron bunches, and a more reasonable cavity length could be possible if higher repetition rates or highly reflective mirrors were available.
The novel idea was to employ the resulting FEL oscillator as seeding source for an oscillator-amplifier layout of the MariX FEL: two different cascaded amplifiers have been proposed at the end of Chapter 3, namely a fresh-bunch three-stage harmonic cascade and an Echo-Enabled Harmonic Generation (EEHG) FEL set-up seeded by the oscillator pulses. In both cases, the X-ray range is reached through harmonic up-conversion techniques, thus extending the operation of conventional seeded schemes to higher repetition rates and shorter wavelengths. The generation of coherent, stable, ultra-short ($1 - 10$ fs) and highly brilliant radiation pulses, carrying $10^8 - 10^{10}$ photons/shot at 0.5 MHz, has been successfully simulated up to the 35th and 50th harmonic of the seed fundamental wavelength, respectively.
In order to verify the stability of the proposed set-ups, further analysis might include their simulations with a start to end electron beam, taking into account possible degradations due to non-ideal electron beam properties and collective instabilities. Moreover, a very precise timing control is assumed in the investigated fresh-bunch harmonic cascade, and further tolerance studies and optimizations are crucial for a possible future experiment. The analysis of these schemes are based on the MariX super-conducting LINAC, which operates in CW mode at 1 MHz. A proof-of-principle experiment of the proposed schemes would benefit from operation at higher repetition rate, and experimental tests should be foreseen to assess their feasibility and identify technical limitations, such as the high power density on the mirrors and their reflectivity. The oscillator start-up from shot-noise has been considered: even if still depending on the availability of suitable mirrors, this choice is driven by the fact that the fundamental wavelength is independent of seed laser sources and allows to conceive a more tunable radiation source. The start-up from a low repetition rate seed laser could be investigated as well: this operation, recently proposed in literature, allows to synchronize the seed laser with an higher repetition rate seeded FEL pulse for pump-probe experiments, but an higher frequency up-conversion ratio would be required to reach the X-ray range.

A similar cavity configuration has been adopted to study an X-ray Free-Electron Laser oscillator, whose cavity is equipped with Diamond crystal mirrors, as direct source of coherent and high repetition rate tender X-rays for MariX. This case study contributes to the ongoing efforts towards the design and future development of oscillators directly operating in such ambitious and fruitful spectral range. The amplification of stable and monochromatic radiation pulses at 3 keV and 1 MHz was simulated in this case.
The reported simulations of the oscillator configuration rely upon the present

mirror availability in the different spectral ranges as well as experimental studies that have been published in literature; however, due to the poor availability of experimental data in some cases, adequate mirrors need to be experimentally checked and their reflectivities determined.

Recently published results and design studies in collaboration with SPARC_LAB in the framework of EuPRAXIA are detailed in Chapter 4. Its first part reports two interesting results: the first one concerns the first proof-of-principle experiment demonstrating self-amplified spontaneous emission in a Free-Electron Laser driven by a centimeter-scale beam-driven plasma accelerator; a second experiment demonstrated production of stabilized radiation pulses by laser seeding the same set-up. Based on the experimentally achieved electron beam properties, I contributed with the simulation of the amplification process and analysis of the experimental data. Hundreds nJ to μJ-level pulse energies at about 830 nm after a chain of six planar undulators were observed and simulated in the two experiments, respectively, and the seed laser allowed to enhance the radiation stability and reproducibility. Further studies on the bunches' generation and plasma acceleration are ongoing to increase the achieved transformer ratio.

The second part of Chapter 4 deals with the design of the EuPRAXIA FEL beamlines. In particular, I focused on the longer wavelength line, namely a High-Gain Harmonic Generation Free-Electron Laser seeded by a near-ultraviolet laser pulse and working between 50 nm and 180 nm: theoretical studies and simulations of its performances starting from a LINAC-driven high-charge and a plasma-driven low-charge electron beam were presented, highlighting the flexibility of the source and showing its potentials for establishing a user community from the early start-up of the project. As a future step in the design of this FEL, the inclusion of the full-6D electron beam phase space and tolerance studies of its fluctuations are foreseen.

Appendix A

Light sources: from Synchrotrons to Free-Electron Lasers

Synchrotron light sources are based on the synchrotron radiation tangentially emitted by relativistic charged particles travelling bent trajectories under the influence of magnetic fields [203]. For a particle of energy E and mass m, the emission of synchrotron radiation power is proportional to $(E/m)^4$, so that synchrotron light sources are basically particle accelerators for electrons or positrons rather than protons.

The history of light sources [204] follows the development of particle accelerators: the growing demand for higher electron beam energies and stored beam currents led to the invention of storage rings, which are the technological basis for all circular light sources nowadays. Synchrotron radiation was first demonstrated in 1947 in General Electric's research laboratories [203], and was considered as a limiting factor for high-energy physics experiments, leading to energy losses. For this reason, the first generation of synchrotron light sources parasitically used the synchrotron radiation emitted in bending magnets of storage rings operated for particle physics. Two examples, later upgraded into the second generation, were the DORIS (Double Orbit Ring System) at DESY and CESR (Cornell Electron-positron Storage Ring) at Cornell. The potential use of the light produced for studies of matter was soon discovered and led to the second generation light sources in the 1970s. It was a necessary upgrade due to the demands of high-energy physics experiments: the machines' geometry was changed and longer arcs delivering more synchrotron radiation were installed. The third generation features machines optimized for smaller emittance beams and using many straight sections; linear accelerators (LINACs), aiming at the generation of short and narrow-bandwidth pulses, were developed in this period. These sections usually host insertion devices, such as undulators or wigglers, whose concept was proposed by V. Ginzburg in 1947: it is an array of alternating magnets whose field forces the electrons passing through to move on sinusoidal trajectories. Novel technologies, based on electron accelerators,

lasers and their combination, have determined the upgrade from the third to the fourth generation of synchrotron radiation sources based on diffraction-limited storage rings, such as MAX IV [205] and PETRA IV [206], as well as the successful implementation of Free-Electron Lasers (FELs) and inverse-Compton scattering (ICS) light sources. The FEL basic principle and concept, based on the synchrotron radiation tangentially emitted by relativistic charged particles travelling bent trajectories under the influence of magnetic fields, was originally introduced in 1971 by John Madey [1] and was soon demonstrated by Madey and colleagues [3]: most of the experiments initially used low-gain oscillators, where the light was generated and amplified in consecutive passes through an undulator enclosed in an optical cavity. Single-pass high-gain FELs exploiting long undulators and high quality electron beams to reach saturation were introduced by Kondratenko and Saldin [7], and the FEL collective instability was then theoretically described by Bonifacio, Pellegrini and Narducci [41]. This FEL configuration opened the way to shorter wavelengths reaching the X-rays: FLASH [] was the first X-ray FEL (XFEL) to start operation in 2005, and many other XFEL user facilites were studiued and built worldwide.

Some peculiar properties of the light generated by radiation sources are its bandwidth, flux, coherence and brilliance (also called brightness). The bandwidth represents the radiation spectral width $BW = \Delta\lambda/\lambda$ for a certain wavelength λ, the flux $\Phi = N_{ph}/s$ is given by the number of photons emitted per second, while the coherence refers to the pulses' stability. Coherence is an important property describing the degree of phase correlation of a light wave at two different spatio-temporal positions. In particular, the transverse (or spatial) coherence degree is estimated by a normalized auto-correlation function [] considering two different positions r_1,r_2 in the transverse plane:

$$G_{transverse} = \frac{\langle E(r_1)E^*(r_2)\rangle}{\sqrt{\langle |E(r_1)|^2|E(r_2)|^2\rangle}} \tag{A.1}$$

where E indicates the electric field wave. It is experimentally measured with the Young's double slit experiment. The longitudinal (or temporal) coherence can be roughly measured by comparing the wave bandwidth to the bandwidth of the transform-limited case corresponding to the measured pulse duration, or the pulse duration to the coherence time $\tau_c = \int \left(\exp\left(-\frac{\sigma_\omega^2(z)t^2}{2}\right)\right)^2 \mathrm{d}t \approx \frac{\sqrt{\pi}}{\sigma_\omega(z)}$. In this case, the longitudinal coherence degree considers two different temporal positions t_1,t_2

$$G_{longitudinal} = \frac{\langle E(t)E^*(t-\tau)\rangle}{\sqrt{\langle |E(t)|^2|E(t-\tau)|^2\rangle}} \tag{A.2}$$

where $t = t_1$ and $\tau = t_1 - t_2$. The longitudinal coherence of a wave pulse is experimentally measured with a Michelson Interferometer. The range of the coherence degree is $0 \leq G \leq 1$.

The source brilliance is an important property and the most significant

figure of merit, that describes the number of photons per unit time (flux), per 0.1% bandwidth (BW) and per unit phase space area, thus quantifying the radiation quality. It is defined as

$$B = \frac{\Phi}{(2\pi)^2 0.1\% BW \Sigma_x \Sigma'_x \Sigma_y \Sigma'_y}$$

where $\Sigma_{x,y} = \sqrt{\sigma_{x,y}^2 + \sigma_R^2}$ and $\Sigma'_{x.y} = \sqrt{\sigma\prime_{x,y}^2 + \sigma\prime_R^2}$ are a convolution of the electron beam $(\sigma_{x,y}, \sigma'_{x,y})$ and radiation (σ_R, σ'_R) transverse rms sizes and divergences. No optical technique can improve the radiation brightness: adding a monochromator can improve the longitudinal coherence but it reduces the flux, adding an aperture and reducing the vertical size decreases the flux and increases the divergence, respectively. The peak brilliance of different synchrotron radiation sources is shown in Fig. A.1. The synchrotron radiation emitted from

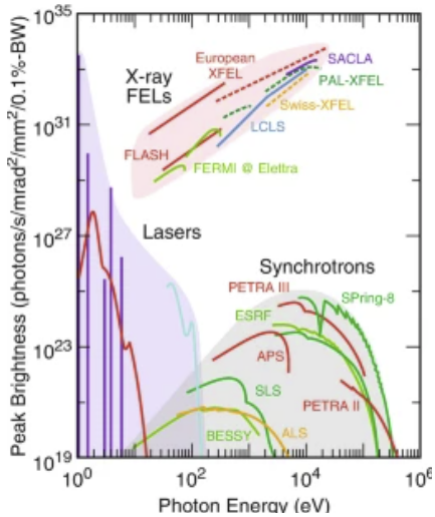

FIGURE A.1: Peak brilliance of synchrotron radiation sources as a function of photon energy.

bending magnets is characterized by a broad spectral range, which limits the brilliance to about $B = 10^{12}\text{mm}^{-2}\text{mrad}^{-2}\text{s}^{-1}(0.1\%BW)^{-1}$, not sufficient for the investigation of atomic structures. The undulator radiation has a narrower spectral range (smaller bandwidth and opening angle), achieving peak brilliances in the order of $B = 10^{21}\text{mm}^{-2}\text{mrad}^{-2}\text{s}^{-1}(0.1\%BW)^{-1}$. One of the most brilliant third generation synchrotron light sources is the PETRA synchrotron light source at DESY [206]. FEL radiation provides a peak brightness which is up to ten orders of magnitude higher compared to third-generation storage rings. The brilliance, intensity and spectrum improvements from bending magnets to FELs is shown in Fig. A.2. The average brilliance is the product of the peak brilliance, the pulse repetition rate and the pulse duration with the Super

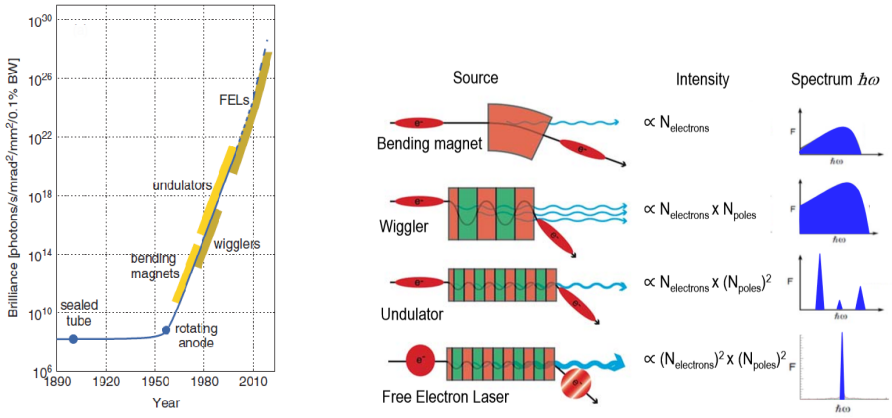

FIGURE A.2: Increase in brilliance due to new technologies (left) and Spectral range and intensity for different devices used in radiation sources (right).

Conducting technology providing MHz repetition rates and a strong increase in average brightness.

Science with synchrotron radiation

The radiation produced from a synchrotron light source, tipically based on a large infrastructure shared by thousands of users, has become a successful and widespread advanced analytical tool for the determination of the properties of matter. Electromagnetic radiation is exceptionally well suited for these purposes as it interacts mainly with the electronic clouds of atoms, ultimately responsible for the chemical and physical properties of materials [8]; its wavelength can be adjusted to match the interatomic distances to study structures with diffraction, while its energy can be tuned to match electronic resonances to amplify signals and gain chemical selectivity. Photon beams with energies ranging from 10 eV to 300 keV can be focused onto small samples, usually after monochromatization, and their scattering or absorption by the material under study provides invaluable information, from the atom positions in crystals and molecules, to the electronic and magnetic microscopic organization, to the mesoscopic and microscopic distribution of particles, defects and domains. For these reasons, despite the drawback of requiring a high level of concentrated economical investment, synchrotron radiation has grown in popularity in the last 30 years.

Science with FEL radiation

Electromagnetic radiation from FELs must be used for experiments otherwise impossible with the more traditional synchrotron radiation sources. Table A.1 highlights the advantage of using FELs in experiments, compared to other light sources, while Figure A.4 (see next page) reports the time scales accessible by FEL based experiments [8].

TABLE A.1: Properties of different light sources: comparison.

Source	Photon Flux	Tuneability	Brilliance	Time resolution
X-ray tube	Low	No	Low ($\sim 10^7$)	Low (ns)
Synchrotron	High	Yes	High average ($\sim 10^{22}$)	Good (ps)
FEL	Medium	Yes	High peak ($\sim 10^{33}$)	High (fs)

The interest in X-ray FELs is motivated by their characteristics of tuneability, coherence, high peak power, short pulse length which allow to explore matter at the length and time scale typical of atomic and molecular phenomena.
With the peak brilliance of an FEL, one has many photons ($10^{11} - 10^{13}$ photons reaching the sample in a $10 - 100$fs flash). Usually this light is concentrated in a focal spot of few micron diameter and is absorbed in a depth of the order of 1 micron in condensed matter. This means that, on average, every atom in the interaction volume absorbs or scatters one photon in a time of few tens of femtoseconds: a very strong perturbation to the system, that often leads to the explosion of molecules and the sublimation of solid samples if the intensity of the beam is not reduced [8].
Fig.s A.3-A.4 show typical electron beam temporal structures from some examples of FEL facilities worldwide and time scales investigated in FEL experiments, respectively.
Whenever possible, the sample is made to flow, as gas or liquid or microcrystal suspension in a liquid, and automatically fresh sample is exposed to each flash of UV or X-ray radiation. But even then one has to be confident that the alteration in the molecular and electronic structure does not happen before the radiation pulse has finished interacting with the sample: it is the " diffract before destroy" approach. The same approach is much more difficult to realize in the case of solids, even if one thinks of moving the sample continuously under the beam; therefore, the pulse energy is usually reduced when dealing with solids.

The large number of photons per pulse allows to determine the structures of complex molecules or nanosystems in a single shot, to study non linear phenomena and high energy density systems. The transverse coherence gives new possibilities of imaging at the nano and sub-nano scale. An X-FEL opens a

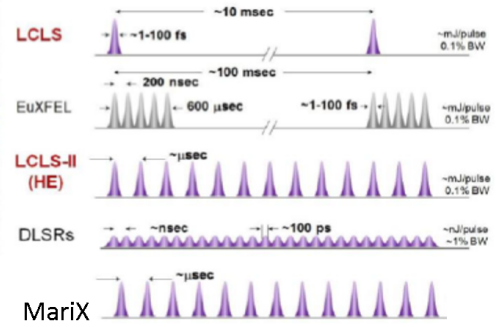

FEL	Repetition Rate
LCLS	120 Hz
SACLA	30-60 Hz
FERMI	10-50 Hz
PAL	30-60 Hz
PSI	100 Hz
EuXFEL	27 kHz
LCLS II	1 MHz
MariX	1MHz

FIGURE A.3: Temporal pulse structure achieved by MariX compared to other facilities worldwide, from [8].

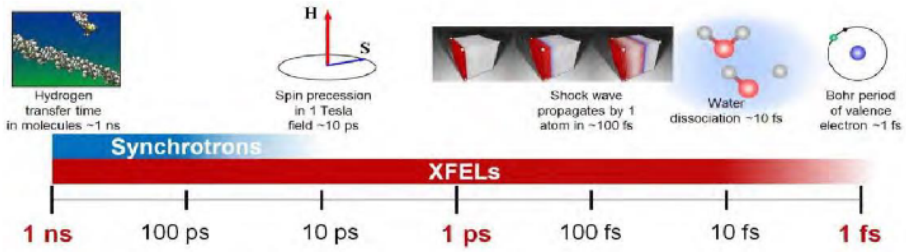

FIGURE A.4: Time scales accessible by FEL-based experiments, from [8].

new physics, leading to the observation of new interesting processes like: make movies of chemical dynamics in action, study the structure and time-resolved function of single molecules, do 3D imaging and dynamical studies of the bio-world, solve the transient structure of liquids, characterize the transient states of matter created by radiation or pressure.

Appendix B

Free Electron Laser Theory

This Appendix deals with the main notions and equations governing the FEL physics. Some basics of accelerator physics are given in the first section. The second section deals with undulator physics and the electron motion within. It follows the FEL theory with the derivation of the FEL integral equation in the different regimes.

B.1 Accelerator & Electron beam physics

The dynamics of relativistic charged particles in the presence of electro-magnetic fields is the main object of accelerator physics.

Here, the case of linear electron accelerators is considered. High-gain FELs put stringent requirements on beam size, divergence and bunch length (which is directly associated to the peak current): the first two, beam size and divergence, are related to the beam transverse dynamics, while the bunch length is controlled with the compression and related to the longitudinal beam dynamics.

B.1.1 Transverse Dynamics

The electron beam is described by a 6D phase space $(x, x', y, y', \delta, s)$, where the coordinates x and y are the transverse horizontal and vertical displacements respectively, $x' = p_x/p$ and $y' = p_y/p$ are the transverse angular displacements (p is the beam momentum), $\delta = \Delta p/p_0$ is the relative momentum offset (p_0 is the nominal momentum) and s is the longitudinal intra-bunch coordinate along the trajectory. The reference particle has the nominal energy and always stays on the design trajectory, thus (x=0, x'=0, y=0, y'=0, δ=0, s=0).

Even if the electron bunches follow the nominal trajectory, the single electrons within each bunch tend to diverge. Transverse magnetic fields are therefore used to keep them as close as possible to the nominal trajectory defined by the reference particle: electrons experience the Lorentz force

$$F = e(E + vxB)$$

where e is the electron charge, while E and B represent the electric and magnetic fields. For an electron in equilibrium with the centrifugal force $F_c = m_e v_z^2/R_c$ (m_e is the electron rest mass and R_c the radius of curvature of the trajectory), moving with a purely longitudinal velocity v_z and experiencing a magnetic field B_y, the Lorentz force is $F_x = -ev_z B_y$. The magnetic rigidity is determined by equating these two forces

$$B_y R_c = \frac{p}{e} \ .$$

Assuming relatively small transverse displacements of the electron, the magnetic field B_y can be expanded in series; dividing all the resulting terms by p/e, different multipole terms are found.

The first term, scaling as $1/R_c$, is the dipole term: in an accelerator, dipoles are used to keep the electrons close to the nominal path by steering the trajectory of all electrons independently of their position, if The linear term in the transverse displacement, scaling as $x(p/e)^{-1}$, is the quadrupole term: quadrupoles focus and defocus transversely the beam. The quadratic term in the transverse displacement, scaling as $x^2(p/e)^{-1}$, is the non-linear sextupole term: sextupoles are used to compensate for the so-called chromaticity and for field correction.

A matrix formalism in linear approximation is tipically used to describe how each electron's six coordinates are affected along a transport line, and is suitable to treat beamlines including linear elements such as dipoles and quadrupoles [207]. Each of the transfer matrix elements, R_{ij}, describes the correlation between two sets of coordinates $(x_i, x_i', y_i, y_i', \delta_i, s_i)$ and $(x_f, x_f', y_f, y_f', \delta_f, s_f)$: the final set of coordinates can be calculated with the transfer matrix M of the elements along the transport line causing the change. Each element in the accelerator has its characteristic transfer matrix. A certain sequence of elements can be described by a single transfer matrix, which is the product of the matrices that describe the independent elements in reverse order:
R_{56} is the longitudinal dispersion and denotes the correlation between the longitudinal position s and the energy δ of the electrons.

A snapshot of the single electron trajectories at a certain longitudinal position z along the line determines an electron bunch, which is an ensemble of electrons characterized by some parameters.
The bunch properties are usually described as moments of the particle distribution in phase space, for example the squared rms beam size $\sigma_x^2(z) = \langle x^2 \rangle$, the squared rms beam angular divergence $\sigma_{x'}^2(z) = \langle x'^2 \rangle$ and the rms beam correlation $\langle xx' \rangle$. Based on these basic parameters, it is useful to introduce the

Twiss parametrization[1], which defines three important parameters describing the beam envelope and divergence

$$\begin{aligned} \beta(z) \\ \alpha(z) &= -\frac{1}{2}\beta'(z) \\ \gamma(z) &= \frac{1+\alpha^2(z)}{\beta(z)} \ . \end{aligned}$$

The emittance ϵ is defined as the area covered by the bunch in the phase space divided by π; according to the Liouville's theorem, it is a constant of motion when conservative forces, such as dipole and quadrupole magnetic fields, are considered.

The rms emittance is a statistical property and is also known as geometric emittance

$$\epsilon_x = \sqrt{\langle x^2 \rangle \langle x'^2 \rangle - \langle x x' \rangle^2} \ .$$

Another commonly used definition of emittance is the normalized emittance $\epsilon_N = \epsilon_x \gamma$, which is conserved during acceleration. Its equation in phase space can be written in terms of the Twiss parameters

$$\epsilon = \gamma(z) x^2(z) + 2\alpha(z) x(z) x'(z) + \beta(z) x'^2(z) \ .$$

The emittance describes an ellipse in phase space, and the Twiss parameters describe its shape and orientation. The beta function, $\beta(z)$, is the position-dependent part of the amplitude of the transverse oscillations performed by each electron along the accelerator and is therefore linked to the rms beam size $\sigma_x(z)$; $\alpha(z)$ is directly proportional to the derivative of the beta function, while the gamma function $\gamma(z)$ is related to the rms beam divergence $\sigma_{x'}(z)$

$$\begin{aligned} \sigma_x(z) &= \sqrt{\epsilon_x \beta_x(z)} \\ \sigma_{x'}(z) &= \sqrt{\epsilon_x \gamma(z)} \ . \end{aligned}$$

The emittance determines the electron beam quality: high-gain FELs need high-quality electron beams characterized by relatively low emittance levels for the FEL successful operation. Good electron beam qualities are even more important for the generation of short-wavelength radiation.

[1] The matching of an electron beam to the undulator in a FEL machine is performed imposing the periodicity of the Twiss functions ($\alpha(z)$ and $\beta(z)$), and the existence of the solution of this problem depends on beam parameters, such as average beam energy and normalized transverse emittance, and on the emitted radiation wavelength too. The quadrupoles and the drifts are described by their associated transfer matrix, and the product between the 6D vector associated with the beam and these matrices gives the transferred beam vector after the propagation. From the transfer line equivalent matrix, obtained multiplying all the matrices associated with the optic elements, one can obtain the transfer matrix for the Twiss parameters and figure out how to design a transfer line.

The requirements on beam parameters such as emittance, peak current and energy spread need to be satisfied in the longitudinal portion of the electron beam where lasing is desired. The term *slice* is associated with a portion of the "lasing" part of the beam, while the term *projected* refers to a property of the whole beam.

B.1.2 Longitudinal Dynamics

A figure of merit of the quality of the electron beam is the 6D electron beam brightness [208], which is defined as the electron bunch charge divided by the product of the rms horizontal, vertical and longitudinal emittances.

High peak currents, needed for efficient energy conversion in the FEL, are achieved by compressing the electron beam. The electron bunch length is then associated with the output FEL pulse duration.

Magnetic bunch compressors, consisting of dipole magnets that deflect the electrons with an energy-dependent angle, are commonly used in FELs for longitudinal compression. For an effective compression, the electron bunch needs to have a linear energy chirp h, meaning that the energy and longitudinal position of electrons are linearly correlated. The energy offset δ of any electron at the entrance of the bunch compression can be expressed as a function of its initial longitudinal intra-bunch coordinate s_i as

$$\delta = \delta_0 + hs_i + h's_i^2 + ...$$

where δ_0 represents the uncorrelated energy offset.
The linear energy chirp is defined as $h = \frac{dE}{ds}\frac{1}{E}$, where E is the electron beam energy, and can be introduced in the LINAC during the RF acceleration process.

The energy gain ΔE_{gain} of the electrons by the RF wave is described by $\Delta E_{gain} = eV_{RF}\cos(K_{RF}s + \phi_{RF})$, where V_{RF} is the amplitude of the RF voltage, k_{RF} is the RF wavenumber and ϕ_{RF} the RF phase. Maximum acceleration occurs when $\phi_{RF} = 0$ and the beam is "on crest"; maximum deceleration occurs for $\phi_{RF} = \pi$ and beam is at "zero crossing" for $\phi_{RF} = \pi/2$.

An "off crest" acceleration is needed to get a chirped electron bunch. An energy-chirped electron bunch during acceleration is achieved with $-\pi/2 < \phi_{RF} < 0$ or $0 < \phi_{RF} < \pi/2$.

After a bunch compressor with a longitudinal dispersion R_{56}, an electron of energy offset δ has a new longitudinal coordinate

$$s_f = s_i + R_{56}\delta = s_i(1 + hR_{56}) + R_{56}\delta_0$$

where the second expression is obtained by substituting the energy offset δ for a linear energy chirped beam.

The bunch compression factor, proportional to the ratio between the initial and final electron bunch lengths, is derived by differentiating

$$l_{BC} = \frac{ds_i}{ds_f} = (1 + hR_{56})^{-1} \ .$$

An energy chirp and longitudinal dispersion of opposite signs allow to reduce the bunch length longitudinally.

Higher order terms are important for RF acceleration and bunch compression. A (decelerating) harmonic cavity or optics linearization with sextupole magnets are usually employed in arc-type bunch compressors to reduce their contribution and detrimental effects on the beam. Typically, bunch compression stages are used in FEL beamlines to reduce the sensitivity to RF jitter: two stages are commonly used; FERMI has been operating in the past with only one bunch compressor in order to minimize the effect of the microbunching instability which plays an important role in seeding.

B.2 Undulator

The hardware part of a Free-Electron Laser (FEL) is an undulator or wiggler. Its main purpose is to force the electrons to oscillate ('wiggle') while moving through. The main feature of an undulator and wiggler is a series of paired magnets along the main axis, placed opposite to each other and separated by a gap.
If the plane of the gap is fixed, the undulator or wiggler is planar, while the helical undulator involves the rotation of the magnets along the main axis in the form of a double helix.

A Cartesian coordinate system, where the z-axis coincides with the undulator axis, will be considered throughout this Appendix. The transverse coordinates x and y are chosen so that the magnetic field for a planar undulator or wiggler is parallel with the y-axis (see Fig. B.1). Due to the rotational symmetry, the choice of the coordinate system orientation for the helical undulator is arbitrary.
For sake of simplicity, the case of a planar undulator is treated.

The magnetic field on the undulator axis is a harmonic function of the longitudinal position z:

$$\mathbf{B} = (0, B_0 \sin(k_u z), 0) \tag{B.1}$$

where λ_u and $k_u = 2\pi/\lambda_u$ are the undulator period length and wave number respectively. The field points in the y-direction and has an amplitude B_0 given by

$$B_0 = 2B_r \frac{M}{\pi} \sin(\frac{\pi}{M}) \left(1 - \exp(-\frac{2\pi h}{\lambda_u})\right) \exp(-\frac{\pi g}{\lambda_u})$$

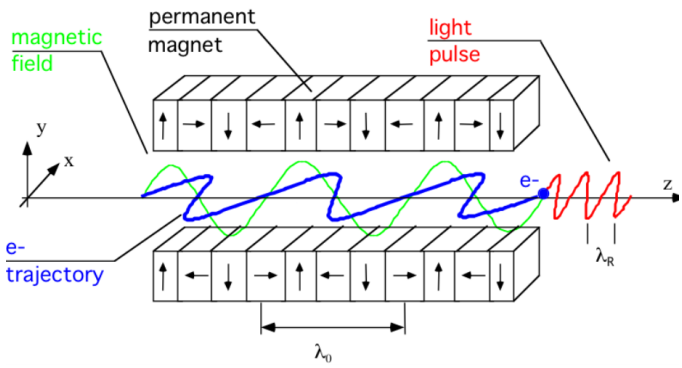

FIGURE B.1: Undulator sketch and coordinate system.

where B_r is the remanent field, M indicates the number of blocks per period, h each block height and g the gap size.

Undulator technology

A general undulator magnetic channel is made by several undulator modules whose total length covers the distance required to reach the saturation in the FEL. A single undulator (with no segmentation), tens of meters long, presents difficulties both from the point of view of the construction and of the electron beam transport: the magnetic field of the single undulator module is not able to impart a significant focusing effect to a high-energy electron beam passing through it, so that the undulator is almost equivalent to a long drift section, which will make the beam diverging during propagation. The undulator is thus divided in sections with some Focusing-Drift-Defocusing-Drift (FODO) cells with alternate gradient quadrupoles.

Fig. B.2 reports the peak magnetic field versus the gap to period ratio g/λ_w for various magnet types and for the different polarizations.
Depending on the magnet type, the state-of-the-art undulator technologies can be grouped in four main categories:

- The conventional Halbach schemes (Pure Permanent Magnets PPM)
- The Hybrid Permanent Magnets (HBM)
- The Super conducting (SC)
- The Electromagnetic Undulators

Electromagnetic undulators have limited performances in terms of magnetic field vs. gap to period ratio, and a peak magnetic field of 1 T is tipically desired.

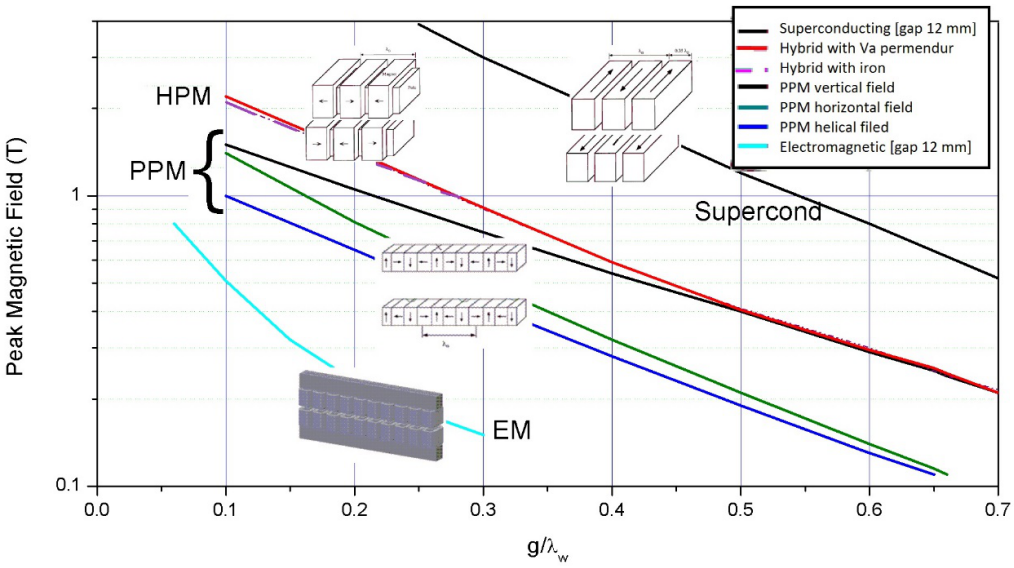

FIGURE B.2: Undulator technology status, from [8]. Peak magnetic field as function of the gap (g) to period (λ_w) ratio.

The superconducting technology seems to be the most efficient, permitting to produce fields in excess of 1 T also with g/λ_w of the order of 0.5. However, due to the complex cryogenic and mechanical structures, superconducting undulators are not used for routinely operations.
The Pure Permanent Magnet undulator technology is until now the most used in most FEL facilities: these magnets operate without a cooling system and can be used both in vacuum or in air, in which case a waveguide between the two magnet bars should allow the electrons to move under vacuum. The Cornell Synchrotron Undulator [209], with a period $\lambda_u = 2.4$ cm, is an example of in-vacuum undulator: these devices allow to vertically close the gaps without constraints and to reach a higher magnetic field than the in-air undulators, where the inter-magnet gap is limited by the dimension of the electron pipe (typically of several millimeters).

The Apple undulators, first designed for the Athos beam line of SwissFEL at PSI [210] (see Fig. B.3) are based on a modular structure made by four independent sectors with various shapes, for instance rectangular (Apple II) or triangular (Apple III). The modularity permits to shift the magnets longitudinally[2]. All versions in Fig. B.3 feature the room for a round vacuum chamber of 5-7 mm in the center, with a 2.5 mm space delimited by the magnets for magnetic measurements.

[2]Shifting two adjoining magnets with respect to each other allows to vary the field intensity, while shifting alternate magnets permits to change the polarization from linear to circular.

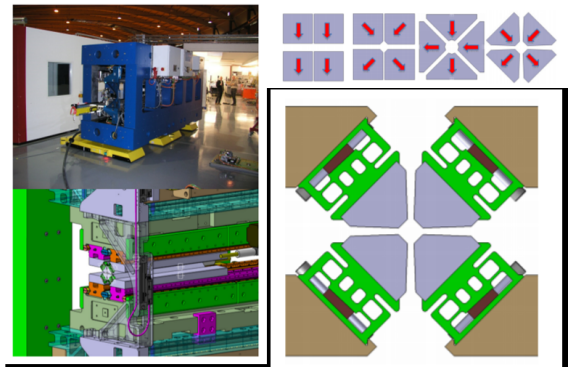

FIGURE B.3: Apple undulator scheme, undulator of the Athos line at SwissFEL [210]. Left: images of the structure. Right top: various possible magnet configurations: APPLE II, APPLE III, DELTA, proposed SwissFEL UE40. Right bottom: actual magnet scheme of the Radia model of UE40 magnet structure.

APPLE undulators are routinely used on synchrotrons and FELs since years; the most recent geometry is represented by the APPLE-X type, allowing to achieve higher magnetic field strengths.

The state of the art of short period undulators actually tested in FEL experiments is represented by the Kyma-ENEA [130] quadrefoil prototype at SPARC_LAB, with period of 1.4 cm and peak field of about 0.6 T. Apart from guaranteeing compactness of the structure and smaller transverse dimensions, the quadrefoil shape facilitates the positioning of a beam pipe, whose external and internal dimensions are respectively 5 and 4 mm, large enough to allow an easy control of the electron beam.
Other undulators of similar period ($\lambda_u = 1.5$ cm) were implemented at the Aramis line at the SwissFEL: they are arrays of planar undulators, made by a new type of permanent magnet, mounted in vacuum tanks with an inter-magnet gap of about 4.5 mm.

B.2.1 Electron Motion

The electron motion can be solved assuming the energy loss for radiative effects negligible, meaning $\gamma' = 0$. Under this assumption, the equation of motion for the electron becomes

$$\mathbf{p'} = m_e c\gamma\beta' = \frac{e}{c}\mathbf{v}x\mathbf{B}$$

where $\beta = \sqrt{1 - \frac{1}{\gamma^2}}$ represents the modulus of the normalized electron velocity. By expressing the cross product $(\mathbf{v}x\mathbf{B})$ one obtains the first derivatives of the

transverse velocities:

$$\beta_x' = \frac{e}{m_e c\gamma} B_0 \sin(k_u z)\beta_z$$
$$\beta_y' = 0$$
$$\beta_z' = -\frac{e}{m_e c\gamma} B_0 \sin(k_u z)\beta_x \ .$$

By integrating β_x', considering that $c\beta_z dt = dz$, the electron transverse motion is described by

$$\beta_x = \beta_{x,0} + \frac{e}{m_e c\gamma}\int_0^z B_0 \sin(k_u z)dz = \beta_{x,0} - \frac{eB_0\lambda_u}{2\pi m_e c^2\gamma}\left(\cos(k_u z) - 1\right)$$

and the coefficient of the second equality, namely

$$K = \frac{eB_0\lambda_u}{2\pi m_e c^2} \ , \tag{B.2}$$

represents the undulator strength (in literature it sometimes refers to its rms value $a_u = K/\sqrt{2}$. The initial condition is $\beta_{x,0} = \frac{K}{\gamma}$.
Using the relation $\beta^2 = \beta_x^2 + \beta_y^2 + \beta_z^2$, the longitudinal component of the velocity is $\beta_z \sim \bar{\beta_z} - \frac{K^2}{4\gamma^2}\cos(2k_u ct)$, with its average being $\bar{\beta_z} = 1 - \frac{1}{2\gamma^2}\left(1 + \frac{K^2}{2}\right)$.

The electron trajectory in the various directions is then found by integrating the corresponding velocity components:

$$x(t) = \frac{K}{\gamma k_u}\sin(k_u ct)$$
$$y(t) = 0$$
$$z(t) = \bar{\beta_z} ct - \frac{K^2}{8\gamma^2}\left(\frac{1}{k_u}\right)\sin(2k_u ct)$$

The electrons oscillate around the undulator axis, with an angle of deflection $\left(\frac{\beta_x}{\beta_z}\right)_{max} = \frac{K}{\gamma}$.

The time in which the radiation pulse and the electron beam travel the undulator length $L_u = N\lambda_u$ (N being the number of undulator periods) are given by $\delta t_p = L_u/c$ and $\delta t_e = L_u/c\bar{\beta_z}$ respectively. The arrival time difference at the end of the undulator, representing the pulse length, is $\delta t_e - \delta t_p = \frac{L_u}{c\beta_z}\frac{1}{2\gamma^2}\left(1 + \frac{K^2}{2}\right) = \frac{1}{c}N\frac{\lambda_u}{2\gamma^2}\left(1 + \frac{K^2}{2}\right)$. The pulse is a sequence of N optical cycles $\lambda_0 = \frac{\lambda_u}{2\gamma^2}\left(1 + \frac{K^2}{2}\right)$. The so-called slippage length of the radiation pulse with respect to the electron beam is approximately $L_{slip} = N\lambda_0$, and we define the resonant frequency as $\omega_0 = \omega_u \frac{2\gamma^2}{1+\frac{K^2}{2}}$, where $\omega_u = \frac{2\pi c}{\lambda_u}$.

The spectral brightness of the linear undulator

$$\frac{d}{d\Omega}\left(\frac{dI(\omega)}{d\omega}\right) \propto \left|\mathrm{sinc}\left(\pi N\left(\frac{\omega - n\omega_0}{\omega_0}\right)\right)\right|^2$$

is composed by a sequence of harmonics centered at $n\omega_0$ (n odd integer), with a width $\Delta\omega/\omega \propto \frac{1}{2N}$.

Electron Dynamics & Collective Effects

The emission from a single electron moving in the undulator needs to be extended to an electron beam, characterized by a certain longitudinal charge density ρ_{t_0}. The field produced by the whole beam can be expressed as $A_{beam}(t) = \int_{-\infty}^{\infty} A_{1e}(t-t_0)\rho_{t_0}dt_0$, where $A_{1e}(t-t_0)$ is the field generated by one electron. In Fourier space, it is simply given by the product between the Fourier transform of both the field A_{1e} and the charge density.

The temporal distribution of the electrons can be represented by a delta function $\rho_t = \sum_{i=1}^{n_e}\delta(t-t_i)$, where n_e is the number of electrons. The normalized electron distribution is $\bar{\rho}(t) = \frac{1}{n_e}\sum_{i=1}^{n_e}\delta(t-t_i)$, and

$$\bar{\rho}(\omega) = \int_{-\infty}^{\infty} e^{i\omega t}\left[\frac{1}{n_e}\sum_{i=1}^{n_e}\delta(t-t_i)\right] = \frac{1}{n_e}\sum_{i=1}^{n_e} e^{i\omega t_i}$$

in the frequency space. The power spectrum is $|P(\omega)|^2 = |A_{1e}|^2|\rho(\omega)|^2$: for uncorrelated electrons, $|\rho(\omega)|^2 \propto n_e$ and the power is proportional to the beam current (synchrotrons)[3]; for correlated electrons, $|\rho(\omega)|^2 \propto n_e^2$.

The electrons exchange energy with the co-propagating optical wave inside the undulator: this interaction depends on the phase difference between the electron transverse velocity and the electric field, $\Delta\gamma \propto \bar{\beta}_\perp \cdot \bar{E}$. The electron beam is first modulated in energy with a periodicity equal to that of the electromagnetic wave, and this energy modulation is converted into a density modulation by the dispersion $R_{56-und} = 2N\lambda_0$ in the undulator, two particles with non-equal momentum having a path length difference $\delta z = R_{56-und}\delta\gamma/\gamma$.

The dynamics of electrons inside the undulator in presence of a radiation field can be described by combining the Field equation derived from Maxwell's Equations and the Particle equation from Lorentz force equation. Let's start from the Lorentz force equation.

The electron momentum is $\bar{p} = m_e c\gamma\bar{\beta}$ and the Lorentz force is

$$\frac{d\bar{p}}{dt} = \bar{F} = e\left[\bar{E} + c\bar{\beta}\mathrm{x}(\bar{B}_u + \bar{B})\right]$$

[3] Regarding SASE FELs, emission is coherent within a spike and the emitted power is proportional to n_e^2.

where $\bar{\beta} = (\beta_x, 0, \beta_z)$, $\hat{n} = n_z$ are the electron beam velocity and direction of propagation respectively, while $\bar{E} = E_x$ and $\bar{B} = \frac{1}{c}(\bar{n}\mathrm{x}\bar{E})$ are the radiation magnetic and electric fields. By expressing the cross product $\bar{\beta}\mathrm{x}(\bar{n}\mathrm{x}\bar{E}) = (-\beta_z E_x, 0, \beta_x E_x)$, it simplifies to

$$\left(\frac{d\bar{p}}{dt}\right)_{\perp} = e\left[\bar{v}\mathrm{x}\bar{B_u} + (1-\beta_z)E_x\right] \ .$$

The derivative of the momentum is explicitly given by $\frac{d\bar{p}}{dt} = \frac{d}{dt}(m_e c\gamma\beta) = m_e c\left[\beta\frac{d}{dt}(\gamma) + \gamma\frac{d}{dt}\beta\right]$, and the first contribution can be expressed as $m_e c\frac{d}{dt}\gamma = e\bar{\beta}cdot\bar{E}$.

In the slowly varying envelope approximation (SVEA), the electric field $\bar{E}$ can be expressed as a slowly varying function η multiplied by a fast oscillating term:

$$\bar{E}(\bar{r},t) = Re\left[\eta(\bar{r},t)e^{k_r z-\omega t}\hat{x}\right]$$

where $\eta(\bar{r},t) = |\eta(\bar{r},t)|e^{i\Phi(\bar{r},t)}$, $\omega = k_r c$ and horizontal polarization has been assumed.
Using this expression for the electric field and the horizontal velocity component $\beta_x = -\frac{K}{\gamma(t)}\cos(k_u z(t))$, the energy variation is given by

$$\frac{d}{dt}\gamma(t) = \frac{\omega}{\gamma(t)}K_r(\bar{r},t)K\cos(k_u z(t))\cos(\psi(\bar{r},t)) \ .$$

where $\psi(\bar{r},t)) = k_r z - \omega t + \Phi(\bar{r},t)$ and $K_r(\bar{r},t) = \frac{e|\eta(\bar{r},t)|}{m_e c\omega}$, in analogy to the undulator strength K, is a parameter for the electric field of the electromagnetic wave of wavelength λ_r.
By explicitly writing $z(t)$, K_r and K, and expanding the exponential of oscillating functions in terms of Bessel functions $e^{-ix}\sin(y) = \sum_{-\infty}^{\infty} e^{-imy}J_m(x)$,

$$\frac{d}{dt}\gamma = \frac{\omega_r}{2\gamma}K_r(\bar{r},t)K\sum_{n=-\infty}^{\infty}(-1)^{\frac{n-1}{2}}\left[J_{\frac{n-1}{2}}(\xi) - J_{\frac{n+1}{2}}(\xi)\right]\cos\theta_n(t) + \Phi(\bar{r},t)$$

where n=1-2m, $\xi = \frac{1}{4}\frac{K^2}{1+\frac{K^2}{2}}$ and $\theta_n(t) = (nk_u + k_r)\bar{z}(t) - \omega t \simeq n\omega_u t\left(\frac{n\omega_0-\omega_r}{n\omega_0}\right)$ is the ponderomotive phase.

There is a resonance, with net exchange of energy, when the time derivative of θ_n is small, meaning $\nu_n(t) = n\omega_u\left(\frac{n\omega_0-\omega_r}{n\omega_0}\right) \sim 0$. For this reason, the term n=1 in the sum gives the main contribution, while the $n > 0$ terms account for coupling with higher order harmonics:

$$\frac{d}{dt}\nu(t) = \frac{\omega_r\omega_u}{\gamma^2(t)}K_r(\bar{r},t)K\sum_{n=1}^{\infty}(-1)^{\frac{n-1}{2}}\left[J_{\frac{n-1}{2}}(\xi) - J_{\frac{n+1}{2}}(\xi)\right]\cos\theta_n(t) + \Phi(\bar{r},t)$$

At the first resonance n=1, it follows

$$\frac{d}{dt}\nu(t) = \frac{d^2}{dt^2}\theta(t) = \frac{\omega\omega_u}{\gamma^2}K_r(\bar{r},t)K\left[J_0(\xi) - J_1(\xi)\right]\cos\theta_n(t) + \Phi(\bar{r},t) \ .$$

In the analysis of low gain FELs, the position along the undulator (time) is tipically scaled with the undulator length L_u, so that time is substituted by $\tau = \beta_z ct/L_u$.
Under this scaling, the equation for the evolution of the electron ponderomotive phase originally derived by Colson [4] is:

$$\frac{d^2}{d\tau^2}\theta(\tau) = \tilde{a}(\bar{r},\tau)\cos\theta(\tau) + \Phi(\bar{r},\tau) \ , \tag{B.3}$$

where $\tilde{a}(\bar{r},\tau) = \left(\frac{L_u}{\beta_z c}\right)^2 \frac{\omega\omega_u}{\gamma^2}K_r(\bar{r},t)K\left[J_0(\xi) - J_1(\xi)\right]$ is mainly linked to the radiation field. Electrons longitudinal motion is described by a pendulum-like equation: (ν,θ) are canonical variables of this equation, and are given by $\theta(\tau) = 2\pi N\left(\frac{\omega_0-\omega_r}{\omega_0}\right)$ and $\nu(\tau) = \frac{d}{d\tau}\theta(\tau)$ respectively. The Hamiltonian describing the phase space orbits is $H(\nu,\theta) = \frac{1}{2}\nu^2 - |\tilde{a}|\sin(\theta+\Phi)$. The radiation intensity I comes from its square modulus $|\tilde{a}(r,\tau)|^2 = \left(\frac{N^2}{\gamma^2}\frac{4\pi^2}{\lambda_r}\lambda_u K[JJ]\right)^2 |K_r(r,\tau)|^2$, where $[JJ] = [J_0(\xi) - J_1(\xi)]$ and $|K_r(r,\tau)|^2 \sim I(r,\tau)$.

Radiation field dynamics

The field equation is derived starting from the wave equation for the vector potential $\bar{A}(\bar{r},t) = \frac{1}{2\omega_r}\left[\eta(\bar{r},t)e^{i\phi_r(\bar{r},t)} + \eta^*(\bar{r},t)e^{-i\phi_r(\bar{r},t)}\right]$,written in terms of the complex slowly varying function $\eta(\bar{r},t)$ and the fast phase $\phi_r = k_r(z-ct)$, in presence of a transverse current $\bar{J}_\perp$

$$\left(\bar{\nabla}^2 - \frac{1}{c^2}\frac{d^2}{dt^2}\bar{A}(\bar{r},t)\right) = -\mu_o\bar{J}_\perp(rr,t) \ .$$

In the SVEA, assuming that the relative change of the electric field is small on the time scale of an optical cycle and on the spatial scale of the optical wavelength, i.e. $\frac{d}{dt}|\eta(\bar{r},t)| << |\eta(\bar{r},t)|\omega_r$ ($\frac{d}{dt}\psi_r(\bar{r},t) << \omega_r$) and $\frac{d}{dz}|\eta(\bar{r},t)| << |\eta(\bar{r},t)|k_r$ ($\frac{d}{dz}\psi_r(\bar{r},t) << k_r$), it is possible to discard the second derivatives of the slow function.

By averaging over a small volume V and over a small time interval $\lambda_u/\beta_z c$, the fast oscillating phase ϕ_r averages to zero while the slow functions are constant:

$$\bar{\nabla}_\perp^2\bar{\eta}(\bar{r},t) + 2ik_r\left|\frac{d}{dz}\bar{\eta}(\bar{r},t) + \frac{1}{c}\frac{d}{dt}\bar{\eta}(\bar{r},t)\right| = -2\omega_r\mu_o\frac{1}{V}\int dV\int_t^{t+\lambda_u/\beta_z c} dt'\bar{J}_\perp(\bar{r},t')e^{i\phi_r(\bar{r},t')} \ .$$

Regarding the source term, for a single electron $\bar{J}_\perp(\bar{r},t) = ec\beta_x(t)\delta(r-r_i)$ and for a beam of n_e electrons in the volume V $\bar{J}_\perp(\bar{r},t) = ec\beta_x(r_i)n_e\left[\frac{1}{n_e}\sum_i^{n_e}\delta(r-r_i)\right]$.

After some algebra, integrating over space and time, one gets the wave equation for an electron charge density n_e:

$$\left(\frac{-i}{2k_r}\bar{\nabla}_\perp^2 + \frac{d}{dz} + \frac{1}{c}\frac{d}{dt}\right)\bar{\eta}(\bar{r},t) = \frac{1}{2}ec^2\mu_0\frac{K}{\gamma}n_e(z-\beta_z ct)\frac{1}{n_e}\sum_{i=1}^{n_e}e^{-i\theta_i(t)}\left[J_0(\xi)-J_1(\xi)\right]$$

where the term $\frac{1}{n_e}\sum_{i=1}^{n_e}e^{-i\theta_i(t)} =< e^{-i\theta_i(t)} >_i$ corresponds to the average of θ over the "small" volume in which the slowly varying variables may be considered constant and uniform. Assuming no dependence on the transverse coordinates, the term containing the operator $\bar{\nabla}$ can be neglected. It is possible to express the equation for a current density $j(z-\beta_z ct) = ecn_e((z-\beta_z ct) = \frac{I_e(z-\beta_z ct}{\Sigma_e}$, namely

$$\left(\frac{d}{dz} + \frac{1}{c}\frac{d}{dt}\right)\eta(z,t) = -\frac{1}{2}Z_0 j(z-\beta_z ct)\frac{K}{\gamma}[JJ] < e^{-i\theta_i} >$$
$$\left(\frac{d}{dz} + \frac{1}{c}\frac{d}{dt}\right)K_r(z,t) = -\frac{\lambda_r}{I_A}j(z-\beta_z ct)\frac{K}{\gamma}[JJ] < e^{-i\theta_i} > \ ,$$

where $I_A = ec/r_0 = 17040$ A is the Alfvèn current, as function of the electron classical radius $r_0 = \frac{e^2/m_e c^2}{4\pi\epsilon_0}$, and $Z_0 = \sqrt{\mu_0/\epsilon_0} = 377\Omega$ is the vacuum impedance.

The e-beam current in the source term drifts with velocity $\beta_z c$ while the light propagates in vacuum at c: the two variables z and t are strongly correlated, this correlation being reduced by scaling the coordinates in a frame moving with velocity $\beta_z c$. In addition, even if the fields are expressed through the dimensionless parameters K_r and K, distances are still dimensional in the above equations. The following coordinates transformation allows to derive dimensionless equations:

$$t -> u = \beta_z ct/L_1$$
$$z -> \xi = (z-\beta_z ct)/L_2$$

where $L_{1,2}$ have to be defined. The wave equation in the new coordinate system, in terms of K_r and the dimensionless field $a(u,\xi)$, reads

$$L_1\left[\frac{1}{L_2}\frac{1}{2\gamma^2}(1+\frac{K^2}{2})\frac{d}{d\xi} + \frac{1}{L_1}\frac{d}{du}\right]K_r(u,\xi) = -\frac{\lambda_r}{I_A}j(\xi)\frac{K}{\gamma}[JJ]L_1 < e^{-i\theta_i} >$$
$$\left[\frac{L_1}{L_2}\frac{\lambda_0}{\lambda_u}\frac{d}{d\xi} + \frac{d}{du}\right]a(u,\xi) = -2\pi^2\frac{1}{I_A}j(\xi)\frac{K^2}{\gamma^3}\frac{L_1^3}{\lambda_u}[JJ]^2 < e^{-i\theta_i} >_i \ .$$

By introducing a normalized current density $j_n(\xi)$ such that $j(\xi) = \frac{I_{peak}}{\Sigma_e} j_n(\xi)$, it is possible to rewrite the second wave equation as

$$\left[\frac{L_1}{L_2}\frac{\lambda_0}{\lambda_u}\frac{d}{d\xi} + \frac{d}{du}\right] a(u,\xi) = -R j_n(\xi) < e^{-i\theta_i} >_i \quad , \tag{B.4}$$

where $R = \frac{2\pi^2}{\gamma^3}\left[\frac{I_{peak}}{I_A \Sigma_e}\right](K[JJ]\lambda_u)^2 L_1^3$.
In the new coordinates, the ponderomotive phase and its derivative are respectively given by

$$\theta(u,\xi) = (k_u + k_r)L_2\xi + k_u L_1 u\left[\frac{\omega_0 - \omega_r}{\omega_0}\right]$$
$$\nu(u) = \frac{d}{du}\theta(u,\xi) = k_u L_1\left[\frac{\omega_0 - \omega_r}{\omega_0}\right] \quad ,$$

and assuming $\beta_z \simeq 1$, the pendulum-like equation becomes

$$\frac{d^2}{du^2}\theta(u) = 2a(u,\xi)\cos(\theta(u) + \Phi(u,\xi)) \ . \tag{B.5}$$

In literature, the dimensionless field is often indicated by $\tilde{a} = 2a$.

The particle and field equations B.4-B.5 are two coupled equations that govern the energy exchange between the electron current and the field: the longitudinal motion of charges in presence of an radiation wave is described by a pendulum like equation, while the wave equation follows from the Maxwell equations in the SVEA, averaged on the fast wiggling

B.2.2 FEL integral equation

The electron beam temporal distribution $\rho_\xi = \frac{1}{n_e}\sum_{i=1}^{n_e}\delta(\xi - \xi_i)$ can be equally written as a distribution over the phases $\rho_\theta = \frac{1}{n_e}\sum_{i=1}^{n_e}\delta(\theta - \theta_i)$. The bunching factors $b_n(\tau,\xi) = \frac{1}{\lambda}\int_\xi^{\xi+\lambda} d\xi' \rho_e(\xi') e^{-in\theta_i(\tau)}$ are the result of the the density modulation of the electrons. For a periodic distribution $\rho_e(\xi)$ of period λ, the coefficient b_n is the nth Fourier coefficient of the distribution. the first Fourier component is

$$b_1 = \rho_1(\omega) = \int_0^{2\pi}\rho(\theta)e^{-i\theta}d\theta = \frac{1}{n_e}\sum_{i=1}^{n_e} e^{-i\theta_i(t)} = < e^{-i\theta_i(t)} >_i \ .$$

There are different regimes of operation: here the high-gain, low field regime is treated, in the simplifying assumption of a transversally and longitudinally uniform field $a = a(\tau)$.

High gain, low field

In the limit of low field $a << 1$, the start-up dynamics can be studied by expanding the pendulum equation (B.8) to the lowest order in τ:

$$\theta(\tau) = \theta(0) + \nu(0)\tau + \delta\theta(\tau) \text{ , with } \frac{d^2}{d\tau^2}\delta\theta(\tau) = 2a(\tau,\xi)e^{i\theta(\tau)} + cc \text{ .}$$

Integrating twice with initial conditions $d/du(\delta\theta)|_{u=0} = (\delta\theta)|_{u=0} = 0$, at the lowest order in a,

$$\frac{d}{du}a(u) = -R\left\langle e^{-i(\theta_{0l}+\nu_{0l}u)}\left\{1 - i\int_0^u \left\{(u-u')a(u')e^{i(\theta_{0l}+\nu_{0l}u')} + cc\right\}du'\right\}\right\rangle$$

where $l = 1, ..., n_e$, $\theta(0) = \theta_0$ and $\nu(0) = \nu_0$. For a monoenergetic beam ($\nu(0l) = \nu(0)$), by changing variable to $u'' = u - u'$

$$\begin{aligned}\frac{d}{du}a(u) = &- R\left\langle e^{-i(\theta_0+\nu_0 u)}\right\rangle - iR\left\langle\int_u^0 u''a(u-u'')e^{-i\nu_0 u''}du''\right\rangle \\ &+ iR\left\langle e^{-2i(\theta_0+\nu_0 u)}\int_u^0 u''a^*(u-u'')e^{i\nu_0 u''}du''\right\rangle \text{ ,}\end{aligned} \tag{B.6}$$

where $b_1(u) = \left\langle e^{-i(\theta_0+\nu_0 u)}\right\rangle$ and $b_2(u) = \left\langle e^{-2i(\theta_0+\nu_0 u)}\right\rangle$. The FEL integral equation starting from a pre-modulated beam reads

$$\begin{aligned}\frac{d}{du}a(u) = &- Rb_1(0)e^{-i\nu_0 u} + iR\int_0^u u'a(u-u')e^{-i\nu_0 u'}du' \\ &- iRb_2(0)e^{-2i\nu_0 u}\int_0^u u'a^*(u-u')e^{i\nu_0 u'}du' \text{ .}\end{aligned} \tag{B.7}$$

The first term $\propto b_1$ stands for the emission from shot noise or a pre-bunched beam, the second term (feedback term), where the derivative of the field is proportional to the input field, accounts for the exponential growth, and the third one $\propto a, b_2$ vanishes when starting from a uniform beam at start-up.

Small gain, low field

In this low-gain regime, the position along the undulator is tipically scaled with the undulator length, so that $L_1 = L_u = N\lambda_u$ and $L_2 = 1$ n Eq. (B.4). In terms of the small gain coefficient $g_0 = 2\pi\frac{N^3}{\gamma^3}\left[\frac{I_{peak}}{I_A\Sigma_e}\right](K[JJ]\lambda_u)^2$, $R = \pi g_0$ and,

by setting $u = \tau = z/N\lambda_u$, the equations become

$$\left[N\lambda_0 \frac{d}{d\xi} + \frac{d}{d\tau}\right] a(\tau,\xi) = -\pi g_0 j_n(\xi) < e^{-i\theta_i} >_i \tag{B.8}$$

$$\frac{d^2}{d\tau^2}\theta(\tau) = \left(\frac{L_1}{\beta_z c}\right)^2 \frac{1}{\gamma^2(\tau)}(\omega_r K_r)(\omega_u K)[JJ]\cos(\theta(\tau)+\Phi(\tau)) \tag{B.9}$$

$$= 2a(\tau,\xi)\cos(\theta(\tau)+\Phi(\tau,\xi)) \ . \tag{B.10}$$

The integral equation, with $\tilde{a} = 2a$, then reads

$$\frac{d}{d\tau}\tilde{a}(\tau) = -2\pi g_0 b_1(0) e^{-i\nu_0\tau} + i\pi g_0 \int_0^\tau \tau' \tilde{a}(\tau-\tau') e^{-i\nu_0\tau'} d\tau'$$
$$- i\pi g_0 b_2(0) e^{-2i\nu_0\tau} \int_0^\tau \tau' \tilde{a}^*(\tau-\tau') e^{i\nu_0\tau'} d\tau' \ .$$

By neglecting the terms proportional to the input field in the previous, the integral equation for the spontaneous emission is $\frac{d}{d\tau}\tilde{a}(u) = -2\pi g_0 b_1(0) e^{-i\nu_0\tau}$, which is easily integrated to give $\tilde{a}(u) = -2\pi g_0 b_1(0)\frac{1}{-i\nu_0}\{e^{-i\nu_0\tau} - 1\}$. At the end of the undulator $\tau = 1$ and

$$\tilde{a}(1) = -2\pi g_0 b_1(0) e^{-i\nu_0/2} \frac{\sin(\nu_0/2)}{\nu_0/2} \ .$$

The spontaneous emission is proportional to $|a|^2$ and therefore to the $sinc^2$ function of the spectral shape of the undulator radiation. For a beam of randomly distributed point charges, the bunching factor $b_1 \propto \frac{1}{\sqrt{n_e}} \propto \frac{1}{\sqrt{I}}$, and it is normalised to one in the expression. For this reason, even if $g_0 \propto I$, the undulator radiation power is linearly proportional to the beam current I.

Starting from an input field in the low gain approximation, i.e. $B_1 = b_2 = 0$ at $\tau = 0$ with the field $\tilde{a}$ only weakly dependent on τ, one obtains
$\tilde{a}(\tau) = \tilde{a}_0 + i\pi g_0 \tilde{a}$
$int_0^\tau \int_0^{\tau'} \tau'' e^{-i\nu_0\tau''} d\tau'' d\tau'$.
Integrating both integrals in the previous expression by parts:

$$\tilde{a}(\tau) = \tilde{a}_0 + i\pi g_0 \tilde{a}' \left\{ \frac{2i}{\nu_0^3}(e^{-i\nu_0\tau - 1}) - \frac{\tau}{\nu_0^2}(e^{-i\nu_0\tau+1}) \right\} \ .$$

The small signal gain is defined as

$$G = \frac{|a(1)|^2 - |a(0)|^2}{|a(0)|^2} \ .$$

Assuming $a(0) = 1$, $G = \left|1 + i\pi g_0 \tilde{a}' \left\{ \frac{2i}{\nu_0^3}(e^{-i\nu_0\tau-1}) - \frac{\tau}{\nu_0^2}(e^{-i\nu_0\tau+1}) \right\}\right|^2 - 1$. In the weak coupling approximation $g_0 << 1$, and setting $\tau = 1$, it follows the

Madey theorem

$$G \simeq 2\pi g_0 \sin(\frac{\nu_0}{2}) \left[\frac{4}{\nu_0^3} \sin(\frac{\nu_0}{2}) - \frac{2}{\nu_0^2} \cos(\frac{\nu_0}{2}) \right] = .\pi g_0 \frac{d}{d\nu_0} \left[\left(\frac{\sin(\frac{\nu_0}{2})}{\frac{\nu_0}{2}} \right)^2 \right] ,$$

according to which the gain is proportional to the derivative of the spontaneous emission distribution, with $\nu_0 = 2\pi N(\frac{\omega_0 - \omega_r}{\omega_0})$. Oscillators operate in this low gain regime.

Small gain, strong field

A strong field initiating the FEL emission helps in reaching saturation. In order to achieve energy growth until saturation, $\delta\nu_0 < 2\pi$

High gain, low field

Starting from the wave equation (B.4), we now consider R=1 so that L_1 now reduces to $L_1 = \frac{\lambda_u}{4\pi\rho}$, with

$$\rho = \frac{1}{4\pi} \left[\frac{2\pi^2}{\gamma^3} (\lambda_u K[JJ])^2 \frac{I_{peak}}{\Sigma_e I_A} \right]^{1/3} .$$

Being $L_2 = \frac{\lambda_0}{4\pi\rho}$, the wave equation reads

$$\left[\frac{d}{d\xi} + \frac{d}{du} \right] a(u,\xi) = -j_n(\xi) < e^{-i\theta_i} >_i$$

and is still coupled to the electron dynamics

$$\frac{d^2}{du^2}\theta(u) = 2|a(u)| \cos(\theta(u) + \Phi(u,\xi)) ,$$

where $\theta_n(u) = \frac{nu}{2\rho} \left(\frac{n\omega_0 - \omega_r}{n\omega_0} \right)$ and $\nu_n(u) = \frac{d}{du}\theta_n(u) = \frac{n}{2\rho} \left(\frac{n\omega_0 - \omega_r}{n\omega_0} \right)$.

The laser power can be derived from the dimensionless field definition and the relation with the Poynting vector:

$$|a(u,\xi)|^2 = \frac{4\pi^4}{\gamma^4} \left[\frac{1}{4\pi\rho} \right]^4 \frac{(\lambda_u K[JJ])^2}{\lambda_r^2} |K_r(u,\xi)^2|$$

where $|K_r(u,\xi)|^2 = 8\frac{\lambda_r^2}{Z_0 I_A^2} I(u,\xi)$. Inverting with respect to the laser intensity, one finds

$$I(u,\xi) = m_e c^2/e |a(u,\xi)|^2 \left[\frac{I_{peak}}{\Sigma_e} \right] [\rho\gamma] .$$

The power carried by the electron beam and the laser intensity are respectively

$$P_{beam} = m_e c^2 \gamma I_{peak}/e$$
$$I(u,\xi) = |a(u,\xi)|^2 \rho \frac{P_{beam}}{\Sigma_e} \ .$$

Assuming a uniform beam and R=1, the FEL integral equation (B.6) depends only on ν_0

$$\frac{d}{du}\tilde{a}(u) = i\int_0^u u'\tilde{a}(u-u')e^{-i\nu_0 u'}du' \ .$$

After some algebra, the second derivative leads to a third order equation

$$\frac{\partial^3}{du^3}a(u) + 2i\nu_0\frac{d^2}{du^2}a(u) - \nu_0^2\frac{d}{du}a(u) - ia(u) = 0 \ .$$

The associated characteristic polynomial is $x^3 + 2i\nu_0 x^2 - \nu_0^2 x - i = 0$ and the solution is given by the linear combination of its three roots:

$$a(u) = \sum_{i=1}^{3}\alpha_i exp(r_i u) \ ,$$

where the α_i are set by the initial conditions.

When $\nu_0 = 0$, the associated polynomial is simply $x^3 = i$, with the following roots $(-i, \frac{1}{2}/(\sqrt{3}+i), \frac{1}{2}/(-\sqrt{3}+i)$.
The solution is therefore $a(u)\frac{a_0}{3}\left\{e^{-iu} + e^{\frac{1}{2}/(\sqrt{3}+i)u} + e^{\frac{1}{2}/(-\sqrt{3}+i)u}\right\}$: the only growing root is $a(u)\frac{a_0}{3}e^{\frac{1}{2}/(\sqrt{3}+i)u}$, which corresponds to a field power dependent on u.
Expressing u in terms of z, i.e. $u = \frac{z}{\sqrt{3}L_g}$ with $L_g = \frac{\lambda_u}{4\pi\sqrt{3}\rho}$, the power is approximately $P(z) \propto \frac{1}{9}P_0 e^{z/L_g}$.

The previous equation is valid in the so called 1-d "cold" beam limit, i.e. mono-energetic and with very low emittances. This simplified one-dimensional model of the FEL does not consider the transverse motion of the electrons nor the limited size of the radiation field. A dispersion in the beam energy causes a dispersion in the resonance condition for individual electrons, thus leading to an inhomogeneous broadening of the FEL resonance condition

$$\omega_0 = \frac{2\gamma^2\omega_u}{(1 + \frac{K(x,y)^2}{2} + \gamma^2\theta^2)} \ .$$

A similar effect is associated with the electron beam transverse phase space distribution: the resonant condition depends on the transverse position, via the undulator K parameter, and on the orbit angle with respect to the undulator

axis. A dispersion in angle and transverse position induces therefore a dispersion in the wavelength of emission. The natural diffraction of the radiation field affects the FEL gain as well, setting a lower limit to the transverse size of the optical mode. The inclusion of all these factors lead to a reduction of the gain, a growth of the gain length, and a reduction of the final output power.

These effects have been extensively studied boh numerically and analytically. They cannot be studied with the 1D FEL theory but relies on fits to simulations. The rms radius of a focused electron beam is determined by its normalized emittance $\epsilon_n = \gamma\epsilon_x$ (with the geometric emittance $\epsilon_g = \epsilon_x$).

$$\bar{\beta} = \frac{\sigma_{beam}^2}{\epsilon_g} \tag{B.11}$$

where $\bar{\beta}$ is the transverse Twiss coefficient. If $j = 1, .., N$ is the index representing the single electrons in the beam, one has

$$\begin{aligned} \sigma_x^2 &= \langle x^2 \rangle = \frac{1}{N}\sum_j x_j^2 \rightarrow \text{ Beam rms size} \\ \sigma_{\dot{x}}^2 &= \langle \dot{x}^2 \rangle = \frac{1}{N}\sum_j \dot{x}_j^2 \rightarrow \text{ Beam rms divergence} \\ \langle x\dot{x} \rangle &= \frac{1}{N}\sum_j x_j\dot{x}_j \rightarrow \text{ Correlation coefficient} \end{aligned} \tag{B.12}$$

and the same for y. The beam rms emittance is defined as

$$\epsilon_x = \sqrt{\langle x^2 \rangle \langle \dot{x}^2 \rangle - \langle x\dot{x} \rangle^2} \tag{B.13}$$

and it is not a constant of motion when the beam gets accelerated. For this reason, one tipically introduces the normalized emittance

$$\epsilon_{n,x} = \beta\gamma\epsilon_x \approx \gamma\epsilon_x \ . \tag{B.14}$$

Optical diffraction is measured by the radiation Rayleigh length z_R. For a radiation beam of wavelength λ and r.m.s. size equal to the projected electron beam r.m.s. transverse size σ_{beam}, it is given by the square of the electron beam's rms radius in the undulator divided by the photon beam's emittance $\lambda/4\pi$

$$z_R = \frac{4\pi\sigma_{beam}^2}{\lambda} \ . \tag{B.15}$$

In order to neglect diffraction 3D effecs, the gain length must be shorter than the Rayleigh length

$$L_g \leq z_R \tag{B.16}$$

Betatron motion slows down the electrons and spreads their velocities, thus leading to a violation of the resonance condition. For emittance 3D effects to be small, the electron beam's geometric emittance must be smaller than the photon beam emittance

$$\epsilon_g < \frac{\bar{\beta}}{2\sqrt{2}\gamma_R^2}\rho \rightarrow \epsilon_n \leq \frac{\gamma\lambda}{4\pi} \tag{B.17}$$

There exists another constraint on the electron beam's energy spread: since particles far from resonance have low gain, electrons must maintain the same axial velocity during the coherence length $l_c = N_c\lambda$, where $N_c = 1/4\pi\rho$ is the number of wavelengths in a coherence length (equal to $\sqrt{3}$ times the number of periods in one gain length).
In order to neglect 3D effects due to energy spread, the relative rms energy spread must be less than ρ

$$\frac{\sigma_\gamma}{\gamma} \leq \rho \sim \frac{1}{4\pi N_c} \tag{B.18}$$

A correction taking into account these three-dimensional effects, which is widely used in the design of FEL amplifiers, is provided by the Ming Xie relations [9]. Starting from the 1D values of the gain length $L_{g,1d} =$ and the final output power $P_{F,1d} =$, the correction is of the following form

$$L_{g,3d} = \frac{L_{g,1d}}{\chi}$$
$$P_{F,3d} = \chi^2 P_{F,1d}$$

where χ is the correction factor, which depends on three parameters accounting for diffraction effects, emittance (beam divergence) effects, and energy spread related effects

$$\begin{cases} \eta_d = \frac{L_{g,1d}}{z_R} & \text{Diffraction} \\ \eta_\epsilon = \frac{L_{g,1d}}{\bar{\beta}}\frac{4\pi\epsilon_g}{\lambda} & \text{Emittance} \\ \eta_\gamma = \frac{4\pi L_{g,1d}}{\lambda_w}\frac{\sigma_\gamma}{\gamma} & \text{Energy spread} \end{cases} \tag{B.19}$$

Ming Xie parameters should be less than 1 to minimize 3D effects. The gain and power deterioration due to non ideal electron beam qualities is described by the correction factor

$$\chi(\eta_d, \eta_\epsilon, \eta_\gamma) = \left(1 + \sum_{n=1}^{7} a_n \eta_d^{\alpha_n} \eta_\epsilon^{\delta_n} \eta_\gamma^{\alpha_n}\right)^{-1}$$

with fitted coefficients, which are not reported here.

The general solution to the FEL integral equation is $a(u)|_{u=0} = \sum_{i=1}^{3} \alpha_i = a_0$ with $\frac{d}{du}a(u) = \sum_{i=1}^{3} \alpha_i r_i = 0$ and $\frac{d^2}{du^2}a(u) = \sum_{i=1}^{3} \alpha_i^3(r_i) = 0$.

High gain, strong field

As in the low gain case, the spectral bandwidth is linked to the energy detuning via $\frac{\delta\omega}{\omega} = 2\frac{\delta\gamma}{\gamma}$ and the FEL power is $P_L = \frac{1}{2}\frac{\delta\omega}{\omega}P_{beam}$. The efficiency is therefore related with the gain bandwidth. - figura slide 27 lez7

If radiation slippage is neglected, there is no energy transfer from a given time interval to another and $P_{tot} = P_e + P_{FEL} = \text{const}$. Only a small fraction of the beam power P_e gets converted into laser power. The ratio

$$\eta = \frac{P_{FEL}}{P_e} = \frac{P_{E_f} - P_{E_0}}{P_e} = \frac{\delta P_e}{P_e} = \frac{\delta\gamma}{\gamma}$$

defines the efficiency of the process.

The saturation process can be efficiently described by looking at a FEL source driven by a single electron. At start-up, the field is generated at the phase and frequency characterised by the highest gain: the frequency is approximately given by the resonant frequency of the undulator, while the phase will depend on the start-up shot noise and, w.r.t. the field, it will be the phase of maximum gain $\phi_0 = 3\pi/2$. Saturation is an interferential process, the gain being zero when the bunched beam shifts in phase by $\delta\phi_0 \approx \pi/2$ with respect to the phase without energy loss ϕ_0 and becoming negative if $\delta\phi_0 > \pi/2$.

The dispersion in the undulator induces a shift of the position of the bunching with respect to radiation proportional to the position along the undulator: after N undulator periods, we have $\delta z = R_{56}\frac{\delta\gamma}{\gamma} = 2N\lambda_0\frac{\delta\gamma}{\gamma}$. The field power grows exponentially as $P(z, z_0) = P_0 e^{\frac{z-z_0}{L_g}}$, where P_0 is the power at some position z_0 along the undulator and L_g is the gain length. According to the energy conservation,

$$\frac{\delta\gamma(z)}{\gamma} = \frac{P_0 e^{\frac{z-z_0}{L_g}}}{P_e}$$

so that the energy detuning induces a phase shift

$$\delta z(\Delta z, z_0) = 2(\frac{\lambda_0}{\lambda_u})\int_{z_0}^{z_0+\Delta z} \frac{P_0 e^{\frac{z'-z_0}{L_g}}}{P_e} dz' = 2(\frac{\lambda_0}{\lambda_u})\frac{P_0}{P_e}L_g(e^{\frac{\Delta z}{L_g}} - 1) \ .$$

We indicate as z_{sat} the position where the gain goes to zero because of the phase shift: $z_{sat} = z_0 + \Delta z$, with $\delta z(\Delta z, z_0) \simeq \frac{\lambda_0}{4}$. Inverting the last relation for δz we find

$$\frac{P_0}{P_e} = \frac{1}{8}\frac{\lambda_u}{L_g}(e^{\frac{\Delta z}{L_g}} - 1) \ .$$

The effective energy loss occurs in the last few gain lengths, and about 60% of the energy is emitted in the last gain length, where a substantial phase shift due to the energy loss occurs. Let's then consider the approximation $\Delta z = L_g$: by using the definition of L_g, $\frac{P_0}{P_e} = \frac{\pi}{2}\sqrt{3}\rho(e^{\frac{\Delta z}{L_g}} - 1)^{-1}$ and the laser power at one gain length from saturation amounts to

$$P_L \simeq P_0 = \frac{\frac{\pi}{2}\sqrt{3}\rho}{e-1} P_e \sim 1.6\rho P_e \ .$$

In the high gain, low field regime (R=1), the FEL integral equation starting from a pre-bunched beam ($b_1 \neq 0$ with $|a(0)| = 0$) reduces to

$$\frac{\partial}{\partial u} a(u) = -\left\langle e^{-i(\theta_0 + \nu_0 u)} \right\rangle$$

from which $a(u) = -b_1 \frac{1-e^{-i\nu_0 u}}{\nu_0} \rightarrow |a_{coh}(u)|^2 = |b_1|^2 u^2$ in the limit $\nu_0 = 0$. In the first part of the undulator, coherent spontaneous emission takes place, where the radiated power grows quadratically with the position along the undulator

$$\rightarrow P_{coh}(z) = |a|^2 \rho P_{beam} = \frac{1}{3}\rho |b_1|^2 P_{beam} \left(\frac{z}{L_g}\right)^2 \ .$$

After some distance in the undulator, when the field $a(\nu_0) \neq 0$, the homogeneous term of Eq. (B.6) becomes larger than the source term, i.e. $|-b_1 e^{-i\nu_0 u}| < |i\int_0^u du'' u'' e^{-i\nu_0 u''} a(u-u'')$, and the growth will turn from quadratic into exponential. This occurs at $u = 2^{1/3} \sim 1$, when $|a_{coh}(u)|^2 = 2^{2/3}|b_1|^2$: the transition between these two growth trends corresponds to a threshold distance $z_{th} \sim 2^{1/3}\sqrt{3} L_g \sim 2L_g$ and a power level $P_{th} = 2^{2/3}\rho|b_1|^2 P_{beam} \sim \rho |b_1|^2 P_{beam}$.

It is possible to define an equivalent input power associated to a given beam prebunching, by impose that the power associated to the exponentially growing root starting from a virtual seed of power P_{eq} (or field a_{eq}) equals the power at the threshold from a prebunched beam

$$\frac{|a_{eq}|^2}{9} e^{2^{1/3}\sqrt{3}} = 2^{2/3}|b_1|^2 \rightarrow |a_{eq}|^2 \sim 1.6|b_1|^2 \ .$$

The intensity required to ensure a growth equivalent to the one induced by an existing pre-bunching is therefore

$$I_{eq} = |a_{eq}|^2 \rho \frac{P_e}{\Sigma_e} \sim 1.6\rho |b_1|^2 \frac{P_e}{\Sigma_e} \ ,$$

so that $\frac{P_F}{P_{eq}} = \frac{1}{|b_1|^2} = n_e$.

The number of electrons in a length corresponding to a single optical wavelength λ is $N_{e,1\lambda} = \frac{I_{peak}\lambda_0}{ec} = 2I_{peak}[A]\lambda_0[A]$. In order to account for the

interference of the fields emitted by electrons separated by more than one wavelength, a characteristic length Δ and a distribution of correlated electrons $\rho_{corr}(\xi) = e^{-\frac{\xi^2}{2\Delta^2}}$ are introduced, from which

$$n_e = \frac{I_{peak}}{ec}\int_{-\infty}^{\infty} d\xi \rho_{corr}(\xi) = \sqrt{2\pi}\frac{I_{peak}}{ec}\Delta \ .$$

In general a random, infinitely extended, point-like electron distribution has a white-noise spectral distribution, but only the spectral components in the FEL gain bandwidth will be then amplified up to saturation. For this reason, the electrons in an interval of length $\Delta = c\sigma_\tau \sim c/\sigma_\omega$ are considered, where σ_ω is the bandwidth of the frequency spectrum that will reach saturation, or the end of the amplifying regions, i.e. the gain bandwidth. The number of correlated electrons is

$$n_e \sim \sqrt{2\pi}\frac{N_{e,1\lambda}}{\lambda_0}\Delta = \frac{1}{\sqrt{2\pi}}N_{e,1\lambda}\frac{\sqrt{2z/L_g}}{6\rho}$$

and the bunching factor is a function of the position z along the undulator

$$|b_1| = \sqrt{\frac{6\sqrt{2\pi}\rho}{N_{e,1\lambda}\sqrt{2z/L_g}}} \ .$$

The "effective" shot-noise depends on the length of the amplifying region. The saturation length L_{sat} can be defined as the distance along the undulator such that $\frac{1}{9}P_{eq}e^{L_{sat}/L_g} = P_{sat}$. An implicit equation in $x = L_{sat}/L_g$ follows:

$$\frac{L_{sat}}{L_g} \sim ln\left(\frac{9P_{sat}}{P_{eq}}\right) = ln\left(9\frac{N_{e,1\lambda}\sqrt{L_{sat}/L_g}}{6\sqrt{\pi}\rho}\right) \ .$$

By setting $a = ln\left(\frac{N_{e,1\lambda}}{\rho}\right)$, the equation reads

$$x \approx a + \frac{1}{2}ln(x) \rightarrow x_n = a + \frac{1}{2}ln(a + \frac{1}{2}ln(a + ...)) \ .$$

The solution x_n converges rapidly, because ln is a very slowly growing function, so that $x \approx a + \frac{1}{2}ln(a)$, i.e. tipically $L_{sat}/L_g = 17 - 20$. The gain bandwidth is a function of the square root of the amplification length. In a SASE FEL starting from shot noise and amplifying radiation up to saturation, we have $z/L_g \approx 18$ and

$$\frac{\sigma_\omega(z)}{\omega} = \frac{6\rho}{\sqrt{2z/L_g}} \approx \rho \ .$$

The coherence length is $L_c = \frac{c}{2\omega_0\sigma_{\Delta\omega/\omega}} = \frac{\lambda_0}{4\pi\rho}$.

Appendix C

Plasma acceleration

This Appendix deals with the basic concepts and implementation of plasma acceleration.

The worldwide interest in plasma-based electron accelerators is driven by the need of a new technology to overcome the multi-TeV barrier for particle accelerators and the desire to make electron-beam and associated radiation facilities (FELs, synchrotrons, etc.) available to a larger user base [116]. For this reason, the next generation of light sources should feature a size and cost reduction for the facility of at least one order of magnitude.

Plasma acceleration is a technique for accelerating charged particles using the large electric fields generated in a plasma. In this case, the accelerating medium is the plasma itself, which can provide accelerating field gradients of some GeV/m compared to the maximum 100 MeV/m sustainable in RF-based machines [117].

Plasma accelerators can be realised with two main techniques: the drive beam propagating through the plasma and inducing electron density oscillations can be either a laser pulse in the laser-driven wakefield acceleration (LWFA) or a relativistic electron beam in the particle-driven wakefield acceleration (PWFA) [119, 120].
The excited wakefields feature high field strengths

$$E_0[V/m] \approx 96\sqrt{n_0[cm^{-3}]}...$$

with a characteristic plasma wavelength

$$\lambda_p = \frac{2\pi c}{\omega_p} = \frac{2\pi c}{e}\sqrt{\frac{m\epsilon_0}{n_0}} \approx 3.3 \times 10^4 \sqrt{n_0[cm^{-3}]}$$

where n_0 s the background plasma density, ϵ_0 the vacuum permittivity, c the speed of light in vacuum and e,m the electron charge and mass, respectively [116].

A short electron beam, termed the witness beam, placed into this plasma wakefield with the correct phase, can be accelerated and focused to reach GeV energies over centimetre to metre distances.

Two different mechanisms, the self-injection and the external injection, are employed to place the witness beam into the plasma wakefield. In the self-injection case, the witness beam is directly generated from a fraction of electrons of the background plasma, which gets trapped co-propagating inside the accelerating wakefield: the plasma target acts primarily as an injector creating the electron beam, and can also significantly accelerate it. The witness beam is instead pre-generated in case of external injection, and pre-accelerated in an RF-injector or a plasma injector before being injected into the plasma target where it gains energy. Both techniques offer a way to build high-performance particle accelerators of much smaller size than conventional devices: current experimental devices show accelerating gradients several orders of magnitude greater than conventional particle accelerators over very short distances (1 GeV/m [3] vs 0.1 GeV/m for an RF accelerator). Therefore, plasma accelerators have immense promise for innovation of affordable and compact accelerators for various applications ranging from high energy physics to medical and industrial applications.

C.1 Laser-Driven Wakefield Acceleration (LWFA)

In laser-driven plasma acceleration, the plasma wakefield is driven by a TW-scale, fs-duration laser pulse. Both the plasma density and the laser parameters, such as the normalised vector potential A_0, determine the properties of the wakefield.

The value of the laser normalised vector potential a_0 individuates three different operation regimes: a linear regime, in which $a_0^2 << 1$, a quasi-linear regime, in which $a_0^2 \sim 1$ and a non-linear one ($a_0^2 >> 1$). The accelerating field gradient increases with higher nonlinearity, in which case the acceleration process also becomes less stable: for this reason, the linear and quasi-linear regimes are more suitable for plasma acceleration stages.

The acceleration length is another factor limiting the maximum electron beam energy gain, and is mainly affected by laser diffraction in linear plasma accelerators. Before the laser intensity decreases significantly, the useful acceleration length is limited to a few Rayleigh ranges $z_R = \pi \frac{w_0^2}{\lambda}$, where w_0 is the laser focal spot size and λ its wavelength.
Electron dephasing due to the different velocities of the accelerated beam, moving close to the speed of light, and the plasma wave, which moves at close to the group velocity of the driving laser pulse within the plasma, plays another important role. The beam eventually slips into the decelerating phase of the

wakefield and starts to lose energy thus limiting the useful accelerating distance to the dephasing length [116].

C.2 Beam-Driven Wakefield Acceleration (PWFA)

In beam-driven plasma wakefield acceleration (PWFA), a relativistic, charged particle beam is used as a driver generating the plasma wakefield. Similarly to LWFA, different wakefield regimes can be distinguished depending on the properties of the drive beam. For a bi-Gaussian electron beam, a single value α as the ratio of peak beam density and background density is relevant with a value larger than one designating the blowout regime.

For non-ideal drive bunches of different shape, an additional measure is the reduced charge factor, which defines how much charge the drive bunch carries compared to the maximum charge that can be contained in a plasma skin depth volume [116]:

$$Q_{rc} = Q_{bunch} \frac{k_p^3}{n_0 e}$$

where k_p is the skin depth and Q_{bunch} the bunch charge. Again, values strongly above one indicate a nonlinear response and formation of a full plasma blowout. Values below or around unity, on the other hand, point to a linear or weakly nonlinear wakefield, respectively.

To maximise the accelerating field strength reached in a PWFA stage, the drive beam dimensions can be optimised with an ideal RMS length of $\sigma_z = \sqrt{2}/k_p$. The radius of the bubble structure in the plasma wakefield can be approximated as

$$R_{bubble} = 2.5\sigma_r\sqrt{\alpha}$$

with σ_r the radial transverse beam size [116]. Another important variable for efficient acceleration in a beam-driven plasma accelerator is the transformer ratio R_T, defined as the ratio between maximum accelerating field in the witness bunch and maximum decelerating field in the driver bunch.

It determines the ratio between energy gain by the witness beam and energy loss by the driver, thus determining the maximum energy gain of the witness bunch inside the beam-driven wakefield as $\Delta E_{wit,max} = R_T \Delta E_{driv,max}$ with $\Delta E_{driv,max}$ the average particle energy loss in the driver bunch.

The goal for efficient PWFA is to achieve a high transformer ratio and to continue the acceleration process until the drive beam reaches depletion. As symmetrical drive beams have a limit in R_T of at maximum 2, PWFA setups typically work with asymmetric beams.

Specific ways to reach higher transformer ratio values include, for example, bunch shaping [116].

Bibliography

[1] J. M. Madey. "Stimulated emission of bremmstrahlung in a periodic magnetic field". In: *Journal of Applied Physics* 42, 5 (1971).

[2] G. Dattoli, M. Del Franco, et al. "Introduction to the Physics of Free Electron Laser and Comparison with conventional laser sources". In: *Free Electron Lasers, edited by Sandor Varro* (2012). DOI: 10.5772/35429.

[3] L. R. Elias et al. "Observation of stimulated emission of radiation by relativistic electrons in a spatially periodic transverse magnetic field". In: *Physical Review Letters* 36 (1976), pp. 717–720. DOI: 10.1103/PhysRevLett.36.717.

[4] W. Colson. "The Nonlinear Wave Equation for Free Electron Lasers driven by Single-Particle Currents". In: *Physics Letters* 76A (1980).

[5] W. Colson. "The Nonlinear Wave Equation for Higher Harmonics in Free-Electron Lasers". In: *Journal of Quantum Electronics* 17 (1981).

[6] D. A. G. Deacon et al. "First operation of a Free-Electron Laser". In: *Physical Review Letters* 38 (1977), pp. 892–894. DOI: 10.1103/PhysRevLett.38.892.

[7] A. M. Kondratenko and E. L. Saldin. "Generation of coherent radiation by a relativistic electron beam in an ondulator". In: *Particle Accelerators* 10.3-4 (1980), pp. 207–216.

[8] L. Serafini et al. *MariX Conceptual Design Report.* (2019).

[9] M. Xie. *Design optimization for an X-ray Free Electron Laser Driven by SLAC Linac.* 1996. URL: https://accelconf.web.cern.ch/p95/ARTICLES/TPG/TPG10.PDF.

[10] E. L. Saldin, E. A. Schneidmiller, and M. V. Yurkov. "Statistical properties of radiation from VUV and X-ray free-electron laser". In: *Optics Communications* 148, 4–6 (1998), pp. 383–403.

[11] O. Y. Gorobtsov, G. Mercurio, et al. "Statistical properties of a free-electron laser revealed by Hanbury Brown–Twiss interferometry". In: *Physical Review A* 95, 023843 (2017).

[12] O. Y. Gorobtsov, G. Mercurio, et al. "Seeded X-ray free-electron laser generating radiation with laser statistical properties". In: *Nature Communications* 9:4498 (2018). DOI: 10.1038/s41467-018-06743-8.

[13] G. Dattoli, L. Giannessi, and A. Torre. "Unified view of free-electron laser dynamics and of higher-harmonics electron bunching". In: *Journal of the Optical Society of America B* 10.11 (1993). DOI: 10.1364/JOSAB.10.002136.

[14] G. Dattoli et al. "Dynamical behaviour of a free-electron laser operating with a prebunched electron beam". In: *Physical Review E* 49.6 (1994).

[15] M. Couprie and L. Giannessi. "Seeding Free Electron Lasers with High Order Harmonics Generated in gas". In: *Springer Series in Optical Sciences* 197 (2015). DOI: 10.1007/978-3-662-47443-3_5.

[16] D. Nolle. "FEL operation at the European XFEL facility". In: *Proc. of International Free-Electron Laser Conference FEL'19, Hamburg, Germany* (2019). DOI: 10.18429/JacoW-FEL2019-FRA01.

[17] A. Brachmann, M. Dunham, and J. F. Schmer. "LCLS-II - status and upgrades". In: *Proc. of International Free-Electron Laser Conference FEL'19, Hamburg, Germany* (2019). DOI: 10.18429/JacoW-FEL2019-FRA02.

[18] Z. Zhao, D. Wang, et al. "SCLF: an 8-GeV CW SCRF Linac-based X-ray FEL facility in Shanghai". In: *Proc. of International Free-Electron Laser Conference FEL'17* (2018). DOI: 10.18429/JacoW-FEL2017-MOP055.

[19] F. Ciocci et al. "Design considerations on a high-power VUV FEL". In: *IEEE Journal of Quantum Electronics* 31(7) (1995), pp. 1242–1252.

[20] V. Kumar and S. Krishnagopal. "A simple theory of gain and saturation in FEL oscillators". In: *Nuclear Instruments and Methods in Physics, Research Section A* 407 (1998). DOI: 10.1016/S0168-9002(97)01372-7.

[21] G. Neil. "FEL oscillators". In: *Proc. of Particle Accelerator Conference PAC2003* 1 (2003). DOI: 10.1109/PAC.2003.1288873.

[22] G. Isoyama et al. "Development of FEL and SASE in the far-infrared region at ISIR, Osaka University". In: *Infrared Physics and Technology* 81 (2008), pp. 371–374.

[23] Y. U. Jeong et al. "First lasing of the KAERI compact far-infrared free-electron laser driven by a magnetron-based microtron". In: *Nuclear Instruments and Methods in Physics, Research Section A* 475 (2001), pp. 47–50.

[24] D. Oepts, A. F. G. van der Meer, and P. W. van Amersfoort. "The free-electron-laser user facility FELIX". In: *Infrared Physucs and Technology* 36 (1995), pp. 293–308.

[25] J. M. Ortega and F. Glotin abd R. Prazeres. "Extension in far-infrared of the CLIO free-electron laser". In: *Infrared Physics and Technology* 49 (2006), pp. 133–138.

[26] R. Hajima et al. "Analyses of superradiance and spiking-mode lasing observed at JAERI-FEL". In: *Nuclear Instruments and Methods in Physics, Research Section A* 475 (2021), pp. 270–275.

[27] V. P. Bolotinand others. "Status of the Novosibirsk Terahertz FEL". In: *Proc. of the International Free-Eòectron Laser Conference FEL'04* 226 (2004).

[28] S. Winnerl et al. "FELBE Free-Electron Laser: Status and Application for Time Resolved Spectroscopy Experiments". In: *Proc. of the Joint 31st International Conference on Infrared and Millimeter Waves and 14th International Conference on Terahertz Electronics* (2007).

[29] S. V. Benson et al. "Photon Source Capabilities of the Jefferson Lab FEL". In: *Journal of Physics: Conference Series, 11th International Conference on Synchrotron Radiation Instrumentation* 423 (2013).

[30] M. Singh and J. M. Braat. "Design of multilayer extreme-ultraviolet mirrors for enhanced reflectivity". In: *Applied Optics* 39.13 (2000), pp. 2189–2197. DOI: 10.1364/AO.39.002189.

[31] M. F. Bal, M. Singh, and J. M. Braat. "Optimization of multilayer reflectors for extreme ultraviolet lithography". In: *Journal of Microlithography, Microfabrication and Microsystems* 3.4 (2004).

[32] S. Schröder et al. "EUV reflectance and scattering of Mo/Si multilayers on differently polished substrates". In: *Optics Express* 15, 13997 (2007).

[33] B. Faatz et al. "Regenerative FEL amplifier at the TESLA test facility at DESY". In: *Nuclear Instruments and Methods in Physics, Research Section A* 429.1 (1999), pp. 424–428. DOI: 10.1016/S0168-9002(99)00123-0.

[34] H. P. Freund, P. J. M. Van der Slot, and Y. Shvyd'ko. "An x-ray regenerative amplifier free-electron laser using diamond pinhole mirrors". In: *New Journal of Physics* 21.9 (2019). DOI: 10.1088/1367-2630/ab3f72.

[35] K.-J. Kim, Y. Shvyd'ko, and S. Reiche. "A proposal for an X-ray Free-Electron Laser oscillator with an energy-recovery Linac". In: *Physical Review Letters* 100 (2008). DOI: 10.1103/PhysRevLett.100.244802.

[36] Y. Shvyd'ko et al. "High-reflectivity high-resolution X-ray crystal optics with diamonds". In: *Nature Physics* 6 (2010). DOI: 10.1038/NPHYS1506.

[37] R. R. Lindberg et al. "Performance of the X-ray Free-Electron Laser oscillator with crystal cavity". In: *Physical Review ST Accelerators and Beams* 14, 010701 (2011).

[38] Y. Shvyd'ko and R. R. Lindberg. "Spatiotemporal response of crystals in X-ray Bragg diffraction". In: *Physical Review ST Accelerators and Beams* 15, 100702 (2012).

[39] K. Li and H. Deng. "Systematic design and three-dimensional simulation of X-ray FEL oscillator for Shanghai Coherent Light Facility". In: *Nuclear Instruments and Methods in Physics, Research Section A: Accelerators, Spectrometers, Detectors and Associated Equipment* 895 (2018), pp. 40–47.

[40] R. Bonifacio, F. Casagrande, and G. Casati. "Cooperative and chaotic transition of a free-electron laser: Hamiltonian model". In: *Optics Communications* 40.3 (1982), pp. 219–223. DOI: 10.1016/0030-4018(82)90265-6.

[41] R. Bonifacio, C. Pellegrini, and L. M. Narducci. "Collective instabilities and high-gain regime in a free-electron laser". In: *Optics Communications* 50.6 (1984), pp. 373–378. DOI: 10.1016/0030-4018(84)90105-6.

[42] L. Giannessi et al. "Self-amplified spontaneous emission for a single pass free-electron laser". In: *Physical Rev.iew ST Accelerators and Beams* 14 (2011). DOI: 10.1103/PhysRevSTAB.14.060712.

[43] P. Emma et al. "First lasing and operation of an ångstrom-wavelength free-electron laser". In: *Nature Photonics* 4.9 (2010), pp. 641–647. DOI: 10.1038/nphoton.2010.176.

[44] B. D. Patterson et al. "Coherent science at the SwissFEL X-ray laser". In: *New Journal of Physics* 12(3), 035012 (2010). DOI: 10.1088/1367-2630/12/3/035012.

[45] D. Pile. "First light from SACLA". In: *Nature Photonics* 5, 456 (2011).

[46] B. Faatz and S. Schreiber. "First lasing of FLASH2 at DESY". In: *Synchrotron Radiation News* 27, 6 (2014).

[47] Z. T. Zhao et al. "First lasing of an echo-enabled harmonic generation free-electron laser". In: *Nature Photonics* 6 (2012).

[48] G. Geloni et al. "Frequency-Mixing Lasing Mode at European XFEL". In: *Applied Sciences* 11(18), 8495 (2021). DOI: 10.3390/app11188495.

[49] I. S. Ko et al. "Construction and commissioning of PAL-XFEL facility". In: *Applied Sciences* 7, 479 (2017).

[50] J. Rosenzweig et al. "Generation of ultra-short, high brightness electron beams for single-spike SASE FEL operation". In: *Nuclear Instruments and Methods in Physics, Research Section A* 593, 39 (2008).

[51] A. Marinelli et al. "Experimental demonstration of a single-spike hard-X-ray free-electron laser starting from noise". In: *Applied Physics Letters* 111, 151101 (2017). DOI: 10.1063/1.4990716.

[52] F. Villa et al. "Generation and characterization of ultra-short electron beams for single spike infrared FEL radiation at SPARC_LAB". In: *Nuclear Instruments and Methods in Physics, Research Section A* 865 (2017), pp. 43–46. DOI: 10.1016/j.nima.2017.02.042.

[53] H. Freund et al. "Non-linear harmonic generation and proposed experimental verification in SASE FELs". In: *Nuclear Instruments and Methods in Physics, Research Section A* 445 (2000).

[54] W. Ackermann et al. "Operation of a free-electron laser from the extreme ultraviolet to the water window". In: *Nature Photonics* 1, 336 (2007).

[55] D. Ratner et al. "Second and third harmonic measurements at the linac coherent light source". In: *Physical Review ST Accelerators and Beams* 14 (2011).

[56] S. Benson and J. Madey. "Demonstration of harmonic lasing in a free-electron laser". In: *Physical Review A* 39 (1989).

[57] R. Warren et al. "Lasing on the third harmonic". In: *Nuclear Instruments and Methods in Physics, Research Section A* 296 (1990).

[58] R. Hajima et al. "Third-harmonic lasing at JAERI-FEL". In: *Nuclear Instruments and Methods in Physics, Research Section A* 475 (2001).

[59] B. W. J. McNeil et al. "Harmonic lasing in an FEL amplifier". In: *Proc. of International Free Electron Laser Conference FEL'15, Stanford, California* C0508213 (2015).

[60] E. A. Schneidmiller and M. V. Yurkov. "Harmonic lasing in X-ray free-electron lasers". In: *Physical Review ST Accelerators and Beams* 15, 080702 (2012).

[61] A. A. Zholents. "Method of an enhanced self-amplified spontaneous emission for x-ray free electron lasers". In: *Physical Review ST Accelerators and Beams* 8, 040701 (2005).

[62] Z. Zhang et al. "Experimental demonstration of enhanced self-amplified spontaneous emission by photocathode temporal shaping and self-compression in a magnetic wiggler". In: *New Journal of Physics* 22, 083030 (2020).

[63] N. R. Thompson, B. W. J. McNeil, and J. Dunning. "High Brightness SASE Operation of X-ray FELs". In: *Physics Procedia* 52 (2014), pp. 52–61. DOI: 10.1016/j.phpro.2014.06.009.

[64] L. Giannessi et al. "Self-amplified spontaneous emission free-electron laser with an energy-chirped electron beam and undulator tapering". In: *Physical Review Letters* 106.14 (2011).

[65] E. L. Saldin et al. "Self-amplified spontaneous emission FEL with energy-chirped electron beam and its application for generation of attosecond x-ray pulses". In: *Physical Review ST Accelerators and Beams* 9 (2006).

[66] R. Bonifacio et al. "Physics of the High-Gain FEL and Superradiance". In: *Rivista del nuovo cimento* 13.9 (1990).

[67] S. Reiche. "Overview of seeding methods for FELs". In: *Proc. of International Particle Accelerator C onference IPAC2013, Shangai, China* (2013).

[68] L. Giannessi. "Seeding and Harmonic Generation in Free-Electron Lasers". In: *Springer, Synchrotron Light Sources and Free-Electron Lasers* (2016). DOI: 10.1007/978-3-319-04507-8_3-1.

[69] M. Labat et al. "Pulse Splitting in short wavelength seeded Free Electron Lasers". In: *Physical Review Letters* 103(26), 26480 (2009).

[70] L. Giannessi et al. "High-Order-Harmonic Generation and Superradiance in a Seeded Free-Electron Laser". In: *Physical Review Letters* 108, 164801 (2012). DOI: 10.1103/PhysRevLett.108.164801.

[71] E. Allaria et al. "The FERMI free-electron lasers". In: *Journal of Synchrotron Radiation* 22 (2015), pp. 485–491. DOI: 10.1107/S1600577515005366.

[72] Z. Tong et al. "FEL Polarization Control Studies on Dalian Coherent Light Source". In: *Chinese Physics C* 37(11) (2013). DOI: 10.1088/1674-1137/37/11/118101.

[73] G. Lambert et al. "Seeding high gain harmonic generation with laser harmonics produced in gases". In: *Proc. of the International Free-Electron Laser Conference FEL'04* (2004), pp. 153–158.

[74] L.-H. Yu et al. "High-Gain Harmonic Generation Free Electron Laser". In: *Science* 289 (2000).

[75] G. Stupakov. "Echo-enabled harmonic generation for seeded FELs". In: *Proc. of SPIE 8078, Advances in X-ray Free-Electron Lasers: Radiation Schemes, X-ray Optics, and Instrumentation* (2011).

[76] G. Stupakov. "Using the Beam-Echo effect for generation of short-wavelength radiation". In: *Physical Review Letters* 102 (2009).

[77] J. Felhaus, E. Saldin, et al. "Possible application of X-ray optical elements for reducing the spectral bandwidth of an X-ray SASE FEL". In: *Optics Communications* 140 (1997).

[78] G. Geloni, V. Kocharyan, and E. Saldin. "A novel self-seeding scheme for hard X-ray FELs". In: *Journal of Modern Optics* 58 (2011), pp. 1391–1403.

[79] M. Yabashi and T. Tanaka. "Self-seeded FEL emits hard X-rays". In: *Nature Photonics* 6 (2012), pp. 648–649. DOI: 10.1038/nphoton.2012.237.

[80] E. Allaria et al. "Two stage seeded soft X-Ray Free Electron Laser". In: *Nature Photonics* (2013).

[81] Ben-Zvi, K. M. Yang, and L. H. Yu. “The "fresh-bunch" technique in FELs”. In: *Nuclear Instruments and Methods in Physics, Research Section A* 318 (1992), pp. 726–729. DOI: 10.1016/0168-9002(92)91147-2.

[82] L.-H. Yu and I. Ben-Zvi. “High-gain harmonic generation of soft x-rays with the fresh-bunch technique”. In: *Nuclear Instruments and Methods in Physics, Research Section A* (1997).

[83] In: ().

[84] L.-H. Yu et al. “First ultraviolet high-gain harmonic generation free electron laser”. In: *Physical Review Letters* 91 (2003).

[85] G. Lambert et al. “High harmonics from gas, a suitable source for seeding FEL from the vacuum-ultraviolet to soft X-ray region”. In: *Proc. of the International Free-Electron Laser Conference FEL'11, Shangai, China* MOOB12 (2011).

[86] F. Ciocci et al. “Proposition of Experiment at SPARC: harmonic generation seeded by high order harmonics produced in gas”. In: *SPARC-FEL-04/005 Report* (2004).

[87] M. Labat et al. “High-Gain harmonic generation free-electron laser seeded by harmonics generated in gas”. In: *Physical Review Letters* 107 (2011).

[88] L. Giannessi et al. “First lasing of FERMI FEL-2 (1st stage) and FERMI FEL-1 recent results”. In: *Proc. of the International Free-Electron Laser Conference FEL'12, Nara* (2012).

[89] B. Liu et al. “Demonstration of a widely-tunable and fully-coherent high-gain harmonic-generation free-electron laser”. In: *Physical Review ST Accelerators and Beams* 16, 020704 (2013). DOI: 10.1103/PhysRevSTAB.16.020704.

[90] A. S. Artamonov et al. “The first experiments with an optical klystron installed on the VEPP-3 storage ring”. In: *Nuclear Instruments and Methods in Physics, Research Section A* 177.1 (1980). DOI: 10.1016/0029-554X(80)90557-1.

[91] V. N. Livtinenko et al. “Operation of the OK-4/Duke storage ring FEL below 200nm”. In: *Nuclear Instruments and Methods in Physics, Research Section A* 475.1 (2001). DOI: 10.1016/S0168-9002(01)01559-5.

[92] Y. Ding et al. “Optical klystron enhancement to self-amplified spontaneous emission free electron lasers”. In: *Physical Review ST Accelerators and Beams* 9 (7 2006), p. 070702. DOI: 10.1103/PhysRevSTAB.9.070702. URL: https://link.aps.org/doi/10.1103/PhysRevSTAB.9.070702.

[93] G. Penco et al. "Experimental Demonstration of Enhanced Self-Amplified Spontaneous Emission by an Optical Klystron". In: *Physical Review Letters* 114 (1 2015), p. 013901. DOI: 10.1103/PhysRevLett.114.013901. URL: https://link.aps.org/doi/10.1103/PhysRevLett.114.013901.

[94] G. Paraskaki et al. "Optimization and stability of a high-gain harmonic generation seeded oscillator amplifier". In: *Physical Review ST Accelerators and Beams* 24, 034801 (2021).

[95] G. Paraskaki et al. "Advanced schemes to generate MHz, fully coherent FEL pulses at nm wavelength". In: *Applied Sciences* 11, 6058 (2021).

[96] G. Paraskaki, E. Allaria, et al. "High repetition rate seeded free-electron laser with an optical klystron in high-gain harmonic generation". In: *Physical Review ST Accelerators and Beams* 24, 120701 (2021).

[97] S. Ackermann et al. "Novel method for the generation of stable radiation from free-electron lasers at high repetition rates". In: *Physical Review ST Accelerators and Beams* 23, 071302 (2020).

[98] J. Yan et al. "Self-Amplification of Coherent Energy Modulation in Seeded Free-Electron Lasers". In: *Physical Review Letters* 126, 084801 (2021).

[99] D. Xiang, G. Stupakov, et al. "First demonstration of the Echo-enabled harmonic generation technique for short wavelength seeded free electron lasers". In: *Physical Review Letters* 105 (2010).

[100] G. Penn. "Stable, coherent free-electron laser pulses using echo-enabled harmonic generation". In: *Physical Review Accelerators and Beams* 17 (2014).

[101] C. Evain, M.-E. Couprie, et al. "Study of high harmonic generation at synchrotron soleil using echo-enabling technique". In: *Proc. of the International Particle Accelerator Conference IPAC2010, Kyoto, Japan* (2010).

[102] D. Xiang, Z. Huang, et al. "Feasibility study for a seeded hard x-ray source based on a two-stage echo-enabled harmonic generation FEL". In: *Proc. of the International Free-Electron Laser Conference FEL'08, Liverpool, UK* (2009).

[103] M. Dunning et al. "A proof-of-principle echo-enabled harmonic generation experiment at SLAC". In: *Proc. of the International Particle Accelerator Conference IPAC2010, Kyoto, Japan* TUPE069 (2010).

[104] P. R. Ribič et al. "Coherent soft X-ray pulses from an echo-enabled harmonic generation free-electron laser". In: *Nature Photonics* 13 (2019), pp. 555–561. DOI: 10.1038/s41566-019-0427-1.

[105] H. Yang et al. "Optimization and stability analysis of the cascaded EEHG-HGHG free-electron laser". In: *Nuclear Instruments and Methods in Physics, Research Section A* 1039, 167065 (2022). DOI: 10.1016/j.nima.2022.167065.

[106] V. Miltchev, J. Rossbach, et al. "Simulation studies on the self-seeding option at FLASH". In: *Proc. of the International Free-Electron Laser Conference FEL'06, Berlin, Germany* (2006).

[107] C. Bostedt et al. "Ultra-fast and ultra-intense x-ray sciences: first results from the Linac Coherent Light Source free-electron laser". In: *Journal of Physics B: Atomic, Molecular and Optical Physics* 46(16):164003 (2013). DOI: 10.1088/0953-4075/46/16/164003.

[108] E. Saldin et al. "X-ray FEL with a meV bandwidth". In: *Nuclear Instruments and Methods in Physics, Research Section A* 475 (2001).

[109] J. Amann et al. "Demonstration of self-seeding in a hard X-ray free-electron laser". In: *Nature Photonics* 6 (2012).

[110] J. Wu, A. Marinelli, and C. Pellegrini. "Generation of longitudinally coherent ultra high power X-ray FEL pulses by phase and amplitude mixing". In: *Proc. of the International Free-Electron Laser Conference FEL'11, Japan* (2012).

[111] H. Podlech. "Superconducting versus normal conducting cavities". In: (2013). DOI: 10.5170/CERN-2013-001.151.

[112] A. Bacci et al. "Two-pass two-way acceleration in a superconducting continuous wave linac to drive low jitter x-ray free electron lasers". In: *Physical Review Accelerators and Beams* 2, 111304 (2019).

[113] A. Bacci et al. "GeV-Class Two-Fold CW Linac Driven by an Arc-Compressor". In: *Instruments* 3, 54 (2019). DOI: 10.3390/instruments3040054.

[114] M. Tigner. "A possible apparatus for electron clashing-beam experiments". In: *Nuovo Cimento* 37, 1228 (1965).

[115] J. Sekutowicz et al. "Proposed continuous wave energy recovery operation of an x-ray free electron laser". In: *Physical Review Accelerators and Beams* 8, 010701 (2005).

[116] R. W. Assmann et al. *EuPRAXIA Conceptual Design Report*. 2019. URL: http://www.eupraxia-project.eu/eupraxia-conceptual-design-report.html.

[117] B. Hidding et al. *Plasma Wakefield Accelerator Research 2019 - 2040: A communitydriven UK roadmap compiled by the Plasma Wakefield Accelerator Steering Committee (PWASC) 2019*. 2019.

[118] T. Tajima and J. M. Dawson. "Laser Electron Accelerator". In: *Physical Review Letters* 43, 267 (1979). DOI: 10.1103/PhysRevLett.43.267.

[119] C. Joshi and A. Caldwell. "12.1 Plasma Accelerators". In: *Book 'Accelerators and Colliders'* (2013). DOI: 10.1007/978-3-642-23053-0_47.

[120] R. Bingham. "Basic Concepts in Plasma Accelerators". In: *Philosophical Transactions of The Royal Society A Mathematical Physical and Engineering Sciences* 364(1840) (2006). DOI: 10.1098/rsta.2005.1722.

[121] R. Pompili et al. "Energy spread minimization in a beam-driven plasma wakefield accelerator". In: *Nature Physics* 17 (2021), pp. 499–503.

[122] W. Wang et al. "Free-electron lasing at 27 nanometers based on a laser wakefield accelerator". In: *Nature* 595 (2021), pp. 516–520. DOI: 10.1038/s41586-021-03678-x.

[123] R. Pompili et al. "Free-electron lasing with compact beam-driven plasma wakefield accelerator". In: *Nature* 605 (2022), pp. 659–662. DOI: 10.1038/s41586-022-04589-1.

[124] V. Petrillo et al. "Coherent, high repetition rate tender X-ray Free-Electron Laser seeded by an Extreme Ultra-Violet Free-Electron Laser Oscillator". In: *New Journal of Physics* 22, 073058 (2020). DOI: 10.1088/1367-2630/ab9bbf.

[125] L. Serafini et al. "MariX, an advanced MHz-class repetition rate X-ray source for linear regime time-resolved spectroscopy and photon scattering". In: *Nuclear Instruments and Methods in Physics, Research Section A* (2019). DOI: 10.1016/j.nima.2019.03.096.

[126] E. Karantzoulis et al. "ELETTRA status and future prospects". In: *Proc. of the International Particle Accelerator Conference IPAC2015* (2015).

[127] S. Di Mitri. "Feasibility study of a periodic arc compressor in the presence of coherent synchrotron radiation". In: *Nuclear Instruments and Methods in Physics, Research Section A: Accelerators, Spectrometers, Detectors and Associated Equipment* 806 (2016).

[128] S. Di Mitri and M. Cornacchia. "Transverse emittance-preserving arc compressor for high-brightness electron beam-based light sources and colliders". In: *EPL (Europhysics Letters)* 109(6): 62002 (2015).

[129] M. Rossetti Conti et al. "Optimization of the arc compressor performance in the MariX free electron laser". In: *Journal of Physics: Conference Series* 1596, 012035 (2020).

[130] F. Ciocci et al. "Segmented undulator operation at the SPARC-FEL test facility". In: *International Society for Optics and Photonics, Advances in X-ray Free-Electron Lasers Instrumentation III* 9512 (2015).

[131] D. Giove, L. Serafini, et al. *BriXSinO Technical Design Report*. 2022. URL: https://marix.mi.infn.it/wp-content/uploads/2022/04/BriXSino_TDR.pdf.

[132] V. Petrillo et al. "High brilliance Free-Electron Laser Oscillator operating at multi-MegaHertz repetition rate in the short-TeraHertz emission range". In: *Nuclear Instruments and Methods in Physics, Research Section A: Accelerators, Spectrometers, Detectors and Associated Equipment* (2022). DOI: 10.1016/j.nima.2022.167289.

[133] V. N. Litvinenko, R. Hajima, and D. Kayran. "Merger designs for ERLs". In: *Nuclear Instruments and Methods in Physicsm Research Section A* 557, 1 (2006), pp. 165–175.

[134] C. Gulliford and D. Kayran. "Demonstration of low emittance in the Cornell energy recovery linac injector prototype". In: *Physical Review ST Accelerators and Beams* 16, 073401 (2013).

[135] A. Bacci, V. Petrillo, and M. Rossetti Conti. "GIOTTO: a genetic code for demanding Beam-dynamics optimizations". In: *Proc. of the 7th International Particle Accelerator Conference IPAC2016, Busan, Korea* (2016), pp. 3073–3076.

[136] M. Placidi et al. "Compact FEL-driven inverse compton scattering gamma-ray source". In: *Nuclear Instruments and Methods in Physicsm Research Section A* 855 (2017), pp. 55–60.

[137] R. W. Assmann et al. "Eupraxia conceptual design report". In: *Eur. Phys. J. Spec. Top.* 229 (2020), pp. 3675–4284.

[138] M. Ferrario et al. *EuPRAXIA@SPARC_LAB Conceptual Design Report*. 2018. URL: http://sparclab.lnf.infn.it/sparc_lab-home/eupraxiasparc_lab/.

[139] AD. Nguyen, S. Russell, and N. Moody. *U. S. Particle Accelerator School 2009, Theory and Practice of Free-Electron Lasers Day 2*. 2009. URL: https://uspas.fnal.gov/materials/09UNM/Day\%202.pdf.

[140] K.-J. Kim and Y. Shvyd'ko. "unable optical cavity for an X-ray Free-Electron Laser Oscillator". In: *Physical Review ST Accelerators and Beams* 12, 030703 (2009).

[141] Z.-Y. Zhao, H.-T. Li, and Q.-K. Jia. "Cavity Length Adjustment and Output FEL Intensity Optimization". In: *IEEE Journal of Quantum Electronics* 27(11) (1991), pp. 2370–2372. DOI: 10.1109/3.100874.

[142] C.L. Andrews. "Demonstration of Babinet's Principle". In: *American Journal of Physics* 39, 122 (1971).

[143] P. J. M. Van der Slot et al. "Time-dependent Three dimensional simulation of free-electron laser oscillators". In: *Physical Review Letters* 102, 24480 (2009).

[144] Z. Huang and R. D. Ruth. "Fully coherent X-ray pulses from a Regenerative-Amplifier Free-Electron Laser". In: *Physical Review Letters* 96, 144801 (2006).

[145] B. W. J. McNeill et al. "A design for the generation of temporally-coherent radiation pulses in the VUV and beyond by a self-seeded high gain free electron laser amplifier". In: *New Journal of Physics* 9, 239 (2007).

[146] P. A. Belanger. "Beam propagation and the ABCD ray matrices". In: *Optics Letters* 16 196 (1991).

[147] S. Reiche. "GENESIS 1.3: a fully 3D time-dependent FEL simulation code". In: *Nuclear Instruments and Methods in Physics, Research Section A: Accelerators, Spectrometers, Detectors and Associated Equipment* 429 243 (1999).

[148] W. Xu and H. Xu. "Review of the high-power vacuum tube microwave sources based on Cherenkov radiation". In: (2021). URL: https://arxiv.org/ftp/arxiv/papers/2003/2003.04288.pdf.

[149] A. Acharyya and J. P. Banerjee. "Prospects of IMPATT devices based on wide bandgap semiconductors as potential terahertz sources". In: *Applied Nanosciences* 4.11 (2014).

[150] Y. Ochi et al. "Yb:YAG thin-disk chirped pulse amplification laser system for intense terahertz pulse generation". In: *Optics Express* 23 (2015), pp. 15057–15064.

[151] Y. S. Lee. "Principles of Terahertz Science and Technology". In: *Springer, Berlin/Heidelberg, Germany* (2009).

[152] C. Koral et al. "Multi-pass Free-Electron Laser-assisted spectral and imaging applications in the THz/FIR range using the future superconducting electron source BriXSinO". In: *Frontiers of Physics* 10: 172590 (2022). DOI: 10.3389/fphy.2022.725901.

[153] I. Drebot et al. "BriXSinO High-Flux Dual X-Ray and THz Radiation Source Based on Energy Recovery Linacs". In: *Proc. of the International Particle Accelerator Conference IPAC2022* (2022).

[154] A. Curcio et al. "Free electron laser oscillator efficiency". In: *Optics Communications* 425 (2018), pp. 29–37.

[155] R. Hajima et al. "Analyses of superradiance and spiking-mode lasing observed at JAERI-FEL". In: *Nuclear Instruments and Methods in Physics, Research Section A* 475 (2021), pp. 270–275.

[156] P. L. Ottaviani et al. "Deep saturated Free Electron Laser oscillators and frozen spikes". In: *Nuclear Instruments and Methods in Physics, Research Section A* 834 (2016), pp. 108–117.

[157] M. Opromolla and V. Petrillo. "Two Color TeraHertz Radiation by a Multi-Pass FEL Oscillator". In: *Applied Sciences* 11, 6495 (2021).

[158] R. Prazeres et al. "Two-colour operation and applications of the CLIO FEL in the mid-infrared range". In: *Nuclear Instruments and Methods in Physics, Research Section A* 407 (1998), pp. 464–469.

[159] V. Petrillo et al. "Synchronised TeraHertz Radiation and Soft X-rays Produced in a FEL Oscillator". In: *Applied Sciences* (2022). DOI: 10.3390/app12168341.

[160] N. S. Mirian, M. Opromolla, et al. "High repetition rate and coherent Free-Electron Laser in the tender X-rays based on the Echo-Enabled Harmonic Generation of an Ultra-Violet Oscillator pulse". In: *Physical Review Accelerators and Beams* 24, 050702 (2021).

[161] Q. Huang et al. "High efficiency structured EUV multilayer mirror for spectral filtering of long wavelengths". In: *Journal of Optical Society of America* 22 (2014), pp. 19365–19374.

[162] A. A. Zameshin et al. "Angular and spectral bandwidth of EUV multilayers near spacer material absorption edges". In: *Journal of Nanoscience and Nanotechnology* 19, 602 (2019).

[163] M. Opromolla et al. "High Repetition Rate and Coherent Free-Electron Laser Oscillator in the Tender X-ray range tailored for linear spectroscopy". In: *Applied Sciences* 11, 5892 (2021). DOI: 10.3390/app11135892.

[164] *Software XOP, Download from European Synchrotron Radiation Facility Website*. accessed on 1 May 2020. URL: https://www.esrf.fr/Instrumentation/software/data-analysis/xop2.4.

[165] R. Margraf et al. "Ringdown Demonstration of a Low-Loss 14 m Hard X-Ray Cavity". In: *presented at the International Free-Electron Laser FEL2022, Trieste, Italy* THBO3 (2022).

[166] M. Veronese et al. "Intra Undulator Screen Diagnostics for the FERMI@Elettra FEL". In: *Proc. of IBIC2012* TUPB76 (2012).

[167] F. Capotondi et al. "Multipurpose end-station for coherent diffraction imaging and scattering at FERMI@Elettra free-electron laser facility". In: *Journal of Synchrotron Radiation* 22 (2015), pp. 544–552.

[168] J. Bodewadt, J. RoBdach, and E. Hass. "Commissioning Results of the Photon–Electron Diagnostic Unit at SFLASH". In: *Proc. of DIPAC2011* MOPD54 (2011).

[169] D. Xiang and G. Stupakov. "Echo-enabled harmonic generation free electron laser". In: *Physical Review ST Accelerators and Beams* (2009).

[170] *SPARC_LAB Website*. URL: http://sparclab.lnf.infn.it/.

[171] M. Ferrario et al. "SPARC_LAB present and future". In: *Nuclear Instruments and Methods B* 309 (2013), pp. 183–188.

[172] *CompactLight Project*. URL: https://www.compactlight.eu/Main/Objectives.

[173] L. Serafini and M. Ferrario. "Velocity bunching in photo-injectors". In: *AIP Conference Proceedings* 581 (2001), pp. 87–106.

[174] M. Ferrario et al. "Experimental demonstration of emittance compensation with velocity bunching". In: *Physical Review Letters* 104, 054801 (2010).

[175] M. Ferrario et al. "Laser comb with velocity bunching: Preliminary results at SPARC". In: *Nuclear Instruments and Methods in Physics, Research Section A* 637 (2011). DOI: 10.1016/j.nima.2010.02.018.

[176] F. Villa et al. "Laser pulse shaping for multi-bunches photoinjectors". In: *Nuclear Instruments and Methods in Physics, Research Section A* 740 (2014). DOI: 10.1016/j.nima.2013.11.060.

[177] S. Romeo et al. "Beam-based characterization of plasma density in a capillary-discharge waveguide". In: *AIP Advances* 11 (2021). DOI: 10.1063/5.0051423.

[178] A. Biagioni et al. "Gas-filled capillary-discharge stabilization for plasma-based accelerators by means of a laser pulse". In: *Plasma Physocs Control. Fusion* 63 (2021). DOI: 10.1088/1361-6587/ac1f68.

[179] F. Filippi et al. "Plasma density characterization at SPARC_LAB through Stark broadening of Hydrogen spectral lines". In: *Nuclear Instruments and Methods in Physics, Research Section A* 829 (2016). DOI: 10.1016/j.nima.2016.02.071.

[180] A. Biagioni et al. "Temperature analysis in the shock waves regime for gas-filled plasma capillaries in plasma-based accelerators". In: *Journal of Instruments* 14, C03002 (2019).

[181] A. Biagioni et al. "Wake fields effects in dielectric capillary". In: *Nuclear Instruments and Methods in Physics, Research Section A* 909 (2018). DOI: 10.1016/j.nima.2018.01.028.

[182] R. Pompili et al. "Compact and tunable focusing device for plasma wakefield acceleration". In: *Review of Scientific Instruments* 89, 033302 (2018).

[183] M. Galletti et al. "Advanced Stabilization Methods of Plasma Devices for Plasma-Based Acceleration". In: *Symmetry* 14 (2022). DOI: 10.3390/sym14030450.

[184] V. Shpakov et al. "First emittance measurement of the beam-driven plasma wakefield accelerated electron beam". In: *Physical Review Accelerators and Beams* 24, 051301 (2021).

[185] C. Vicario et al. "Commissioning of the laser system for the seeding experiment at SPARC". In: *EUROFEL-Report-2007-DS4-093* (2007).

[186] M. Labat et al. "Seeding experiments at SPARC". In: *Proc. of the International Free-Electron Laser Conference FEL'09, Liverpool UK* (2009).

[187] L. Giannessi. "Superradiant cascade in a seeded free-electron laser". In: *Physical Review Letters* 110 (2013).

[188] M. Labat et al. "Commissioning of the HHG source at SPARC". In: *EUROFEL-Report-2007-DS4-094* (2007).

[189] L. Giannessi et al. "Implementing a HHG Laser as seed in a HGHG-FEL". In: *EUROFEL-Report-2007-DS4-094* (2007).

[190] V. Petrillo et al. "Observation of Time-Domain Modulation of Free-Electron-Laser Pulses by Multipeaked Electron-Energy Spectrum". In: *Physical Review Letters* 111, 114802 (2013). DOI: 10.1103/PhysRevLett.111.114802.

[191] L. Poletto et al. "Spectral and intensity diagnostics of the SPARC free-electron-laser". In: *Journal of Physics: Conference Series* 425 (2013). DOI: 10.1088/1742-6596/425/12/122011.

[192] M. Ferrario et al. "EuPRAXIA@SPARC_LAB design study towards a compact FEL facility at LNF". In: *Nuclear Instruments and Methods in Physics, Research Section A* 909 (2018), pp. 134–138.

[193] M. Galletti et al. "Stable oepration of a free-electron laser driven by a plasma accelerator". In: *Physical Review Letters* (2022).

[194] N. S. Mirian et al. "Generation and measurement of intense few-femtosecond superradiant extreme-ultraviolet free-electron laser pulses". In: *Nature Photonics* 15 (2021). DOI: 10.1038/s41566-021-00815-w.

[195] C. Vaccarezza et al. "EUPRAXIA@SPARC_Lab: beam dynamics studies for the X-band Linac". In: *Nuclear Instruments and Methods in Physics, Research Section A* 909 (2018), pp. 314–317.

[196] V. Petrillo et al. "Free electron laser in the water window with plasma driven electron beams". In: *Nuclear Instruments and Methods in Physics, Research Section A* 909 (2018), pp. 303–308.

[197] F. Villa et al. "ARIA - A VUV Beamline for EuPRAXIA@ SPARC_LAB". In: *Condensed Matter* (2022).

[198] F. Nguyen et al. "FEL performance of the EuPRAXIA@SPARC_LAB AQUA beamline". In: *Proc. of the International Free-Electron Laser Conference FEL'22, Trieste, Italy* MOP46 (2022).

[199] M. Opromolla et al. "ARIA - A VUV Beamline for EuPRAXIA@ SPARC_LAB". In: *Proc. of the International Free-Electron Laser Conference FEL'22, Trieste, Italy* TUP75 (2022).

[200] E. Ferrari et al. "Widely tunable two colour seeded free electron laser source for resonant pump resonant probe magnetic scattering". In: *Nature Communications* 7, 10343 (2016).

[201] M. Bogana et al. "Leaving the fullerene road: presence and stability of sp chains in sp2 carbon clusters and cluster-assembled solids". In: *New Journal of Physics* 7, 81 (2005).

[202] Y. Chang et al. "Tunable VUV photochemistry using vacuum ultraviolet free electron laser combined with H-atom Rydberg tagging time of-flight spectroscopy". In: *Review of Scientific Instruments* 89, 063113 (2018).

[203] F. R. Elder et al. "Radiation from electrons in a synchrotron". In: *Physical Review* 71 (1947), pp. 829–830. DOI: 10.1103/PhysRev.71.829.5.

[204] A. L. Robinson et al. "Hystory of Synchrotron Radiation". In: *Synchrotron Radiation News* 28.4 (2015), pp. 4–9. DOI: 10.1080/08940886.2015.1059228.

[205] P. F. Tavares et al. "The MAXIV storage ring project". In: *Journal of Synchrotron Radiation* 21.5 (2014), pp. 862–877. DOI: 10.1107/81600577514011503.

[206] I. V. Agapov et al. "Status of the PETRA IV project". In: *Proc. of the International Particle Accelerator Conference IPAC2019, Melbourne, Australia* (2019), pp. 1404–1407. DOI: 10.18429/JaCoW-IPAC2019-TUPGW011.

[207] K. Wille. "The physics of particle accelerators". In: *Oxford Univ. Press* (2000). URL: https://catalogue.library.cern/literature/ct722-yam11.

[208] S. Di Mitri. "On the Importance of Electron Beam Brightness in High Gain Free Electron Lasers". In: *Photonics* 2.2 (2015), pp. 317–341. DOI: 10.3390/photonics2020317.

[209] A. B. Temnykh. "Delta undulator for Cornell energy recovery linac". In: *Physical Review ST Accelerators and Beams* 11 (2008).

[210] *PSI-SwissFEL Conceptual Design Report*. URL: https://www.psi.ch/swissfel/HomeEN/SwissFEL_CDR__v19_03.03.11-small.pdf.